Institut für Theoretische Physik
Fakultät Mathematik und Naturwissenschaften
Technische Universität Dresden

Simulation of signal and background processes for collider experiments

Dissertation
zur Erlangung des akademischen Grades
Doctor rerum naturalium

vorgelegt von
Steffen Schumann
geboren am 4. Mai 1978 in Dresden

Dresden 2008

Eingereicht am 20. September 2007

1. Gutachter: Prof. Dr. Michael Kobel

2. Gutachter: Dr. Frank Krauss

3. Gutachter: Dr. Michelangelo L. Mangano

Verteidigt am 18. Januar 2008

Contents

Dedicated to the memory of Prof. Dr. Gerhard Soff, 1949 - 2004.

1 Introduction

With the start-up of the Large Hadron Collider (LHC) at CERN in early 2008 accelerator based particle physics will enter a new era. This machine will provide proton–proton collisions at centre-of-mass energies of 14 TeV with tremendous luminosity. Designed like this the LHC will allow for very precise tests of our current standard explanation theory for particle physics phenomena, the Standard Model (SM), that provides a quantum field theoretic description of the strong, weak and electromagnetic interactions.

The major task at the LHC will be to reveal the nature of electroweak symmetry breaking. In the framework of the SM this is accomplished by the Higgs mechanism, leading to the prediction of a fundamental scalar Higgs particle, which, however, has not been discovered yet. There are strong reasons to believe that the SM is not the ultimate theory, in fact, it can be expected that new physics will appear at the TeV scale, which will directly be probed for the first time at the LHC. So despite the enormous success of the SM so far, one must think about possible extensions of the theory. These extensions, however, have to embed the SM as the effective field theory below the electroweak scale what yields stringent bounds on the nature of physics beyond the SM.

Possible scenarios for new physics include extensions of the theory's Higgs sector or the introduction of additional heavy states like a fourth fermion generation or extra gauge bosons. Lots of attention is currently being paid to models where additional spatial dimensions are considered and that try to incorporate the fourth fundamental force in nature, gravity. Maybe the most prominent and for sure the most studied new physics hypothesis is weak-scale supersymmetry. It can account for the naturalness problem of the SM and provides an attractive road towards a unification of the electroweak and strong interactions. Considering supersymmetry (SUSY) as a local symmetry it can naturally embed gravity. In its minimal version global supersymmetry introduces a partner for each SM field with identical quantum numbers and mass and differing only in spin by one-half unit. Since so far there exists no experimental evidence for any supersymmetric particle – if realised in nature – the symmetry must be broken. In typical supersymmetric models the newly introduced particles then will obtain masses around the TeV scale.

The occurrence of additional heavy states that rapidly decay once produced in a collider experiment is generic for many extensions of the SM. As a consequence the signatures for new

physics will often consist of many-particle final states that need to be precisely understood in order to gain some confidence about the existence of physics beyond the SM. The theoretical modelling of such complex multi-particle final states is a rather complicated task. It requires techniques for carrying out a multitude of multi-leg matrix-element calculations that have to be supplemented with models that account for the experimental environment. This is an issue especially at hadron colliders, where *every* hard production process is accompanied by additional QCD radiation due to the presence of coloured partons in the initial state.
Besides the need for a sophisticated description of presumed physics beyond the SM the quality of the SM predictions, that will always constitute a "background" for new phenomena, has to be considerably improved. The most urgent issue is to provide a better description of QCD dynamics in the theoretical tools, that are used to develop strategies to look for deviations from the SM in the data, or to extract SM parameters from the measurements – the Monte Carlo event generators.

1.1 Physics simulation for future colliders

As indicated in the above, the new generation of collider experiments (being the LHC or a potential new e^+e^- collider operated at $\sqrt{s} = 500$ GeV or higher) requires a new generation of theoretical tools for the modelling of multi-particle final states from production processes within or beyond the SM.
In the past decades, such simulation programs, known as multi-purpose Monte Carlo event generators, have played a significant rôle in analysing the measured data and comparing it with theoretical predictions. Event generators decompose the scattering process into a sequence of different stages, which can be characterised by different energy scales. The enormous success of these tools, like FORTRAN PYTHIA [1, 2] or HERWIG [3, 4], in describing a full wealth of various experimental data confirms this decomposition as a valid approach. Typically a scattering event is considered to contain a $2 \to 2$ hard interaction at a rather high scale. The coloured initial- and final-state particles participating in the scattering then undergo parton showering, thereby accounting for QCD bremsstrahlung. The shower evolution is stopped at scales of order Λ_{QCD}, where phenomenological hadronisation models are imposed to transform the produced partons into primary hadrons, that subsequently decay into the final states as they are observed in the detectors. Besides the hard scattering, in hadron–hadron collisions the interaction of the left-over beam remnants needs to be considered, what is known as the underlying event.
To meet the new challenges posed by the new experiments, the traditional event generators HERWIG and PYTHIA are being rewritten in C++. Their new versions are called HERWIG++ [5] and PYTHIA8 [6]. There exists now a third independent approach for a multi-purpose Monte Carlo generator, called SHERPA [7], that will briefly be introduced in the next section. Apart from the need for better transparency and modularity, the construction of new event

generators is driven by the development of new physics models for the various aspects of event generation.
For HERWIG++ a new parton-shower algorithm has been developed that uses an angular variable for the ordering of subsequent emissions and has a sophisticated treatment of finite parton masses [8]. Furthermore, a modified version of the old cluster hadronisation model has been constructed [9]. The simulation of production processes beyond the SM will no longer have to rely on the explicite implementation of a corresponding matrix element, instead a library to automatically construct $2 \to 2$ processes from a set of generic interaction vertices has been incorporated [10].
The PYTHIA8 project is less far developed. However, revised models for parton showering and the underlying event, cf. Ref. [11], have been constructed and implemented into the latest FORTRAN version PYTHIA 6.4 [2] and will soon be incorporated also in PYTHIA8.
There have been lots of efforts over the past few year to incorporate also higher-order corrections into event generators. One major research line thereby aims at the matching of next-to-leading-order (NLO) QCD calculations with initial- and final-state parton showers [12, 13, 14, 15]. Besides various feasibility studies [16, 17, 18, 19] this has led to the publicly available MC@NLO generator [20]. Within MC@NLO NLO calculations for a decent list of processes can be supplemented with the FORTRAN HERWIG parton shower, hadronisation and underlying event description. In this approach the inclusive production rate for a given process is correct at the next-to-leading order and the first emission is appropriately described through the exact real emission matrix element. An alternative approach relies on the combination of tree-level matrix elements for different numbers of final-state partons and their merging with the parton showers, cf. Chapter 2. This method yields inclusive production rates at the leading order only but several final-state jets can be described through corresponding tree-level matrix elements. Such an algorithm has been implemented in the SHERPA generator, that will be discussed in the following.

1.2 The SHERPA Monte Carlo

Likewise HERWIG and PYTHIA, SHERPA, acronym for Simulation of High Energetic Reactions of PArticles, is intended to be a full fledged multi-purpose event generator capable of simulating particle production processes at lepton–lepton and hadron–hadron colliders in the framework of the Standard Model and some of its prominent extensions. It has and is being developed independently from the other approaches and from the beginning has been written in C++. SHERPA is a publicly available code and can be obtained from `http://www.sherpa-mc.de`.
As in all Monte Carlo event generators the simulation of an actual event is split into different phases that correspond to the evolution stages of a scattering process from the high scale of the hard interaction down to scales of order Λ_{QDC} where hadronisation sets in and the

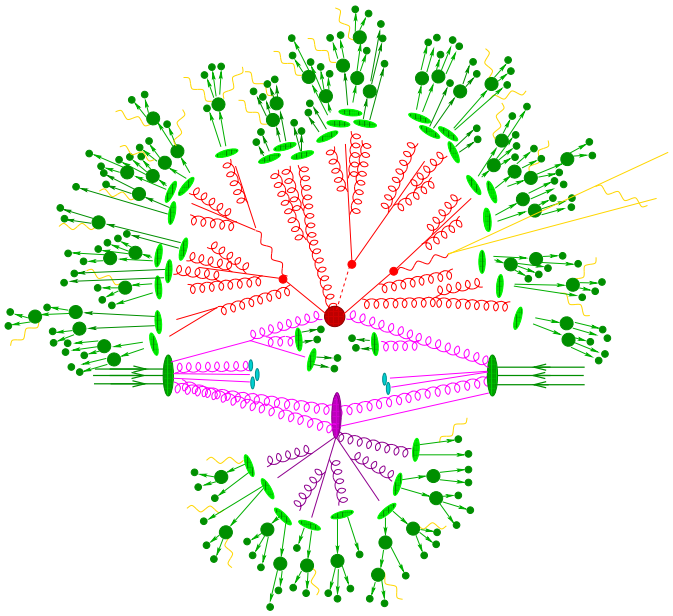

Figure 1.1: Pictorial representation a $t\bar{t}h$ event in hadron–hadron collisions. Apart from the hard signal process (dark red blob) followed by the decays of the unstable top-quarks and the Higgs boson (red blobs), it also contains an additional hard parton interaction (purple blob). The partons are dressed with secondary radiation, before the parton ensemble is transformed into primary hadrons which then decay further and eventually produce additional photons.

hadrons seen in the detectors are formed. A sketch of an fictitious $t\bar{t}h$ event produced in a hadron–hadron collision, from an event generator's point of view, is depicted in Fig. 1.1. Within SHERPA the different stages of the event evolution are hosted by different physics modules. The most important of them shall be briefly reviewed here.

For the description of the hard processes SHERPA relies on its built-in matrix-element generator AMEGIC++ [21] that is capable of calculating exact tree-level matrix elements with up to ten final-state particles in various physics scenarios. From a given set of Feynman rules, specifying the interactions present in a theory, the program automatically generates all the Feynman diagrams contributing to a given process, translates those into helicity amplitudes, and subsequently determines suitable phase-space mappings for cross section evaluation and event generation. At present AMEGIC++ can be used to generate processes in the framework of the Standard Model, the extension of the SM by a general set of anomalous triple- and quartic gauge couplings [22, 23], the Two-Higgs-Doublet Model, the ADD model of large extra spatial dimensions [24, 25] and the Minimal Supersymmetric Standard Model (MSSM). Besides providing matrix elements for the hard process supplemented with appropriate phase-space integrators AMEGIC++ is used to describe particle decays through exact matrix elements.

The perturbative initial- and final-state QCD parton showers, relating partons participating in the hard interaction to partons at scales of order Λ_{QCD}, are accounted for by the parton-shower code APACIC++ [26, 27]. The shower evolution is organised through an ordering in the parton's virtual mass. QCD coherence effects are approximately included by enforcing an ordering of the opening angles in subsequent parton branchings by explicite vetoes. One of the key features of SHERPA is that it contains a general implementation of the Catani–Krauss–Kuhn–Webber (CKKW) prescription to consistently combine multi-leg tree-level matrix elements, describing the hard interaction, with the parton showers [28, 29, 30, 31]. Accordingly, SHERPA can deliver an improved description of QCD multi-jet production by incorporating the advantages of both, the exact matrix elements and the parton-shower approach.

The underlying event simulation within SHERPA is hosted by the program AMISIC++ [32]. It models additional semi-hard parton–parton interactions, occurring for the same hadron–hadron collision that triggered the hard process, according to the approach outlined in Ref. [33]. Since no factorisation theorem exists that covers the scattering of more than one parton per hadron, the current modelling of multiple interactions relies on the incorporation of subsequent $2 \to 2$ QCD processes, employing appropriately rescaled parton distribution functions. The individual interactions, however, are treated in a perturbative way, and in SHERPA actually undergo initial- and final-state showering. A new underlying event description for SHERPA that relies on $k_\perp$-factorisation is currently under development. First steps into this direction have been reported in Ref. [34].

The last step to be accomplished in order to obtain a complete description of events as they can be observed in collider experiments is the transition of the parton ensemble obtained after parton showering to the experimentally observed hadrons. As up to now there is no fundamental theory describing QCD confinement, one has to rely on phenomenological approaches like the Lund string [35, 36] or the cluster fragmentation model [37, 38] for the hadronisation process. Currently SHERPA uses an interface to the Lund string fragmentation of PYTHIA 6.214 [39], but an own cluster hadronisation type of model has already been developed, cf. Ref. [40], and will soon replace the interface. Per default the decays of unstable hadrons are also accomplished by PYTHIA, but a library for all the possible τ-lepton decays and a number of B and D meson decay channels has already been implemented. For their modelling use is made of matrix-element methods and various form factor models.

It should be noted here, that the actual SHERPA program more or less just steers all the different subprograms mentioned above, and thereby initialises, controls and evaluates the different phases of event generation. It is this modularity that allows one to modify, improve, or even replace a certain physics model within SHERPA, without loosing the functionality of the complete event generator. Accordingly, SHERPA represents a very convenient framework to develop, implement, and test new ideas in theoretical particle physics.

1.3 Outline of this thesis

This thesis mainly deals with the development, implementation and validation of various physics models in the framework of the SHERPA event generator.
In Chapter 2 the principles of methods to consistently combine tree-level matrix-element calculations with initial- and final-state parton showers will be reviewed. The focus hereby is on the CKKW prescription as implemented in SHERPA. The electroweak gauge boson production channel is used to validate the method through various consistency checks, comparisons with higher-order calculations, and, ultimately, comparison with experimental data. In the last part of Chapter 2 a detailed comparative study of all the currently existing tree-level merging approaches is presented. Special attention is paid to the assessment of the theoretical uncertainties of the various approaches.
Chapter 3 is devoted to the presentation of a newly developed parton shower algorithm that relies on the Catani–Seymour dipole subtraction scheme. The construction principles of the model are explained and the complete set of splitting operators and phase-space kinematics for initial- and final-state branchings is derived. The obtained shower formulation is then compared analytically with exact matrix-element calculations and an extensive comparison with precise data taken at LEP and Tevatron is presented.
Chapter 4 of this thesis reports on the implementation of the Minimal Supersymmetric Standard Model into SHERPA. Some details about the working principles of the matrix-element generator AMEGIC++ are given and the extensions necessary to allow for the simulation of supersymmetric theories are discussed. The complexity of the MSSM Lagrangian makes careful tests of the implementation unavoidable. Accordingly, several hundred supersymmetric processes have been compared with the two other available programs capable of calculating multi-particle processes in the framework of the MSSM. Finally, by studying sbottom-quark production at the LHC and a future linear collider, it is illustrated that accurate multi-particle final-state calculations are needed to properly account for off-shell effects induced by QCD, photon radiation, or by intermediate on-shell states.
A summary and conclusions can be found in Chapter 5.

2 Merging matrix elements and parton showers

2.1 Introduction

In the past decades, parton-shower Monte Carlo programs, such as PYTHIA [1, 2] or HERWIG [3, 4] have been indispensable tools for planning and analysing particle physics experiments at different colliders. There are a number of reasons for the success of these workhorses. One of the most important ones rests in their ability to bridge the gap between few-parton final states, as described by fixed-order perturbative calculations, and the real world, where a multitude of hadrons, leptons and photons fills the detectors of the experiments. The transformation of the partons of perturbation theory into the visible hadrons, hadronisation, is a direct consequence of the confinement property of QCD. At present, this phenomenon can be described in terms of phenomenological models only, which depend on various phenomenological parameters tuned to data. These parameters and hence the validity of the models in turn depends on the properties (such as the flow of energy and other QCD quantum numbers) of the parton ensemble; therefore it is important that these properties are kept under control. It is the merit of parton showers that they provide a well-understood, theoretically sound and universal framework of translating the few-parton states of fixed-order perturbation theory, calculated at some high scale, with multi-parton states at much lower scales, of the order of a few Λ_{QCD}, where hadronisation sets in. In so doing the parton showers help guarantee the validity of the tuned parameters of the hadronisation models.
To achieve this translation of few-parton to multi-parton states, the parton-shower programs rely on correctly describing QCD particle production in the dominant soft and collinear regions of phase space, giving rise to the bulk of radiation. It is in this region, where the complicated radiation pattern of multiple particle emission factorises into nearly independent - up to ordering in terms of a suitably chosen parameter - individual emissions of single partons. This approximation, namely expanding around the soft or collinear limit, ultimately leads to the resummation of the corresponding leading logarithms, which are then typically encapsulated in exponential form in the Sudakov form factors. Their probabilistic interpretation in fact is the central feature allowing for a straightforward implementation

in an event generator, producing unweighted events. Due to the resummation of leading logarithms it should thus not be too surprising that the parton-shower programs more than often produce answers for QCD-related questions, which approximate exact results very well.

However, the quality of the answers provided by the parton-shower approximation alone relies on whether the question is related to the soft and/or collinear region in the phase space of particle production. Unfortunately, for many final states that need to be studied at the LHC when looking for the appearance new physics, this will not be the case. They can be classified by the occurrence of hard QCD jets or the relevance of non-trivial correlations between final-state objects, such as leptons and jets. In such cases, evidently, a full quantum mechanical treatment as provided by fixed-order calculations becomes mandatory. Therefore, the problem of systematically including higher-order effects into parton-shower programs is in the center of research since a few years. In principle, there are two major avenues of investigation. One deals with the question of how to include the correct QCD next-to-leading-order correction to total cross sections [12]-[19], and has led to an implementation ready for use by the experiments in form of the MC@NLO code [20]. The other, that shall be discussed here, considers the inclusion of tree-level multi-leg matrix elements into the simulation [28, 29, 41, 42, 43, 44].

The key idea of all prescriptions for merging tree-level matrix elements with the parton showers is to separate the phase space for parton emission into a hard region of jet production, accounted for by suitable matrix elements, and the softer region of jet evolution, covered by the parton showers. In order for a merging prescription to give reliable results a number of issues needs to be resolved:

(i) It has to be ensured that the full phase space for QCD radiation gets filled and no phase-space regions are left out.

(ii) A double counting of perturbative terms present in both the parton shower and the matrix-element calculation must be avoided.

(iii) A rather weak dependence on unphysical scales introduced by the merging procedure, *e.g.* cut-off parameters, has to be accomplished.

At present there exist three solutions to the problem. One based on Catani–Krauss–Kuhn–Webber (CKKW), that has been outlined in [28, 29] and forms a cornerstone of the SHERPA [7] generator, an alternative formulation of the same algorithm, proposed in [41], that is implemented in ARIADNE [45, 46], and the MLM scheme, based on [42, 44], that has been incorporated in ALPGEN [47], MADGRAPH/MADEVENT [48, 49, 50], and HELAC [51, 52].

In general, all those merging procedures follow a similar strategy:

1. A jet measure is defined and all relevant cross sections including jets are calculated for the process under consideration. I.e. for the production of a final state X in pp-collisions, the cross sections for the processes $pp \to X + n\text{jets}$ with $n = 0, 1, \ldots, n_{\max}$ are evaluated.

2. Hard parton samples are produced with a probability proportional to the respective total cross section, in a corresponding kinematic configuration following the matrix element.

3. The individual configurations are accepted or rejected with a dynamical, kinematics-dependent probability that includes both effects of running coupling constants and of Sudakov form factors. In case the event is rejected, step 2 is repeated, i.e. a new parton sample is selected, possibly with a new number of jets.

4. The parton shower is invoked with suitable initial conditions for each of the legs. In some cases, like, e.g. in the MLM procedure described below, this step is performed together with the step before, i.e. the acceptance/rejection of the jet configuration. In all cases the parton shower is constrained not to produce any extra jet; stated in other words: Configurations that would fall into the realm of matrix elements with a higher jet multiplicity are vetoed in the parton-shower step.

The three merging procedures differ mainly

- in the jet definition used in the matrix elements;

- in the way the acceptance/rejection of jet configurations stemming from the matrix element is performed;

- and in details concerning the starting conditions of and the jet vetoing inside the parton showering.

To begin with, the CKKW prescription as implemented in SHERPA will be discussed in some detail in Sec. 2.2. In Sec. 2.3 the electroweak gauge boson production channel is used to validate the CKKW implementation through various consistency checks, comparisons with fixed-order calculations, and, ultimately, comparison with experimental data. Sec. 2.4 is devoted to a large scale comparison of all the available tree-level merging approaches with special emphasis being paid to the assessment of the systematic uncertainties of the different algorithms.

2.2 The CKKW merging prescription

The merging prescription proposed in [28, 29], known as the CKKW scheme, has been implemented and further developed in the event generator SHERPA for SM production processes at lepton–lepton and hadron–hadron colliders [30, 31].
For hadron–hadron collisions, that shall only be considered in what follows, the internal jet identification of the SHERPA-merging approach proceeds through a $k_\perp$-measure [53, 54, 55], where $Q_{\rm cut}$ denotes the internal separation cut, also called the merging scale. In that scheme two final-state particles belong to two different jets, if their relative transverse momentum squared

$$Q_{ij}^2 = 2\min\left\{p_{\perp,i},\, p_{\perp,j}\right\}^2 \frac{\left[\cosh(\eta_i-\eta_j)-\cos(\phi_i-\phi_j)\right]}{D^2} \tag{2.1}$$

is larger than $Q_{\rm cut}^2$. In the above equation, η and ϕ denote the pseudo-rapidities and azimuthal angles of the two particles, respectively, and D is a parameter of order 1 [56]. The transverse momentum of each jet is required to be larger than the merging scale $Q_{\rm cut}$. The weight attached to the generated matrix elements consists of two components, a strong-coupling weight and an analytical Sudakov form-factor weight. For their determination, a $k_\perp$-jet clustering algorithm guided by only physically allowed parton combinations is applied on the initial matrix-element configurations. The identified nodal $k_\perp$-values are taken as scales in the QCD running coupling and replace the predefined choice in the initial generation. The Sudakov weight attached to the matrix elements accounts for having no further radiation resolvable at $Q_{\rm cut}$. The NLL-Sudakov form factors employed are defined by [53]

$$\begin{aligned}
\Delta_q(Q,Q_0) &= \exp\left\{-\int_{Q_0}^{Q} dq\,\Gamma_q(Q,q)\right\}\,, \\
\Delta_g(Q,Q_0) &= \exp\left\{-\int_{Q_0}^{Q} dq\,\left[\Gamma_g(Q,q)+\Gamma_f(q)\right]\right\}\,,
\end{aligned} \tag{2.2}$$

where $\Gamma_{q,g,f}$ are integrated splitting functions $q\to qg$, $g\to gg$ and $g\to q\bar{q}$ given through

$$\Gamma_q(Q,q) = \frac{2C_F}{\pi}\frac{\alpha_{\rm S}(q)}{q}\left(\ln\frac{Q}{q}-\frac{3}{4}\right)\,, \tag{2.3}$$

$$\Gamma_g(Q,q) = \frac{2C_A}{\pi}\frac{\alpha_{\rm S}(q)}{q}\left(\ln\frac{Q}{q}-\frac{11}{12}\right)\,, \tag{2.4}$$

$$\Gamma_f(q) = \frac{N_f}{3\pi}\frac{\alpha_{\rm S}(q)}{q}\,. \tag{2.5}$$

They contain the running coupling constant and the two leading, logarithmically enhanced terms in the limit $Q_0 \ll Q$. The single logarithmic terms $-3/4$ and $-11/12$ may spoil an interpretation of the NLL-Sudakov form factor as a non-branching probability. Therefore,

without affecting the logarithmic order of the result, $\Gamma(Q,q)$ is cut off at zero, such that $\Delta_{q,g}(Q,Q_0)$ retains its property to define the probability for having no emission resolvable at scale Q_0 during the evolution from Q to Q_0. These factors are used to reweight in accordance to the appearance of external parton lines. A ratio of two Sudakov form factors $\Delta(Q,Q_0)/\Delta(q,Q_0)$ accounts for the probability of having no emission resolvable at Q_0 during the evolution from Q to q. Hence, it can be employed for the reweighting according to internal parton lines. The lower limit is taken to be $Q_0 = Q_{\rm cut}$ or $Q_0 = D\,Q_{\rm cut}$ for partons that are clustered to a beam or to another final-state parton, respectively.
The sequence of clusterings, stopped after the eventual identification of a $2 \to 2$ configuration (the core process), is used to reweight the matrix element. Moreover, this also gives a shower history, whereas the $2 \to 2$ core process defines the starting conditions for the vetoed shower where all emissions above $Q_{\rm cut}$ get rejected.
The very important feature of the CKKW approach as outlined above is the cancellation of the dependence on $Q_{\rm cut}$ to NLL accuracy, for which the formal proof has been given in [28] considering the case of lepton–lepton initial states. This particularly is achieved through the combination of the Sudakov-reweighted matrix elements with vetoed parton showers subjected to appropriate starting conditions.

2.2.1 The actual algorithm

The merging prescription sketched above shall now be formulated in an algorithmic language for the case of hadron–hadron collisions, with special emphasis given to details of its implementation in SHERPA. The description of the preferred scale choices for different process configurations will be exemplified for W boson production in Sec. 2.2.2. Details on the treatment of matrix elements with the highest jet multiplicity will be considered in Sec. 2.2.3.
The merging algorithm proceeds as follows:

1. One process out of all processes under consideration is selected according to the probability
$$P_i^{(0)} = \frac{\sigma_i^{(0)}}{\sum_i \sigma_i^{(0)}}\,. \tag{2.6}$$
This choice provides the initial jet rates, subject to the additional Sudakov and coupling weight rejection. For instance, a typical selection of processes for W^--boson production at the Tevatron would include:
$$\begin{aligned}
&p\bar{p} \to jet\,jet \to e^-\bar{\nu}_e\,,\\
&p\bar{p} \to jet\,jet \to e^-\bar{\nu}_e + jet\,,\\
&p\bar{p} \to jet\,jet \to e^-\bar{\nu}_e + jet\,jet\,,\\
&p\bar{p} \to jet\,jet \to e^-\bar{\nu}_e + jet\,jet\,jet\,.
\end{aligned}$$

The cross sections $\sigma_i^{(0)}$ are calculated using the corresponding tree-level matrix elements; the only phase-space restriction is given by the $k_\perp$-measure [1]. The renormalisation scale μ_R and the factorisation scale μ_F are fixed to the cut-off scale Q_{cut}, with an exception only for the process with the highest number of jets, cf. Sec. 2.2.3.

2. Having chosen a single process, the respective momenta are distributed according to the corresponding differential cross section.

3. The nodal values q_i are determined. In doing so a corresponding parton-shower history is reconstructed. The backward clustering procedure is guided by the $k_\perp$-measure, respecting additional constraints:

   - Unphysical combinations like (qq) and $(\bar{q}\bar{q})$ are ignored. Within the SHERPA framework this is implemented by employing the knowledge of the Feynman diagrams contributing to the process under consideration. Thus, "unphysical" translates into the non-existence of a corresponding Feynman diagram.
   - When an outgoing parton of momentum p_j is to be clustered with a beam, the $k_\perp$-measure does not provide the information as to which beam it has to be clustered. In general the beam with the same sign as its longitudinal momentum component is preferred. In addition the new incoming momentum given by $p_i' = p_i - p_j$ must exhibit a positive energy in the frame where the initial-state shower is performed.

4. The backward clustering stops with a $2 \to 2$ process. The hardest scale of this "core" process has to be found. It depends both on the process and its kinematics (cf. Sec. 2.2.2).

5. The weight is determined, employing the nodal values q_i, according to the following rules:

   - For every internal (QCD) line with nodal values q_i and q_j for its production and its decay, a factor $\Delta(q_i, Q_{\text{cut}})/\Delta(q_j, Q_{\text{cut}})$ is added. For outgoing lines, a factor $\Delta(q_i, Q_{\text{cut}})$ is added.
   - For every QCD node a factor $\alpha_s(q_i)/\alpha_s(Q_{\text{cut}})$ is added.

6. The event is accepted or rejected according to this weight. If the event is rejected, the procedure starts afresh, with step 1.

[1] In cases where the matrix elements considered exhibit other than just the soft and collinear singularities of QCD, these singular phase-space regions have to be avoided by applying suitable cuts. One such example is inclusive Drell-Yan production of a pair of leptons mediated by an off-shell photon. This process has a physical divergence as the invariant di-lepton mass tends to zero. This, however, is easily removed by requiring a minimum virtuality for the photon propagator.

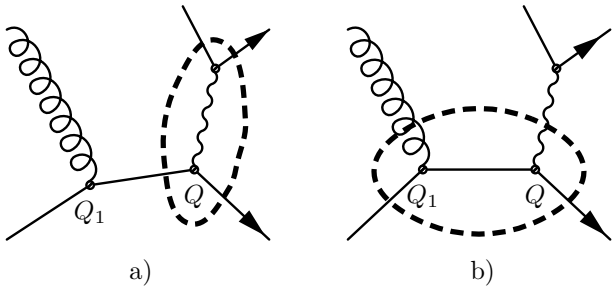

Figure 2.1: Two possible cluster configurations of a W+1 jet event. The dashed line highlights the hard $2 \to 2$ process.

7. The initial- and final-state showers emerge from the core $2 \to 2$ process. The reconstructed matrix-element branchings are included as predetermined splittings within the shower. The starting conditions are determined by the clustering performed before (in step 3), i.e. the evolution of a parton starts at its production scale [2]. The first emission from the initial-state shower has to take the factorisation scale μ_F into account, used during the matrix-element calculation.

8. Any parton-shower emission with a $k_\perp$ above the jet resolution scale Q_{cut} gets vetoed.

2.2.2 Example: W boson production at hadron colliders

The algorithm described above and, in particular, the incorporated scale choices, will be illustrated with a few examples dealing with W-boson production at hadron colliders:
The leading-order contributions to W^- production are of the Drell–Yan type, i.e. processes of the form

$$q\,\bar{q}' \to e^-\bar{\nu}_e\ .$$

Clustering does not take place, since this is already a $2 \to 2$ process. Furthermore, there is no strong coupling involved, and the rejection weight is given by two quark Sudakov factors only:

$$\mathcal{W} = \Delta_q(Q, Q_{\text{cut}})\,\Delta_{\bar{q}'}(Q, Q_{\text{cut}})\,. \tag{2.7}$$

The hard scale Q is fixed by the invariant mass of the lepton-neutrino pair $Q^2 = M^2_{e^-\bar{\nu}_e}$. Possible configurations resulting from the clustering of $\mathrm{W}+1$jet events are exhibited in Fig. 2.1. The hard $2 \to 2$ process either is again a Drell–Yan process (Fig. 2.1a) or of the type $q\bar{q}' \to gW$ (Fig. 2.1b). The weight in the first case reads:

$$\mathcal{W} = \Delta_q(Q, Q_{\text{cut}})\,\Delta_{\bar{q}'}(Q, Q_{\text{cut}})\,\Delta_g(Q_1, Q_{\text{cut}})\frac{\alpha_s(Q_1)}{\alpha_s(Q_{\text{cut}})}\ , \tag{2.8}$$

[2] Since a virtuality-ordered shower is employed within SHERPA, the virtuality of its predecessor, i.e. its invariant mass, is used.

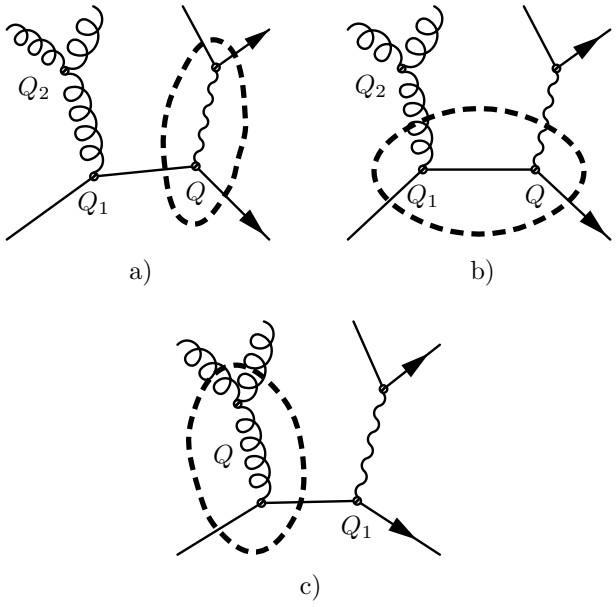

Figure 2.2: Three possible cluster configurations of a W+2 jet event. The dashed line highlights the hard $2 \to 2$ process, being either of Drell–Yan type (a), a vector boson production (b) or a pure QCD process (c).

where $Q^2 = M^2_{e^-\bar{\nu}_e}$ and the nodal value Q_1 is given by the $k_\perp$-algorithm. For this configuration the gluon jet tends to be soft, i.e. Q_1 preferentially is close to Q_{cut}. The second configuration differs from the first only by the result of the clustering. The transverse momentum of the gluon jet $p^2_{T,g}$ now is of the order of the W-boson mass or larger. The weight looks still the same only the scale definitions are altered. In such a case, the hard scale is now given by

$$Q^2 = p^2_{T,g} + M^2_{e^-\bar{\nu}_e}\,, \tag{2.9}$$

i.e. the transverse mass of the W. Also, the nodal value Q_1 has not been determined by the cluster algorithm, since it belongs to the (in principle unresolved) core process. A natural choice is the transverse momentum of the corresponding jet

$$Q_1 = p_{T,g}\,. \tag{2.10}$$

These scale definitions guarantee a smooth transition between the two regimes, i.e. from the case where the gluon is soft to a case where the gluon is hard.
More complicated processes involve the production of at least two extra jets. There are many processes contributing to this category. Some illustrative examples are displayed in Fig. 2.2. Cases a) and b) of Fig. 2.2 are very similar to the example with one extra jet only. The corresponding weight reads:

$$\mathcal{W} = \Delta_q(Q, Q_{\text{cut}})\,\Delta_{\bar{q}'}(Q, Q_{\text{cut}})\,\Delta_g(Q_1, Q_{\text{cut}})\,\Delta_g(Q_2, Q_{\text{cut}})\frac{\alpha_s(Q_1)}{\alpha_s(Q_{\text{cut}})}\,\frac{\alpha_s(Q_2)}{\alpha_s(Q_{\text{cut}})}\,. \tag{2.11}$$

The nodal value Q_2 is given by the $k_\perp$-algorithm. The scales Q_1 and Q are chosen as in the one-jet case.
In contrast a new situation arises when a pure QCD process has been chosen as the "core" $2 \to 2$ process, see Fig. 2.2c). Since the "core" process is not resolved, there is only one scale available, $Q^2 = (2stu)/(s^2+t^2+u^2) \approx p_T^2$, the transverse momentum of the outgoing jets. The correction weight consequently reads:

$$\mathcal{W} = \Delta_q(Q, Q_{\text{cut}}) \frac{\Delta_q(Q, Q_{\text{cut}})}{\Delta_q(Q_1, Q_{\text{cut}})} \Delta_{\bar{q}'}(Q_1, Q_{\text{cut}}) \left[\Delta_g(Q, Q_{\text{cut}})\right]^2 \left[\frac{\alpha_s(Q)}{\alpha_s(Q_{\text{cut}})}\right]^2 . \tag{2.12}$$

The extension to higher multiplicities is straightforward. However, the number of extra jets accounted for by matrix elements is limited. This limitation in available matrix elements enforces a specific treatment of the processes with the highest multiplicity.

2.2.3 Treatment for the highest multiplicity matrix element

In general, the initial cross sections $\sigma_i^{(0)}$ used in step 1 of the merging algorithm above are defined by

$$\sigma_i^{(0)} = \int dx_1\, dx_2\, d\Omega\; f_1(x_1, \mu_F) f_2(x_2, \mu_F) \left|\mathcal{M}_i\right|^2 , \tag{2.13}$$

where $d\Omega$ represents the appropriate invariant phase-space element and $\mathcal{M}_i$ is the Feynman amplitude for the respective process. The choice $\mu_F = Q_{\text{cut}}$ together with the Sudakov factors and the coupling weight leads to a modified cross section $\sigma_i = \mathcal{W}\,\sigma_i^{(0)}$. Adding all cross sections with the same number of strong particles yields the cross section for production processes accompanied by – exclusively – n jets,

$$\sigma_{n-jet}^{(\text{excl})} = \sum_{i(n\,jet)} \sigma_i \; . \tag{2.14}$$

Of course the number of extra jets that can be considered in this respect is limited by the available matrix elements; in SHERPA, this number is usually in the range of three to four. In order to compensate for all the omitted processes with more jets, the treatment of processes with the highest number of extra jets differs slightly from the handling of lower jet multiplicities. The changes are as follows:

- the factorisation scale is set dynamically to $\mu_F = Q_{\text{min}} \geq Q_{\text{cut}}$, i.e. to the smallest nodal value as determined by the $k_\perp$-algorithm,
- the resolution scale Q_{cut} of the Sudakov weights is also replaced by Q_{min}, and
- the shower veto is applied with Q_{min} instead of Q_{cut}.

This guarantees that parton showers attached to matrix elements with the highest number of jets are allowed to produce jets softer than Q_{min}. In other words: the merging procedure

is meant to take into account quantum interference effects in jet production at leading order up to a maximal number of jets; any softer jet is left to the parton shower. For the configuration shown in Fig. 2.2a), the modified Sudakov and coupling weight reads:

$$\tilde{\mathcal{W}} = \Delta_q(Q, Q_{\min})\, \Delta_{\bar{q}'}(Q, Q_{\min})\, \Delta_g(Q_1, Q_{\min})\, \frac{\alpha_s(Q_1)}{\alpha_s(Q_{\text{cut}})}\, \frac{\alpha_s(Q_2)}{\alpha_s(Q_{\text{cut}})}\,, \tag{2.15}$$

with the lowest scale $Q_{\min} = Q_2$. Following this procedure, the sum of all cross sections $\tilde{\sigma}_i = \tilde{\mathcal{W}}\, \tilde{\sigma}_i^{(0)}$ for a number of jets n can be interpreted as an inclusive cross section

$$\sigma_{n-jet}^{(\text{incl})} = \sum_{i(n\,jet)} \tilde{\sigma}_i\,, \tag{2.16}$$

i.e. the probability to find at least n jets. Adding all the exclusive cross sections for multiplicities lower than a maximal multiplicity $n_{\max}$ to the inclusive cross section for the highest multiplicity yields the desired fully inclusive cross section. In the CKKW approach this treatment ensures that the full phase space for jet production is consistently filled without double counting any terms in the perturbative expansion.

2.3 Gauge boson production at the Tevatron

The production of electroweak gauge bosons, e.g. $W^{\pm}$ and Z^0, is one of the most prominent processes at hadron colliders. Especially through their leptonic decays they leave a clean signature, namely either one charged lepton accompanied by missing energy for W bosons or two oppositely charged leptons for the Z^0 bosons. The combination of clear signatures and copious production rates allows a measurement of some of their parameters, e.g. the W mass and width, with a precision comparable with that reached at LEP2 at the Tevatron [57]-[66], or even better at the LHC [67, 68]. The same combination, clear signature and large production rate, renders them a good candidate process for luminosity measurements, especially at the LHC [69]-[72]. This holds true in particular for W-bosons, since their production rate is enhanced by roughly an order of magnitude with respect to Z^0 production. At present W+multi-jet production is one of the most studied final states because of its important rôle as a background to top-quark studies at the Tevatron. Furthermore, at the LHC, W+jets, as well as Z^0+jets processes, will provide the main irreducible backgrounds to signals such as multi-jet plus missing transverse energy, typical of supersymmetry and of other manifestations of physics beyond the SM. The understanding of W+multi-jet production at the Tevatron is therefore an essential step towards the validation and tuning of Monte Carlo event generators, prior to their utilization at the LHC.
In the following the merging procedure implemented in SHERPA shall be validated and benchmarked for single-boson production at the Tevatron collider [3]. In a first step, the

[3] Similar studies for gauge boson production at the LHC have been presented in Ref. [73]

self-consistency of the method will be checked by analysing the dependence of different observables on the merging scale and on the maximum number of extra jets described through matrix elements, see Sec. 2.3.1. This will be supplemented with a first comparison of the predicted boson p_T spectra with published Tevatron data. In Sec. 2.3.2 SHERPA predictions for the extra jet transverse momentum spectra will be compared with full next-to-leading-order QCD calculations for the processes $\mathrm{W}/\mathrm{Z}^0 + 1, 2$ jets. Finally, Sec. 2.3.3 reports on a detailed comparison of DØ data for the Z^0/γ^*+jets channel with Monte Carlo simulations from PYTHIA and SHERPA. Special attention thereby is given to observables sensitive to the modelling of QCD radiation in the generators.

2.3.1 Validation of the CKKW predictions

In this section the self-consistency of the results obtained with SHERPA is checked by analysing the sensitivity of different observables on the key parameters of the merging procedure, namely the separation scale Q_{cut} and the highest multiplicity of included matrix elements n_{max}. Per construction these dependencies should be moderate and a wide range of settings will be probed. However, in practice educated choices can be made, that are guided by the event selection criteria in an analysis:

- The choice of Q_{cut} should be related to the jet cuts. Requiring jets with transverse momenta greater than p_T^{min}, the choice $Q_{\mathrm{cut}} \approx p_T^{\mathrm{min}}$ is recommended. If $Q_{\mathrm{cut}} \gg p_T^{\mathrm{min}}$ lots of the analysed jets will originate from the parton showers and will miss the advantages of a full matrix-element calculation. However, choosing Q_{cut} much smaller than p_T^{min} results in a rather low event generation efficiency. Similarly, the choice of the D parameter in Eq. 2.1 should be adapted to the analysis cuts. If the analysis is to be carried out with a cone-jet algorithm, the choice $D \approx R$, with R the jet-cone radius, is advisable.

- A similar argumentation holds for the choice of n_{max}. If studying an n-jet observable n_{max} should best be chosen equal or greater than n.

- The remaining dependencies on the concrete choices for the merging parameters have to be accounted as systematic uncertainties of the prescription or can be used to tune the Monte Carlo predictions to data.

In the following two paragraphs W^- boson production at the Tevatron will be considered, with $\sqrt{s} = 1960$ GeV and $\mathrm{W}^- \to e^- \bar{\nu}_e$; the SM input parameters used can be found in Appendix A.1.1, the D parameter of the internal jet algorithm has been fixed to $D = 1$, SHERPA version 1.0.6 has been used [4]. If not stated otherwise, the distributions shown

[4] The results presented here have been published in [30]. Similar studies for the pair production of W bosons have been presented in [74].

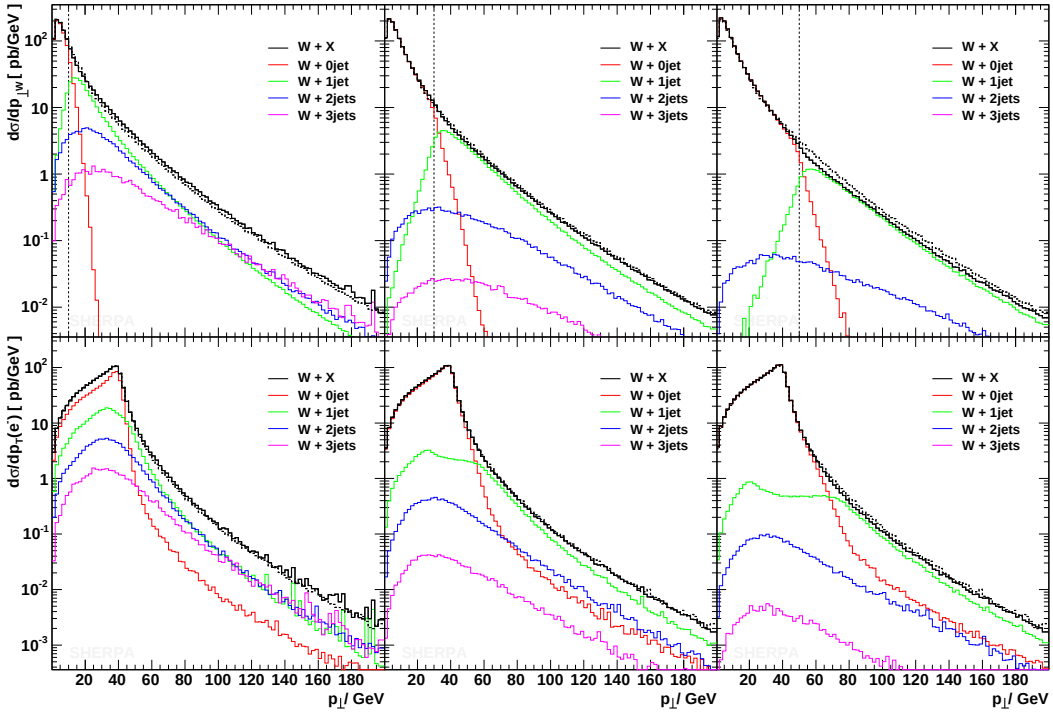

Figure 2.3: $p_T(W^-)$ (upper row) and $p_T(e^-)$ (lower row) for $Q_{\text{cut}} = 10$ GeV, 30 GeV and 50 GeV in comparison with $Q_{\text{cut}} = 20$ GeV (dashed curve).

are inclusive hadron-level results, i.e. no cuts have been applied. The last paragraph of this section contains a first comparison of SHERPA predictions with experimental data, this however will be largely extended in Sec. 2.3.3.

Variation of the separation cut Q_{cut}

In all figures of this paragraph, the black, solid line represents the total inclusive result as obtained by SHERPA. A vertical dashed line indicates the respective separation cut Q_{cut}, which has been varied between 10 GeV and 50 GeV. To guide the eye, all plots also show the same observable as obtained with a separation cut of 20 GeV, shown as a dashed black curve. The coloured lines give the contributions of different multiplicity processes. Note that the separation cut always marks the transition between n-jet and $n+1$-jet matrix elements. Figs. 2.3 and 2.4 show the transverse momentum and the rapidity distribution of the W^- boson and the corresponding electron. For the transverse momentum of the W below the cut, the distribution is dominated by the LO matrix element with no extra jet, i.e. the transverse momentum is generated by the initial-state parton shower only. Around the cut, a small dip is visible in Fig. 2.3. The p_T distribution of the electron, in contrast, is hardly altered. The rapidity distributions in Fig. 2.4 exhibit the asymmetry, which has been anticipated when considering merely the negatively charged W boson. The shape of

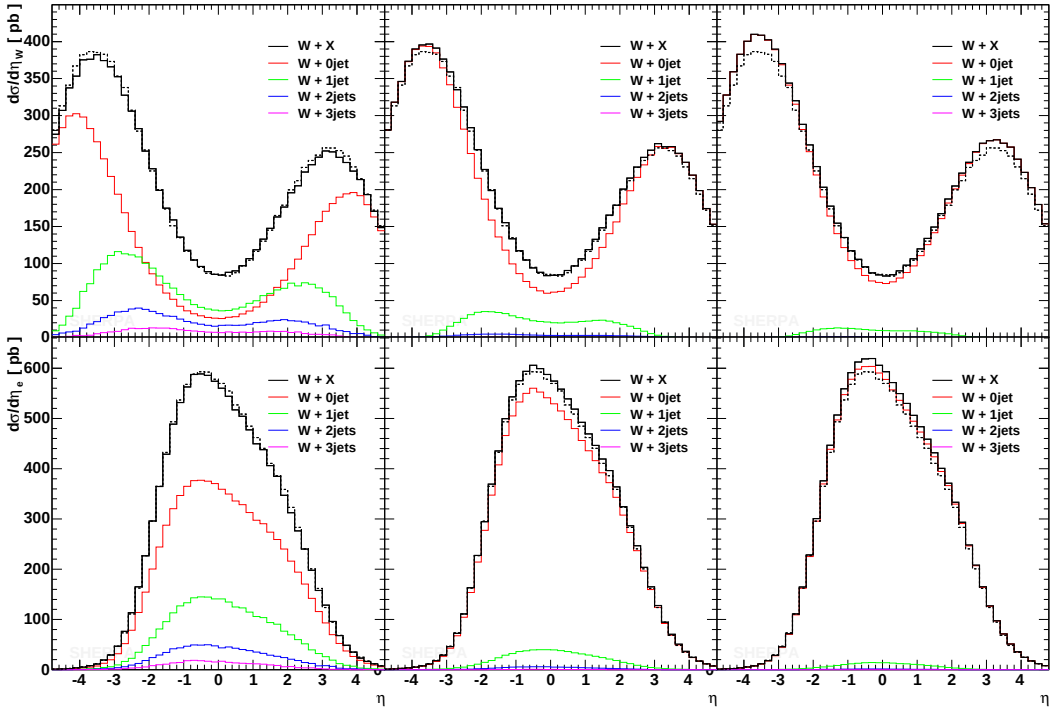

Figure 2.4: $\eta(W^-)$ (upper row) and $\eta(e^-)$ (lower row) for $Q_{\text{cut}} = 10$ GeV, 30 GeV and 50 GeV in comparison with $Q_{\text{cut}} = 20$ GeV (dashed curve).

these distributions is very stable under a variation of the separation cut. In all observables a small increase of the total cross section of a few percent when changing Q_{cut} from 10 GeV to 50 GeV is visible. This underlines the fact that the dependence on the separation cut is weak.

Differential jet rates with respect to the $k_\perp$-algorithm are interesting observables, since they basically exhibit the distributions of nodal values when running the cluster algorithm. For simplicity the Run II $k_\perp$-algorithm, cf. Ref. [56], has been used with $D = 1$ for the analysis. Differential jet rates are of special interest, since the nodal values are very close to the measure used to separate matrix elements from parton-shower emissions. Accordingly, deficiencies with respect to the separation should immediately manifest themselves in these distributions. In Fig. 2.5 the $1 \to 0$, $2 \to 1$ and $3 \to 2$ differential jet rates are shown. The dependence of the results on Q_{cut} is rather weak. The largest effects are observed for $Q_{\text{cut}} = 50$ GeV where the parton shower starts to fail in filling the phase space for emissions of order Q_{cut}. However, within the given approximations the independence on Q_{cut} is satisfactory. A more detailed assessment of the variations introduced by using different values for the merging scale in the CKKW approach is presented in Sec. 2.4.

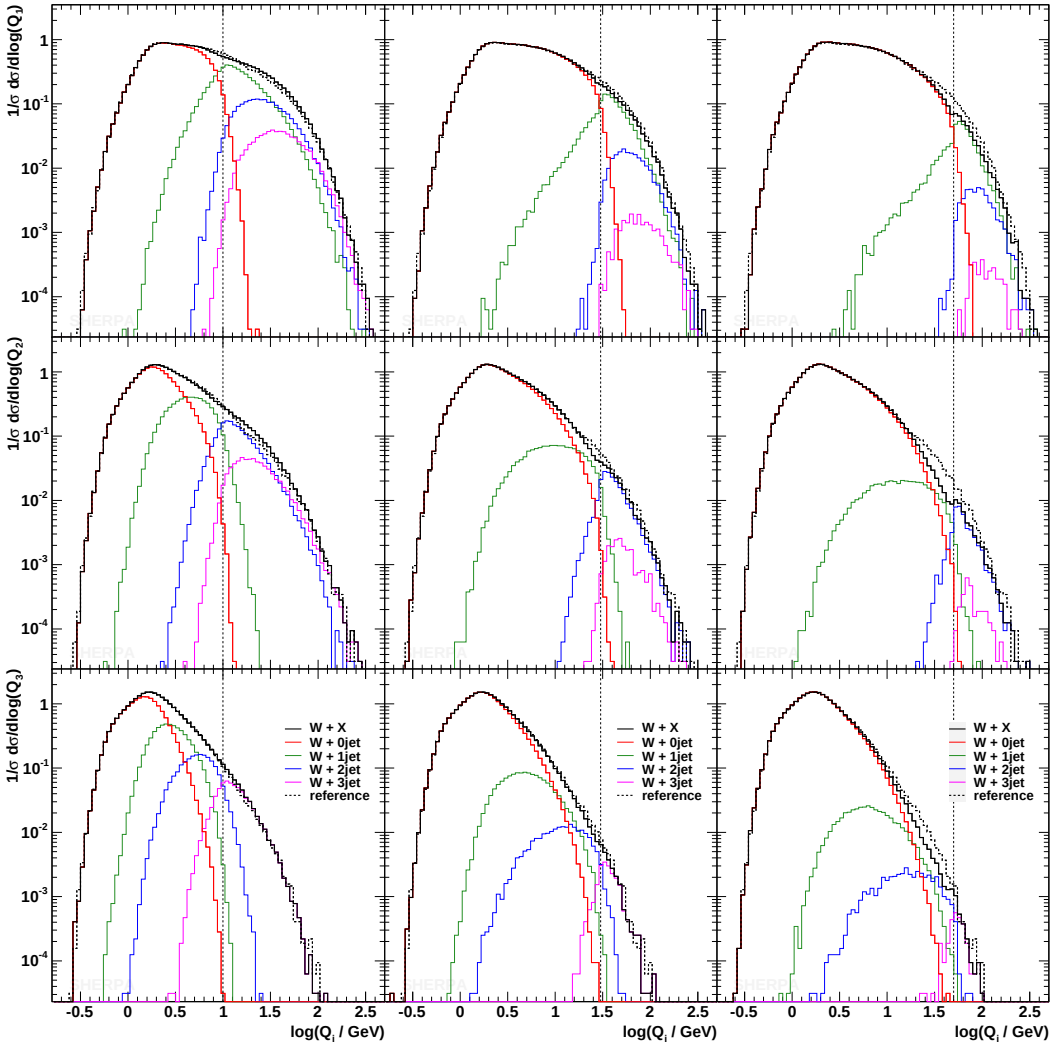

Figure 2.5: Differential jet rates for the $1 \to 0$, $2 \to 1$ and $3 \to 2$ transition (top to bottom), for $Q_{\text{cut}} = 10$ GeV, 30 GeV, and 50 GeV (from left to right). In each plot, the results are compared with those for $Q_{\text{cut}} = 20$ GeV (dashed curve).

Variation of the maximal jet multiplicity $n_{\max}$

For very inclusive observables such as transverse momentum and rapidity of the W boson, it is usually sufficient to include the matrix element with only one extra jet in order to obtain a reliable prediction. Consequently, the inclusion of matrix elements with more than one extra jet in the simulation should not significantly change the result. This can be used as another consistency check. Figs. 2.6 and 2.7 impressively picture the dependence on the maximal jet number in the matrix elements included. They show that the treatment of the highest multiplicity, cf. Sec. 2.2.3, sufficiently compensates for the missing matrix elements, whereas the contribution of the lowest multiplicity is not altered.

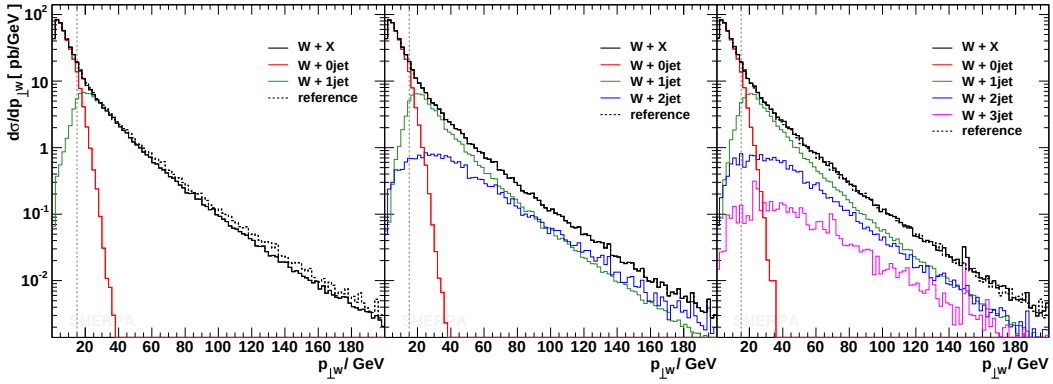

Figure 2.6: $p_T(W^-)$ for $Q_{\mathrm{cut}} = 15$ GeV and different maximal numbers of matrix-element jets included. The dashed reference curve corresponds to the case $n_{\mathrm{max}} = 2$.

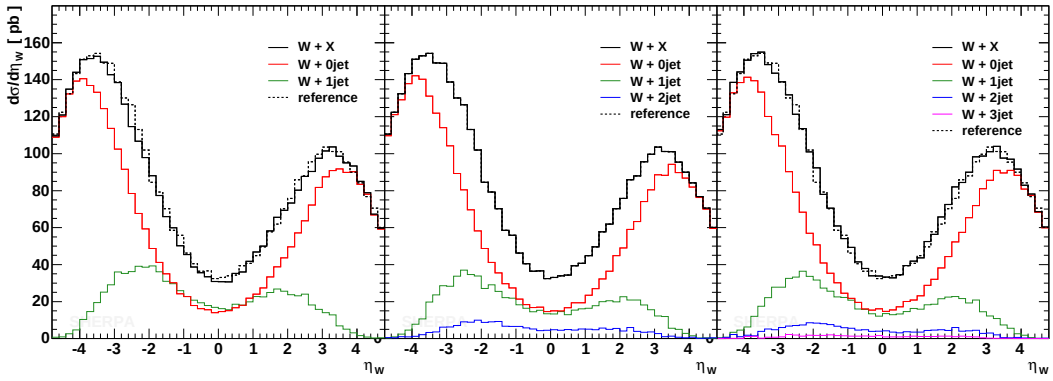

Figure 2.7: $\eta(W^-)$ for $Q_{\mathrm{cut}} = 15$ GeV and different maximal numbers of matrix-element jets included. The dashed reference curve corresponds to the case $n_{\mathrm{max}} = 2$.

First comparison with data

The comparison with experimental data provides an ultimate test for a theoretical calculation. Unfortunately, so far only very few distributions measured at the Tevatron in the gauge boson channel have been published. Amongst them are the transverse momentum distributions of produced W and Z^0 bosons. These distributions are very sensitive to both hard and soft radiation that accompanies the produced gauge boson. Accordingly, they provide a very good testbed for the CKKW approach, that aims at describing the two regions consistently in one sample.

Matrix elements with up to four (W) or three (Z^0) extra jets have been included in the calculation. The black line represents the sum of the different multiplicity contributions, that are indicated by the different colours. For both samples $Q_{\mathrm{cut}} = 20$ GeV has been used. In Fig. 2.8, the (inclusive) p_T distribution of the W is compared with DØ data taken at

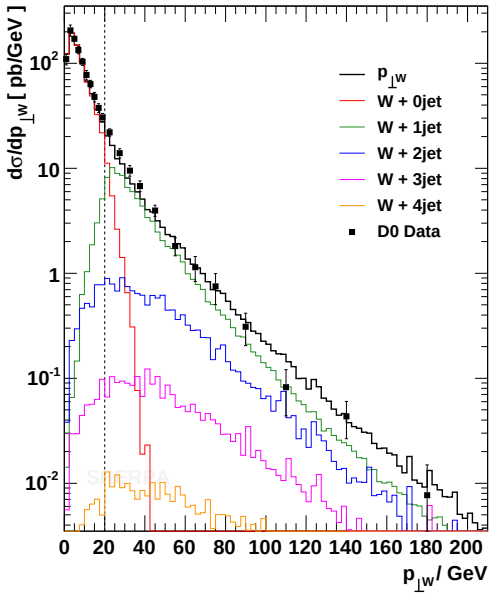

Figure 2.8: The p_T distribution of the W-boson in comparison with data from DØ at the Tevatron, Run I [75]. The applied separation cut is $Q_{\text{cut}} = 20$ GeV and $n_{\text{max}} = 4$ has been used.

$\sqrt{s} = 1800$ GeV [75]. The agreement with data is excellent. It can be recognised that approaching the merging scale from below, the W+0jet contribution steeply falls and the distribution for larger momenta is mainly covered by the W+1jet part, as expected. In order to match the measured distribution, the SHERPA result has been multiplied by a constant K-factor of 1.25.

Similarly, in Fig. 2.9, the (inclusive) p_T distribution of the Z^0 is compared with data, this time taken by CDF, but also during Run I [76]. Again the overall agreement, both in the soft and hard region, is excellent. This time the result has been multiplied by a constant K-factor of 1.6 to match the measured cross section. The result is perfectly smooth around the merging scale of $Q_{\text{cut}} = 20$ GeV. This is especially highlighted in the right panel of Fig. 2.9, which concentrates on the low momentum region. It is interesting to note that the description of the data for momenta smaller than the merging scale is almost only covered by the $Z^0 + 0$jet contribution and is therefore very sensitive to the details of the parton showers and the treatment of beam remnants. A parameter of specific impact on the very low momentum region therefore is the primordial (or intrinsic) $k_\perp$ used for the interacting partons. This is modelled through a Gaussian distribution with a central value of 0.8 GeV. Nevertheless, the shower performance of SHERPA has not been especially tuned; the low momentum behaviour may therefore still be improved once a detailed parameter tune is available.

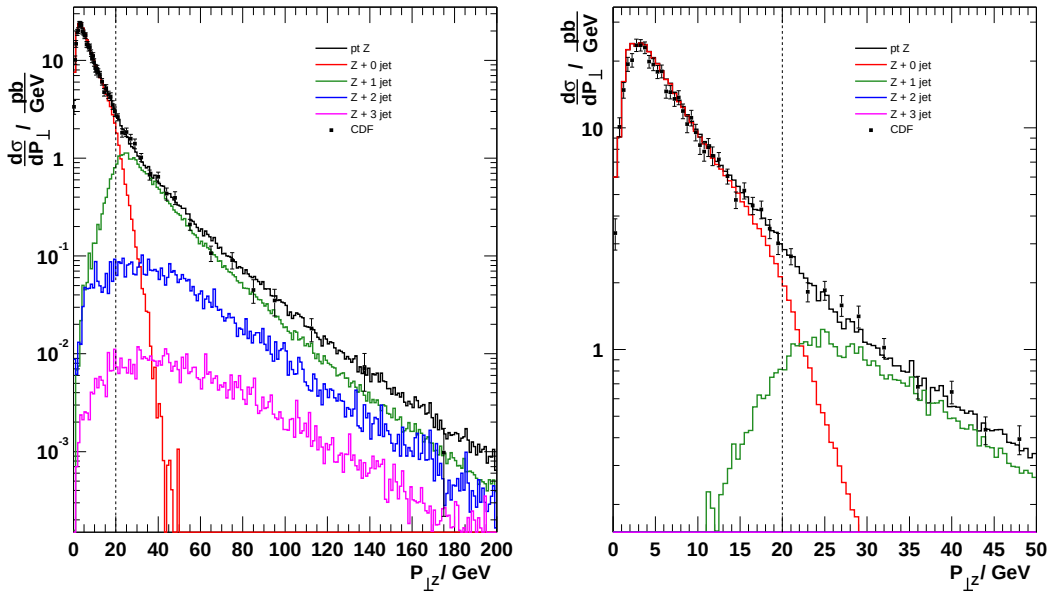

Figure 2.9: The p_T distribution of the Z^0-boson in comparison with data from CDF at the Tevatron, Run I [76]. The applied separation cut is $Q_{\text{cut}} = 20$ GeV and $n_{\text{max}} = 3$ has been used. The right plot just focuses on the low momentum region of the left one.

2.3.2 Comparison with higher-order calculations

The SHERPA predictions for W/Z^0+1jet and W/Z^0+2jet production at the Tevatron collider shall be compared with corresponding parton-level next-to-leading-order calculations. For this a two-step procedure is chosen. First matrix elements reweighted with Sudakov form factors and a strong coupling weight according to the CKKW prescription are compared with exclusive NLO results obtained with the parton-level Monte Carlo MCFM [77, 78]. In the case of the next-to-leading-order calculation, the exclusiveness of the final states boils down to a constraint on the phase space for the real parton emission. The exclusive SHERPA results consist of appropriate leading-order matrix elements with scales set according to the $k_\perp$-cluster algorithm and made exclusive by suitable Sudakov form factors, cf. Sec. 2.2.1. In a second step, the jet spectra for inclusive production processes are compared. For the next-to-leading-order calculation, this time the phase space for real parton emission is not restricted and the SHERPA predictions are obtained from a fully inclusive sample, using matrix elements with up to two extra jets and the parton showers attached. If not stated otherwise, all results have been obtained using the input parameters and phase-space cuts summarised in Appendix A.1. Jets are found using the Run II $k_\perp$-clustering algorithm defined in [56] with a pseudo-cone size of $D = 0.7$ and a minimal p_T of 15 GeV. The merging scale in SHERPA is set to $Q_{\text{cut}} = 15$ GeV. The results of this study have been published in [30]. The case of gauge boson production at the LHC was considered in Ref. [73] where similar results and conclusions than presented in the following have been found.

Exclusive jet p_T spectra

In Fig. 2.10 the jet p_T distribution for the exclusive production of $W+1$jet and Z^0+1jet are shown. In both figures, the SHERPA prediction is compared with the exclusive NLO result obtained with MCFM and with the naive LO prediction, which is the same for the two programs. For the fixed-order NLO and LO result, the renormalisation and factorisation scales have been set to $\mu_R = \mu_F = m_W = 80.419$ GeV. All distributions have been normalised to the corresponding total cross section. This allows for a direct comparison of the distributions shape. As stated above, the SHERPA results stem from Sudakov and α_s reweighted $W+1$jet or Z^0+1jet LO matrix elements. The change between the naive leading-order and the next-to-leading-order distribution is significant. At next-to-leading order the distributions become much softer. For a high-p_T jet it is much more likely to emit a parton that fulfils the jet criteria and therefore removes the event from the exclusive sample. The SHERPA predictions show the same feature. The inclusion of Sudakov form factors and the scale setting according to the merging prescription improves the LO prediction, resulting in a rather good agreement with the next-to-leading-order result.
In the high-p_T tail, however, the NLO calculations from MCFM tend to be a bit below the SHERPA results. The reason is simply connected to the fact that relevant scales in the high-

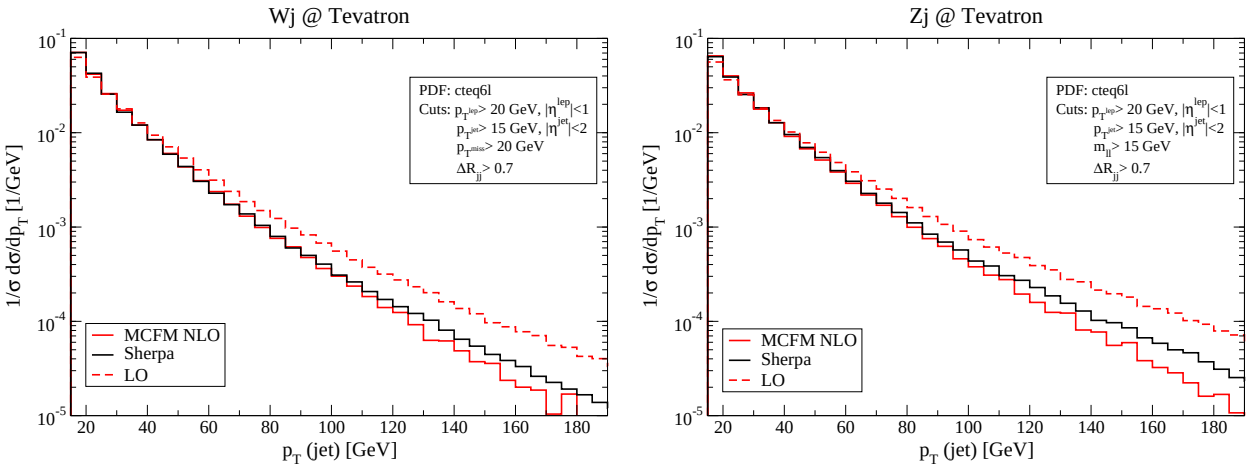

Figure 2.10: Jet p_T distribution of exclusive W + 1jet (left) or Z^0 + 1jet (right) events at the Tevatron, Run II.

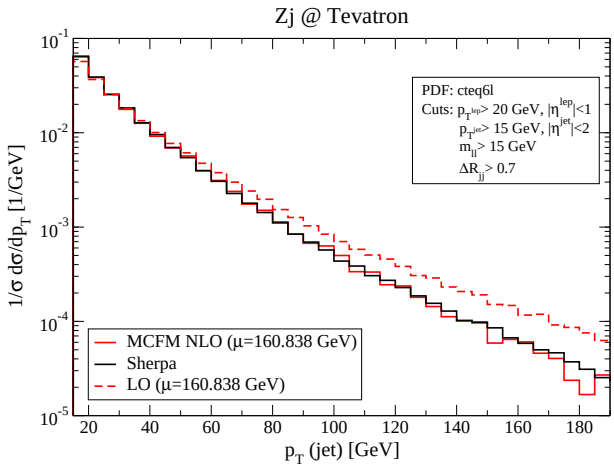

Figure 2.11: Jet p_T distribution of Z^0 + 1jet events at the Tevatron where for the NLO and LO calculation the renormalisation and factorisation scales have been chosen to be $\mu_R = \mu_F = 160.838$ GeV.

p_T tail are much larger than the default choice of $\mu_R = \mu_F = m_W$. In order to highlight this, Fig. 2.11 contains the jet p_T distribution in Z^0+1jet events. In this plot, the renormalisation and factorisation scales have been chosen to be $\mu_R = \mu_F = 2m_W = 160.838$ GeV. Changing the scale in this manner indeed has quite a small impact on the total cross section at NLO, but the tail of the distribution becomes considerably enhanced. With the above choice for μ_R and μ_F the agreement of the NLO and the SHERPA result is impressive.

The p_T distribution of the first and second jets in W + 2jet and Z^0 + 2jet production are presented in Fig. 2.12. Again, the next-to-leading-order distributions are softer than the leading-order ones, for the same reason as for the 1jet case. In addition, at low-p_T

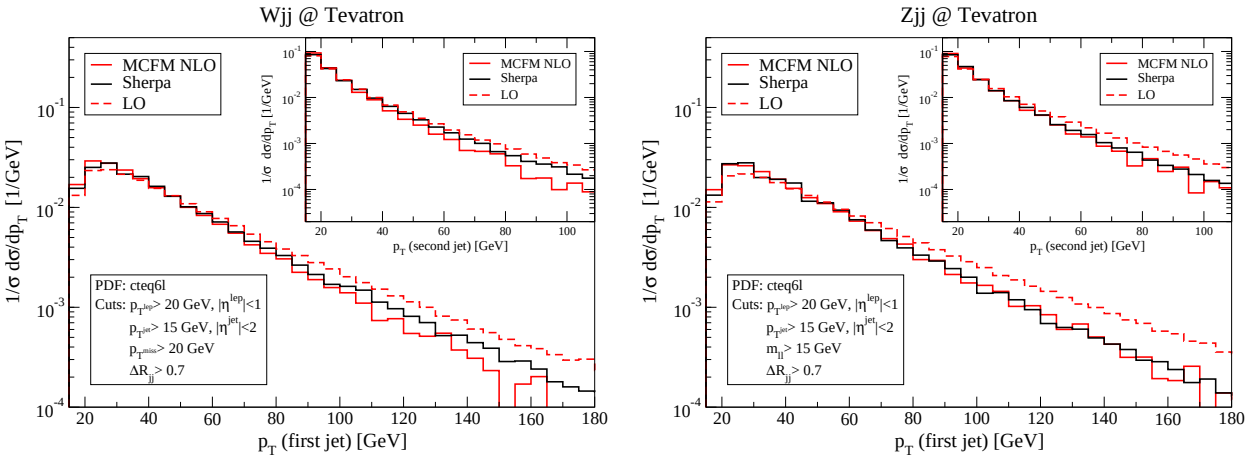

Figure 2.12: The p_T distribution of the first and second jets in exclusive W + 2jet (left) and in exclusive Z^0 + 2jet (right) events at the Tevatron, Run II.

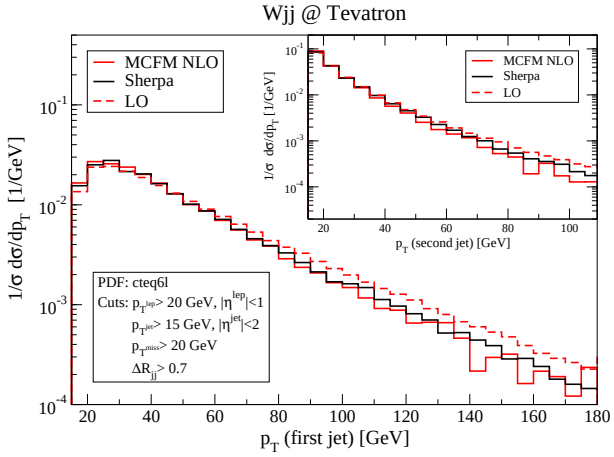

Figure 2.13: The p_T distribution of the first and second jets in exclusive W + 2jet events at the Tevatron where for the NLO and LO calculation the renormalisation and factorisation scales have been chosen to $\mu_R = \mu_F = 160.838$ GeV.

the leading-order result is smaller than the next-to-leading-order one. Taken together, the curves have a significantly different shape over the whole interval. This situation clearly forbids the use of constant K-factors in order to match the leading order with the next-to-leading-order result. Nevertheless, as before, the SHERPA prediction reproduces to a very good approximation the shape of the NLO result delivered by MCFM. Fig. 2.13 shows that, similar to the Z^0 + 1jet case for W + 2jet in the high-p_T tail, the situation is even better using higher renormalisation and factorisation scales (e.g. $\mu_R = \mu_F = 160.838$ GeV) in the NLO calculation.

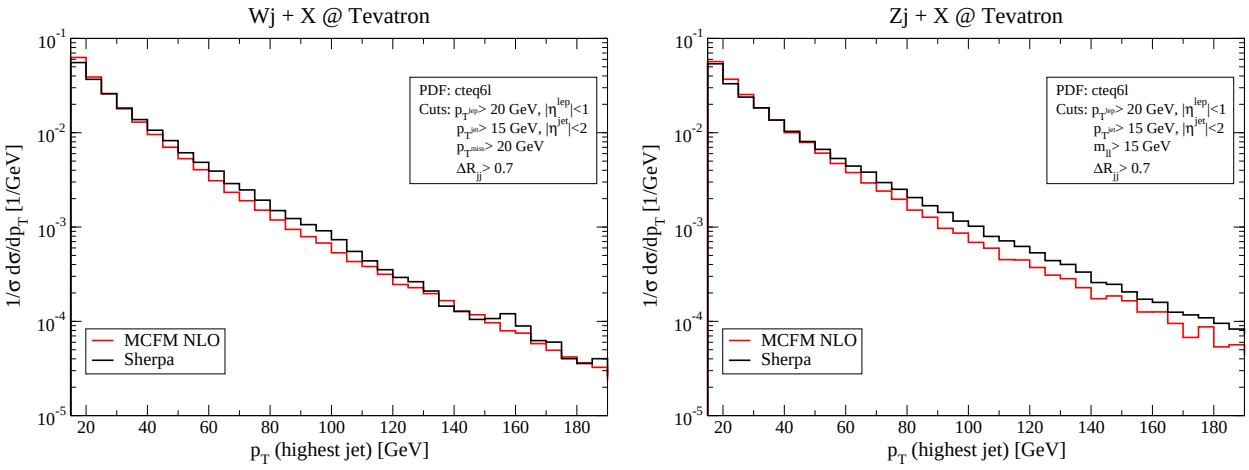

Figure 2.14: The p_T distribution of the hardest jet for inclusive W + 1jet (left) and for inclusive Z^0 + 1jet (right) production at the Tevatron, Run II.

Inclusive jet p_T spectra

NLO results for inclusive boson plus jet(s) production obtained with MCFM are compared with fully inclusive samples generated with SHERPA. There, the matrix elements for $W/Z^0 + 0, 1, 2$jet production have been used including the highest multiplicity treatment for the $W/Z^0 + 2$jet case. The Sudakov and α_s reweighted matrix elements have now been combined with the initial and final state parton showers. The hadronisation phase for the SHERPA events has been discarded. As for the exclusive case the naive leading-order prediction is given by the corresponding leading-order matrix element that is identical to the one in Figs. 2.10 and 2.12. For the NLO prediction again the renormalisation and factorisation scales have been chosen to coincide, namely $\mu_R = \mu_F = m_W$.

In Fig. 2.14, the p_T spectra for the hardest jet in inclusive W/Z^0 + 1jet production are shown. Compared with the exclusive predictions, the high-p_T tail is filled again and, hence, the differences between the NLO calculations and the LO ones appear to be smaller. For both cases the SHERPA result and the NLO calculation are in good agreement.

In Fig. 2.15 the p_T spectra for the first and second hardest jets in inclusive W/Z^0 + 2jet production are presented. Considering the scale dependence of the next-to-leading-order result in the high-p_T region, as already studied in Fig. 2.13 for the exclusive result, the curves are in pretty good agreement.

Altogether, the merging procedure in SHERPA, including the scale-setting prescription of the approach and the Sudakov reweighting of the LO matrix elements, proves to lead to a significantly improved leading-order prediction. Seemingly, it takes proper care of the most relevant contributions of higher-order corrections. Although it should be stressed that the rate predicted by SHERPA is still a leading-order value only, a constant K-factor is sufficient to recover excellent agreement with a full next-to-leading order calculation for

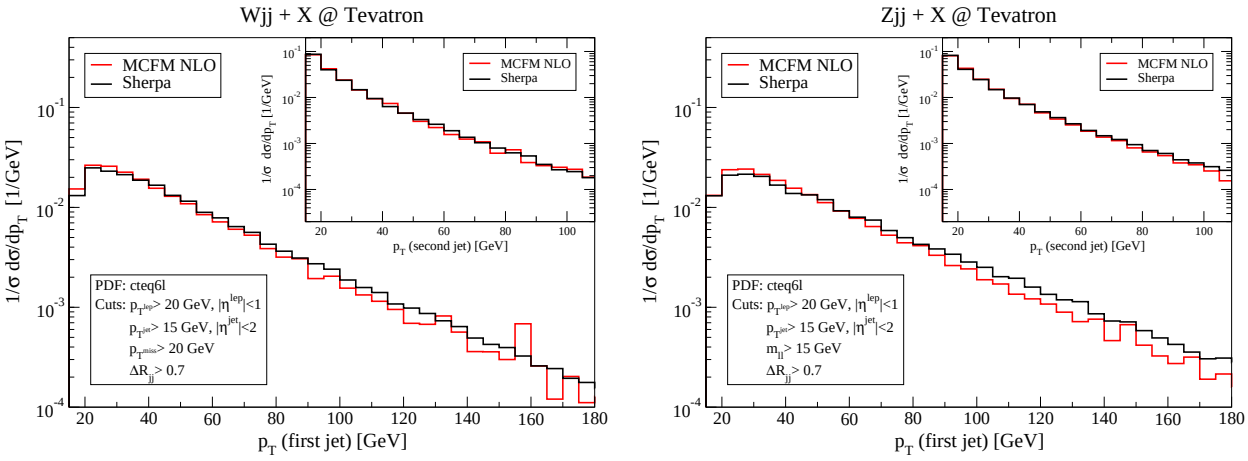

Figure 2.15: The p_T distribution of the hardest two jets for inclusive W + 2jet (left) and for inclusive Z^0 + 2jet (right) production at the Tevatron, Run II.

the distributions considered. Furthermore, by looking at the inclusive spectra it is obvious that this statement still holds true after the inclusion of parton showers and the merging of exclusive matrix elements of different jet multiplicities.

2.3.3 Confronting Monte Carlo predictions with DØ data

This section reports on an experimental analysis to compare DØ data and predictions of the event generators PYTHIA and SHERPA for the Z^0/γ^*+ jets channel with $Z^0/\gamma^* \to e^+e^-$. The analysis focuses on the description of jet observables. For the production of additional jets accompanying the produced gauge boson PYTHIA relies on a conventional parton-shower model, whereas in SHERPA exact tree-level matrix elements are taken into account according to the CKKW prescription. The main objective is to determine how accurately jet production in Z^0/γ^* events is modelled by the two approaches. Preliminary results of this study have been presented in [79].

Data and Monte Carlo samples

The data used for the analysis was collected during October 2002 and November 2005 by the DØ experiment at the Fermilab Tevatron collider at $\sqrt{s} = 1960$ GeV. The integrated luminosity corresponds to about 950 pb^{-1}.

The PYTHIA sample was generated with version PYTHIA 6.319 [80]. For the parton densities the CTEQ6l1 set was used and the parameters of the underlying event model correspond to what is known as PYTHIA Tune A, cf. Ref. [81]. The SHERPA sample has been generated with SHERPA version 1.0.6 and the CTEQ6l PDF set has been used. Tree-level matrix elements with up to three final-state partons have been enabled. In correspondence with the jet cuts to be applied the matching scale was chosen to be $Q_{\text{cut}} = 20$ GeV. For the

underlying event SHERPA's default tune was used. Both Monte Carlo samples have been overlayed with zero bias events to account for additional $p\bar{p}$ collisions in the same beam crossing. The samples had to pass the full DØ detector simulation and reconstruction chain and have been normalised to the total number of Z^0/γ^* events found in the data sample. Note, that no separate normalisation is used for subsamples of different jet multiplicity.

Event selection

Two oppositely charged electrons are required, both with a transverse momentum above 25 GeV. Both leptons have to be found in the pseudo-rapidity range $|\eta| < 2.5$, but at least one of them is required to be reconstructed in the central detector, accordingly $|\eta| < 1.1$. The di-electron invariant mass has to fulfil 70 GeV $< M_{e^+e^-} <$ 100 GeV. An efficient background suppression of fake electrons from QCD jets has been employed, cf. [79].
Jets are reconstructed according to the DØ Run II cone algorithm with a cone parameter of $R = 0.5$ and a required jet transverse momentum of $p_T > 15$ GeV. To diminish backgrounds from uninstrumented detector parts or electrons, certain additional criteria for jet candidates have been included [79]. A Gaussian smearing of the jet energies in Monte Carlo events has been applied.

Comparison between data and Monte Carlo

The transverse momentum distribution of the produced gauge bosons provides insight into the jet production models of the theoretical tools without the need to actually reconstruct jets. In fact the di-electron system has to compensate for the total transverse momentum of the associated jet system. Fig. 2.16 contains a comparison of DØ data for the p_T distribution of the di-electrons with both PYTHIA (left panel) and SHERPA (right panel). The shaded ranges in the histograms show the Monte Carlos central values $\pm 1\sigma$ the statistic error. In the lower half of each plot the bin wise ratio data over Monte Carlo is displayed. The slope of the PYTHIA distribution indicates that PYTHIA predicts less high-p_T gauge bosons compared to what is seen in data, corresponding to less high-p_T jets. SHERPA's agreement with data is good for $p_T < 100$ GeV, above SHERPA tends to be harder than data. To quantify the jet activity predicted by the two theoretical models Fig. 2.17 shows a comparison of the observed exclusive jet multiplicities with the simulations. The red bands indicate $\pm 1\sigma$ the statistical error for the Monte Carlo predictions, whereas the combined red and blue bands show the central values $\pm$ the statistical and systematic errors added in quadrature. Correspondingly, the grey data points are given with statistical error only, whereas the black points include the systematic errors from jet-energy scale uncertainties. The numbers of events found in the data and predicted by the two Monte Carlos are collected in Tab. 2.1 for the different multiplicity bins. The central values predicted by PYTHIA for the jet production processes are lower than seen in data, corresponding to too few hard jets produced by PYTHIA's parton-

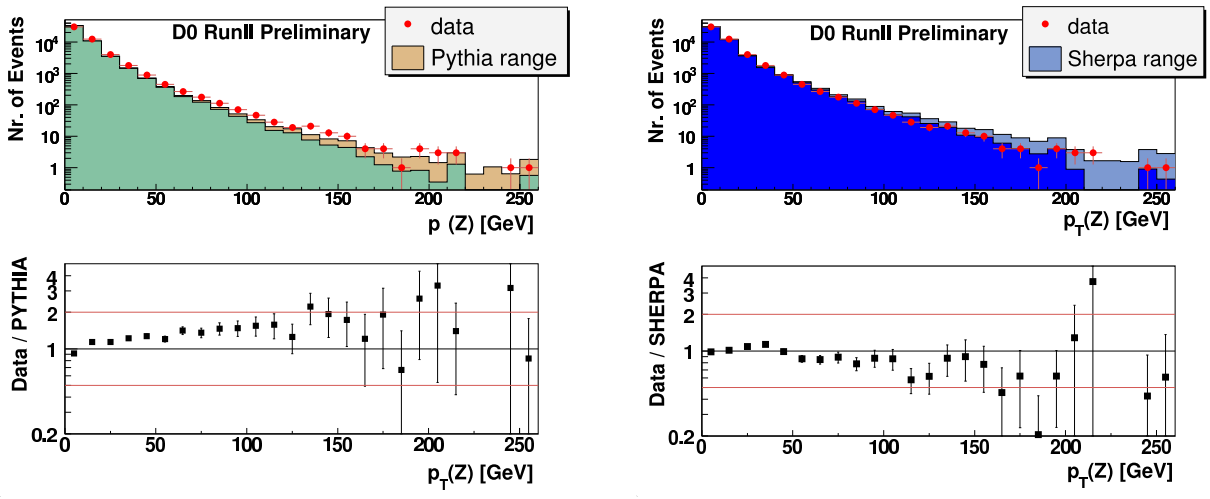

Figure 2.16: The transverse momentum distribution of the di-electron system ($p_T(Z^0)$). Presented is a comparison of DØ data with PYTHIA (left panel) and SHERPA (right panel). The lower part shows the bin wise ratio data/MC with the red lines indicating factors of 2 and 0.5.

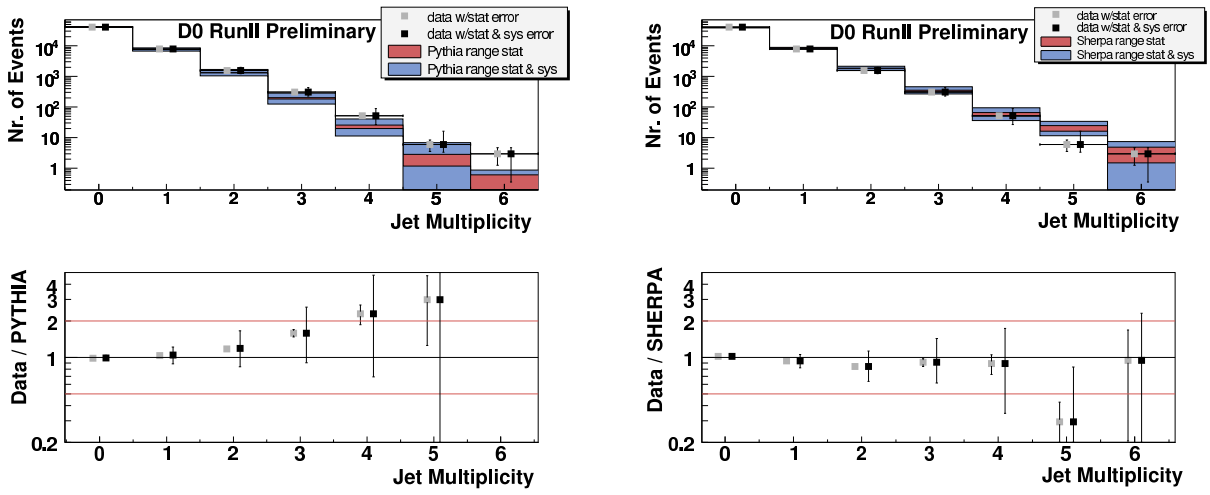

Figure 2.17: The jet-multiplicity distribution for $e^+e^- + n$ jet events. Comparison of DØ data and the PYTHIA (left panel) and SHERPA predictions.

shower model. SHERPA on the other hand slightly overshoots the data, however, giving fairly good estimates for the $n \geq 3$ bins, where PYTHIA is significantly lower. However, taking into account the large systematic uncertainties arising from low-p_T jets, the predictions of both event generators agree with the data. To gain some further insight into the quality of the modelling of jet physics with the two approaches the transverse momentum spectra of jets accompanying the Drell-Yan pair have been considered. Figs. 2.18 - 2.20 show

Sample	Inclusive	0-jet	1-jet	2-jet	3-jet	4-jet
Data	50417	40624	7877	1552	306	52
PYTHIA	50417	41271	7604	1324	193	23
SHERPA	50417	39746	8410	1842	335	58

Table 2.1: Event numbers observed in data and predicted by PYTHIA and SHERPA after normalisation [79].

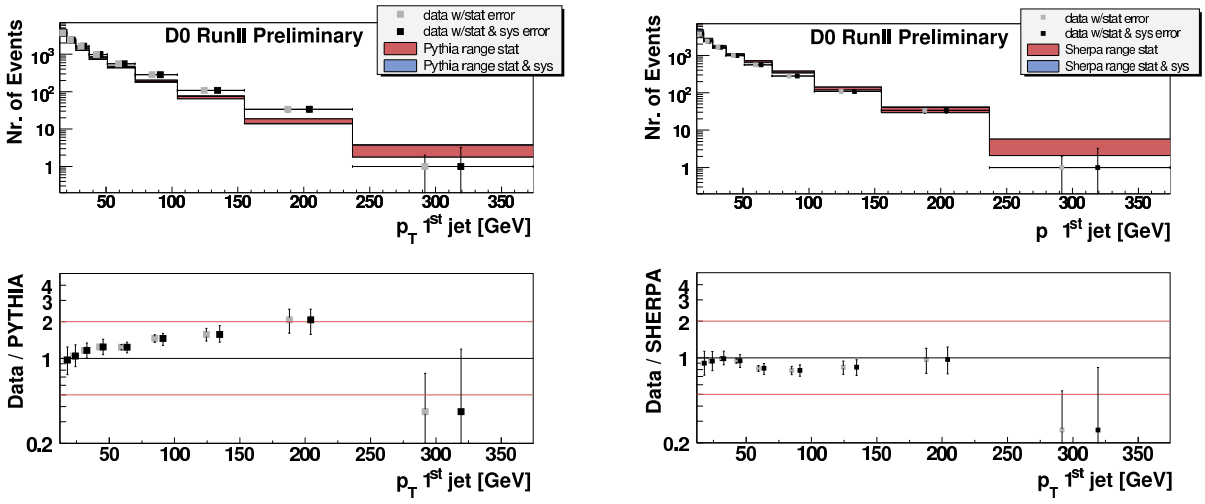

Figure 2.18: The transverse momentum distribution of the hardest jet accompanying the produced boson. Compared are DØ data and predictions made with PYTHIA (left panel) and SHERPA (right panel).

the inclusive p_T distributions of the three hardest jets. Accordingly, in Fig. 2.20 events are included that possess *at least* one jet that passes the selection criteria stated above. Correspondingly, events included in Fig. 2.19 (2.20) have to have at least two (three) jets. When looking at the leading jet it is apparent that PYTHIA's spectrum is much soft than what is seen in data. SHERPA on the other hand follows the shape of the experimental result, the predicted inclusive rate, however, is slightly larger than the measured value. SHERPA's second-jet and third-jet p_T spectra show an equally good agreement with data. Taking into account the experimental uncertainties SHERPA's theoretical prediction clearly is consistent with the experimental measurements over the whole region of phase space covered. For PYTHIA the situation for the second and third jet is different, the plain parton-shower approach used for the production of extra jets, clearly underestimates the amount of hard radiation. This, however, could have been expected as the production of Drell-Yan pairs accompanied by three hard jets all above 50 GeV is obviously beyond the soft and collinear approximations used in a conventional parton-shower calculation, such as done

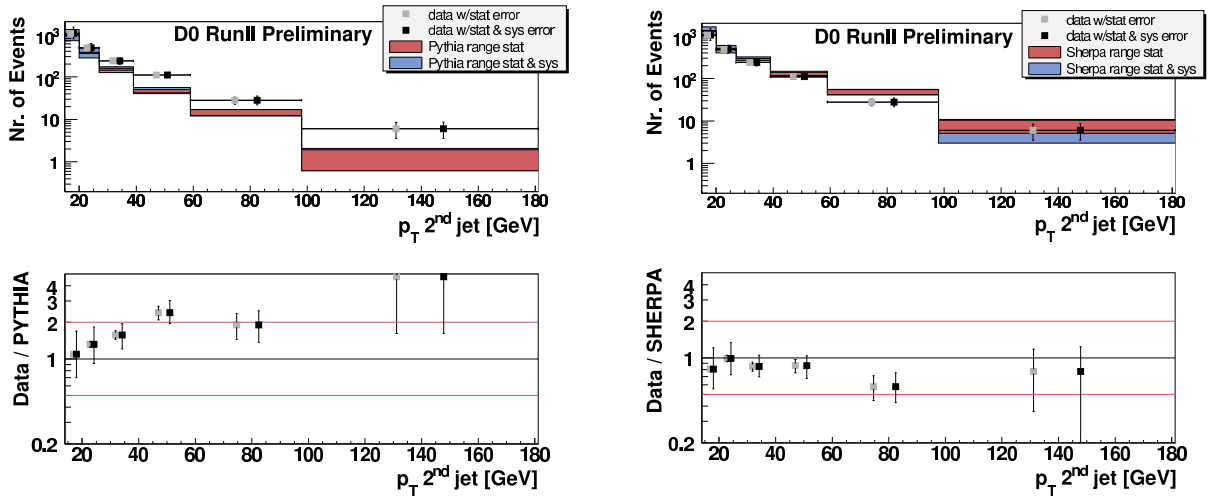

Figure 2.19: Comparison of DØ data and predictions made with PYTHIA (left panel) and SHERPA (right panel) for the p_T distribution of the second hardest jet in Drell-Yan events with at least two additional jets.

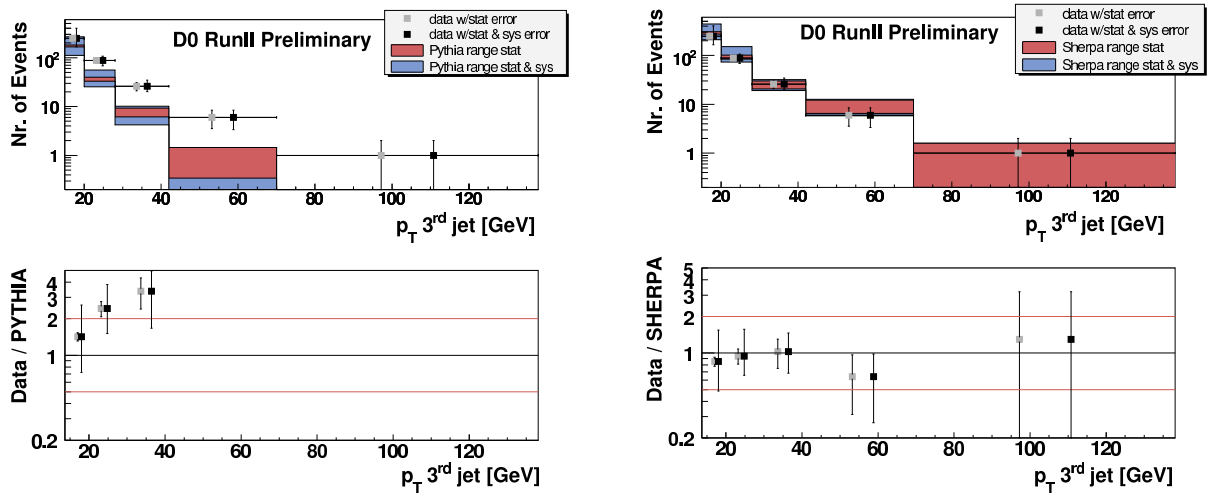

Figure 2.20: The p_T distribution of the third hardest jet associated to an e^+e^- Drell-Yan pair. In the left panel a prediction obtained with PYTHIA is compared to DØ data, the right panel shows a comparison of SHERPA with this data set.

in PYTHIA. Besides allowing for additional hard radiation it is expected that the matrix-element–parton-shower merging approach used in SHERPA yields an improved description of observables sensitive to angular correlations. While such spatial correlations are are not taken into account in a conventional parton-shower approach they are included in the calculations of the full matrix elements. Fig. 2.21 contains a comparison for the azimuthal angle between the two hardest jets, $\Delta\phi = |\phi_1 - \phi_2|$, with ϕ_i the azimuthal angle of the ith

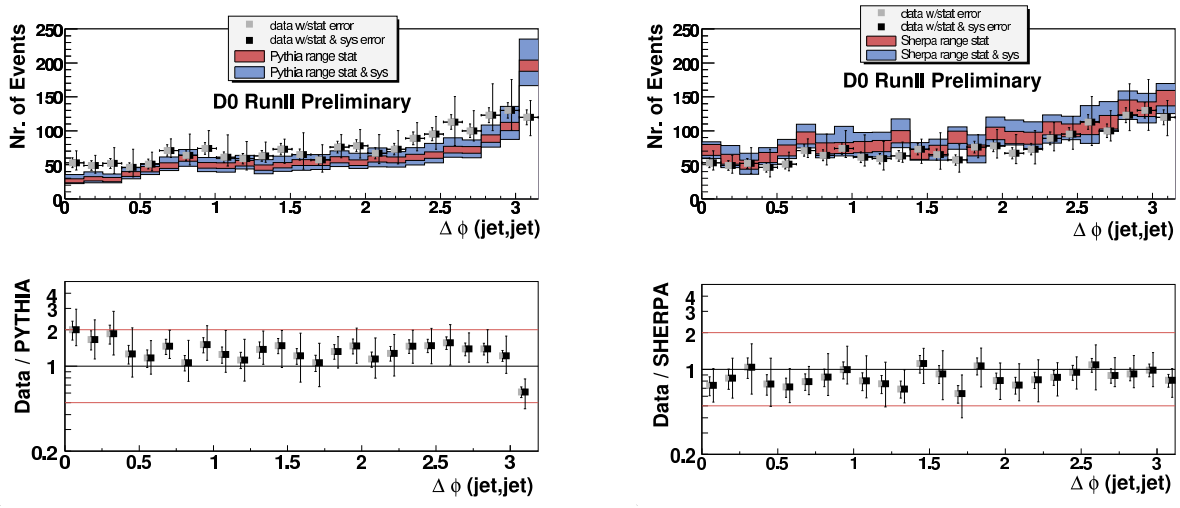

Figure 2.21: The azimuthal angle between the hardest and second-hardest jet, $\Delta\phi = |\phi_1 - \phi_2|$, in inclusive Drell-Yan events. DØ data is compared to predictions obtained with PYTHIA (left panel) and SHERPA (right panel).

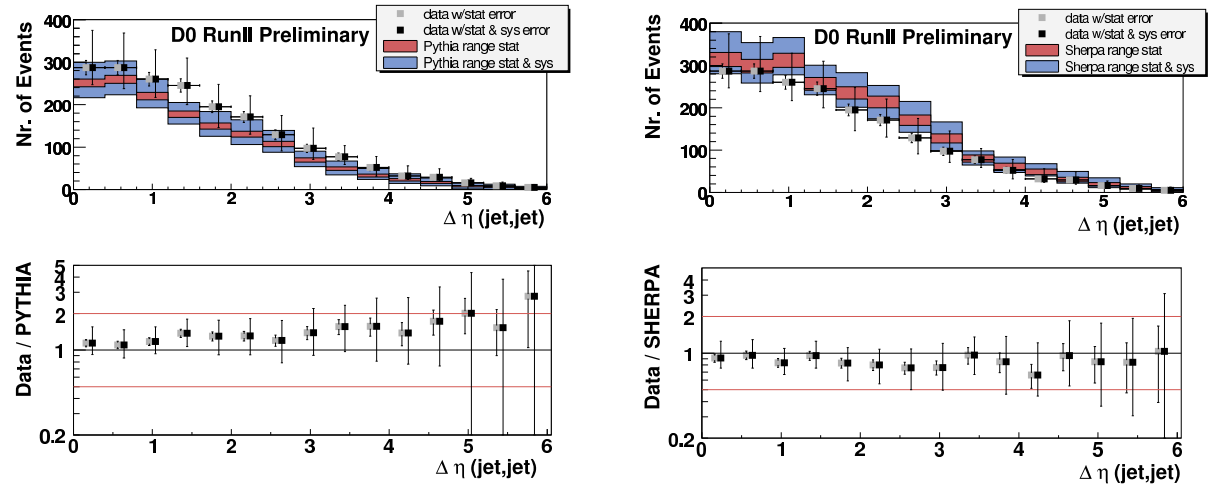

Figure 2.22: The pseudo-rapidity distance between the hardest and second-hardest jet, $\Delta\eta = |\eta_1 - \eta_2|$, in Drell-Yan events with at least two extra jets. DØ data is compared PYTHIA (left panel) and SHERPA (right panel) predictions.

hardest jet. The SHERPA curve agrees quite nicely with data, but the PYTHIA result shows a significant excess at $\Delta\phi = \pi$. This excess was traced back to originate from PYTHIA's underlying simulation [82]. In the model used, cf. Ref. [33], the underlying event activity is described through additional semi-hard QCD $2 \to 2$ processes. In the version of PYTHIA used for the comparison these processes are not equipped with a parton-shower simulations, such that the produced outgoing partons of a single underlying event will remain back-

to-back, correspondingly at $\Delta\phi = \pi$. When including parton showers for the multiple interactions (as it is done for SHERPA) this structure would disappear. However, this result reveals that in the PYTHIA sample a good fraction of the second and higher jets originate from the underlying event and not from the parton shower off the Drell-Yan core process. In the SHERPA approach the phase space for additional uncorrelated QCD $2 \to 2$ scatters is restricted such, that the underlying event must not spoil the jet topologies described by the hard event [32]. Although leaving much less phase space to multiple interactions, SHERPA very satisfactory describes the underlying event activity found in dedicated analyses, cf. Ref. [32].
In Fig. 2.22 the pseudo-rapidity distance between the hardest two jets is considered, namely $\Delta\eta = |\eta_1 - \eta_2|$, with η_i the pseudo-rapidity of the ith hardest jet. Here both Monte Carlo generators are within the uncertainties of the experimental data. The last observable to be considered is the so called Zeppenfeld variable η^*, defined according to

$$\eta^* = \eta_3 - \frac{\eta_1 + \eta_2}{2}\,, \tag{2.17}$$

where the jets have to pass the additional criteria

$$|\eta_1 - \eta_2| > 2.0\,, \tag{2.18}$$

and

$$\eta_1 < \eta_3 < \eta_2 \quad \text{or} \quad \eta_2 < \eta_3 < \eta_1\,. \tag{2.19}$$

The Zeppenfeld variable is of phenomenological interest as it constitutes a strong discriminator in searches for the production of Higgs bosons in the weak-boson-fusion channel for separating the signal from QCD backgrounds [83]. A good theoretical modelling of this quantity is therefore of great importance especially at the LHC, where weak-boson-fusion is dealt as one of the most promising Higgs discovery channels. In Fig. 2.23 the distribution of η^* as measured by DØ is shown. The used data sample contains only few events that pass the above selection criteria. Accordingly, the statistical errors are sizable. SHERPA seems to describe both the overall rate and the shape of the distribution seen in data. PYTHIA predicts much less three-jet events but the shape of the distribution is in agreement with data when taking into account the experimental uncertainties.

In this section it has been reported on a detailed comparison of DØ data and Monte Carlo predictions obtained with PYTHIA and SHERPA for the inclusive production of e^+e^- Drell-Yan pairs. Focusing on the description of jet quantities the theoretical models for jet production in the two generators have been compared. It can be concluded that the incorporation of exact tree-level matrix elements in the simulation of QCD radiation processes, as done in SHERPA according to the CKKW prescription, yields an improved agreement with data for both the overall rates and the shapes of jet distributions.

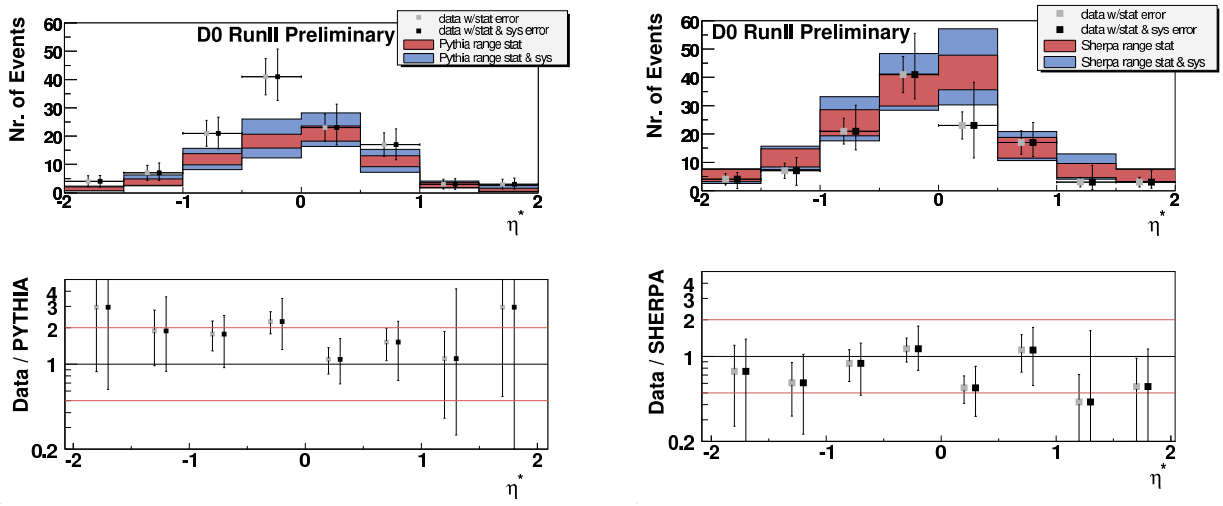

Figure 2.23: The Zeppenfeld variable η^*. The left panel contains a comparison of DØ data with the corresponding PYTHIA prediction, the right panel with SHERPA.

2.4 Comparison of various merging prescriptions

Besides the CKKW prescription for the consistent combination of multi-parton matrix-element calculations with parton-shower simulations, over the past few years other solutions to the problem have been developed. The most prominent one is the MLM procedure developed by M. L. Mangano, that has been encoded in the ALPGEN generator [42, 47]. Only recently variants of the MLM method have also been employed for the MADEVENT [50] and the HELAC [51, 52] generators. Another alternative approach, the Lönnblad scheme, has been developed by L. Lönnblad for combining the dipole model implemented in ARIADNE with tree-level matrix elements.

Here it will be reported on an extended comparison of all the presently available approaches. The benchmark process chosen is W+jets production at Tevatron and LHC. Besides comparing various distributions and rates for the different approaches an attempt is made to quantify the intrinsic systematic uncertainties of the different solutions to the same problem. An extended version of this comparative study has been presented in [84].

After briefly reviewing the prescriptions alternative to CKKW in Sec. 2.4.1, the details of the generator setups are discussed in Sec. 2.4.2. In Secs. 2.4.3 and 2.4.4 cross sections and distributions predicted by the different approaches are compared for $p\bar{p}$ (pp) collisions at Tevatron (LHC) energies. Sec. 2.4.5 focuses on the assessment of the systematic uncertainties intrinsic to these multi-scale calculations.

2.4.1 Alternatives to CKKW

Combining matrix elements and the Dipole Cascade model

The merging prescription developed for the dipole cascade in the ARIADNE program [45] is similar to CKKW, but differs in the way the shower history is constructed, and in the way the Sudakov form factors are calculated. Also, since the ARIADNE cascade is ordered in transverse momentum the treatment of starting scales is simplified and there is no need for a vetoed parton shower. Before discussing the merging prescription it is useful to describe some details of the dipole cascade, since it is quite different from conventional showers.

The dipole model [85, 86] as implemented in the ARIADNE program is based around iterating $2 \to 3$ partonic splittings instead of the usual $1 \to 2$ branchings in conventional parton shower. Gluon emission is modelled as coherent radiation from colour–anti-colour charged parton pairs. This has the advantage of eg. including first order correction to the matrix elements for $e^+e^- \to q\bar{q}$ in a natural way and it also automatically includes the coherence effects modelled by angular ordering in conventional showers. The process of quark–anti-quark production does not come in as naturally, but can be added [87]. The emissions in the dipole cascade are ordered according to invariant transverse momentum defined as

$$p_\perp^2 = \frac{s_{12}s_{23}}{s_{123}}, \tag{2.20}$$

where s_{ij} is the squared invariant mass of parton i and j, with the emitted parton having index 2.

When applied to hadronic collisions, the dipole model does not separate between initial- and final-state gluon radiation. Instead all gluon emissions are treated as coming from final-state dipoles [88, 89]. To be able to extend the dipole model to hadron collisions, spatially extended coloured objects are introduced to model the hadron remnants. Dipoles involving hadron remnants are treated in a similar manner to the normal final-state dipoles. However, since the hadron remnant is considered to be an extended object, emissions with small wavelength are suppressed. This is modelled by only allowing a fraction of the remnant to take part in the emission. The fraction that is resolved during the emission is given by

$$a(p_\perp) = \left(\frac{\mu}{p_\perp}\right)^\alpha, \tag{2.21}$$

where μ is the inverse size of the remnant and α is the dimensionality. These are semi-classical parameters which have no correspondence in conventional parton cascades, where instead a suppression is obtained by ratios of quark densities in the backward evolution. The main effect is that the dipole cascade allows for harder gluon emissions in the beam directions, enabling it to describe properly eg. forward jet rates measured at HERA (see eg. [90]).

There are two additional forms of emissions which need to be included in the case of hadronic

collisions. One corresponds to an initial state $g \to q\bar{q}$ [91]. This does not come in naturally in the dipole model, but is added by hand in a way similar to that of a conventional initial-state parton shower [91]. The other corresponds to the initial-state $q \to gq$ (with the gluon entering into the hard sub-process) which could be added in a similar way, but this has not yet been implemented in ARIADNE.

When implementing CKKW for the dipole cascade [41, 46], the procedure is slightly different from what has been described above. First, rather than just constructing emission scales using the $k_\perp$-algorithm, a complete dipole shower history is constructed for each state produced by the matrix-element generator, basically answering the question *how would ARIADNE have generated this state*. This will produce a complete set of intermediate partonic states, S_i, and the corresponding emission scales, $p_{\perp i}$. Note that this means that only coloured particles are clustered, which differs from eg. SHERPA, where also the W and its decay products are involved in the clustering.

The Sudakov form factors are then introduced using the Sudakov veto algorithm. The idea is to exactly reproduce the Sudakov form factors used in ARIADNE. This is done by performing a trial emission starting from each intermediate state S_i with $p_{\perp i}$ as a starting scale. If the emitted parton has a $p_\perp$ higher than $p_{\perp i+1}$ the state is rejected. This correspond to keeping the state according to the no emission probability in ARIADNE, which is exactly the Sudakov form factor.

It should be noted that for initial-state showers, there are two alternative ways of defining the Sudakov form factor. The definition in Eq. (2.2) is used in eg. HERWIG, while eg. PYTHIA uses a form which explicitly includes ratios of parton densities. Although formally equivalent to leading logarithmic accuracy, only the latter corresponds exactly to a no-emission probability, and this is the one generated by the Sudakov-veto algorithm. This, however, also means that the constructed emissions in this case need not only be reweighted by the running α_s as in the standard CKKW procedure above, but also with ratios of parton densities, which in the case of gluon emissions correspond to the suppression due to the extended remnants in Eq. (2.21) as explained in more detail in [46], where the complete algorithm is presented.

The MLM procedure

The goal of this approach is to achieve leading logarithmic (LL) accuracy for the lowest-order contribution to a given inclusive observable. This means correctly describing, for all ℓ, the coefficient of the $\alpha_s^m \times [\alpha_s\ L^2]^\ell$ contributions to an observable that, at the partonic leading-order level, starts at order α_s^m. The absolute scale of the order α_s^m term is set by the matrix-element calculation of the parton-level event, while the series of logarithms is taken care of by the shower evolution. The task is to make sure that none of the logarithms is double counted. This is achieved by the so-called "matching" algorithm described below.

1. The first step is the generation of parton-level configurations for all final-state parton multiplicities n up to a given $n_{\max}$ (*i.e.* $\mathrm{W} + n_{\max}$ partons). They are defined by the following kinematical cuts:

$$p_T^{part} > p_T^{min} \ , \quad |\eta_{part}| < \eta_{max} \ , \quad \Delta R_{jj} > R_{min} \ , \tag{2.22}$$

where p_T^{part} and η_{part} are the transverse momentum and pseudo-rapidity of the final-state partons, and ΔR_{jj} is their minimal separation in the (η, ϕ) plane. The parameters p_T^{min}, η_{max} and R_{min} are called generation parameters, and are the same for all $n = 1, \ldots, n_{\max}$.

2. The renormalisation scale is set according to the CKKW prescription. The necessary tree branching structure is defined for each event, allowing however only for branchings which are consistent with the colour structure of the event, which in ALPGEN is extracted from the matrix-element calculation [92]. For a pair of final-state partons i and j the $k_\perp$ measure defined by

$$k_\perp = \Delta R_{ij} \min(p_{\mathrm{T}i}, p_{\mathrm{T}j}) \ , \tag{2.23}$$

is used, where $\Delta R = \sqrt{\Delta\eta^2 + \Delta\phi^2}$, while for a pair of initial/final-state partons this becomes $k_\perp^2 = p_{\mathrm{T}}^2$, i.e. the p_{T} of the final-state one.

3. The $k_\perp$-value at each vertex is used as a scale for the relative power of α_{s}. The factorisation scale for the parton densities is given by the hard scale of the process, $Q_0^2 = m_W^2 + p_{T,W}^2$. It may happen that the clustering process stops before the lowest-order configuration is reached. This is the case, e.g., for an event like $u\bar{u} \to Wc\bar{s}g$. Flavour conservation allows only the gluon to be clustered, since $u\bar{u} \to Wc\bar{s}$ is a LO process, first appearing at $\mathcal{O}(\alpha_s^2)$. In such cases, the hard scale Q_0 is adopted for all powers of α_{s} corresponding to the non merged clusters.

4. Events are then showered, using PYTHIA or HERWIG. The upper cut-off to the shower evolution is given by the hard scale of the process, Q_0. After evolution, a jet cone algorithm is applied to the partons produced in the shower. Jets are defined by a cone size R_{clus}, a minimum transverse energy $E_{\mathrm{T}}^{\mathrm{clus}}$ and a maximum pseudo-rapidity $\eta_{\mathrm{max}}^{clus}$. These parameters are called matching parameters, and should be kept the same for all samples $n = 0, 1, \ldots, n_{\max}$. These jets provide the starting point for the matching procedure, described in the next bullet. In the default implementation, the choices $R_{\mathrm{clus}} = R_{min}$, $\eta_{\mathrm{max}}^{clus} = \eta_{max}$ and $E_{\mathrm{T}}^{\mathrm{clus}} = p_T^{min} + \max(5\ \mathrm{GeV}, 0.2 \times p_T^{min})$ are made, but these can be varied as part of the systematics assessment. To ensure a complete coverage of phase space, however, it is necessary that $R_{\mathrm{clus}} \geq R_{min}$, $\eta_{\mathrm{max}}^{clus} \leq \eta_{max}$ and $E_{\mathrm{T}}^{\mathrm{clus}} \geq p_T^{min}$.

5. Starting from the hardest parton, the jet which is closest to it in (η, ϕ) is selected. If the distance between the parton and the jet centroid is smaller than $1.5 \times R_{\text{clus}}$, it is said that the parton and the jet *match*. The matched jet is removed from the list of jets, and the matching test for subsequent partons is performed. The event is fully matched if each parton matches to a jet. Events which do not match are rejected. A typical example is when two partons are so close that they cannot generate independent jets, and therefore cannot match. Rejection removes double counting of the leading double logarithms associated to the collinear behaviour of the amplitude when two partons get close. Another example is when a parton is too soft to generate its own jet, again failing matching. This removes double counting of some single logarithms.

6. Events from the parton samples with $n < n_{\text{max}}$ which survive matching are then required not to have extra jets. If they do, they are rejected, a suppression which replaces the Sudakov reweighting used in the CKKW approach. This prevents the double counting of events which will be present in, and more accurately described by, the $n + 1$ sample. In the case of $n = n_{\text{max}}$, events with extra jets can be kept since they will not be generated by samples with higher n. Nevertheless, to avoid double counting, it is required that their transverse momentum is smaller than that of the softest of the matched jets.

When all the resulting samples from $n = 0, \ldots, n_{\text{max}}$ are combined, an inclusive W+jets sample is obtained. The harder the threshold for the energy of the jets used in the matching, $E_{\text{T}}^{\text{clus}}$, the fewer the events rejected by the extra-jet veto (i.e. smaller Sudakov suppression), with a bigger rôle given to the shower approximation in the production of jets. Using lower thresholds would instead enhance the rôle of the matrix elements even at lower E_T, and lead to larger Sudakov suppression, reducing the rôle played by the shower in generating jets. The matching/rejection algorithm ensures that these two components balance each other, and that physical observables be independent of the generation parameters.
As stated above this algorithm is realised in the ALPGEN generator, where shower evolution with both HERWIG and PYTHIA is enabled.

The MADEVENT approach

The approach used in MADGRAPH/MADEVENT [48, 49] is based on the MLM prescription, but uses a different jet algorithm for defining the scales in α_{s} and for the jet matching. The phase-space separation between the different multi-jet processes is achieved using the $k_\perp$-measure as in SHERPA, while the Sudakov reweighting is performed by rejecting showered events that are not matched to the parton-level jets, as in ALPGEN. The details of the procedure are as follows.
Matrix-element multi-parton events are produced using MADGRAPH/MADEVENT version 4.1 [50], with a cut-off $Q_{\text{min}}^{\text{ME}}$ in clustered $k_\perp$. The multi-parton state from the matrix-element

calculation is clustered according to the $k_\perp$ algorithm, but allowing only clusterings that are compatible with the Feynman diagrams of the process. The factorisation scale is taken to be the clustering momentum in the last $2 \to 2$ clustering (the "central process"), *e.g.* in W-boson production this will corresponding to the transverse mass of the boson. The $k_\perp$-scales of the QCD clustering nodes are used as scales in the calculation of the various powers of α_s.

As in the ALPGEN procedure, no Sudakov reweighting is performed. Instead, Pythia 6.4 [2] is used to shower the event, with the starting scale of the shower set to the factorisation scale. In the present study the virtuality-ordered showers were used. The showered (but not yet hadronised) event is then clustered to jets using the $k_\perp$-algorithm with the cut-off $Q^{\text{jet}}_{\text{min}} > Q^{\text{ME}}_{\text{min}}$, and the matrix-element partons are matched to the resulting jets. A parton is considered to be matched to the closest jet if the jet measure $Q(\text{parton}, \text{jet})$ is smaller than the cut-off $Q^{\text{jet}}_{\text{min}}$. For events with the highest multiplicity n_{max}, the partons are considered to be matched if $Q(\text{parton}, \text{jet}) < Q^{\text{parton}}_{n_{\text{max}}}$, the smallest $k_\perp$-measure in the parton-level event, which is similar to SHERPA's highest multiplicity treatment, cf. Sec. 2.2.3. Events where not all partons are matched to jets are rejected. For events with multiplicity smaller than the highest multiplicity, the number of jets must be equal to the number of partons, while for events from the highest multiplicity sample, extra jets are allowed.

HELAC implementation of the MLM procedure

The MLM procedure as described above has also been implemented in the HELAC generator [51, 52]. HELAC thereby provides the matrix elements and parton showering is included via an interface to the transverse momentum ordered shower of PYTHIA 6.4 [2].

The parton-level events are generated requiring $p_{T_j} > p_{T\text{min}}$ for all QCD partons, a minimum parton separation, $\Delta R_{jj} > R_{\text{min}}$ and a maximum pseudo-rapidity $|\eta_j| < \eta_{\text{max}}$. The arguments of the α_s factors are reconstructed using a $k_\perp$-algorithm as outlined above. The colour flow information extracted from the matrix-element calculation is used as a constraint on the allowed clusterings. The so generated parton-level events are interfaced to PYTHIA using the latest Les Houches event file format [93]. After showering each event gets analyses by a cone-jet algorithm. The reconstructed jets are defined by $E^{\text{clus}}_{T\text{min}}$, $\eta^{\text{clus}}_{\text{max}}$ and by a jet cone size R_{clus}. The partons from the parton-level events then are assigned to one of the constructed jets. Starting from the parton with the highest p_T the closest jet ($1.5 \times R_{\text{clus}}$) is selected in the $\eta - \phi$ space. All subsequent partons are matched iteratively to the remaining jets. If no complete match is found the event is rejected. Additionally, for $n < n_{\text{max}}$, matched events with the number of jets greater than n are rejected, whereas for $n = n_{\text{max}}$ events with extra jets are kept, only if they are softer than the n_{max} matched jets.

2.4.2 Event generation setup for the study

The following two sections present results for the Tevatron ($p\bar{p}$ collisions at 1.96 TeV) and for the LHC (pp collisions at 14 TeV). The elements of the analysis common to all codes are the following:

- *Event samples.* Tevatron results refer to the combination of W^+ and W^- bosons, while at the LHC only W^+ are considered. All codes have generated parton-level samples according to matrix elements with up to four final-state partons, using the the PDF set CTEQ6l, with $\alpha_s(m_Z) = 0.118$. Further SM parameters used were: $m_W = 80.419$ GeV, $\Gamma_W = 2.048$ GeV, $m_Z = 91.188$ GeV, $\Gamma_Z = 2.446$ GeV, the Fermi constant $G_\mu = 1.16639 \cdot 10^{-2}$ GeV^{-2}, $\sin^2\theta_W = 0.2222$ and $\alpha_{\rm qed} = 1/132.51$.

- *Jet definitions.* Jets were defined using Frank Paige's `GETJET` cone-clustering algorithm, with a calorimeter segmentation of $(\Delta\eta,\ \Delta\phi) = (0.1,6^\circ)$ extended over the range $|\eta| < 2.5$ ($|\eta| < 5$), and cone size of 0.7 (0.4) for the Tevatron (LHC). At the Tevatron (LHC) jets are required to have $E_T > 10(20)$ GeV, and pseudo-rapidity $|\eta| < 2(4.5)$. For the analysis of the differential jet rates denoted as d_i, the Tevatron Run II $k_\perp$-algorithm [56] was applied to all final-state particles with $|\eta| < 2.5(5)$.

In all cases, except the d_i plots (see below), the analysis is done at the hadron level, but without including the underlying event. For all codes the systematic uncertainties are investigated by varying the merging scale and by varying the scale in α_s and, for some codes, in the parton density functions. For ALPGEN and HELAC, the scale in α_s has been varied only in the α_s-reweighting of the matrix elements, while in the others the scale was also varied in the parton cascade. Note that varying the scale in the final-state parton showers will spoil the tuning done to LEP data for the cascades. A consistent way of testing the scale variations would require a retuning of the hadronisation parameters. However, no strong dependence on the hadronisation parameters are expected in the observables considered, and no attempt to retune them has been made.
The parameter choices specific to the individual codes are as follows:

- ALPGEN: The parton-level matrix elements were generated with ALPGEN [42, 47] and the subsequent evolution used the HERWIG parton shower according to the MLM procedure. Version 6.510 of HERWIG was used [4], with its default shower and hadronisation parameters. The *default* results for the Tevatron (LHC) were obtained using parton-level cuts (see Eq. (2.22)) of $p_T^{min} = 8(15)$ GeV, $\eta_{max} = 2.5(5)$, $R_{min} = 0.7(0.4)$ and matching defined by $E_{\rm T}^{\rm clus} = 10(20)$ GeV, $\eta_{\rm max}^{clus} = \eta_{max}$ and $R_{\rm clus} = R_{min}$. The variations used in the assessment of the systematics cover:

  - Different thresholds for the definition of jets used in the matching: $E_{\rm T}^{\rm clus} = 20$ and 30 GeV for the Tevatron, and $E_{\rm T}^{\rm clus} = 30$ and 40 GeV for the LHC. These

thresholds were applied to the partonic samples produced with the default generation cuts, as well as to partonic samples produced with higher p_T^{min} values. No difference was observed in the results, aside from an obviously better generation efficiency in the latter case. In the following studies of the systematics, these two settings will be referred to as ALPGEN parameter sets ALptX, $E_T$where X labels the value of the threshold. Studies with different values of $R_{\rm clus}$ and R_{min} were also performed, leading to marginal changes, which will not be documented here.

– Different renormalisation scale at the vertices of the clustering tree: $\mu = \mu_0/2$ and $\mu = 2\mu_0$, where μ_0 is the default $k_\perp$ value. In the following studies of the systematics, these two settings will be referred to as ALPGEN parameter sets ALscL (for "Low") and ALscH (for "High").

The publicly available version V2.10 of the code was used to generate all the ALPGEN results.

- ARIADNE: The parton-level matrix elements were generated with MADEVENT and the subsequent evolution used the dipole shower in ARIADNE according to the procedure outlined in section 2.4.1. Hadronisation was performed by PYTHIA. For the *default* results at the Tevatron (LHC) the parton-level cuts were $p_{T,min} = 10(20)$, $Rjj < 0.5(0.4)$ and, in addition, a cut on the maximum pseudo-rapidity of jets, $\eta_{j\,\rm max} = 2.5(5.0)$. The variations used in the assessment of the systematics cover:

  – different value of the merging scales $p_{\perp,min} = 20$ and 30 GeV for the Tevatron (30 and 40 GeV for the LHC). In the following studies of the systematics, these two settings will be referred to as ARIADNE parameter sets ARptX.

  – The values of the soft suppression parameters in Eq. (2.21) were changed from the default value of $\mu = 0.6$ GeV and $\alpha = 1$, to $\mu = 0.6$ GeV and $\alpha = 1.5$ (from a tuning to HERA data). This setting will be referred to as ARs.

  – Also in the ARIADNE case different values of the scale in $\alpha_{\rm s}$ were used: $\mu = \mu_0/2$ and $\mu = 2\mu_0$ (ARscL and ARscH). This scale change was used in all PDF and $\alpha_{\rm s}$ evaluations in the program.

- HELAC: The parton-level matrix elements were generated with HELAC [51, 52] and the phase-space generation is performed by PHEGAS [94]. The subsequent evolution used the default $k_\perp$-ordered shower in PYTHIA 6.4 [2] incorporated according to the MLM procedure. Hadronisation was performed by PYTHIA. The *default* results for the Tevatron (LHC) were obtained using parton-level cuts of $p_T > 8(15)$ GeV, $|\eta| < 2.5(5)$, $Rjj < 0.7(0.4)$ and matching defined by $E_{T\rm min} = 10(20)$ GeV, $|\eta| < 2(4.5)$ and $R_{\rm min} = 0.7(0.4)$. The variations used in the assessment of the systematics cover:

  - different thresholds for the definition of jets used in the matching: $E_{T\min} = 30$ GeV for the Tevatron, and $E_{T\min} = 40$ GeV for the LHC. In the following studies of the systematics, these two settings will be referred to as HELAC parameter sets HELptX, where X labels the value of the threshold.
  - different renormalisation scale at the vertices of the clustering tree: $\mu = \mu_0/2$ and $\mu = 2\mu_0$, where μ_0 is the default $k_\perp$ value. In the following studies of the systematics, these two settings will be referred to as HELAC parameter sets HELscL and HELscH.

- MADEVENT: The parton-level matrix elements were generated with MADEVENT and the subsequent evolution used the PYTHIA shower according to the modified MLM procedure in Sec. 2.4.1. Hadronisation was performed by PYTHIA. For the *default* results at the Tevatron (LHC) the value of the merging scale has been chosen to $k_{\perp,0} = 10(20)$ GeV. The variations used in the assessment of the systematics cover:

  - different value of the merging scales $k_{\perp,0} = 20$ and 30 GeV for the Tevatron, and $k_{\perp,0} = 30$ and 40 GeV for the LHC. In the following studies of the systematics, these two settings will be referred to as MADEVENT parameter sets MEktX.
  - different values of the scales used in the evaluation of α_s in both the matrix-element generation and the parton shower: $\mu = \mu_0/2$ and $\mu = 2\mu_0$, where μ_0 is the default $k_\perp$ value. These two settings will be referred to as MADEVENT parameter sets MEscL and MEscH.

- SHERPA: The parton-level matrix elements used within SHERPA have been obtained from the internal matrix-element generator AMEGIC++ [21]. Parton showering has been conducted by APACIC++ [26, 27], whereas the combination of the matrix elements with this parton shower has been accomplished according to the CKKW procedure. The hadronisation of the shower configurations has been performed by PYTHIA, which has been made available through an internal interface. For the *default* Tevatron (LHC) predictions, the value of the merging scale has been chosen to $Q_{\rm cut} = 10(20)$ GeV. All SHERPA predictions for the Tevatron (LHC) have been obtained by setting the internally used D-parameter (cf. Eq. (2.1) in Sec. 2.2) through $D = 0.7(0.4)$. Note that, these choices directly affect the generation of the matrix elements in SHERPA. The variations used in the assessment of the systematics cover:

  - first, different choices of the merging scale $Q_{\rm cut}$. Values of 20 and 30 GeV, and 30 and 40 GeV have been used for the Tevatron and the LHC case, respectively. In the following studies of the systematics, these settings will be referred to as SHERPA parameter sets SHktX where X labels the value of the internal jet scale.

– and, second, different values of the scales used in any evaluation of the α_s *and* the parton distribution functions [5]. Two cases have been considered, $\mu = \mu_0/2$ and $\mu = 2\,\mu_0$, where μ_0 denotes the corresponding $k_\perp$ values that appear in the default Tevatron (LHC) run. The choice of the merging scale is as in the default run. In the subsequent studies of the systematics they are referred to as SHERPA parameter sets SHscL and SHscH. It should be stressed that these variations have been applied in a very comprehensive manner, i.e. in both the matrix-element and parton-showering phase of the event generation.

All SHERPA results presented in this comparison have been obtained with the publicly available version 1.0.10.

2.4.3 Tevatron studies

Event rates

The comparison of the inclusive jet rates predicted by the different approaches shall be presented here. They are collected in Tab. 2.2. For each code, in addition to the default cross sections, the results of the various individual alternative choices used to assess the systematics uncertainty are presented. Fig. 2.24 shows graphically the cross-section systematic ranges: for each multiplicity, the rates have been normalised to the average of the default values of all the codes.
It should be noted that the scale changes in all codes lead to the largest rate variations. This is reflected in the growing size of the uncertainty with larger multiplicities, a consequence of the higher powers of α_s. Furthermore is can be noted that the systematic ranges of all codes have regions of overlap.

Kinematical distributions

The discussion shall be started with showing in Fig. 2.25 the inclusive $E_\perp$ spectra of the leading four jets. The absolute rate predicted by each code is used, in units of pb/GeV. The relative differences with respect to the ALPGEN results, in this figure and all other figures of this section, are shown in the lower in-sets of each plot, where for the code X the quantity $(\sigma(X) - \sigma_0)/\sigma_0$ is plotted, σ_0 being the values of the ALPGEN curves.
There is generally good agreement between the codes, except for ARIADNE, which predicts harder $E_\perp$ spectra for the leading two jets. There also SHERPA is slightly harder than ALPGEN and HELAC, while MADEVENT is slightly softer. Fig. 2.26 shows the inclusive η spectra of the leading four jets, all normalised to unit area. There is a good agreement between the spectra of ALPGEN, HELAC and MADEVENT, while the ARIADNE and SHERPA

[5] For example, the analytical Sudakov form factors used in the matrix-element reweighting hence vary owing to their intrinsic α_s-coupling dependence.

Code	σ[tot]	$\sigma[\geq 1$ jet]	$\sigma[\geq 2$ jet]	$\sigma[\geq 3$ jet]	$\sigma[\geq 4$ jet]
ALPGEN, def	**1933**	**444**	**97.1**	**18.9**	**3.2**
ALpt20	1988	482	87.2	15.5	2.8
ALpt30	2000	491	82.9	12.8	2.1
ALscL	2035	540	135	29.7	5.5
ALscH	1860	377	72.6	12.7	2.0
ARIADNE, def	**2066**	**477**	**87.3**	**13.9**	**2.0**
ARpt20	2038	459	76.6	12.8	1.9
ARpt30	2023	446	67.9	11.3	1.7
ARscL	2087	553	116	21.2	3.6
ARscH	2051	419	67.8	9.5	1.3
ARs	2073	372	80.6	13.2	2.0
HELAC, def	**1960**	**356**	**70.8**	**13.6**	**2.4**
HELpt30	1993	373	68.0	12.5	2.4
HELscL	2028	416	95.0	20.2	3.5
HELscH	1925	324	55.1	9.4	1.4
MADEVENT, def	**2013**	**381**	**69.2**	**12.6**	**2.8**
MEkt20	2018	375	66.7	13.3	2.7
MEkt30	2017	361	64.8	11.1	2.0
MEscL	2013	444	93.6	20.0	4.8
MEscH	1944	336	53.2	8.6	1.7
SHERPA, def	**1987**	**494**	**107**	**16.6**	**2.0**
SHkt20	1968	465	85.1	12.4	1.5
SHkt30	1982	461	79.2	10.8	1.3
SHscL	1957	584	146	25.2	3.4
SHscH	2008	422	79.8	11.2	1.3

Table 2.2: Cross sections (in pb) for the inclusive jet rates at the Tevatron, according to the default and alternative settings of the various codes.

spectra appear to be broader, in particular for the sub-leading jets. This broadening is expected for ARIADNE since the gluon emissions there are essentially unordered in rapidity, which means that the Sudakov form factors applied to the matrix-element-generated states include also a $\log 1/x$ resummation absent in the other programs.

Fig. 2.27a shows the inclusive $p_\perp$ distribution of the W boson, with absolute normalisation in pb/GeV. This distribution reflects in part the behaviour observed for the spectrum of the leading jet, with ARIADNE harder than SHERPA, which, in turn, is slightly harder than ALPGEN, HELAC and MADEVENT. The region of low momenta, $p_{\perp,W} < 50$ GeV, is expanded

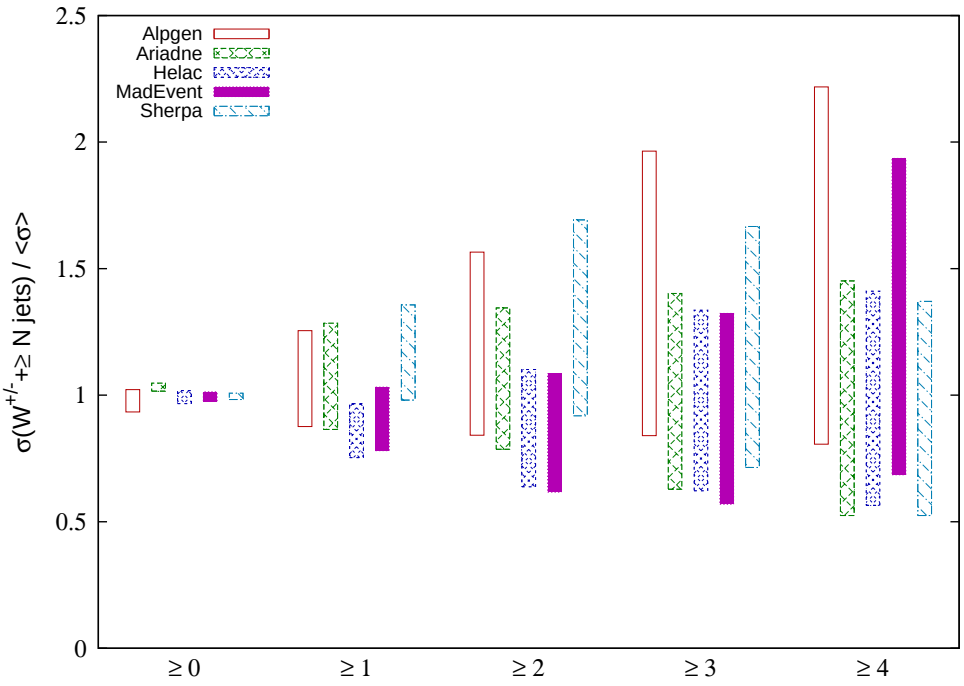

Figure 2.24: Range of variation for the Tevatron cross-section rates of the five codes, normalised to the average value of the default settings for all codes in each multiplicity bin.

in Fig. 2.27b. Fig. 2.27c shows the η distribution of the leading jet, η_1, when its transverse momentum is larger than 50 GeV. The curves are absolutely normalised, so that it is clear how much rate is predicted by each code to survive this harder jet cut. The $|\eta|$ separation between the W and the leading jet of the event above 30 GeV is shown in Fig. 2.27d, normalised to unit area. It is observed that ARIADNE has a broader correlation, while HELAC and MADEVENT are somewhat more narrow than ALPGEN and SHERPA. Finally, in Fig. 2.28, the merging scales d_i as obtained from the $k_\perp$-algorithm are presented, where d_i is the scale in an event where i jets are clustered into $i-1$ jets. These are parton-level distributions and are especially sensitive to the behaviour of the merging procedure close to the merging/matching scale. Note that in the plots showing the difference the wiggles stem from both the individual codes and from the ALPGEN reference. In Sec. 2.4.5 below, the behaviour of the individual codes will be treated separately. Also shown in Fig. 2.28 is the separation in $\Delta R = \sqrt{(\Delta\eta)^2 + (\Delta\phi)^2}$ between successive jet pairs ordered in hardness. The ΔR_{12} is dominated by the transversal-plane back-to-back peak at $\Delta R_{12} = \pi$, while for larger ΔR in all cases the behaviour is more dictated by the correlations in pseudo-rapidity. For these larger values a weaker correlation in ARIADNE and SHERPA is found, which can be expected from their broader rapidity distributions in Fig. 2.26.

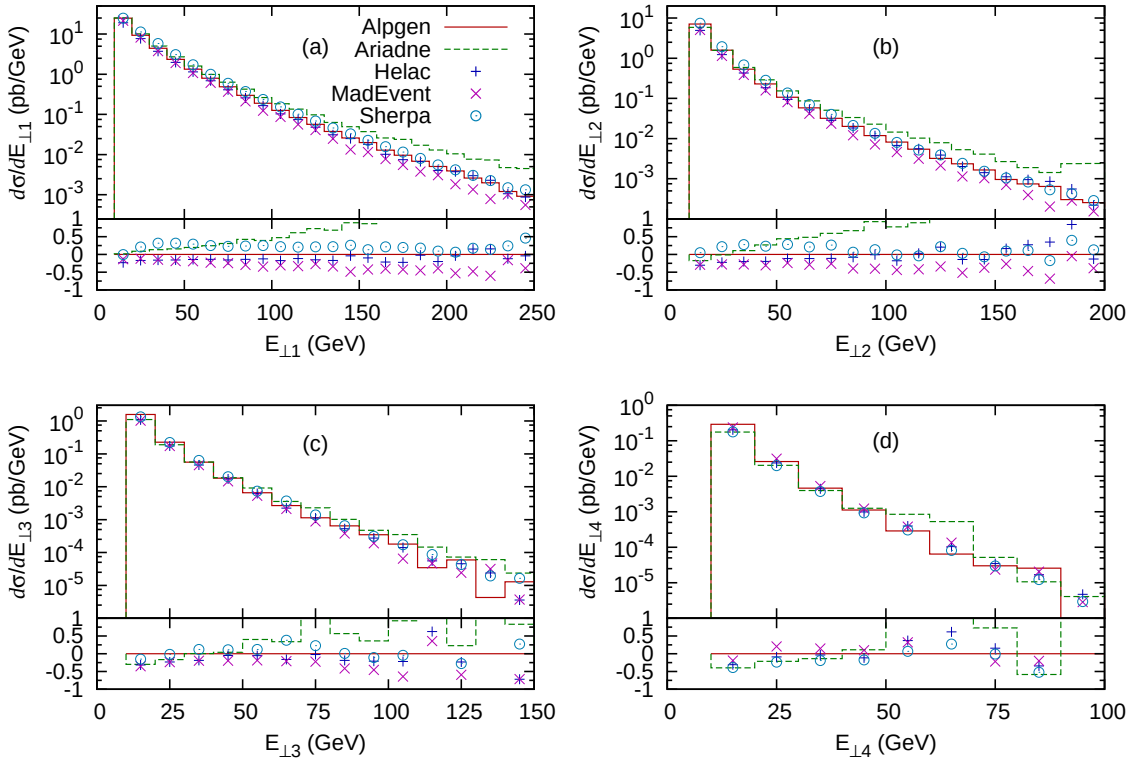

Figure 2.25: Inclusive $E_\perp$ spectra of the leading four jets at the Tevatron (pb/GeV). In all cases the full line gives the ALPGEN results, the dashed line gives the ARIADNE results and the "+", "x" and "o" points give the HELAC, MADEVENT and SHERPA results, respectively.

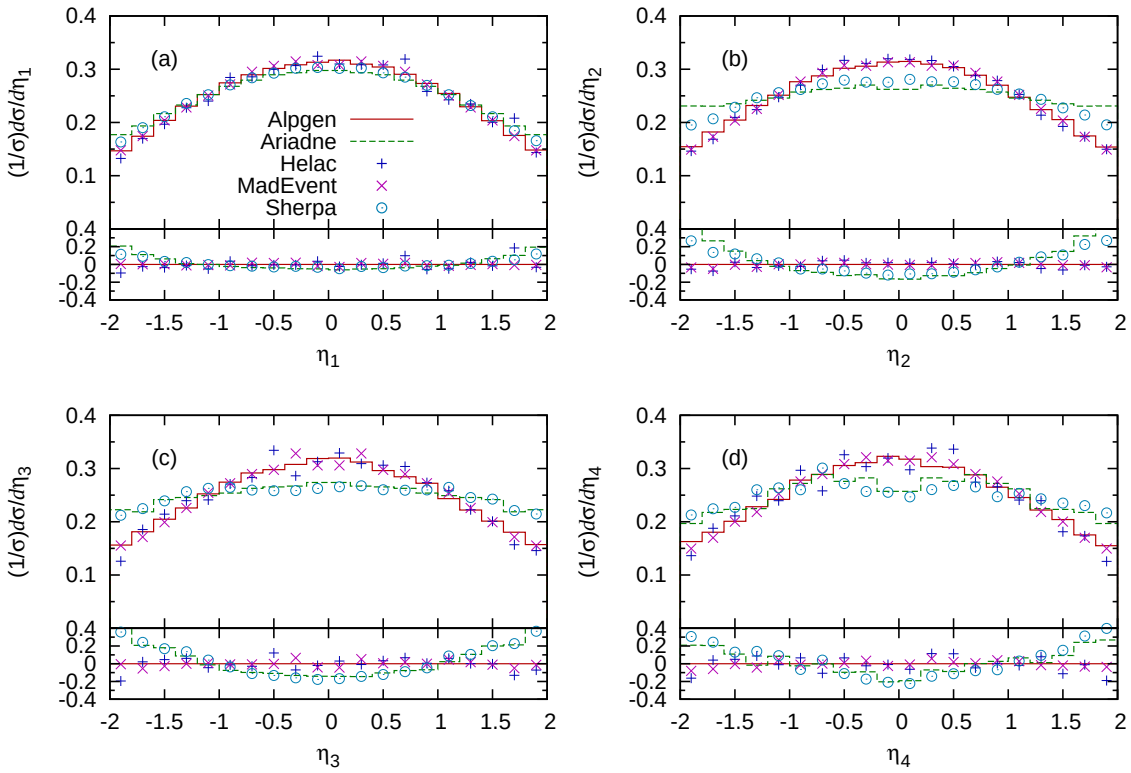

Figure 2.26: Inclusive η spectra of the four leading jets at the Tevatron. All curves are normalised to unit area. Lines and points are as in Fig. 2.25.

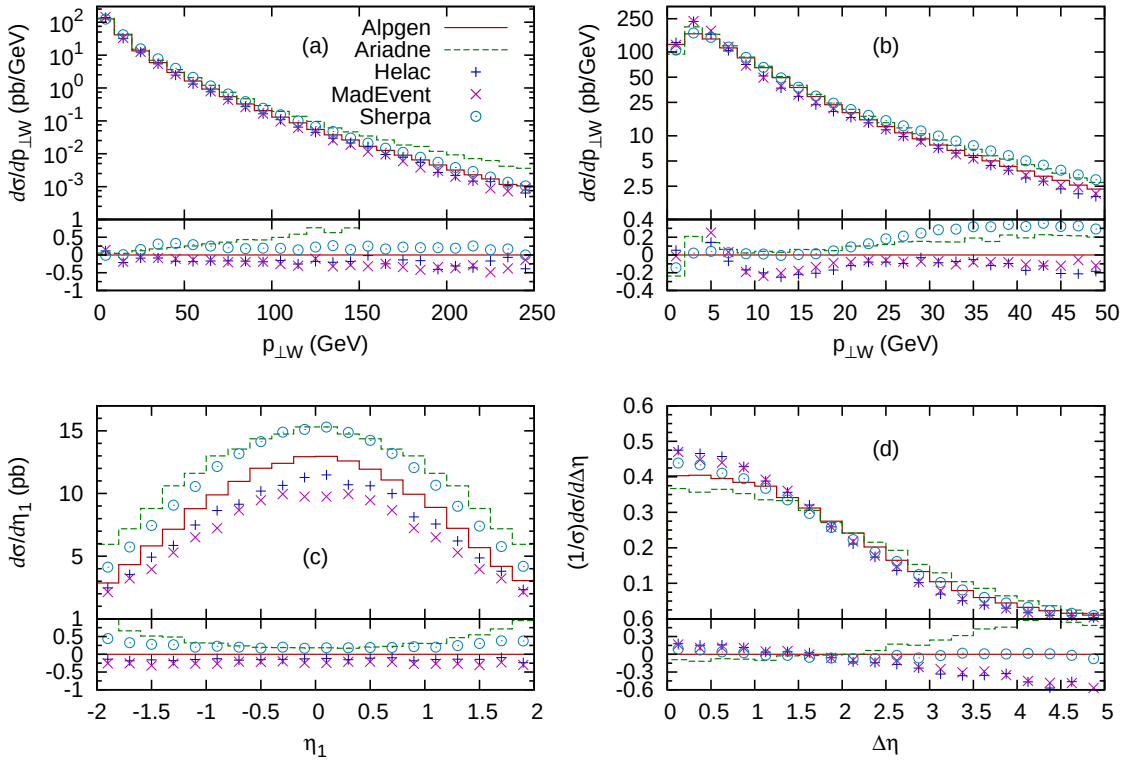

Figure 2.27: (a) and (b) $p_\perp$ spectrum of $W^\pm$ bosons at the Tevatron (pb/GeV). (c) Inclusive η spectrum of the leading jet, for $p_\perp^{\text{jet}_1} > 50$ GeV; absolute normalisation (pb). (d) Pseudo-rapidity separation between the W and the leading jet, $\Delta\eta = |\eta_W - \eta_{\text{jet}_1}|$, for $p_\perp^{\text{jet}_1} > 30$ GeV, normalised to unit area. Lines and points are as in Fig. 2.25.

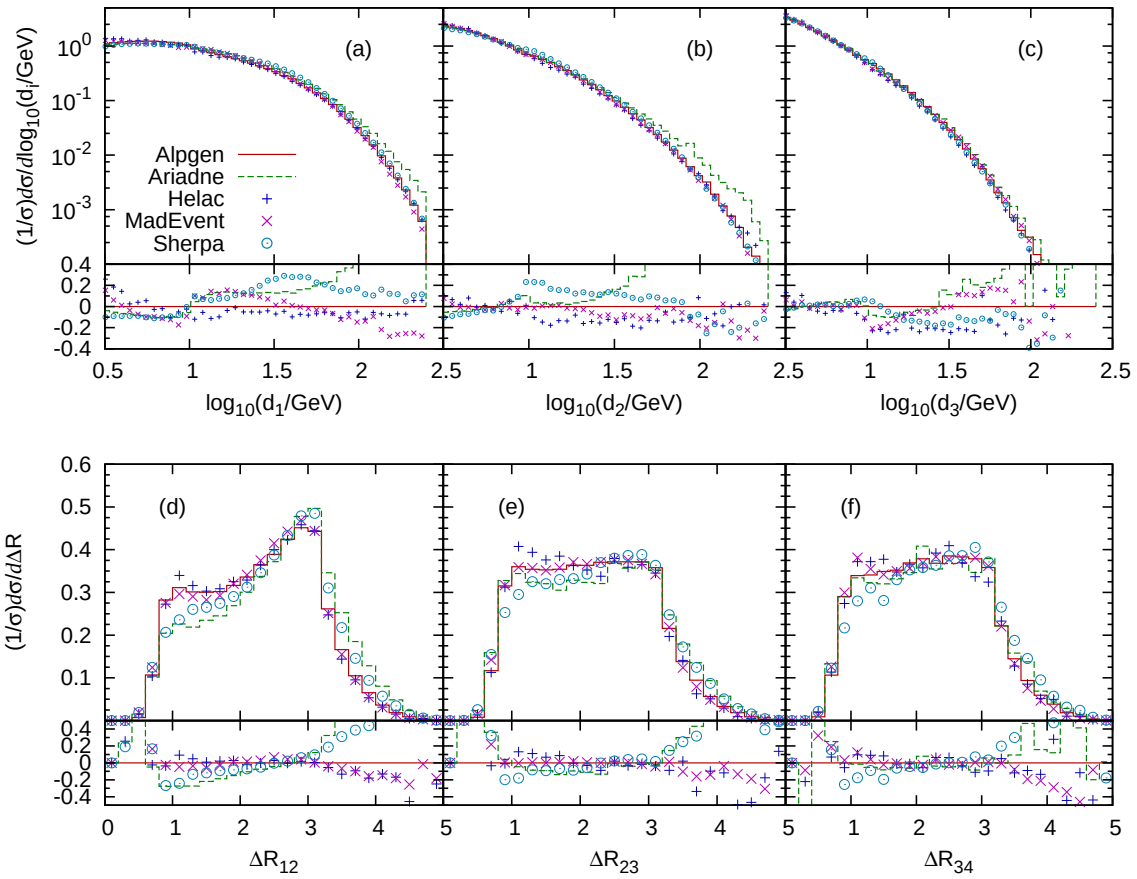

Figure 2.28: (a)–(c) d_i $(i = 1, 2, 3)$ spectra, where d_i is the scale in a parton-level event where i jets are clustered into $i - 1$ jets using the $k_\perp$-algorithm. (d)–(f) ΔR separations at the Tevatron between jet 1 and 2, 2 and 3, and 3 and 4. All curves are normalised to unit area. Lines and points are as in Fig. 2.25.

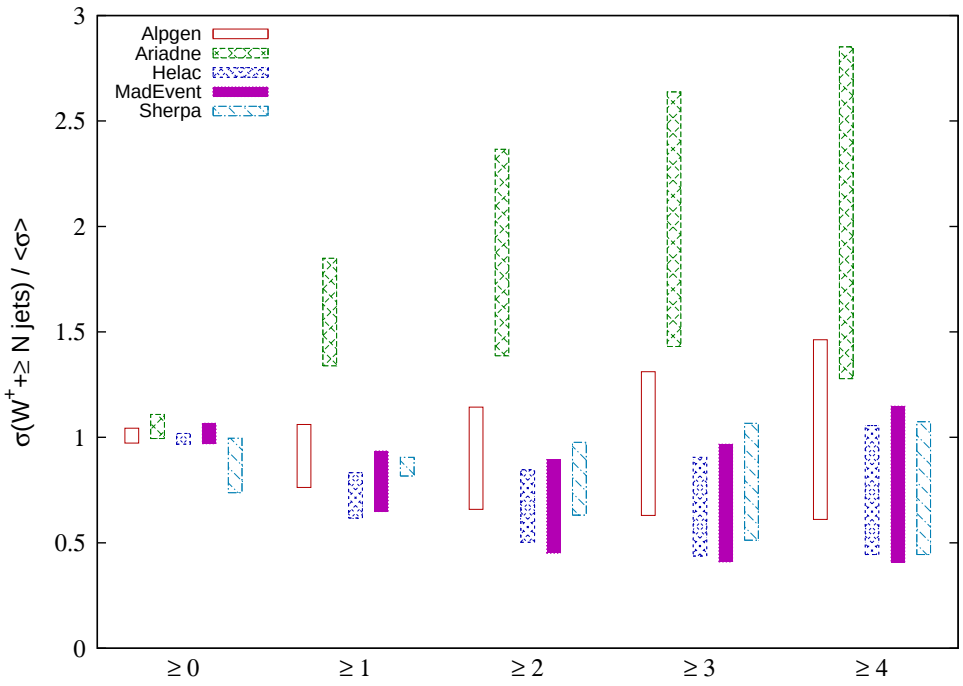

Figure 2.29: Range of variation for the LHC cross-section rates of the five codes, normalised to the average value of the default settings for all codes in each multiplicity bin.

2.4.4 LHC studies

Event rates

Table 2.3 and Fig. 2.29 of this section parallel those shown earlier for the Tevatron. The main feature of the LHC results is the significantly larger rates predicted by ARIADNE (see also the discussion of its systematics, Sec. 2.4.5), which are outside the systematics ranges of the other codes. Aside from this and the fact that SHERPA gives a smaller total cross section (see also the last part of the discussion of the SHERPA systematics in Sec. 2.4.5), the comparison among the other codes shows an excellent consistency, with a pattern of the details similar to what has been seen for the Tevatron.

Kinematical distributions

Following the same sequence of the Tevatron study, it is started by showing in Fig. 2.30 the inclusive $E_\perp$ spectra of the leading four jets. The absolute rate predicted by each code is used, in units of pb/GeV.

Except for ARIADNE, good agreement among the codes is found, with ARIADNE having significantly harder leading jets, wile for sub-leading jets the increased rates noted in Fig. 2.29 mainly come from lower $E_\perp$. Among the other codes, HELAC and SHERPA have consistently

Code	σ[tot]	$\sigma[\geq 1$ jet]	$\sigma[\geq 2$ jet]	$\sigma[\geq 3$ jet]	$\sigma[\geq 4$ jet]
ALPGEN, def	**10170**	**2100**	**590**	**171**	**50**
ALpt30	10290	2200	555	155	46
ALpt40	10280	2190	513	136	41
ALscL	10590	2520	790	252	79
ALscH	9870	1810	455	121	33
ARIADNE, def	**10890**	**3840**	**1330**	**384**	**101**
ARpt30	10340	3400	1124	327	88
ARpt40	10090	3180	958	292	83
ARscL	11250	4390	1635	507	154
ARscH	10620	3380	1071	275	69
ARs	11200	3440	1398	438	130
HELAC, def	**10050**	**1680**	**442**	**118**	**36**
HELpt40	10150	1760	412	116	37
HELscL	10340	1980	585	174	57
HELscH	9820	1470	347	84	24
MADEVENT, def	**10830**	**2120**	**519**	**137**	**42**
MEkt30	10080	1750	402	111	37
MEkt40	9840	1540	311	78.6	22
MEscL	10130	2220	618	186	62
MEscH	10300	1760	384	91.8	27
SHERPA, def	**8800**	**2130**	**574**	**151**	**41**
SHkt30	8970	2020	481	120	32
SHkt40	9200	1940	436	98.5	24
SHscL	7480	2150	675	205	58
SHscH	10110	2080	489	118	30

Table 2.3: Cross sections (in pb) for the inclusive jet rates at the LHC, according to the default and alternative settings of the various codes.

somewhat harder jets than ALPGEN, while MADEVENT is a bit softer, but these differences are not as pronounced.

For the pseudo-rapidity spectra of the jets in Fig. 2.31 it is clear that ARIADNE has a much broader distribution in all cases. Also SHERPA has broader distributions, although not as pronounced, while the other codes are very consistent. The $p_\perp$ distribution of W^+ bosons in Fig. 2.32 follows the trend of the leading-jet $E_\perp$ spectra. Increasing the transverse momentum of the leading jet in Fig. 2.32a does not change much the conclusions for its pseudo-rapidity distribution. Also the rapidity correlation between the leading jet and

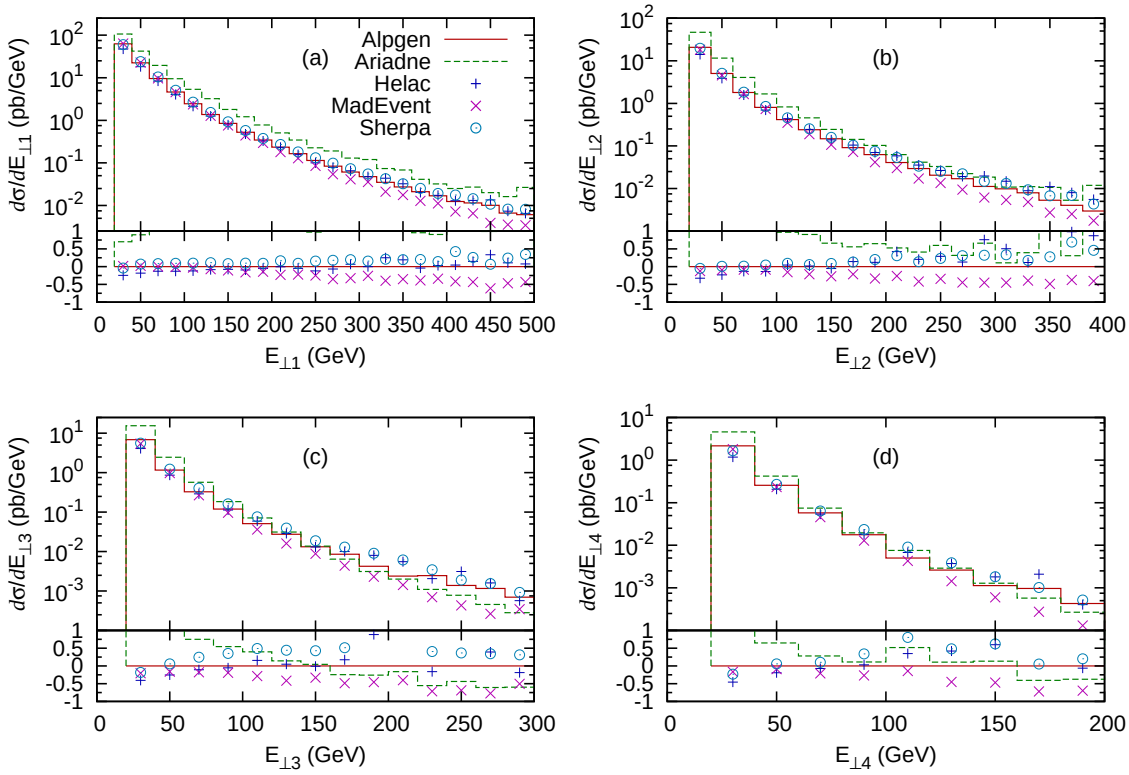

Figure 2.30: Inclusive $E_\perp$ spectra of the leading 4 jets at the LHC (pb/GeV). In all cases the full line gives the ALPGEN results, the dashed line gives the ARIADNE results and the "+", "x" and "o" points give the HELAC, MADEVENT and SHERPA results respectively.

the W^+ follows the trend found for the Tevatron, but the differences are larger, with a much weaker correlation for ARIADNE. Also SHERPA shows a somewhat weaker correlation, while HELAC is somewhat stronger than ALPGEN and MADEVENT. For the d_i distributions depicted in Fig. 2.33, it is again observed that ARIADNE yields by far the hardest predictions. The results given by the other codes are comparable, with the only exception that for the d_1 distribution, where SHERPA gives a somewhat harder prediction compared to the ones made by the MLM-based approaches. For the ΔR distributions in Fig. 2.33 a behaviour is found, which is consistent with the broader rapidity distributions predicted by SHERPA and, in particular for ARIADNE cf. Fig. 2.31. While both SHERPA and ARIADNE are above the other approaches for large values of ΔR, ARIADNE, however, much more pronounced, for lower values they stay below the others with approximately the same amount.

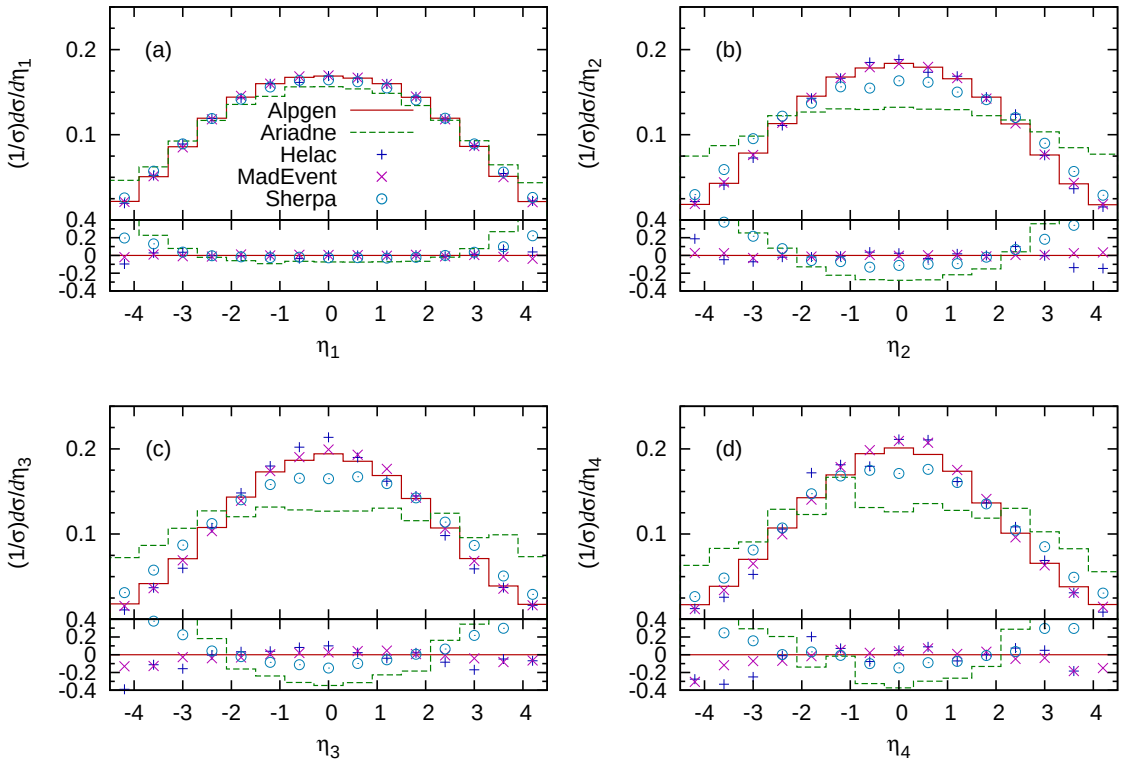

Figure 2.31: Inclusive η spectra of the four leading jets at the LHC. All curves are normalised to unit area. Lines and points are as in Fig. 2.30.

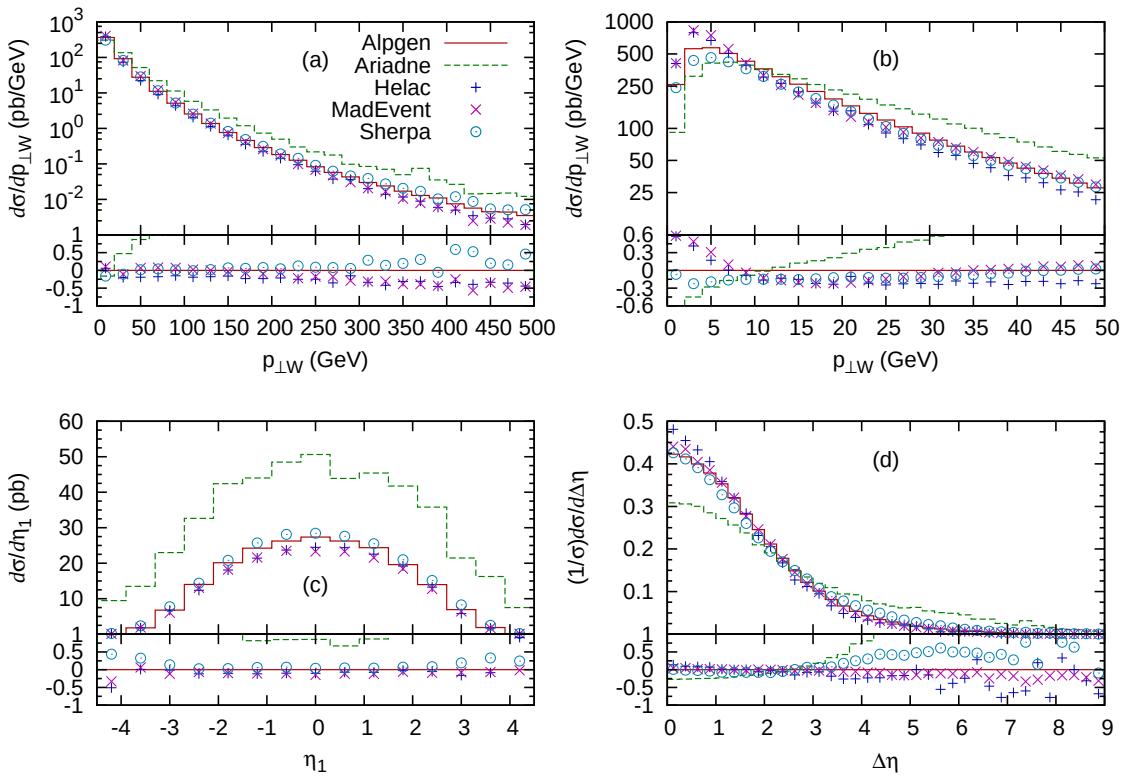

Figure 2.32: (a) and (b) $p_\perp$ spectrum of W^+ bosons at the LHC (pb/GeV). (c) η spectrum of the leading jet, for $p_\perp^{\text{jet}_1} > 100$ GeV; absolute normalisation (pb). (d) Pseudo-rapidity separation between the W^+ and the leading jet, $\Delta\eta = |\eta_{W^+} - \eta_{\text{jet}_1}|$, for $p_\perp^{\text{jet}_1} > 40$ GeV, normalised to unit area. Lines and points are as in Fig. 2.30.

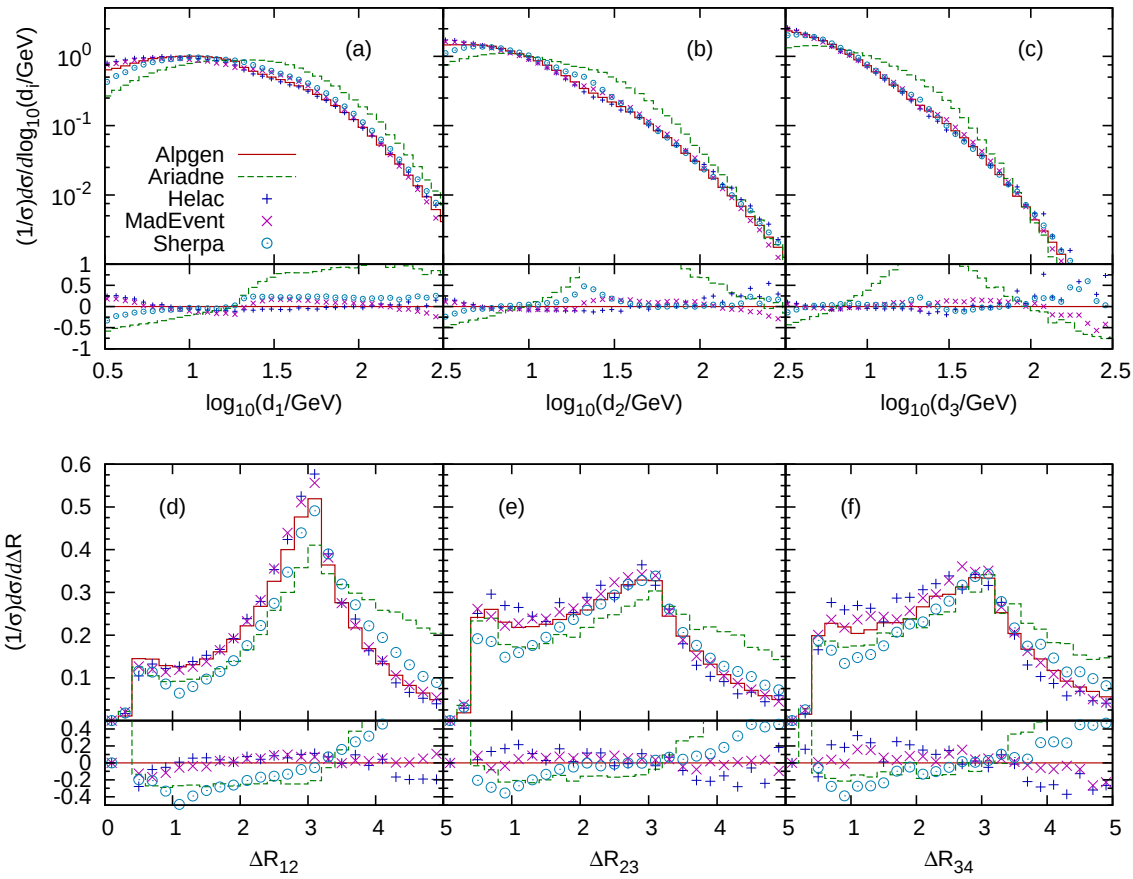

Figure 2.33: (a)–(c) d_i $(i = 1, 2, 3)$ spectra, where d_i is the scale in a parton-level event where i jets are clustered into $i - 1$ jets using the $k_\perp$-algorithm. (d)–(f) ΔR separations at the LHC between jet 1 and 2, 2 and 3, and 3 and 4. All curves are normalised to unit area. Lines and points are as in Fig. 2.30.

2.4.5 Systematic studies

In this section the separate systematic studies for the ALPGEN, ARIADNE and SHERPA approach are presented for both the Tevatron and the LHC, followed by some general comments on differences and similarities between the codes. The corresponding studies for MADEVENT and HELAC can be found in Ref. [84]. In all cases a subset of the plots shown in the previous sections has been chosen: the transverse momentum of the W, the pseudo-rapidity of the leading jet, the separation between the leading and the sub-leading jet, and the d_i logarithmic spectra. As before, all spectra aside from $p_{\perp,W}$ are normalised to unit integral over the displayed range.

ALPGEN systematics

The ALPGEN distributions for the Tevatron are shown in Fig. 2.34. The pattern of variations is consistent with the expectations. In the case of the $p_{\perp,W}$ spectra, which are plotted in absolute scales, the larger variations are due to the change of scale, with the lower scale leading to a harder spectrum. The $\pm 20\%$ effect is consistent with the scale variation of α_s, which dominates the scale variation of the rate once $p_{\perp,W}$ is larger than the Sudakov region. The change of matching scales only leads to a minor change in the region $0 < p_{\perp,W} < 40$ GeV, confirming the stability of the merging prescription. In the case of the rapidity spectrum, it is noticed that the scale change leaves the shape of the distribution unaltered, while small changes appear at the edges of the η range. The d_i distributions show agreement among the various options when $d_i < 1$. This is due to the fact that the region $d_i < 1$ is dominated by the initial-state evolution of an $n = i - 1$ parton event, and both the matching and scale sensitivities are reduced. The matching variation affects the region $1 < d_i < \log E_T^{min}$, but is reduced above that. This is because, when the jet transverse energies are above a given matching scale, the sensitivity to lower matching scales is suppressed (the event will "match" in all cases).

For the LHC, the ALPGEN systematics is shown in Fig. 2.35. The comparison of the various parameter choices is similar to what was encountered at the Tevatron, with variations in the range of $\pm 20\%$ for the matching-scale systematics, and up to 40% for the scale systematics. The pattern of the glitches in the d_i spectra for the different matching thresholds is also consistent with the explanation provided in the case of the Tevatron.

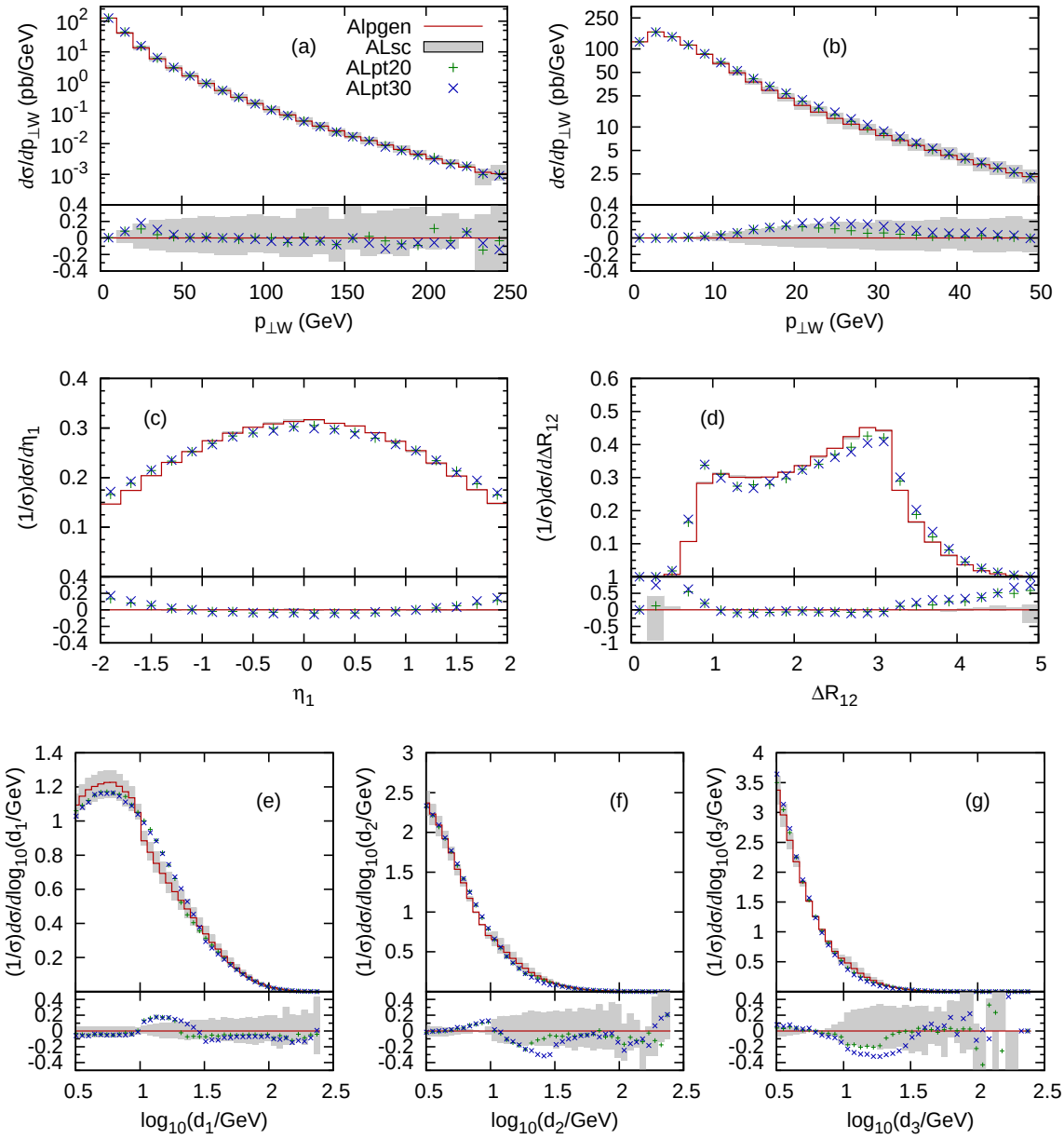

Figure 2.34: ALPGEN systematics at the Tevatron. (a) and (b) $p_\perp$ spectrum of the W. (c) Pseudo-rapidity distribution of the leading jet. (d) ΔR separation between the two leading jets. (e)–(g) Distribution in clustering scales as described in Fig. 2.28. The full line is the default settings of ALPGEN, the shaded area is the range between ALscL and ALscH, while the points represent ALpt20 and ALpt30 as defined in Sec. 2.4.2.

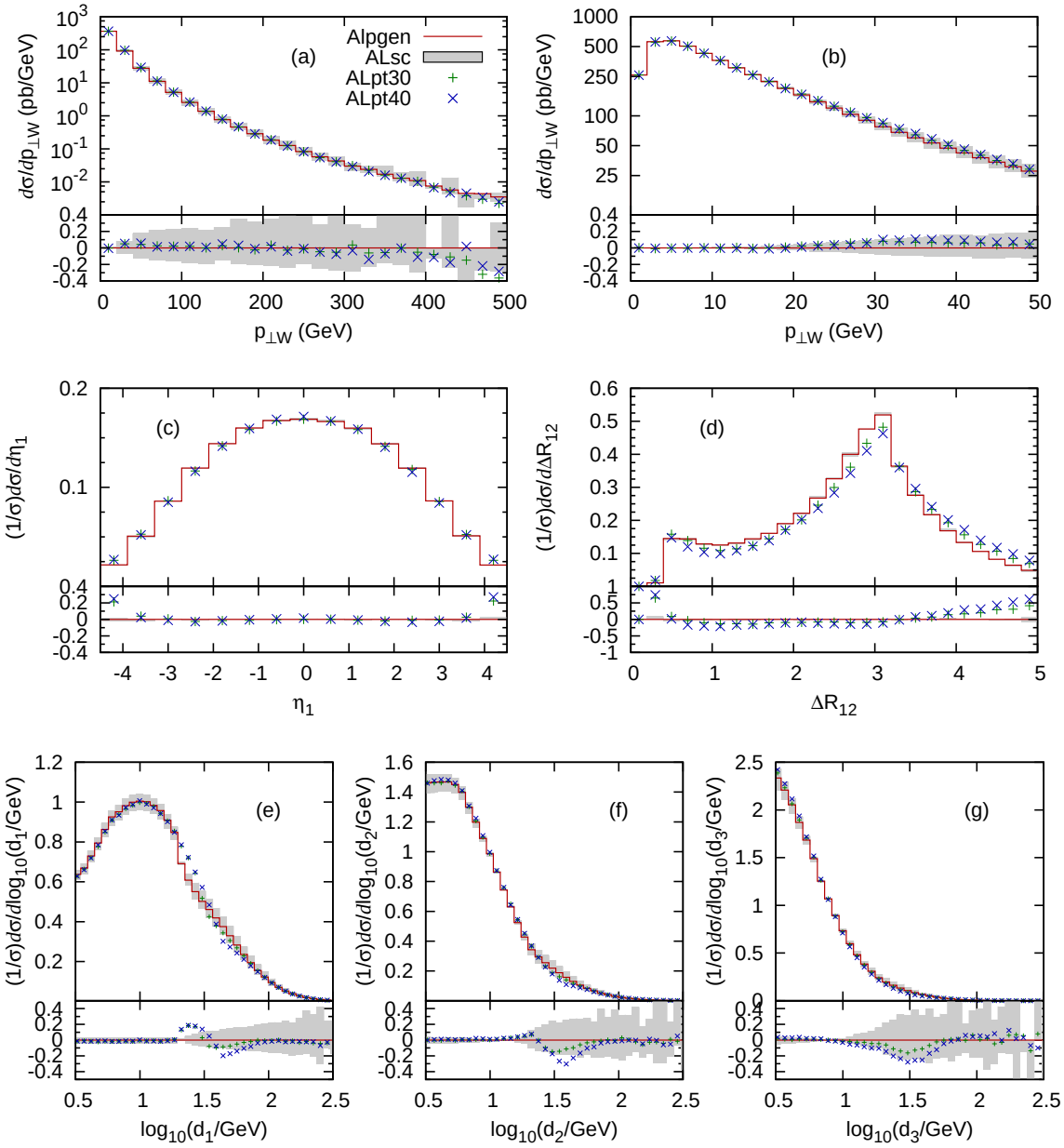

Figure 2.35: ALPGEN systematics at the LHC. (a) and (b) show the $p_\perp$ spectrum of the W, (c) shows the pseudo-rapidity distribution of the leading jet, (d) shows the ΔR separation between the two leading jets, and (e)–(g) show the distribution in clustering scales as described in Fig. 2.33. The full line is the default settings of ALPGEN, the shaded area is the range between ALscL and ALscH, while the points represent ALpt30 and ALpt40 as defined in Sec. 2.4.2.

ARIADNE systematics

The ARIADNE systematics for the Tevatron is shown in Fig. 2.36. Since the dipole cascade by itself already includes a matrix-element correction for the first emission, no dependence on the merging scale is seen in the $p_{\perp,W}$, η_{jet_1} and d_1 distributions, which are mainly sensitive to leading-order corrections. The other distributions are sensitive to higher-order corrections, and here the pure dipole cascade underestimates the matrix element and also tends to make the leading jets less back-to-back in azimuth. The first effect is expected for all parton showers, but is somewhat enhanced in ARIADNE due to the missing initial-state $q \to gq$ splitting, and is mostly visible in the d_2 distribution just below the merging scale. The second effect is clearly visible in the ΔR_{12} distribution, which is dominated by low $E_\perp$ jets. The changing of the soft suppression parameter in ARs has the effect of reducing the available phase space of gluon radiation, especially for large $E_\perp$ and in the beam directions, an effect, which is mostly visible for the hardest emission and in the $p_{\perp,W}$ distribution. As for ALPGEN, and also for the other codes, the change in scale mainly affects the hardness of the jets, but not the η_{jet_1} and the ΔR_{12} distribution.
For the LHC, the ARIADNE systematics is shown in Fig. 2.37. Qualitatively the same effects as in the Tevatron case are found. In particular the strong dependence on the soft suppression parameters in ARs is to be noted, and it is clear that these have to be adjusted to fit Tevatron (and HERA) data before any predictions for the LHC can be made. It should be noted, however, that while eg. the high $p_{\perp,W}$ tail in Fig. 2.37a for ARs is shifted down to be comparable to the other codes (cf. Fig. 2.32a), the medium $p_{\perp,W}$ values are less affected and here the differences compared to the other codes can be expected to remain after a retuning. This difference is mainly due to the fact that the dipole cascade in ARIADNE, contrary to the other parton showers, is not based on standard DGLAP evolution, but also allows for evolution, which is unordered in transverse momentum à la BFKL. This means that in ARIADNE there is also a resummation of logs of $1/x$ besides the standard $\log Q^2$ resummation. This should not be a large effect at the Tevatron, and the differences there can be tuned away by changing the soft suppression parameters in ARIADNE. However, at the LHC quite small x-values contribute, $x \sim m_W/\sqrt{S} < 0.01$, which allow for a much increased phase space for jets as compared to what is allowed by standard DGLAP evolution. As a result one obtains larger inclusive jet rates as documented in Tab. 2.3. The same effect is found in DIS at HERA, where x is even smaller as are the typical scales, Q^2. And here, all DGLAP-based parton showers fail to reproduce final-state properties, especially forward jet rates, while ARIADNE does a fairly good job.
It would be interesting to compare the merging schemes presented here also to HERA data to see if the DGLAP based shower would better reproduce data when merged with higher-order matrix elements. This would also put the extrapolations to the LHC on safer grounds. However, so far there exists one preliminary such study for the ARIADNE case only [95].

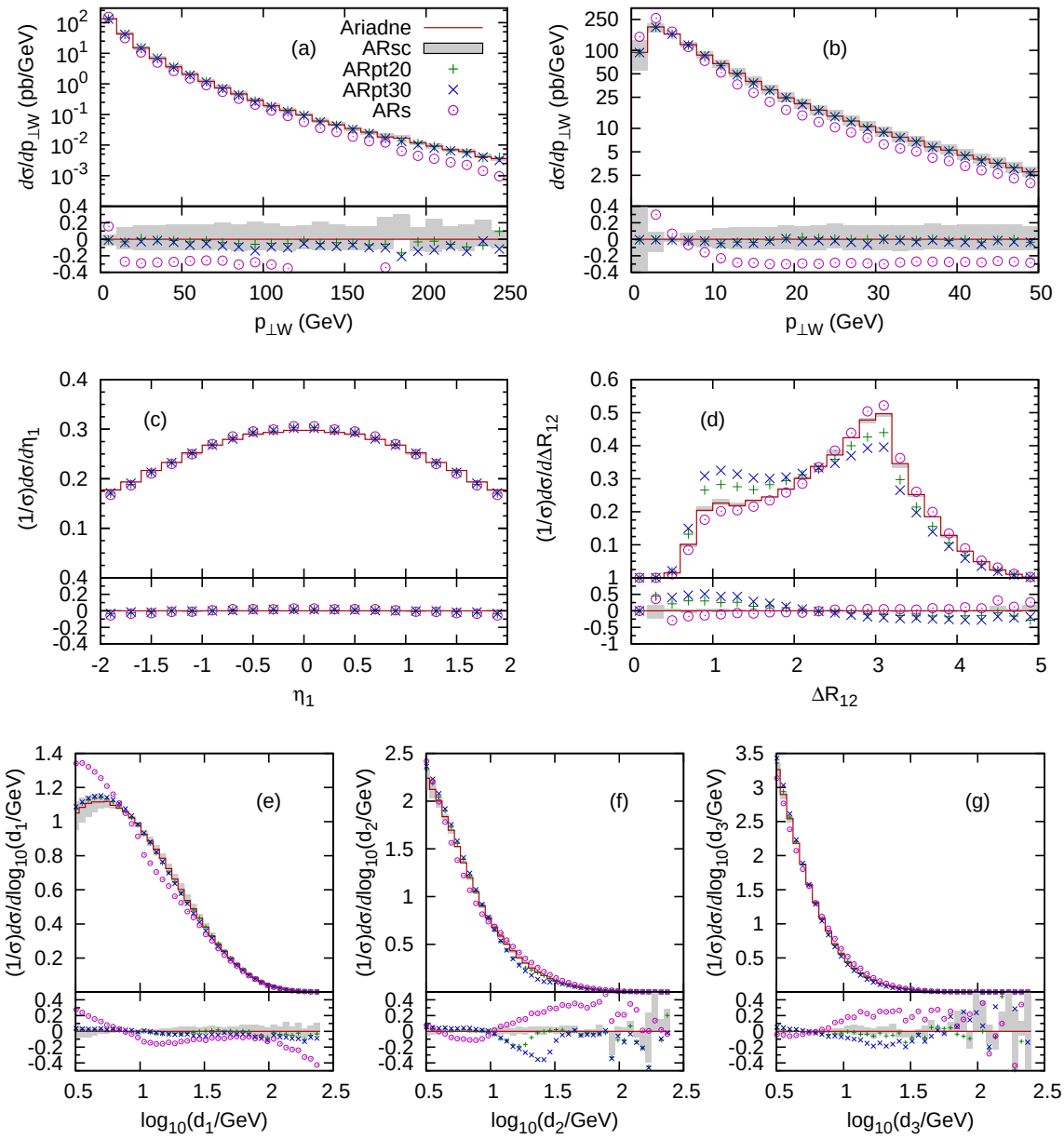

Figure 2.36: ARIADNE systematics at the Tevatron. The plots are the same as in Fig. 2.34. The full line is the default settings of ARIADNE, the shaded area is the range between ARscL and ARscH, while the points represent ARpt20, ARpt30 and ARs as defined in Sec. 2.4.2.

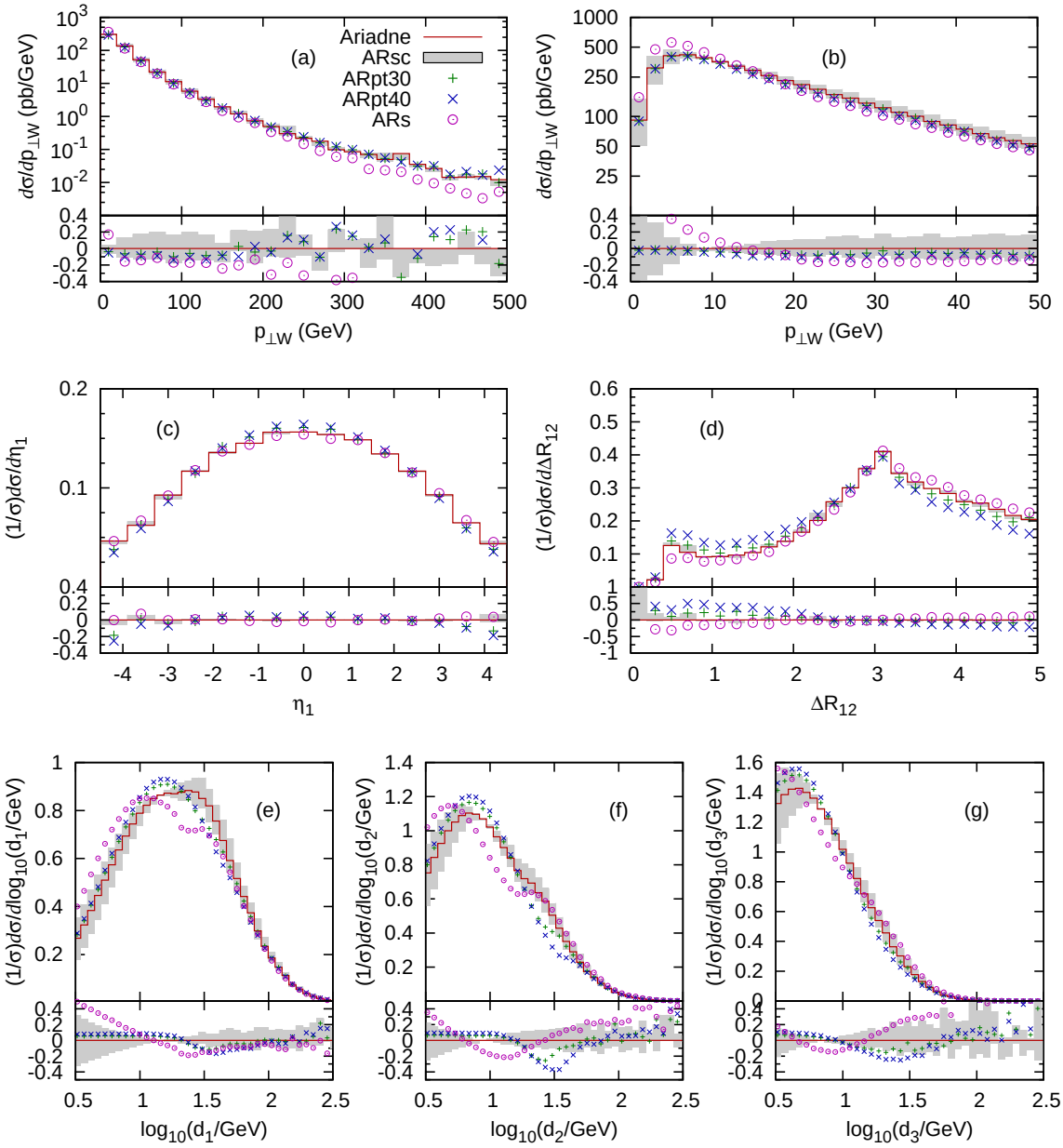

Figure 2.37: ARIADNE systematics at the LHC. The plots are the same as in Fig. 2.35. The full line is the default settings of ARIADNE, the shaded area is the range between ARscL and ARscH, while the points represent ARpt30, ARpt40 and ARs as defined in Sec. 2.4.2.

SHERPA systematics

The systematics of the CKKW algorithm as implemented in SHERPA is presented in Fig. 2.38 for the Tevatron case. The effect of varying the scales in the PDF *and* strong coupling evaluations by a factor of 0.5 (2.0) is that for the lower (higher) scale choice, the W-boson's $p_\perp$ spectrum becomes harder (softer). For this kind of observables the uncertainties given by scale variations dominate the ones emerging through variations of the internal separation cut. This is mainly due to a reduced (enhanced) suppression of hard-jet radiation through the α_s rejection weights. The differential jet rates, $d_{1,2,3}$, shown in Fig. 2.38e–g, have a more pronounced sensitivity on the choice of the merging scale, leading to variations at the 20% level. In the CKKW approach this dependence can be understood since the $k_\perp$-measure intrinsically serves as the discriminator to separate the matrix-element and parton-shower regimes. Hence, the largest deviations from the default typically appear at $d_i \approx Q_{\text{cut}}$. However, the results are remarkably smooth, which leads to the conclusion that the cancellation of the dominant logarithmic dependence on the merging cut is well achieved. Moreover, considering the pseudo-rapidity of the leading jet and the cone separation of the two hardest jets, these distributions show a very stable behaviour under the studied variations, since they are indirectly influenced by the cut scale only. The somewhat more pronounced deviation at low ΔR_{12} is connected to phase-space regions of jets becoming close together, which is affected by the choice of the merging scale and therefore by its variation. Taken together, SHERPA produces consistent results with relative differences of the order of or less than 20% at Tevatron energies.

The SHERPA studies of systematics for the LHC are displayed in Fig. 2.39. Compared to the Tevatron case, a similar pattern of variations is recognised. The $p_\perp$ spectra of the W^+ boson show deviations under cut and scale variations that remain on the same order of magnitude. However, a noticeable difference is an enhancement of uncertainties in the predictions for low $p_\perp$. This phase-space region is clearly dominated by the parton-shower evolution, which in the SHERPA treatment of estimating uncertainties undergoes scale variations in the same manner as the matrix-element part. Therefore, the estimated deviations from the default given for low $p_\perp$ are very reasonable and reflect intrinsic uncertainties underlying the parton showering. For the LHC case, the effect is larger, since the evolution is dictated by steeply rising parton densities at x-values that are lower compared to the Tevatron scenario. The pseudo-rapidity of the leading jet and the cone separation of the two hardest jets show again a stable behaviour under the applied variations, the only slight exception is the region of high $|\eta_{\text{jet}_1}|$ where, using a high $k_\perp$-cut, the deviations are at the 20% level. The effect of varying the scales in the parton distributions and strong couplings now dominates the uncertainties in the differential jet rates, $d_{1,2,3}$, which are presented in Fig. 2.39e–g. This time, owing to the larger phase space, for the low scale choice, $\mu = \mu_0/2$, the spectra become up to 40% harder, whereas, for the high scale choice, the spectra are up to 20% softer. The

variation of the internal merging scale does not induce jumps around the cut region, however it has to be noted that for higher choices, e.g. $Q_{\text{cut}} = 40$ GeV, there is a tendency to predict softer distributions in the tails compared to the default. To summarise, the extrapolation from Tevatron to LHC energies does not yield significant changes in the predictions of uncertainties under merging-cut and scale variations; for the LHC scenario, they have to be estimated slightly larger, ranging up to 40%. The results are again consistent and exhibit a well controlled behaviour when applying the CKKW approach implemented in SHERPA at LHC energies.

Giving a conservative, more reliable estimate, in SHERPA the strategy of varying the scales in the strong coupling *together with* the scales in the parton densities has been chosen to assess its systematics. So, to better estimate the impact of the additional scale variation in the parton density functions, renormalisation-scale variations on its own have been studied as well. Their results show smaller deviations wrt. the default in the observables of this study with the interpretation of potentially underestimating the systematics of the merging approach. Also, then the total cross sections vary less and become 9095 pb and 8597 pb for the low- and high-scale choice, respectively. Note that, owing to the missing simultaneous factorisation-scale variation, their order is now reversed compared to SHscL and SHscH, whose values are given in Tab. 2.3. This once more emphasises that the approach's uncertainty may be underestimated when relying on α_{s}-scale variations only. From Tab. 2.3 it also can be noted that the total inclusive cross section given by the full high-scale prediction SHscH is – unlike SHERPA's default – close to the ALPGEN default. In contrast to the MLM-based approaches, which prefer the factorisation scale in the matrix-element evaluation set through the transverse mass of the weak boson, the SHERPA approach makes the choice of employing the merging scale Q_{cut} instead. This has been motivated in [29] and further discussed in [30]. Eventually, it is a good result that compatibility is achieved under this additional PDF-scale variation for the total inclusive cross sections, however it also clearly stresses that there is a non-negligible residual dependence on the choice of the factorisation scale in the merging approaches.

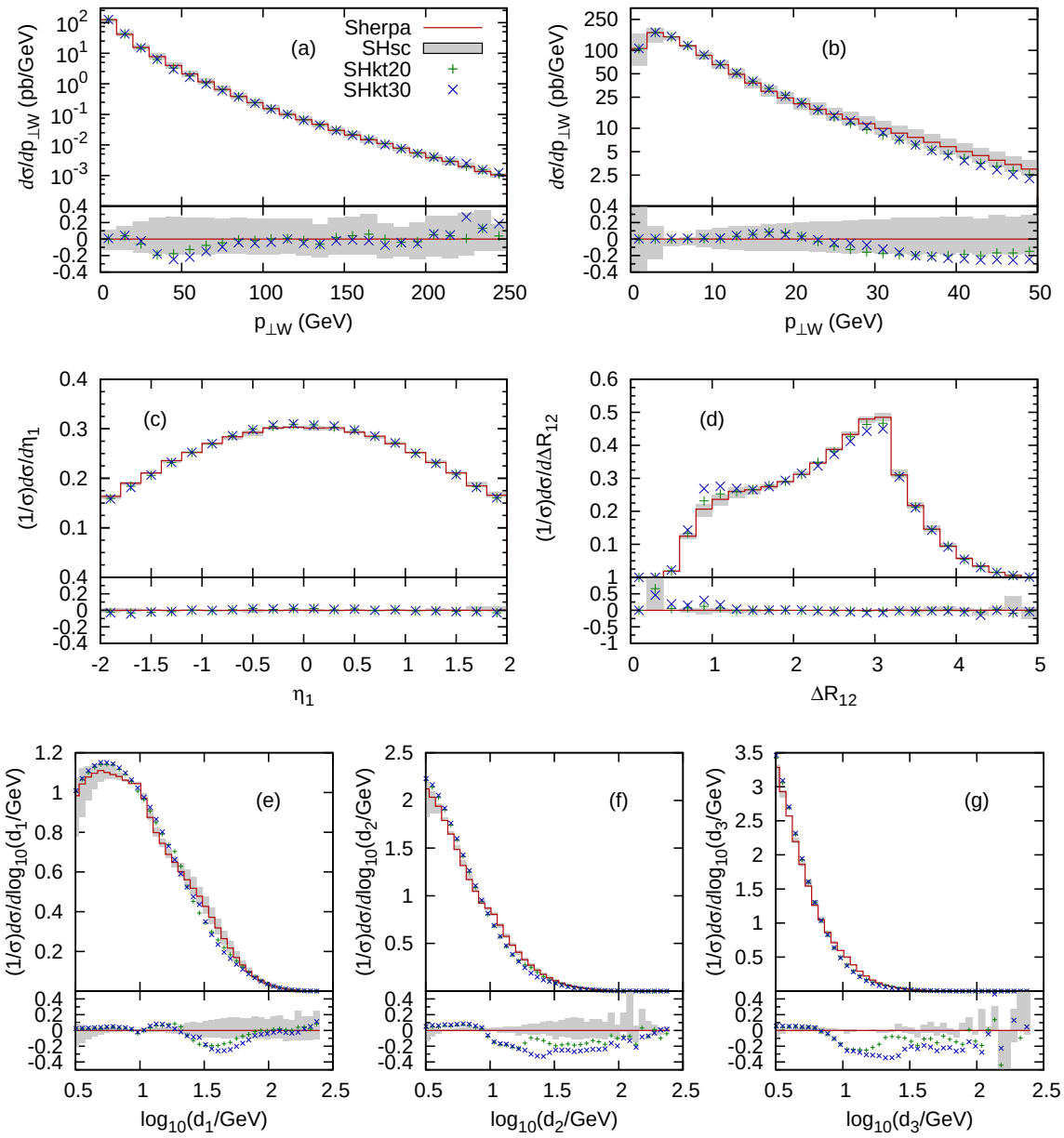

Figure 2.38: SHERPA systematics at the Tevatron. The plots are the same as in Fig. 2.34. The full line is the default settings of SHERPA, the shaded area is the range between SHscL and SHscH, while the points represent SHkt20 and SHkt30 as defined in Sec. 2.4.2.

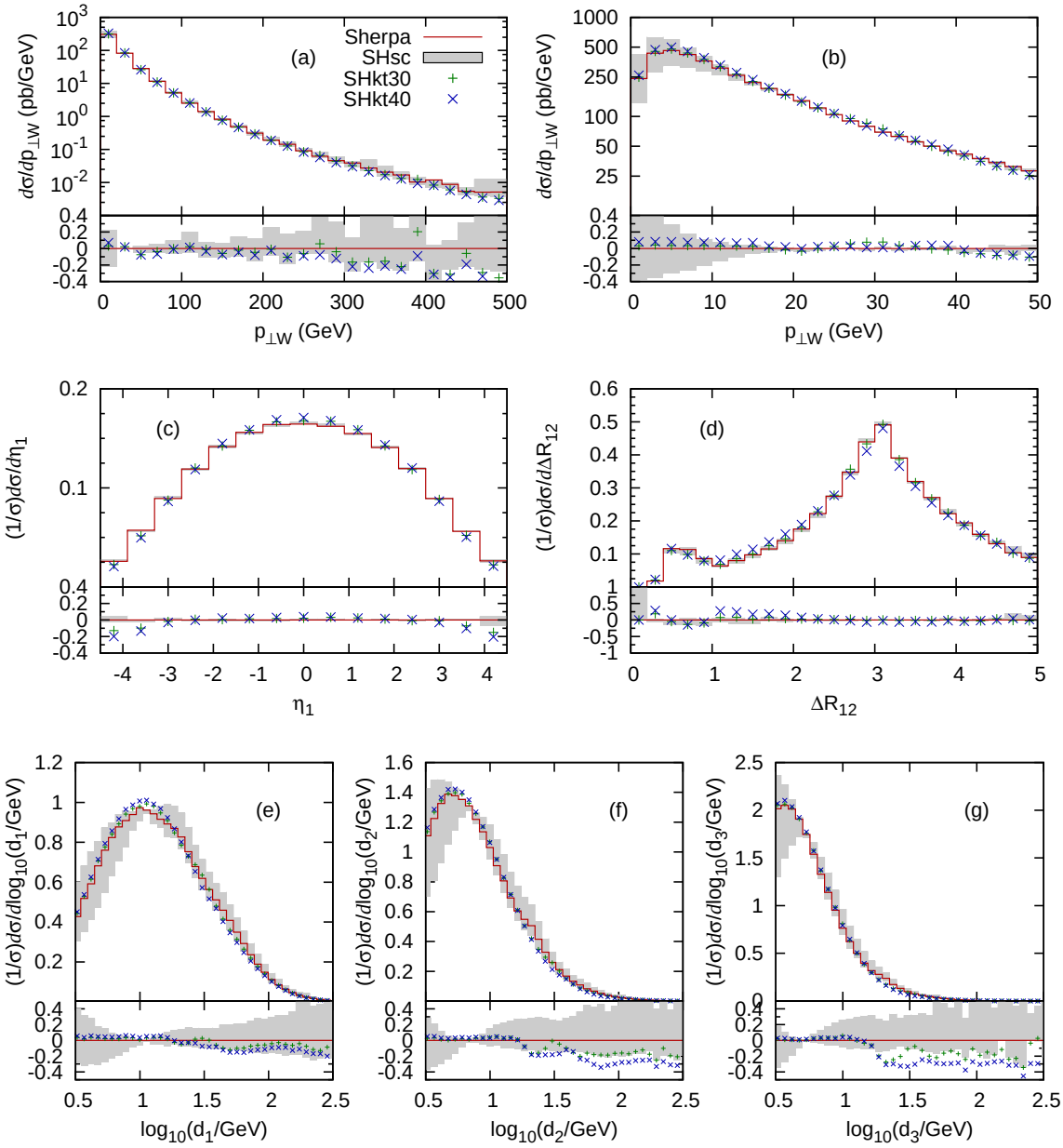

Figure 2.39: SHERPA systematics at the LHC. The plots are the same as in Fig. 2.35. The full line is the default settings of SHERPA, the shaded area is the range between SHscL and SHscH, while the points represent SHkt30 and SHkt40 as defined in Sec. 2.4.2.

Summary of the systematics studies

Starting with the $p_{\perp,W}$ spectra, a trivial $20-40\%$ effect of the scale changes is found, with the lower scale leading to a harder spectrum. In the case of ALPGEN, this only affects the spectrum above the matching scale, while for ARIADNE and SHERPA there is also an effect below, as there the scale change is also implemented in the parton shower. For all the codes the change in merging scale gives effects smaller than or of the order of the change in α_s scale. For ARIADNE, the change in the soft suppression parameter gives a softer spectrum, which is expected as it directly reduces the phase space for emitted gluons.
In the η_{jet_1} and ΔR_{12} distributions the effects of changing the scale in α_s are negligible. In all cases, changing the merging/matching scale also has negligible effects on the rapidity spectrum, while the ΔR_{12} tends to become more peaked at small values for larger merging/matching scales, and also slightly less peaked at $\Delta R_{12} = \pi$. This effect is largest for ARIADNE.
Finally for the d_i distributions changes of the merging scales introduce wiggles of varying size for all the approaches.

2.5 Summary and conclusions

A proper theoretical modelling of multi-jet final states will be of outstanding importance at the LHC as many interesting production channels will manifest themselves through the occurrence of a certain number of high-p_T QCD jets. The description of these rather rare events clearly is beyond the scope of conventional parton-shower simulations. To correctly account for hard QCD emissions higher-order corrections need to be incorporated into the shower algorithms. The general framework of how to combine exact tree-level matrix elements with shower Monte Carlo generators has been presented. Special attention has thereby been given to the CKKW scheme as it is implemented in the SHERPA program. The underlying algorithm has been presented in some detail and careful tests of its implementation have been carried out. The focus here was on single gauge boson production, as it constitutes an important background to many other interesting channels, *e.g.* top-quark or Higgs boson production, or final states originating from the decays of supersymmetric particles.
Where it must be expected, it was verified that the generator predictions only moderately depend on the choices of the parameters introduced by the merging prescription, namely the merging scale Q_{cut} and the number of matrix element jets taken into account.
The Monte Carlo predictions of the PYTHIA and SHERPA generators have been compared with DØ data for the channel $p\bar{p} \to e^+e^-$+jets. The consequences of the two different approaches for filling the phase space of additional QCD radiation have been studied. It can be concluded that the inclusion of higher-order tree-level matrix elements clearly improves

the agreement of the simulation with experimental measurements. A better description of both rates and shapes of multi-jet observables is achieved with the SHERPA approach.
In the last part of this chapter a comparative study of all the currently available approaches to the problem of merging matrix elements with parton showers has been presented. The benchmark process chosen was W+jets production at Tevatron and LHC energies. Special emphasis was given to the assessment of the systematic uncertainties of the various approaches. It was found that all the programs reasonably agree when taking into account systematic uncertainties. And as the systematics at the Tevatron is similar to that at the LHC, it is conceivable that all the codes can be tuned to Tevatron data to give consistent predictions for the LHC.
In summary, it can be concluded that the inclusion of tree-level matrix elements into the simulation of QCD jet production provides a very powerful tool for the description of multi-jet final states. It can be anticipated that these methods will become a standard for the modelling of signal and background processes at future colliders.

3 A parton-shower algorithm based on Catani–Seymour dipole factorisation

3.1 Introduction

The enormous importance of parton-shower models for a realistic simulation of scattering events at collider experiments has already been emphasised in the introduction of Chapter 2. Parton showers relate the partons produced in an hard interaction to partons at the hadronisation scale and thereby allow for the incorporation of universal hadronisation models. This is achieved by accounting for the multiple production of additional QCD partons in the dominant soft and collinear regions of phase space.

Triggered by the research on including higher-order corrections into parton-shower Monte Carlos, it became apparent that in order to systematically improve the event generators, also the parton-shower algorithms themselves must be ameliorated. Some developments in this direction include an improved treatment of angular ordering and massive partons in HERWIG++ [8] or the introduction of a new $k_\perp$-ordered shower in PYTHIA [11]. More recently, and motivated by the wish to include loop-level calculations in a more straightforward and systematic manner, the application of subtraction terms, prevalent in QCD next-to-leading-order calculations, has been proposed. This chapter is devoted to the presentation of a new parton-shower model based on such subtraction terms, that has only recently been presented in [96]. It uses the Catani–Seymour dipole formalism [97, 98] and the corresponding subtractions as a starting point [1]. This formulation of a parton shower has been proposed for the first time in [100, 101]. A similar ansatz relies on antenna subtraction terms [102, 103] and has been presented recently in [104].

The chapter is organised as follows: After briefly introducing the idea of parton shower algorithms based on subtraction terms in Sec. 3.1.1 and a short review of the subtraction formalism of Catani–Seymour in Sec. 3.1.2, Sec. 3.2 states the basic construction principles of the proposed shower description. In Sec. 3.3 the actual parton shower built on Catani–Seymour subtraction terms is constructed. The most general massive and the massless case

[1] This approach has also been employed by a second group, [99].

for all the possible QCD splitting types are discussed in detail, and the modifications needed to include splittings of supersymmetric particles are discussed. The analytic expressions for the first shower emission from various core processes are compared with the corresponding exact tree-level matrix-element calculations in Sec. 3.4. In Sec. 3.5 predictions obtained with the developed shower formalism are confronted with experimental data and other calculations. The focus hereby is on hadron production in e^+e^- collisions, and Drell-Yan and QCD jet production at the Fermilab Tevatron. Sec. 3.6 is devoted to the summary and conclusions.

3.1.1 Parton showers based on subtraction methods

Since its formulation almost a decade ago, the Catani–Seymour dipole formalism [97, 98] has been widely used in the calculation of next-to-leading-order (NLO) corrections in QCD, see for instance [105]-[111].

Such calculations typically face the problem of infrared divergences in both the real and the virtual parts of the NLO correction. In principle, such divergences are not really a problem, since for physically meaningful observables, the Kinoshita-Lee-Nauenberg theorem [112, 113] guarantees their mutual cancellation. To technically perform this cancellation, however, the divergences need to be regularised, which is usually performed by dimensional regularisation, *i.e.* continuing the calculation to d dimensions. There, the infrared divergences manifest themselves as poles in $1/(4-d)$ or $1/(4-d)^2$. To deal with the poles and achieve the cancellation, subtraction methods may be used. In general, they rely on the fact that the infrared divergences in the real correction part follow an universal pattern. This allows to construct simplified terms in a process-independent way that encapsulate all infrared divergences occurring in the full matrix element. Then, subtracting these terms from the real-correction matrix elements will yield an infrared-finite result, such that this subtracted matrix element can be safely integrated numerically in four dimensions. In addition, the subtraction terms are chosen such that they can be analytically integrated in d dimensions over the phase space of the additional soft or collinear particle causing the divergences. This yields the poles in $1/(4-d)$ or $1/(4-d)^2$, which are then added to the virtual part of the correction, and thus cancel the poles there.

The catch with the subtraction methods is that the subtraction terms can be constructed locally from the (colour-ordered) Born matrix element. In the Catani–Seymour method, for instance, pairs of particles are interpreted as emitting particle and spectator and are subjected to a splitting kernel creating a third particle. In this splitting process, one of the particles actually splits, while the recoil is compensated for by the spectator, which may be interpreted as its colour partner. At the same time, the phase space factorises exactly into a phase space over the original particles, already present at the Born level, and into a phase space of the additional particle emerging in the splitting. This exact factorisation

corresponds to an exact mapping of the two original momenta (emitter and spectator) onto three four-momenta. At each point of the procedure all particles remain on their respective mass shell.

This is why constructing parton showers based on such methods currently is being pursued by different groups. It is clear that these showers, in full conformance with original formulations employing the splitting of individual, single partons, are based on the universal soft and collinear dominance of QCD radiation. Similar to the original shower algorithms, the emerging large logarithms occurring with each individual parton emission can be resummed in a straightforward way through a Markovian process. This, in principle, renders both formulations formally equivalent. On the other hand, however, showers based on subtraction terms have the practical advantage that the conservation of four-momentum is built in with particles that remain on their mass shell at any given point [2]. It can be anticipated that these features ultimately will allow for a more transparent merging with multi-leg matrix elements and a drastically alleviated matching with full NLO calculations.

3.1.2 Short review of the Catani–Seymour subtraction method

The Catani–Seymour subtraction method has been introduced in [97] for massless partons and it has been extended to massive partons in [98]. To fix the notation for the rest of the chapter, it will be briefly reviewed here.

The essence of this method is embedded in the dipole factorisation formula

$$|\mathcal{M}_{m+1}|^2 = \sum_{i,j}\sum_{k\neq i,j}\mathcal{D}_{ij,k} + \sum_{i,j}\sum_{a}\mathcal{D}_{ij}^{a} + \sum_{a,i}\sum_{k\neq i}\mathcal{D}_{k}^{ai} + \sum_{a,i}\sum_{b\neq a}\mathcal{D}^{ai,b} + \dots \,. \tag{3.1}$$

The individual dipole contributions $\mathcal{D}$ provide the correct approximation of the $(m+1)$-parton matrix element squared in the different singular regions of phase space [3]. In each term i, j and k denote final-state partons and a and b stand for initial-state partons. The first sum always runs over the two particles to be combined, whereas the second sum takes care of the spectators. Accordingly, the four terms correspond to the splitting of a final-state parton accompanied by a final-state or initial-state spectator and emissions off incoming particles in the presence of a final-state or an initial-state spectator, respectively. Finally, the dots in the equation above denote some potential finite terms which do not exhibit any divergence.

For the case of final-state emitters with a final-state spectator, for instance, the individual

[2] It is interesting to note that the latest refinements of the parton showers in HERWIG and PYTHIA also put more emphasis on the notion of a colour-connected partner compensating recoils etc. [8, 11].

[3] Note that squared matrix elements shall always be understood as properly normalised with respect to the colour degrees of freedom of incoming particles.

dipole contributions read [97]

$$\mathcal{D}_{ij,k} = -\frac{1}{2p_ip_j}\ {}_m\langle 1,\ldots,\widetilde{ij},\ldots,\tilde{k},\ldots,m+1|\frac{\mathbf{T}_k\cdot\mathbf{T}_{ij}}{\mathbf{T}_{ij}^2}\mathbf{V}_{ij,k}|1,\ldots,\widetilde{ij},\ldots,\tilde{k},\ldots,m+1\rangle_m\,, \tag{3.2}$$

when all the involved partons are assumed to be massless. The occurring m-parton states are constructed from the original $(m+1)$-particle matrix element by replacing the partons i and j with the new parton $\widetilde{ij}$, the emitter, and the original parton k with $\tilde{k}$, the spectator. In the massless case, their momenta are given by

$$\tilde{p}_{ij}^{\,\mu} = p_i^\mu + p_j^\mu - \frac{y_{ij,k}}{1-y_{ij,k}}p_k^\mu \quad\text{and}\quad \tilde{p}_k^{\,\mu} = \frac{1}{1-y_{ij,k}}p_k^\mu\,, \tag{3.3}$$

where the dimensionless, Lorentz-invariant quantity $y_{ij,k}$ is given by

$$y_{ij,k} = \frac{p_ip_j}{p_ip_j+p_ip_k+p_jp_k}\,. \tag{3.4}$$

It is simple to show exact four-momentum conservation, *i.e.* $\tilde{p}_{ij}^{\,\mu}+\tilde{p}_k^{\,\mu} = p_i^\mu+p_j^\mu+p_k^\mu$, with all particles on their mass shell. In the matrix element on the right hand side of Eq. (3.2), the $\mathbf{T}_{ij}$, $\mathbf{T}_k$ are the colour charges of the emitter and spectator, respectively, and the $\mathbf{V}_{ij,k}$ are matrices in the emitter's spin and colour space, responsible for its branching. The operators $\mathbf{V}_{ij,k}$ also depend on the dimensionless, Lorentz-invariant quantities

$$\tilde{z}_i = \frac{p_ip_k}{p_ip_k+p_jp_k} = \frac{p_i\tilde{p}_k}{\tilde{p}_{ij}\tilde{p}_k} \quad\text{and}\quad \tilde{z}_j = \frac{p_jp_k}{p_ip_k+p_jp_k} = \frac{p_j\tilde{p}_k}{\tilde{p}_{ij}\tilde{p}_k} = 1-\tilde{z}_i\,. \tag{3.5}$$

For instance, for the case of a quark splitting in the final state with a final-state spectator, *i.e.* $q_{ij}\to q_i+g_j$, where s and s' denote the spins of $\widetilde{ij}$ and i, respectively, and where the subscripts label the momenta,

$$\langle s|\mathbf{V}_{q_ig_j,k}(\tilde{z}_i,y_{ij,k})|s'\rangle = 8\pi\mu^{2\epsilon}\alpha_\mathrm{s}C_\mathrm{F}\left[\frac{2}{1-\tilde{z}_i(1-y_{ij,k})}-(1+\tilde{z}_i)-\epsilon(1-\tilde{z}_i)\right]\delta_{ss'}\,. \tag{3.6}$$

Here, $\epsilon=(4-d)/2$, with d the number of dimensions. Similar expressions emerge for the other QCD splittings or when masses are included. However, as a general property, the matrices $\mathbf{V}_{ij,k}$ do not become singular, if any of the scalar products p_ip_j, p_ip_k or p_jp_k vanishes, and therefore the only soft or collinear divergences in the dipole terms $\mathcal{D}_{ij,k}$ are related to $p_ip_j\to 0$.

The collinear limit of the two final-state partons i and j originating from a splitting $\widetilde{ij}\to i+j$ is defined through their relative transverse momentum $k_\perp\to 0$. This limit can be investigated by decomposing the momenta as

$$p_i^\mu = zp^\mu + \frac{-k_\perp^2}{z}\frac{n^\mu}{2pn}+k_\perp^\mu\,, \tag{3.7}$$

$$p_j^\mu = (1-z)p^\mu + \frac{-k_\perp^2}{1-z}\frac{n^\mu}{2pn}-k_\perp^\mu\,, \tag{3.8}$$

with $z \in [0,1]$ and the lightlike p^μ defining the collinear direction. n^μ is an auxiliary lightlike vector that specifies the spacelike transverse momentum $k_\perp^\mu$, with $k_\perp^2 = -\mathbf{k}_\perp^2$, through $pk_\perp = nk_\perp = 0$. Then, in the collinear limit, the scalar product $p_i p_j$ reads

$$p_i p_j = -\frac{k_\perp^2}{2z\,(1-z)}\,, \quad k_\perp^2 \to 0\,, \tag{3.9}$$

and the dipole variables are given by

$$\begin{aligned} y_{ij,k} &\to -\frac{k_\perp^2}{2z(1-z)pp_k}\,, \quad \tilde{z}_i = 1-\tilde{z}_j \to z\,, \\ \tilde{p}_k^\mu &\to p_k^\mu \quad \text{and} \quad \tilde{p}_{ij}^\mu \to p^\mu\,. \end{aligned} \tag{3.10}$$

It can then be shown that in this limit the matrices $\mathbf{V}_{ij,k}$ become proportional to the Altarelli-Parisi splitting kernels,

$$\mathbf{V}_{ij,k} \to 8\pi\mu^{2\epsilon}\alpha_\mathrm{s}\,\hat{P}_{(ij),i}(z,\,k_\perp;\,\epsilon)\,. \tag{3.11}$$

In this limit the only remaining dependence of the dipole contributions $\mathcal{D}_{ij,k}$ on the spectator k resides in its colour factor $\mathbf{T}_k$ and it can be shown that Eq. (3.2) reproduces the well-known universal collinear behaviour of the $(m+1)$-parton matrix element,

$$\begin{aligned} &{}_{m+1}\langle 1,\,\ldots,\,i,\,\ldots,\,j,\,\ldots,\,m+1||1,\,\ldots,\,i,\,\ldots,\,j,\,\ldots,\,m+1\rangle_{m+1} \\ &\quad\xrightarrow{k_\perp\to 0} \frac{4\pi\mu^{2\epsilon}\alpha_\mathrm{s}}{p_i p_j}\;{}_m\langle 1,\,\ldots,\,ij,\,\ldots,\,m+1|\hat{P}_{(ij),i}(z,\,k_\perp;\,\epsilon)|1,\,\ldots,\,ij,\,\ldots,\,m+1\rangle_m\,, \end{aligned} \tag{3.12}$$

where again, the kernel $\hat{P}$ is a d-dimensional Altarelli-Parisi splitting function.
In contrast, the limit where p_j becomes soft is given by $p_j^\mu = \lambda q^\mu$ with $\lambda \to 0$ and q^μ some, in principle arbitrary, four-vector. In this limit, the dipole variables become

$$\begin{aligned} y_{ij,k} &\to 0\,, \quad \tilde{z}_i = 1-\tilde{z}_j \to 1\,, \\ \tilde{p}_k^\mu &\to p_k^\mu \quad \text{and} \quad \tilde{p}_{ij}^\mu \to p_i^\mu\,, \end{aligned} \tag{3.13}$$

and $\mathbf{V}_{ij,k}$ tends to

$$\frac{1}{1-\tilde{z}_i(1-y_{ij,k})} \xrightarrow{\lambda\to 0} \frac{1}{\lambda}\cdot\frac{p_i p_k}{(p_i+p_k)q}\,. \tag{3.14}$$

Therefore,

$$\lambda\mathbf{V}_{ij,k} \xrightarrow{\lambda\to 0} 16\pi\mu^{2\epsilon}\alpha_\mathrm{s}\mathbf{T}_{ij}^2\frac{p_i p_k}{(p_i+p_k)q}\,. \tag{3.15}$$

It can thus be shown that the well-known soft limit of the $(m+1)$-parton matrix element is recovered, namely

$$\begin{aligned} &{}_{m+1}\langle 1,\,\ldots,\,i,\,\ldots,\,j,\,\ldots,\,m+1||1,\,\ldots,\,i,\,\ldots,\,j,\,\ldots,\,m+1\rangle_{m+1} \\ &\quad\xrightarrow{\lambda\to 0} -\sum_{i,k\neq i}\frac{8\pi\mu^{2\epsilon}\alpha_\mathrm{s}}{\lambda^2(p_i q)}\;{}_m\langle 1,\,\ldots,\,ij,\,\ldots,\,m+1|\frac{\mathbf{T}_k\cdot\mathbf{T}_i(p_i p_k)}{(p_i+p_k)q}|1,\,\ldots,\,ij,\,\ldots,\,m+1\rangle_m\,. \end{aligned} \tag{3.16}$$

Taken together, these considerations and similar reasoning for the other dipole contributions translate into the dipole formula, Eq. (3.1), to provide a point-wise approximation to the full $(m+1)$-parton matrix element, which exactly recovers all the soft and collinear divergences. Before starting the discussion on the construction of a parton-shower algorithm from the Catani–Seymour dipole formula in Sec. 3.2 the generalisation of Eq. (3.9) to the massive case and the analogous result for the splitting of an initial-state parton shall be briefly repeated. First, re-consider the splitting $\widetilde{ij} \to i+j$ from above. This time, however, both the emitter and the splitting products are allowed to be massive, the corresponding mass shell conditions read $p^2 = m_{ij}^2$, $p_i^2 = m_i^2$ and $p_j^2 = m_j^2$. However, in order to avoid on-shell decays it is required that $m_{ij} \leq m_i + m_j$. The momenta p_i and p_j can then again be written in a Sudakov parametrisation according to

$$p_i^\mu = zp^\mu + \frac{-k_\perp^2 - z^2 m_{ij}^2 + m_i^2}{z} \frac{n^\mu}{2pn} + k_\perp^\mu \,, \tag{3.17}$$

$$p_j^\mu = (1-z)p^\mu + \frac{-k_\perp^2 - (1-z)^2 m_{ij}^2 + m_j^2}{1-z} \frac{n^\mu}{2pn} - k_\perp^\mu \,, \tag{3.18}$$

with $n^2 = 0$ and $k_\perp$ perpendicular to both p and n. Identifying $k_\perp^2 = -\mathbf{k}_\perp^2$ the invariant mass of partons i and j is now given by

$$(p_i + p_j)^2 = \frac{\mathbf{k}_\perp^2}{z\,(1-z)} + \frac{m_i^2}{z} + \frac{m_j^2}{1-z} \,, \quad \mathbf{k}_\perp^2 \to 0 \,. \tag{3.19}$$

Accordingly, the collinear singularity is shielded when at least one of the two partons has a finite mass.

Finally, consider the case when final-state parton i becomes collinear to an initial-state parton a. This corresponds to the splitting $a \to \widetilde{ai} + i$, with $\widetilde{ai}$ the initial-state parton that enters the m-parton process. Considering only massless initial states, all the partons involved in the splitting are consistently taken to be massless. Decomposing the final-state momentum p_i according to

$$p_i^\mu = (1-x)p_a^\mu + \frac{-k_\perp^2}{1-x} \frac{n^\mu}{2p_a n} + k_\perp \,, \tag{3.20}$$

with $x \in [0,1]$, the collinear limit is reached for

$$p_a p_i = \frac{\mathbf{k}_\perp^2}{2(1-x)} \,, \quad \mathbf{k}_\perp^2 \to 0 \,, \tag{3.21}$$

with $\mathbf{k}_\perp^2$ the magnitude of the spacelike transverse momentum vector $k_\perp$, namely $k_\perp^2 = -\mathbf{k}_\perp^2$. The definitions Eq. (3.19) and Eq. (3.21) constitute the basic relations for identifying the transverse momentum vector for the different splitting types in terms of the respective splitting variables used to describe the branchings, see Sec. 3.3.

3.2 Construction of the algorithm

To formulate a parton-shower algorithm based on the Catani–Seymour dipole formulae, the corresponding splitting operators $\mathcal{D}$ that describe the emission of an additional parton from an arbitrary m-parton state have to be analyzed and rewritten in a suitable form, before they can be used for a showering algorithm. To this end, a number of issues has to be resolved:

- First of all, only the four-dimensional expressions of the splitting kernels $\mathcal{D}$ will enter the parton shower. In addition, the splitting kernels are employed in their spin-averaged form. This manipulation is straightforward and a detailed discussion is therefore not necessary. The resulting splitting kernels depend on the actual configuration of emitters and spectators in the initial- and final state and they will be listed in the corresponding parts of Sec. 3.3.

- In order to keep the probabilistic notion enabling simulation, to use a Markovian formulation for the showering process and to facilitate the hadronisation at the end of the shower, issues concerning colour correlations have to be solved. While the original Catani–Seymour dipole formulae consider all colour correlations, the shower will account only for the leading terms in $1/N_{\mathrm{c}}$. This will be further discussed in Sec. 3.2.1.

- Also, the phase-space factorisation and the corresponding combination procedure is effectively inverted to construct the kinematics of the individual splittings. This yields splitting kernels for $1 \to 2$ QCD branchings that allow for the inclusion of finite parton masses in quite a general way. Each splitting parton thereby is accompanied by a single colour-connected spectator parton compensating the recoil of the splitting. The only exception here are initial-state splittings in the presence of an initial-state spectator, where the recoil is taken by all final-state partons of the event. The introduction of the spectator allows to assemble the shower kinematics such that four-momentum conservation can be ensured after each individual branching with all external partons on their mass-shell. Accordingly, this parton shower algorithm can be stopped at any intermediate stage as well as started again for a partially evolved parton ensemble. However, the exact procedure for reconstructing the kinematics of each splitting again depends on whether the emitter and spectator are in the initial- or final state, respectively. The corresponding formulae are listed in Sec. 3.3.

- The actual shower evolution variable specifying and ordering subsequent emissions is chosen to be the transverse momentum between the splitting products for branching final-state partons and the transverse momentum with respect to the beam for emissions from the initial state, collectively denoted by $\mathbf{k}_\perp$. The physics underlying this choice will be further detailed in Sec. 3.2.2.

- Furthermore, choices have to be made concerning the scales entering the QCD running coupling constant, α_s, and the parton distribution functions when initial-state partons are present. This will be discussed in Sec. 3.2.3.

- Based on these considerations, appropriate Sudakov form factors are constructed that determine the probability for a certain branching process not to occur for a given range of the evolution variable, $\mathbf{k}_\perp$. These Sudakov form factors constitute the basis of the actual Monte Carlo showering algorithm. Again, their specific form depends on the details of emitter and spectator parton and they will thus be given in corresponding parts of Sec. 3.3, too.

- This section closes with some general considerations concerning the treatment of parton masses, cf. Sec. 3.2.4.

3.2.1 Colour factors and spectators

The starting point for every parton-shower evolution is a given set of partons and their momenta from a fixed-order matrix-element calculation. In the large-N_c approximation a colour flow can be assigned to each parton configuration. Since in most cases the initial matrix-element calculation is already summed and averaged over the colours of final and initial partons, the assignment typically is performed a posteriori in different ways in different codes. However, as a result the partons entering the parton shower after this assignment have a well-defined colour, and, due to the large-N_c limit, one or two uniquely assigned colour partners [4]. Motivated by considerations on the colour dynamics for soft emissions in the Catani–Seymour formalism, in a corresponding shower formulation the spectator parton accompanying a given splitting is colour-connected to the emitter parton. For the case of a splitting gluon/gluino then there are always two possible colour partners, whereas splitting (anti-)quarks/squarks will have only one spectator parton candidate. Following this reasoning, the initial partons will enter the parton-shower stage in well-defined pairs of potential emitters and spectators. The subsequent parton shower will not change this feature.
To formalise the treatment of colour inside the parton shower presented here, consider the colour-operators present in the Catani–Seymour dipole contributions. In the large-N_c limit, they are easily calculated for any m-parton state at the price of losing colour correlations beyond $1/N_c$. However, in this limit only two cases need to be considered. Independent of

[4] Representing the colour flow pictorially by coloured strings of partons, two configurations emerge, namely open or closed strings. An open string consists of a colour-triplet state followed by colour octets and ends with a colour anti-triplet. Mapping the colour flows, initial-state quarks (colour triplets) correspond to final-state anti-quarks (colour anti-triplets), whereas initial-state anti-triplets can be treated as final-state triplets. A closed colour string corresponds to a configuration of colour-octet partons only. Accordingly, the end of a closed string is colour-connected to its beginning and therefore the whole colour string is invariant under cyclic permutations of its individual constituents.

the actual spectator flavour, the colour algebra for a splitting (anti-)quark/squark yields,

$$-\frac{\mathbf{T}_k \cdot \mathbf{T}_{ij}}{\mathbf{T}_{ij}^2} \to 1 + \mathcal{O}(\frac{1}{N_\mathrm{c}^2})\,, \tag{3.22}$$

whereas a splitting gluon/gluino results in

$$-\frac{\mathbf{T}_k \cdot \mathbf{T}_{ij}}{\mathbf{T}_{ij}^2} \to \frac{1}{2} + \mathcal{O}(\frac{1}{N_\mathrm{c}^2})\,. \tag{3.23}$$

For convenience, these two results can be combined by introducing $\mathcal{N}_{ij}^{spec}$, the number of possible spectators the emitting parton possesses, then

$$-\frac{\mathbf{T}_k \cdot \mathbf{T}_{ij}}{\mathbf{T}_{ij}^2} \to \frac{1}{\mathcal{N}_{ij}^{spec}} + \mathcal{O}(\frac{1}{N_\mathrm{c}^2})\,. \tag{3.24}$$

3.2.2 Ordering parameter

Having the individual splitting process under control, *i.e.* having at hand the corresponding splitting kernel with all relevant colour factors and the way the kinematics of the emission is constructed, the full showering algorithm with its sequence of splittings can be addressed. While the individual splitting kernel properly takes into account the soft and collinear divergent regions, in the parton shower itself these regions are cut away and, formally speaking, combined with the virtual bits to yield a probabilistic description of the splitting process. The cut on the soft and collinear region implies the emergence of corresponding logarithms of the cut parameter, which the parton shower aims to resum. Technically, this resummation is achieved by arranging the individual emissions in a Markov chain, treating each emission on the same footing, and by ordering the emissions with some ordering parameter. This has been detailed in textbooks such as [114]. In different parton-shower implementations, there are different ordering parameters realised, such as the invariant mass of the splitting particle [115]-[117], the opening angle of the pair [8, 118], or their relative transverse momentum [45, 11]. At the level of doubly leading logarithms, these choices are all equivalent, but there are substantial differences on the level of next-to leading logarithms, *i.e.* on the level of single soft logarithms. This is closely tied with the treatment of quantum coherence effects [119]-[122], which are properly taken into account by ordering subsequent emissions through their respective opening angles [118]. In [85] it has been shown that another way of properly accounting for coherence effects is evolving in a dipole-like picture with subsequent emissions ordered by transverse momenta.

In the implementation presented here, the parton shower will be ordered by transverse momenta, *i.e.* by the $\mathbf{k}_\perp$ in Eqs. (3.19) and (3.21). Apart from the proper treatment of quantum coherence effects, this choice has additional benefits: First of all, as will be discussed in the next section, cf. Sec. 3.2.3, by ordering with $\mathbf{k}_\perp$ the ordering parameter also enters as the relevant scale in the coupling constant and the parton distribution functions. Second, the

definition used here allows for a shower formulation on the basis of Lorentz-invariant quantities, see for instance *e.g.* Eqs. (3.4) and (3.5). Also, ordering by $\mathbf{k}_\perp$ immediately implies that the parton-shower cut-off is related to some minimal transverse momentum necessary to resolve partons, which seems quite appealing in terms of the physical interpretation of such a resolution criterion. Last but not least an ordering by transverse momenta appears to allow for quite a straightforward merging of the parton shower with multi-leg tree-level matrix elements in the spirit of [28, 29]. The merging method presented there is based on Sudakov suppression weights for matrix elements, which are constructed from the transverse momenta of their nodes, and on a vetoed parton shower respecting the minimal scale of a $k_\perp$-jet definition.

In the parton-shower evolution each colour-singlet is separately evolved. To this end, all emitter-spectator dipoles are iterated over and for each of those configurations a $\mathbf{k}_\perp$ is chosen according to the corresponding Sudakov form factor. The dipole with the largest $\mathbf{k}_\perp$ is selected to split according to the kinematics detailed below. As long as this largest $\mathbf{k}_\perp$-value is larger than the infrared cut-off $\mathbf{k}_{\perp,0}$, the shower evolution will continue, and this largest $\mathbf{k}_\perp$ of the current evolution step serves as the maximal scale for all dipoles in the colour-singlet in the next splitting step.

3.2.3 Scales to be chosen

When discussing the details of a parton-shower implementation, some care has to be taken in the choice of various, in principle undetermined, occurring scales. There are a number of choices to be made, namely:

- The evolution variable and the related evolution cut-off:
  As already discussed in the previous section, in this implementation the relative transverse momentum of the produced parton w.r.t. its emitter has been chosen as the relevant evolution variable. It is given by Eqs. (3.19) and (3.21). Correspondingly, a cut-off has to be set as a tuning parameter, to stay away from phase-space regions where the perturbative expansion for the running coupling is divergent. The choice of this cut-off is dictated by two aspects. First of all, it seems to be more attractive to try to assign as much phase space for particle creation to the, in principle, well-understood perturbative parton shower rather than to a phenomenological hadronisation approach such as the Lund string fragmentation [35, 36] or a cluster model [38, 40, 9]. This implies that the cut-off should be as small as possible. On the other hand, it is clear that perturbative QCD breaks down and loses its predictive power at small scales. This is best exemplified by the infrared behaviour of the running coupling which exhibits a Landau pole at Λ_{QCD}. As will be discussed in the next item, since the running coupling in the shower is evaluated at a scale related to $\mathbf{k}_\perp$, this feature of QCD prohibits

cut-offs in the region of Λ_{QCD}. Therefore, a suitable choice seems to be a cut-off $\mathbf{k}_{\perp,0}$ of the order of 1 GeV, sufficiently separated from the Landau pole.

- The argument of the running coupling constant, μ_R:
  In the previous item it has been already hinted at the choice typically made in parton showers, to take the running coupling at scales of the order of $\mathbf{k}_\perp$. The reason for this choice is that it incorporates and resums some of the higher-order corrections to the splitting. Specifically, in this implementation the choice is to take $\mu_R^{\mathrm{F.S.}} = \mu_R = \mathbf{k}_\perp$ if the emitter is a final-state particle and $\mu_R^{\mathrm{I.S.}} = \mu_R = \mathbf{k}_\perp/2$ if the emitter is a parton in the initial state.

- The argument of the parton density functions, μ_F:
  Similar to the case of the running coupling constant, a choice has also been made at which scale to take the parton distribution functions, if necessary. In parton showers, there are typically two answers, namely to either again take the transverse momentum or to use the virtual mass of the initial emitter. Here the choice again is to use $\mu_F = \mathbf{k}_\perp$.

3.2.4 General considerations on massive particles

Taking into account finite quark mass effects in the Standard Model clearly is of importance when producing heavy quarks, bottom or top quarks, in a hard scattering process. In addition, many extensions of the SM introduce new strongly-interacting heavy particles, whose QCD radiation needs to be modelled to understand the patterns of particle and energy flows in their production and eventual decays. Prime examples are scalar quarks and gluinos in supersymmetric theories [123] or heavy excitations of the SM quark and gluon fields in models with additional space-time dimensions [124]. While at lepton colliders heavy objects only appear in the process' final state, at hadron colliders charm and bottom quarks can also constitute the partonic initial state. An example where these are of phenomenological relevance is the associated production of heavy quarks and scalar Higgs particles in supersymmetric models, which is a promising channel to gain deeper insight into the mechanism of electroweak symmetry breaking, see for instance [125] and references therein.
In the following section, QCD splitting operators will be derived, that fully take into account finite masses of partons in the final state. This includes both emission from heavy particles but also the splitting of gluons into heavy quarks such as charm or bottom. Splittings of gluons into heavier objects or branchings of heavy states into other heavy objects are beyond the scope of this work as they are not well modelled by the soft or quasi-collinear approximation and should rather be described with full matrix elements. For all the formulae presented in Sec. 3.3, the massless limit is smoothly obtained when setting the parton masses to zero. This will be explicitly examined for some of the important results there.
Throughout this work, incoming QCD partons will always be treated as massless. The

leading logarithms that arise for emissions off incoming heavy quarks, logarithms of the type $(\alpha_s \log(Q^2/m_Q^2))^n$, with Q^2 the scale of the hard-scattering process and m_Q the quark mass, are summed to all orders in QCD when using heavy-quark parton distribution functions at the factorisation scale $\mu_F \sim Q$ and considering the incoming quarks as massless [126, 127]. A scheme to consistently incorporate explicit masses for incoming heavy quarks, relying on modified heavy-quark density functions [128], has recently been presented in [129].

3.3 Kinematics of the individual splittings

In the following sections, Secs. 3.3.1-3.3.4, the actual parton shower built on Catani–Seymour subtraction terms is constructed. To this end, all combinations of initial- and final-state emitter and spectator partons are considered in detail, following closely the original publications on the subtraction method [97, 98]. First, the kinematic variables characterising the individual splitting under consideration are discussed. Then the explicit form of the phase-space element for the three-parton state under consideration is re-expressed through the kinematic variables above, and their respective bounds are given. In a next step, the polarisation-averaged splitting kernels for the respective emitter-spectator configuration are listed. This allows to give the factorised form of matrix elements with one additional parton in the soft and collinear limits of its production and the factorised form of the corresponding differential cross section, which includes both matrix-element and phase-space factorisation. From there, it is quite straightforward to deduce the actual Sudakov form factor for the emitter-spectator configuration. Finally, the actual kinematics of the splitting is constructed, which may slightly differ from the evolution parameters due to mass effects. For each case then also the more familiar massless limit is briefly discussed. In Sec. 3.3.5 the QCD splitting functions for supersymmetric particles are presented.

3.3.1 Final-state emitter and final-state spectator

The first case to be investigated is when both the emitter and the spectator parton are in the final state, cf. Fig. 3.1. Accordingly, the splitting $\{\widetilde{ij}, \tilde{k}\} \to \{i, j, k\}$ has to be studied. When considering processes without colour-charged initial-state particles, such as jet production in lepton-lepton collisions, this is the only QCD radiation process and thus constitutes the basis of a corresponding final-state parton shower. However, the observed factorisation of the differential cross section for producing an additional parton also holds in the presence of initial-state partons, where only the additional branching channels discussed below then have to be taken into account as well.

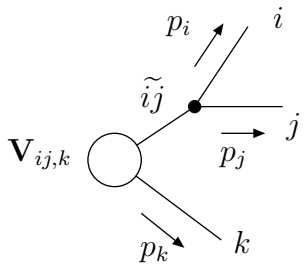

Figure 3.1: Effective diagram for the splitting of a final-state parton connected to a final-state spectator. The blob denotes the m-parton matrix element, and the outgoing lines label the final-state partons participating in the splitting.

Massive case

In the most general case all partons involved in the splitting can have arbitrary masses, *i.e.* $\tilde{p}_{ij}^2 = m_{ij}^2$, $\tilde{p}_k^2 = p_k^2 = m_k^2$, $p_i^2 = m_i^2$ and $p_j^2 = m_j^2$, respectively. In order to avoid on-shell decays, which should be described by their respective proper matrix element, only those situations are considered, where $m_{ij} \leq m_i + m_j$.

- Kinematics:
  Exact four-momentum conservation is ensured by the requirement

$$\tilde{p}_{ij} + \tilde{p}_k = p_i + p_j + p_k \equiv Q\,. \tag{3.25}$$

  The splitting is characterised by the dimensionless variables $y_{ij,k}$, $\tilde{z}_i$ and $\tilde{z}_j$. They are given by

$$y_{ij,k} = \frac{p_i p_j}{p_i p_j + p_i p_k + p_j p_k}\,, \quad \tilde{z}_i = 1 - \tilde{z}_j = \frac{p_i p_k}{p_i p_k + p_j p_k}\,. \tag{3.26}$$

  With these definitions the invariant transverse momentum of partons i and j, defined in Eq. (3.19), can be written as

$$\mathbf{k}_\perp^2 = (Q^2 - m_i^2 - m_j^2 - m_k^2) y_{ij,k}\, \tilde{z}_i(1-\tilde{z}_i) - (1-\tilde{z}_i)^2 m_i^2 - \tilde{z}_i^2 m_j^2\,. \tag{3.27}$$

  For convenience, the rescaled parton masses

$$\mu_n = \frac{m_n}{\sqrt{Q^2}} \quad (n = i, j, k, ij)\,, \tag{3.28}$$

  and the relative velocities between $p_i + p_j$ and p_i (p_k), $v_{ij,i}$ ($v_{ij,k}$),

$$v_{ij,i} = \frac{\sqrt{(1-\mu_i^2-\mu_j^2-\mu_k^2)^2 y_{ij,k}^2 - 4\mu_i^2\mu_j^2}}{(1-\mu_i^2-\mu_j^2-\mu_k^2) y_{ij,k} + 2\mu_i^2}\,, \tag{3.29}$$

$$v_{ij,k} = \frac{\sqrt{\left[2\mu_k^2 + (1-\mu_i^2-\mu_j^2-\mu_k^2)(1-y_{ij,k})\right]^2 - 4\mu_k^2}}{(1-\mu_i^2-\mu_j^2-\mu_k^2)(1-y_{ij,k})}\,, \tag{3.30}$$

as well as the velocity between $\tilde{p}_{ij}$ and $\tilde{p}_k$,

$$\tilde{v}_{ij,k} = \frac{\sqrt{\lambda(1,\mu_{ij}^2,\mu_k^2)}}{1-\mu_{ij}^2-\mu_k^2}\,, \tag{3.31}$$

are introduced.

- Phase space:
  In the case of a final-state emitter with a final-state spectator, the corresponding three-parton phase space $\mathrm{d}\Phi(p_i,p_j,p_k;Q)$ must be analyzed. It exactly factorises into a two-parton contribution $\mathrm{d}\Phi(\tilde{p}_{ij},\tilde{p}_k;Q)$ and a single-parton phase-space factor $[\mathrm{d}p_i(\tilde{p}_{ij},\tilde{p}_k)]$,

$$\mathrm{d}\Phi(p_i,p_j,p_k;Q) = \mathrm{d}\Phi(\tilde{p}_{ij},\tilde{p}_k;Q)\,[\mathrm{d}p_i(\tilde{p}_{ij},\tilde{p}_k)]\,\Theta(1-\mu_i-\mu_j-\mu_k)\,, \tag{3.32}$$

  where the latter is given by

$$[\mathrm{d}p_i(\tilde{p}_{ij},\tilde{p}_k)] = \frac{(\tilde{p}_{ij}+\tilde{p}_k)^2}{16\pi^2}\,\frac{(1-\mu_i^2-\mu_j^2-\mu_k^2)^2}{\sqrt{\lambda(1,\mu_{ij}^2,\mu_k^2)}}\,(1-y_{ij,k})\,\mathrm{d}y_{ij,k}\,\mathrm{d}\tilde{z}_i\frac{\mathrm{d}\phi}{2\pi}\,. \tag{3.33}$$

  Here and in the following, λ denotes the Källen function,

$$\lambda(x,y,z) = x^2+y^2+z^2-2(xy+xz+yz)\,. \tag{3.34}$$

  The boundaries of the full, unconstrained, phase space read $\phi\in[0,2\pi]$, whereas the lower and upper limits for $\tilde{z}_i$ and $y_{ij,k}$ are

$$z_\mp = \frac{2\mu_i^2+(1-\mu_i^2-\mu_j^2-\mu_k^2)y_{ij,k}}{2(\mu_i^2+\mu_j^2+(1-\mu_i^2-\mu_j^2-\mu_k^2)y_{ij,k})}(1\mp v_{ij,i}v_{ij,k})\,, \tag{3.35}$$

$$y_- = \frac{2\mu_i\mu_j}{1-\mu_i^2-\mu_j^2-\mu_k^2}\,,\quad\text{and}\quad y_+ = 1-\frac{2\mu_k\,(1-\mu_k)}{1-\mu_i^2-\mu_j^2-\mu_k^2}\,, \tag{3.36}$$

  respectively.

- Splitting kernels:
  The polarisation-averaged QCD splitting kernels $\langle\mathbf{V}_{ij,k}\rangle$ read

$$\langle\mathbf{V}_{\mathrm{Q}_i\mathrm{g}_j,k}(\tilde{z}_i,y_{ij,k})\rangle = C_\mathrm{F}\left\{\frac{2}{1-\tilde{z}_i+\tilde{z}_i y_{ij,k}}-\frac{\tilde{v}_{ij,k}}{v_{ij,k}}(1+\tilde{z}_i+\frac{m_i^2}{p_ip_j})\right\}, \tag{3.37}$$

$$\begin{aligned}\langle\mathbf{V}_{\mathrm{g}_i\mathrm{g}_j,k}(\tilde{z}_i,y_{ij,k})\rangle &= 2C_\mathrm{A}\left\{\frac{1}{1-\tilde{z}_i+\tilde{z}_i y_{ij,k}}+\frac{1}{\tilde{z}_i+y_{ij,k}-\tilde{z}_i y_{ij,k}}\right.\\ &\qquad\left.+\frac{\tilde{z}_i\,(1-\tilde{z}_i)-z_+z_--2}{v_{ij,k}}\right\},\end{aligned} \tag{3.38}$$

$$\langle\mathbf{V}_{\mathrm{Q}_i\mathrm{Q}_j,k}(\tilde{z}_i)\rangle = T_\mathrm{R}\,\frac{1}{v_{ij,k}}\,\left\{1-2\,[\tilde{z}_i\,(1-\tilde{z}_i)-z_+z_-]\right\}\,. \tag{3.39}$$

Here, Eq. (3.37) describes the QCD splitting $Q \to Qg$, of a massive quark Q, the case of a splitting anti-quark is formally identical. The corresponding expressions for the splitting $g \to gg$, or $g \to Q\bar{Q}$ are given in Eqs. (3.38) and (3.39), respectively. Note that in the above splitting kernels the free parameter κ that occurs in the full NLO subtraction scheme [98] has been set to zero to obtain the simplest expressions for the different $\langle \mathbf{V}_{ij,k} \rangle$.

It should be stressed here that the scalar product $p_i p_j$ present in Eq. (3.37) can be written solely in terms of the splitting variables and the scale $\mathbf{k}_\perp^2$:

$$p_i p_j = \frac{\mathbf{k}_\perp^2}{2\tilde{z}_i\,(1-\tilde{z}_i)} + \frac{(1-\tilde{z}_i)m_i^2}{2\tilde{z}_i} + \frac{\tilde{z}_i m_j^2}{2(1-\tilde{z}_i)}\,. \tag{3.40}$$

However, in Eq. (3.37) the final-state gluon is massless and correspondingly $m_j^2 = 0$ such that the last term of Eq. (3.40) vanishes in this specific case.

- Matrix element:
  Using the above splitting functions, the full $(m+1)$-parton matrix element factorises in the soft and collinear limit according to

$$|\mathcal{M}_{m+1}|^2 = |\mathcal{M}_m|^2 \sum_{ij}\sum_{k\neq ij} \frac{1}{(p_i+p_j)^2 - m_{ij}^2} \frac{1}{\mathcal{N}_{ij}^{spec}}\, 8\pi\alpha_\mathrm{s} \left\langle \mathbf{V}_{ij,k}(\tilde{z}_i, y_{ij,k}) \right\rangle , \tag{3.41}$$

  cf. [97], where the sum covers all the possible emitter-spectator pairs. When combining this with the $(m+1)$-parton phase space a fully factorised expression for the differential cross section is obtained, namely

$$\mathrm{d}\hat{\sigma}_{m+1} = \mathrm{d}\hat{\sigma}_m \sum_{ij}\sum_{k\neq ij} \frac{\mathrm{d}y_{ij,k}}{y_{ij,k}}\,\mathrm{d}\tilde{z}_i\,\frac{d\phi}{2\pi}\,\frac{\alpha_\mathrm{s}}{2\pi}\,\frac{1}{\mathcal{N}_{ij}^{spec}}\,J(y_{ij,k})\langle \mathbf{V}_{ij,k}(\tilde{z}_i, y_{ij,k})\rangle\,, \tag{3.42}$$

  where the Jacobian

$$J(y_{ij,k}) = \frac{1-\mu_i^2-\mu_j^2-\mu_k^2}{\sqrt{\lambda(1,\mu_{ij}^2,\mu_k^2)}}\,\frac{1-y_{ij,k}}{1+\frac{\mu_i^2+\mu_j^2-\mu_{ij}^2}{y_{ij,k}(1-\mu_i^2-\mu_j^2-\mu_k^2)}} \tag{3.43}$$

  emerges from the phase-space factors of Eq. (3.33) combined with the propagator term of Eq. (3.41).

- Sudakov form factor:
  A first step toward the construction of the corresponding Sudakov form factor is achieved by realising that the $y_{ij,k}$-integration in the equation above, Eq. (3.42), can be replaced by an integration over the ordering parameter, the transverse momentum, according to

$$\frac{\mathrm{d}y_{ij,k}}{y_{ij,k}} = \frac{\mathrm{d}\mathbf{k}_\perp^2}{\mathbf{k}_\perp^2}\,. \tag{3.44}$$

Cutting the available phase space through the requirement of a minimal relative transverse momentum squared $\mathbf{k}_\perp^2 > \mathbf{k}_{\perp,0}^2 > 0$ and some upper limit $\mathbf{k}_{\perp,\max}^2$ for the splitting products i and j, the $\tilde{z}_i$ integration boundaries become

$$z_-(\mathbf{k}_{\perp,\max}^2, \mathbf{k}_{\perp,0}^2) = \mathrm{Max}\left(\frac{1}{2}\left(1 - \sqrt{1 - \frac{\mathbf{k}_{\perp,0}^2}{\mathbf{k}_{\perp,\max}^2}}\right), z_-\right), \tag{3.45}$$

$$z_+(\mathbf{k}_{\perp,\max}^2, \mathbf{k}_{\perp,0}^2) = \mathrm{Min}\left(\frac{1}{2}\left(1 + \sqrt{1 - \frac{\mathbf{k}_{\perp,0}^2}{\mathbf{k}_{\perp,\max}^2}}\right), z_+\right), \tag{3.46}$$

with $z_\mp$ taken from Eq. (3.35). Having chosen a valid pair for $\mathbf{k}_\perp^2$ and $\tilde{z}_i$ this can then easily be solved for $y_{ij,k}$,

$$y_{ij,k} = \frac{1}{Q^2 - m_i^2 - m_j^2 - m_k^2}\left(\frac{\mathbf{k}_\perp^2}{\tilde{z}_i(1-\tilde{z}_i)} + \frac{(1-\tilde{z}_i)m_i^2}{\tilde{z}_i} + \frac{\tilde{z}_i m_j^2}{1-\tilde{z}_i}\right). \tag{3.47}$$

If the calculated $y_{ij,k}$ fulfils the requirement $y_{ij,k} \in [y_-, y_+]$, with $y_\mp$ defined in Eq. (3.36), a valid splitting has been constructed, *i.e.* a physical branching allowed by phase space.

The Sudakov form factor corresponding to having no emission from one of the process' final–final dipoles between the maximum transverse momentum squared $\mathbf{k}_{\perp,\max}^2$ and the infrared cut-off $\mathbf{k}_{\perp,0}^2$ reads

$$\begin{aligned}&\Delta_{\mathrm{FF}}(\mathbf{k}_{\perp,\max}^2, \mathbf{k}_{\perp,0}^2)\\ &\quad= \exp\left(-\sum_{ij}\sum_{k\neq ij}\frac{1}{\mathcal{N}_{ij}^{spec}}\int_{\mathbf{k}_{\perp,0}^2}^{\mathbf{k}_{\perp,\max}^2}\frac{\mathrm{d}\mathbf{k}_\perp^2}{\mathbf{k}_\perp^2}\int_{z_-}^{z_+}\mathrm{d}\tilde{z}_i\,\frac{\alpha_\mathrm{s}(\mathbf{k}_\perp^2)}{2\pi}\,J(y_{ij,k})\langle\mathbf{V}_{ij,k}(\tilde{z}_i, y_{ij,k})\rangle\right).\end{aligned} \tag{3.48}$$

As already advertised in Sec. 3.2.3, the scale of the running coupling has thereby been chosen equal to the current transverse momentum squared.

- Physical kinematics:
  Having a valid set of splitting variables, the actual physical branching kinematics must be constructed in order to fully specify the splitting $\{\widetilde{ij}, \tilde{k}\} \to \{i, j, k\}$. In the most general case, both the emitter and the spectator parton are massive, prohibiting a simple Sudakov parametrisation of p_i and p_j in terms of light-like momenta $\tilde{p}_{ij}$ and $\tilde{p}_k$. Instead they are expressed in light-cone kinematics with massive base momenta. The new spectator momentum is determined in the emitter-spectator centre-of-mass

frame,

$$p_k = \frac{\sqrt{\left[2\mu_k^2 + (1-\mu_i^2-\mu_j^2-\mu_k^2)(1-y_{ij,k})\right]^2 - 4\mu_k^2}}{\sqrt{\lambda(1,\mu_{ij}^2,\mu_k^2)}} \left(\tilde{p}_k - \frac{1}{2}\left[1+\mu_k^2-\mu_{ij}^2\right] Q\right) + \left[\frac{1}{2}(1-\mu_i^2-\mu_j^2-\mu_k^2)(1-y_{ij,k}) + \mu_k^2\right] Q\,. \tag{3.49}$$

Then the situation is most easily discussed in a frame where $Q - p_k$ is at rest and the momentum p_k points along the z-direction. In this frame, the light-cone momenta of $Q - p_k$ and p_k can be written as

$$Q - p_k = (M, M, \vec{0}) \quad \text{and} \quad p_k = (m_k\, e^{x}, m_k\, e^{-x}, \vec{0})\,. \tag{3.50}$$

The ansatz for the light-cone momenta of the new emerging final-state partons reads

$$p_i = (m_{i,\perp}\, e^{y}, m_{i,\perp}\, e^{-y}, \vec{l}_\perp)\,, \quad p_j = (m_{j,\perp}\, e^{z}, m_{j,\perp}\, e^{-z}, -\vec{l}_\perp)\,, \tag{3.51}$$

with $m_\perp$ being the transverse mass of the respective parton, defined according to

$$m_\perp = \sqrt{m^2 + \vec{l}_\perp^{\,2}}\,. \tag{3.52}$$

The kinematics is fully determined through energy-momentum conservation and the constraint

$$\tilde{z}_i = 1 - \tilde{z}_j = \frac{p_i p_k}{p_i p_k + p_j p_k}\,. \tag{3.53}$$

Then,

$$\vec{l}_\perp^{\,2} = \left(\frac{M^2 + m_i^2 + m_j^2}{2M}\right)^2 - m_i^2 - \left(\frac{M^2 + m_i^2 + m_j^2 - 2M^2\tilde{z}_i}{2M}\,\left(\frac{\cosh x}{\sinh x}\right)\right)^2\,, \tag{3.54}$$

and

$$\cosh y = \frac{M^2 + m_i^2 - m_j^2}{2M m_{i,\perp}}\,, \quad \sinh y = \frac{\cosh x}{\sinh x}\left(\cosh y - \frac{M\tilde{z}_i}{m_{i,\perp}}\right)\,, \tag{3.55}$$

$$\cosh z = \frac{M^2 - m_i^2 + m_j^2}{2M m_{j,\perp}}\,, \quad \sinh z = \frac{\cosh x}{\sinh x}\left(\cosh z - \frac{M(1-\tilde{z}_i)}{m_{j,\perp}}\right)\,. \tag{3.56}$$

Expressed through ordinary four-vectors the parton momenta in this frame read

$$p_i = (m_{i,\perp}\cosh y, l_\perp\cos\phi, l_\perp\sin\phi, m_{i,\perp}\sinh y)\,, \tag{3.57}$$

$$p_j = (m_{j,\perp}\cosh z, -l_\perp\cos\phi, -l_\perp\sin\phi, m_{j,\perp}\sinh z)\,, \tag{3.58}$$

with the angle ϕ not fixed by the splitting and therefore uniformly distributed in the transverse plane. The kinematics is completed by rotating and boosting back the momenta p_i, p_j and p_k into the laboratory frame.

If the spectator is massless, the new final-state momenta can alternatively be given in a simple Sudakov parametrisation:

$$p_i = \tilde{z}_i\,\tilde{p}_{ij} + \frac{\mathbf{k}_\perp^2 - \tilde{z}_i^2 m_{ij}^2 + m_i^2}{\tilde{z}_i\,2\tilde{p}_{ij}\tilde{p}_k}\,\tilde{p}_k + k_\perp\,, \tag{3.59}$$

$$p_j = (1-\tilde{z}_i)\,\tilde{p}_{ij} + \frac{\mathbf{k}_\perp^2 - (1-\tilde{z}_i)^2 m_{ij}^2 + m_j^2}{(1-\tilde{z}_i)\,2\tilde{p}_{ij}\tilde{p}_k}\,\tilde{p}_k - k_\perp\,, \tag{3.60}$$

$$p_k = \left(\frac{(1-\mu_i^2-\mu_j^2)(1-y_{ij,k})}{1-\mu_{ij}^2}\right)\tilde{p}_k\,, \tag{3.61}$$

with the spacelike transverse-momentum vector $k_\perp$ pointing in a direction perpendicular to both the emitter and the spectator momentum.

Massless case

The case of a final-final splitting is considerably simpler in the massless limit, *i.e.* where all occurring partons can be treated as massless, $\tilde{p}_{ij}^2 = \tilde{p}_k^2 = p_k^2 = p_i^2 = p_j^2 = 0$. In this case, of course, the variables chosen to specify the splitting remain unchanged with respect to the fully massive case. However, neglecting masses the ordering parameter reduces to

$$\mathbf{k}_\perp^2 = Q^2 y_{ij,k}\,\tilde{z}_i(1-\tilde{z}_i) = 2\tilde{p}_{ij}\tilde{p}_k\; y_{ij,k}\,\tilde{z}_i\,(1-\tilde{z}_i)\,, \tag{3.62}$$

with the identification of $Q^2 = 2\tilde{p}_{ij}\tilde{p}_k$ this is identical with the transverse momentum defined in Eq. (3.9). The full phase space for the emission of an extra parton extends to $\tilde{z}_i \in [0,1]$, $y_{ij,k} \in [0,1]$, whereas ϕ again uniformly covers the interval $[0, 2\pi]$.
In the massless limit also the spin averaged splitting kernels $\langle \mathbf{V}_{ij,k} \rangle$ simplify considerably, namely to

$$\langle \mathbf{V}_{\mathrm{q_i g_j},k}(\tilde{z}_i, y_{ij,k})\rangle = C_\mathrm{F}\left\{\frac{2}{1-\tilde{z}_i+\tilde{z}_i y_{ij,k}} - (1+\tilde{z}_i)\right\}\,, \tag{3.63}$$

$$\langle \mathbf{V}_{\mathrm{g_i g_j},k}(\tilde{z}_i, y_{ij,k})\rangle = 2C_\mathrm{A}\left\{\frac{1}{1-\tilde{z}_i+\tilde{z}_i y_{ij,k}} + \frac{1}{\tilde{z}_i + y_{ij,k} - \tilde{z}_i y_{ij,k}} - 2 + \tilde{z}_i\,(1-\tilde{z}_i)\right\}\,, \tag{3.64}$$

$$\langle \mathbf{V}_{\mathrm{q_i q_j},k}(\tilde{z}_i)\rangle = T_\mathrm{R}\left\{1 - 2\tilde{z}_i\,(1-\tilde{z}_i)\right\}\,. \tag{3.65}$$

When combining the factorised form of the $(m+1)$-parton phase space,

$$\mathrm{d}\Phi_{m+1} = \mathrm{d}\Phi_m \sum_{ij}\sum_{k\neq ij} \frac{2p_ip_j}{16\pi^2}\,\frac{\mathrm{d}y_{ij,k}}{y_{ij,k}}\,d\tilde{z}_i\,\frac{d\phi}{2\pi}\,(1-y_{ij,k})\,\Theta(\tilde{z}_i\,(1-\tilde{z}_i))\,\Theta(y_{ij,k}(1-y_{ij,k}))\,, \tag{3.66}$$

with the corresponding expression for the $(m+1)$-parton matrix element,

$$|\mathcal{M}_{m+1}|^2 = |\mathcal{M}_m|^2 \sum_{ij}\sum_{k\neq ij} \frac{1}{2p_ip_j}\,\frac{1}{\mathcal{N}_{ij}^{spec}}\,8\pi\alpha_\mathrm{s}\,\langle \mathbf{V}_{ij,k}(\tilde{z}_i, y_{ij,k})\rangle\,, \tag{3.67}$$

the fully factorised form of the $(m+1)$-parton differential cross section is recovered

$$\mathrm{d}\hat{\sigma}_{m+1} = \mathrm{d}\hat{\sigma}_m \sum_{ij} \sum_{k\neq ij} \frac{\mathrm{d}y_{ij,k}}{y_{ij,k}} \, d\tilde{z}_i \, \frac{d\phi}{2\pi} \, \frac{\alpha_\mathrm{s}}{2\pi} \, \frac{1}{\mathcal{N}_{ij}^{spec}} \, J(y_{ij,k}) \langle \mathbf{V}_{ij,k}(\tilde{z}_i, y_{ij,k}) \rangle \,. \tag{3.68}$$

However, in this case, the Jacobian $J(y_{ij,k})$ simply is given by

$$J(y_{ij,k}) = 1 - y_{ij,k} \,. \tag{3.69}$$

With the transverse momentum defined according to Eq. (3.62) again the identity

$$\frac{\mathrm{d}y_{ij,k}}{y_{ij,k}} = \frac{\mathrm{d}\mathbf{k}_\perp^2}{\mathbf{k}_\perp^2} \,, \tag{3.70}$$

is found. Choosing $\mathbf{k}_\perp^2$ as the evolution variable with its lower cut-off given by $\mathbf{k}_{\perp,0}^2$ and the upper limit by $\mathbf{k}_{\perp,\max}^2$ the $\tilde{z}_i$ integration range reduces to

$$z_\mp(\mathbf{k}_{\perp,\max}^2, \mathbf{k}_{\perp,0}^2) \;=\; \frac{1}{2}\left(1 \mp \sqrt{1 - \frac{\mathbf{k}_{\perp,0}^2}{\mathbf{k}_{\perp,\max}^2}}\right) . \tag{3.71}$$

Given a valid set of $\mathbf{k}_\perp^2$ and $\tilde{z}_i$ this can be solved for

$$y_{ij,k} = \frac{\mathbf{k}_\perp^2}{Q^2 \tilde{z}_i (1 - \tilde{z}_i)} \,, \tag{3.72}$$

completing the determination of the splitting variables. Making the necessary replacements when going from massive partons to massless the Sudakov form factor given in Eq. (3.48) yields the corresponding non-branching probability. The massless kinematics can be derived from Eqs. (3.59)-(3.61) by setting $\mu_{ij} = \mu_i = \mu_j = 0$, accordingly

$$p_i \;=\; \tilde{z}_i \, \tilde{p}_{ij} + \frac{\mathbf{k}_\perp^2}{\tilde{z}_i \, 2\tilde{p}_{ij}\tilde{p}_k} \, \tilde{p}_k + k_\perp \,, \tag{3.73}$$

$$p_j \;=\; (1 - \tilde{z}_i) \, \tilde{p}_{ij} + \frac{\mathbf{k}_\perp^2}{(1 - \tilde{z}_i) \, 2\tilde{p}_{ij}\tilde{p}_k} \, \tilde{p}_k - k_\perp \,, \tag{3.74}$$

$$p_k \;=\; (1 - y_{ij,k}) \, \tilde{p}_k \,. \tag{3.75}$$

3.3.2 Final-state emitter and initial-state spectator

In this section, the case of a final-state emission with the spectator being an initial-state parton a is worked out. The splitting schematically reads $\{\widetilde{ij}, \tilde{a}\} \to \{i, j, a\}$, for a pictorial representation of the configuration, cf. Fig. 3.2. This configuration emerges for the first time when considering deep-inelastic lepton scattering (DIS), where one incoming line carries colour charge, or in configurations like vector boson fusion, with no colour exchange between the two hadrons. However, besides the singularity related to a final-state splitting, there is also a singular region for the splitting of the initial-state QCD parton, which needs to be included in such processes. This situation will be investigated in detail in Sec. 3.3.3.

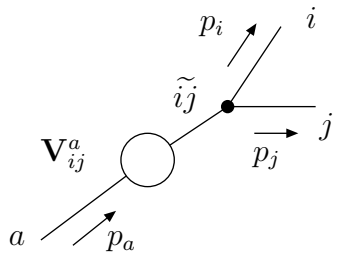

Figure 3.2: Sketch of the splitting of a final-state parton accompanied by an initial-state spectator. The blob denotes the m-parton matrix element. The incoming and outgoing lines label the initial- and final-state partons, respectively.

Massive case

The initial line is always assumed to be massless, however, all final-state particles can be massive. Accordingly,

$$\tilde{p}_{ij}^2 = m_{ij}^2 \quad \tilde{p}_a^2 = p_a^2 = 0 \quad p_i^2 = m_i^2\,, \quad p_j^2 = m_j^2\,. \tag{3.76}$$

To avoid on-shell decays being described incorrectly, again $m_{ij} \leq m_i + m_j$ should hold true.

- Kinematics:
  Four-momentum conservation is incorporated through the condition

$$\tilde{p}_{ij} - \tilde{p}_a = p_i + p_j - p_a \equiv Q\,. \tag{3.77}$$

  Defining the Lorentz-invariants

$$x_{ij,a} = \frac{p_i p_a + p_j p_a - p_i p_j + \frac{1}{2}(m_{ij}^2 - m_i^2 - m_j^2)}{p_i p_a + p_j p_a}\,, \tag{3.78}$$

$$\tilde{z}_i = \frac{p_i p_a}{p_i p_a + p_j p_a}\,, \quad \tilde{z}_j = \frac{p_j p_a}{p_i p_a + p_j p_a} = 1 - \tilde{z}_i\,, \tag{3.79}$$

  the relative transverse momentum of the new emerging final-state partons is given by

$$\mathbf{k}_\perp^2 = 2\tilde{p}_a\tilde{p}_{ij}\,\frac{1 - x_{ij,a}}{x_{ij,a}}\,\tilde{z}_i\,(1 - \tilde{z}_i) - (1 - \tilde{z}_i)^2 m_i^2 - \tilde{z}_i^2 m_j^2\,. \tag{3.80}$$

- Phase space:
  The factorised form of the three-parton phase space reads [98]

$$\mathrm{d}\Phi(p_i, p_j; Q + p_a) = \int_0^1 \mathrm{d}x \mathrm{d}\Phi(\tilde{p}_{ij}; Q + x p_a)\,[\mathrm{d}p_i(\tilde{p}_{ij}; p_a, x)]\,\Theta(x_+ - x)\,, \tag{3.81}$$

  with the single-parton phase-space factor

$$[\mathrm{d}p_i(\tilde{p}_{ij}; p_a, x)] = \frac{2\tilde{p}_{ij}p_a}{16\pi^2}\,\frac{\mathrm{d}\phi}{2\pi}\,\mathrm{d}\tilde{z}_i\,\mathrm{d}x_{ij,a}\,\delta(x - x_{ij,a})\,, \tag{3.82}$$

and the integration boundaries

$$x_- = 0\,, \quad x_+ = 1 + \mu_{ij}^2 - (\mu_i + \mu_j)^2\,, \tag{3.83}$$

$$z_\mp = \frac{1 - x + \mu_{ij}^2 + \mu_i^2 - \mu_j^2 \mp \sqrt{(1 - x + \mu_{ij}^2 - \mu_i^2 - \mu_j^2)^2 - 4\mu_i^2\mu_j^2}}{2(1 - x + \mu_{ij}^2)}\,. \tag{3.84}$$

Here, again rescaled parton masses have been introduced,

$$\mu_n = \frac{m_n}{\sqrt{2\tilde{p}_{ij}\tilde{p}_a/x_{ij,a}}} \quad (n = i, j, ij)\,. \tag{3.85}$$

- Splitting kernels:
  The polarisation-averaged QCD dipole splitting kernels $\langle \mathbf{V}_{ij}^a(\tilde{z}_i, x_{ij,a})\rangle$ read

$$\langle \mathbf{V}_{\mathrm{Q}_i\mathrm{g}_j}^a(\tilde{z}_i, x_{ij,a})\rangle = C_\mathrm{F}\left\{\frac{2}{1 - \tilde{z}_i + (1 - x_{ij,a})} - (1 + \tilde{z}_i) - \frac{m_i^2}{p_i p_j}\right\}\,, \tag{3.86}$$

$$\langle \mathbf{V}_{\mathrm{g}_i\mathrm{g}_j}^a(\tilde{z}_i, x_{ij,a})\rangle = 2C_\mathrm{A}\left\{\frac{1}{1 - \tilde{z}_i + (1 - x_{ij,a})} + \frac{1}{\tilde{z}_i + (1 - x_{ij,a})} - 2 + \tilde{z}_i\,(1 - \tilde{z}_i)\right\}\,, \tag{3.87}$$

$$\langle \mathbf{V}_{\mathrm{Q}_i\mathrm{Q}_j}^a(\tilde{z}_i)\rangle = T_\mathrm{R}\left\{1 - 2(z_+ - \tilde{z}_i)(z_- - \tilde{z}_i)\right\}\,. \tag{3.88}$$

  The scalar product of the *a priori* unknown momenta p_i and p_j in Eq. (3.86) can again be expressed according to Eq. (3.40). The two functions $\langle \mathbf{V}_{\mathrm{Q}_i\mathrm{g}_j}^a\rangle$ and $\langle \mathbf{V}_{\mathrm{g}_i\mathrm{g}_j}^a\rangle$ can take negative values in non-singular regions of the emission phase space. Here they are explicitly set equal to zero instead.

- Matrix element:
  Combining the $(m+1)$-parton phase space with the factorised form of the matrix element,

$$|\mathcal{M}_{m+1}|^2 = |\mathcal{M}_m|^2 \sum_{ij}\sum_a \frac{1}{(p_i + p_j)^2 - m_{ij}^2}\,\frac{1}{\mathcal{N}_{ij}^{spec}}\,\frac{1}{x_{ij,a}}\,8\pi\alpha_\mathrm{s}\,\langle \mathbf{V}_{ij}^a(\tilde{z}_i, x_{ij,a})\rangle\,, \tag{3.89}$$

  one obtains the fully differential cross section for the emission of one additional parton in that configuration

$$\mathrm{d}\hat{\sigma}_{m+1} = \mathrm{d}\hat{\sigma}_m \sum_{ij}\sum_a \frac{\mathrm{d}x_{ij,a}}{x_{ij,a}}\,\mathrm{d}\tilde{z}_i\,\frac{\mathrm{d}\phi}{2\pi}\,\frac{\alpha_\mathrm{s}}{2\pi}\,\frac{1}{\mathcal{N}_{ij}^{spec}}\,\frac{1}{1 - x_{ij,a}}\,\langle \mathbf{V}_{ij}^a(\tilde{z}_i, x_{ij,a})\rangle\,, \tag{3.90}$$

  where the sum covers all the possible colour-connected emitter-spectator pairings. The Jacobian of the variable transformation in this case reads

$$J(x_{ij,a}) = \frac{1}{1 - x_{ij,a}}\,. \tag{3.91}$$

Taking into account that the initial parton actually stems from a hadronic initial state, a corresponding parton distribution function (PDF) emerges. Absorbing it into the Jacobian yields

$$\tilde{J}(x_{ij,a};\mu_F^2) = \frac{1}{1-x_{ij,a}} \frac{f_a(\eta_a/x_{ij,a},\mu_F^2)}{f_a(\eta_a,\mu_F^2)} \,. \tag{3.92}$$

Here, η_a is the momentum fraction of the spectator parton a and $f_a(\eta_a,\mu_F^2)$ the corresponding hadronic PDF evaluated at some scale μ_F^2. In Sec. 3.2.3 this scale has been set to $\mu_F = \mathbf{k}_\perp$. The parton distribution function $f_a(\eta_a/x_{ij,a},\mu_F^2)$ corresponds to the new incoming momentum and is also evaluated at scale μ_F^2.

- Sudakov form factor:
  Note that Eq. (3.80) implies that

$$\frac{\mathrm{d}x_{ij,a}}{x_{ij,a}} = (1-x_{ij,a}) \frac{\mathrm{d}\mathbf{k}_\perp^2}{\mathbf{k}_\perp^2} \,. \tag{3.93}$$

  With $\mathbf{k}_\perp^2$ taken as the evolution scale with an upper limit $\mathbf{k}_{\perp,\max}^2$ and the cut-off $\mathbf{k}_{\perp,0}^2$ the $\tilde{z}_i$ integration boundaries therefore are given by

$$z_-(\mathbf{k}_{\perp,\max}^2,\mathbf{k}_{\perp,0}^2) = \mathrm{Max}\left(\frac{1}{2}\left(1-\sqrt{1-\frac{\mathbf{k}_{\perp,0}^2}{\mathbf{k}_{\perp,\max}^2}}\right), z_-\right), \tag{3.94}$$

$$z_+(\mathbf{k}_{\perp,\max}^2,\mathbf{k}_{\perp,0}^2) = \mathrm{Min}\left(\frac{1}{2}\left(1+\sqrt{1-\frac{\mathbf{k}_{\perp,0}^2}{\mathbf{k}_{\perp,\max}^2}}\right), z_+\right), \tag{3.95}$$

  with $z_\pm$ given in Eq. (3.83). Having determined $\mathbf{k}_\perp^2$ and $\tilde{z}_i$ the variable $x_{ij,a}$ is calculated through

$$x_{ij,a} = 1 - \frac{\mathbf{k}_\perp^2 + (1-\tilde{z}_i)^2 m_i^2 + \tilde{z}_i^2 m_j^2 - \tilde{z}_i(1-\tilde{z}_i)(m_{ij}^2 - m_i^2 - m_j^2)}{\mathbf{k}_\perp^2 + (1-\tilde{z}_i)^2 m_i^2 + \tilde{z}_i^2 m_j^2 + \tilde{z}_i(1-\tilde{z}_i)(Q^2 + 2m_i^2 + 2m_j^2)} \,, \tag{3.96}$$

  and has to fulfil the condition

$$x_{ij,a} \in [\eta_a/\eta_{\max}\,,\, x_+] \tag{3.97}$$

  to yield a valid branching. Here, $\eta_{\max}$ corresponds to the maximal allowed Bjørken-x for the PDF (typically, $\eta_{\max} = 1$). Having at hand all ingredients, the Sudakov form factor associated to the splitting of a final-state parton with an initial-state spectator reads

$$\Delta_{\mathrm{FI}}(\mathbf{k}_{\perp,\max}^2,\mathbf{k}_{\perp,0}^2) = \exp\left(-\sum_{ij}\sum_a \frac{1}{\mathcal{N}_{ij}^{spec}} \int_{\mathbf{k}_{\perp,0}^2}^{\mathbf{k}_{\perp,\max}^2} \frac{\mathrm{d}\mathbf{k}_\perp^2}{\mathbf{k}_\perp^2} \int_{z_-}^{z_+} \mathrm{d}\tilde{z}_i \frac{\alpha_{\mathrm{s}}(\mathbf{k}_\perp^2)}{2\pi} \frac{f_a(\eta_a/x_{ij,a},\mathbf{k}_\perp^2)}{f_a(\eta_a,\mathbf{k}_\perp^2)} \langle \mathbf{V}_{ij}^a(\tilde{z}_i,x_{ij,a})\rangle\right) . \tag{3.98}$$

- Physical kinematics:
  The actual branching kinematics can be given in a Sudakov parametrisation. In the Breit-frame of the emitter and spectator the two final-state momenta can be written as

$$p_i = \tilde{z}_i\,\tilde{p}_{ij} + \frac{\mathbf{k}_\perp^2 + m_i^2 - \tilde{z}_i^2\,m_{ij}^2}{\tilde{z}_i\,2\tilde{p}_{ij}\tilde{p}_a}\,\tilde{p}_a + k_\perp\,, \tag{3.99}$$

$$p_j = (1-\tilde{z}_i)\,\tilde{p}_{ij} + \frac{\mathbf{k}_\perp^2 + m_j^2 - (1-\tilde{z}_i)^2\,m_{ij}^2}{(1-\tilde{z}_i)\,2\tilde{p}_{ij}\tilde{p}_a}\,\tilde{p}_a - k_\perp\,, \tag{3.100}$$

  with the spacelike-$k_\perp$ being perpendicular to both the emitter and the spectator momentum. After the splitting the latter remains parallel to $\tilde{p}_a$ but is rescaled according to

$$p_a = \frac{1}{x_{ij,a}}\tilde{p}_a\,. \tag{3.101}$$

Massless case

The modifications emerging in the massless limit are briefly discussed. The splitting variable $x_{ij,a}$ simplifies to

$$x_{ij,a} = \frac{p_i p_a + p_j p_a - p_i p_j}{p_i p_a + p_j p_a}\,, \tag{3.102}$$

whereas the momentum fractions $\tilde{z}_i$ and $\tilde{z}_j$ are still defined according to Eq. (3.79). The invariant spacelike transverse momentum is simplified and reads

$$\mathbf{k}_\perp^2 = 2\tilde{p}_a\tilde{p}_{ij}\,\frac{1-x_{ij,a}}{x_{ij,a}}\,\tilde{z}_i\,(1-\tilde{z}_i)\,. \tag{3.103}$$

While the $g \to gg$ splitting function remains the same, the mass dependent terms drop out in the $q \to qg$ and $g \to q\overline{q}$ kernels,

$$\langle \mathbf{V}^a_{\mathrm{q_i g_j}}(\tilde{z}_i, x_{ij,a})\rangle = C_\mathrm{F}\left\{\frac{2}{1-\tilde{z}_i+(1-x_{ij,a})} - (1+\tilde{z}_i)\right\}\,, \tag{3.104}$$

$$\langle \mathbf{V}^a_{\mathrm{q_i q_j}}(\tilde{z}_i)\rangle = T_\mathrm{R}\left\{1 - 2\tilde{z}_i\,(1-\tilde{z}_i)\right\}\,. \tag{3.105}$$

Incorporating the factorisation of the $(m+1)$-parton matrix element and the corresponding phase space the fully differential $(m+1)$-parton cross section is still given by Eq. (3.90), with the appropriate Jacobian for hadronic initial states. In the massless limit the phase-space boundaries are no longer constrained through finite mass terms, and therefore extend to

$$x_{ij,a},\ \tilde{z}_i \in [0,1]\,. \tag{3.106}$$

Eq. (3.103) still implies that

$$\frac{\mathrm{d}x_{ij,a}}{x_{ij,a}} = (1-x_{ij,a})\,\frac{\mathrm{d}\mathbf{k}_\perp^2}{\mathbf{k}_\perp^2}\,. \tag{3.107}$$

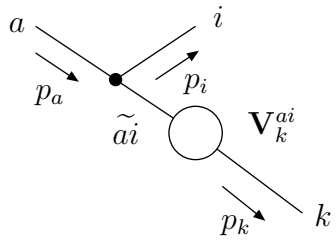

Figure 3.3: Splitting of an initial-state parton accompanied by a final-state spectator. The blob denotes the m-parton matrix element. The incoming and outgoing lines label the initial- and final-state partons, respectively.

When evolving in $\mathbf{k}_\perp^2$ from $\mathbf{k}_{\perp,\max}^2$ and asking for a minimum separation $\mathbf{k}_{\perp,0}^2$ the allowed $\tilde{z}_i$ range is reduced to

$$\tilde{z}_i \in \left[\frac{1}{2}\left(1-\sqrt{1-\frac{\mathbf{k}_{\perp,0}^2}{\mathbf{k}_{\perp,\max}^2}}\right),\frac{1}{2}\left(1+\sqrt{1-\frac{\mathbf{k}_{\perp,0}^2}{\mathbf{k}_{\perp,\max}^2}}\right)\right] \tag{3.108}$$

in the massless case. The expression of the Sudakov from factor, Eq. (3.98), of course remains unaltered.

The kinematics of the new final-state partons simplify to

$$p_i = \tilde{z}_i\,\tilde{p}_{ij} + \frac{\mathbf{k}_\perp^2}{\tilde{z}_i\,2\tilde{p}_{ij}\tilde{p}_a}\,\tilde{p}_a + k_\perp\,, \tag{3.109}$$

$$p_j = (1-\tilde{z}_i)\,\tilde{p}_{ij} + \frac{\mathbf{k}_\perp^2}{(1-\tilde{z}_i)\,2\tilde{p}_{ij}\tilde{p}_a}\,\tilde{p}_a - k_\perp\,, \tag{3.110}$$

with $k_\perp$ still being perpendicular to both the emitter and the spectator momentum. The new spectator momentum is still given by

$$p_a = \frac{1}{x_{ij,a}}\tilde{p}_a\,, \tag{3.111}$$

with $x_{ij,a}$ taken from Eq. (3.102).

3.3.3 Initial-state emitter and final-state spectator

The case of an initial-state parton branching ($\widetilde{ai}$), accompanied by a final-state spectator ($\tilde{k}$) is sketched in Fig. 3.3. This accounts for the situation where the emitter and the spectator parton studied in Sec. 3.3.2 exchange their rôles.

Massive case

As stated above, treating initial-state particles as massless, final-state particles emitted from the initial state are assumed massless as well, the spectator mass, however, is arbitrary.

Accordingly, the momenta involved in the splitting $\{\widetilde{ai}, \tilde{k}\} \to \{a, i, k\}$ have to fulfil the mass-shell relations

$$\tilde{p}_{ai}^2 = p_i^2 = p_a^2 = 0\,, \quad \tilde{p}_k^2 = p_k^2 = m_k^2\,. \tag{3.112}$$

and the momentum conservation condition

$$\tilde{p}_k - \tilde{p}_{ai} = p_i + p_k - p_a \equiv Q\,. \tag{3.113}$$

- Kinematics:
  The splitting can be specified by the variables

$$x_{ik,a} = \frac{p_i p_a + p_k p_a - p_i p_k}{p_i p_a + p_k p_a}\,, \quad u_i = \frac{p_i p_a}{p_i p_a + p_k p_a}\,. \tag{3.114}$$

  The transverse momentum squared parametrising the singular region where the emitted parton i becomes collinear with the initial-state parton a then reads

$$\mathbf{k}_\perp^2 = 2\tilde{p}_{ai}\tilde{p}_k \frac{1 - x_{ik,a}}{x_{ik,a}}\, u_i(1 - u_i)\,. \tag{3.115}$$

  To allow for a more compact notation, the rescaled spectator mass

$$\mu_k = \frac{m_k}{\sqrt{2\tilde{p}_{ai}\tilde{p}_k / x_{ik,a}}} \tag{3.116}$$

  is introduced.

- Splitting kernels:
  The QCD splitting kernels, taking into account possible non-zero spectator masses, read

$$\langle \mathbf{V}_k^{\mathrm{q}_a \mathrm{g}_i}(x_{ik,a}, u_i)\rangle = C_\mathrm{F}\left\{\frac{2}{1 - x_{ik,a} + u_i} - (1 + x_{ik,a})\right\}\,, \tag{3.117}$$

$$\langle \mathbf{V}_k^{\mathrm{q}_a \mathrm{q}_i}(x_{ik,a})\rangle = C_\mathrm{F}\left\{x_{ik,a} + 2\frac{1 - x_{ik,a}}{x_{ik,a}} - \frac{2\mu_k^2}{x_{ik,a}}\frac{u_i}{1 - u_i}\right\}\,, \tag{3.118}$$

$$\begin{aligned}\langle \mathbf{V}_k^{\mathrm{g}_a \mathrm{g}_i}(x_{ik,a}, u_i)\rangle = 2C_\mathrm{A}\Bigg\{&\frac{1}{1 - x_{ik,a} + u_i} + \frac{1 - x_{ik,a}}{x_{ik,a}} - 1 \\ &+ x_{ik,a}(1 - x_{ik,a}) - \frac{\mu_k^2}{x_{ik,a}}\frac{u_i}{1 - u_i}\Bigg\}\,,\end{aligned} \tag{3.119}$$

$$\langle \mathbf{V}_k^{\mathrm{g}_a \mathrm{q}_i}(x_{ik,a})\rangle = T_\mathrm{R}\left\{1 - 2x_{ik,a}(1 - x_{ik,a})\right\}\,. \tag{3.120}$$

  Note that $\langle \mathbf{V}_k^{\mathrm{q}_a \mathrm{g}_i}\rangle$ can turn negative outside the singular region and is set to zero for those rare cases.

- Phase space:
  The three-parton phase space is again obtained by a convolution of a two-parton piece and a single-parton part,

$$\mathrm{d}\Phi(p_i, p_k; Q + p_a) = \int_0^1 \mathrm{d}x \mathrm{d}\Phi(\tilde{p}_k; Q + x p_a)\left[\mathrm{d}p_i(\tilde{p}_k; p_a, x)\right]\,, \tag{3.121}$$

where

$$[\mathrm{d}p_i(\tilde{p}_k;p_a,x)] = \frac{\mathrm{d}^4p_i}{2\pi}\delta(p_i^2)\,\Theta(x)\,\Theta(1-x)\,\delta(x-x_{ik,a})\,\frac{1}{1-u_i}\,, \tag{3.122}$$

or, more conveniently,

$$[\mathrm{d}p_i(\tilde{p}_k;p_a,x)] = \frac{2\tilde{p}_kp_a}{16\pi^2}\,\frac{\mathrm{d}\phi}{2\pi}\,\mathrm{d}x_{ik,a}\,\mathrm{d}u_i\,\Theta(u_i(1-u_i))\,\Theta(x(1-x))\,\delta(x-x_{ik,a})\,. \tag{3.123}$$

The upper limit for the u_i-integration contains a dependence on the spectator mass,

$$u_+ = \frac{1-x_{ik,a}}{1-x_{ik,a}+\mu_k^2}\,. \tag{3.124}$$

- Matrix element:
  Using the factorisation property of the $(m+1)$-parton matrix element

$$|\mathcal{M}_{m+1}|^2 = |\mathcal{M}_m|^2\sum_{ai}\sum_k\frac{1}{2p_ap_i}\,\frac{1}{\mathcal{N}_{ai}^{spec}}\,\frac{1}{x_{ik,a}}\,8\pi\alpha_\mathrm{s}\,\langle\mathbf{V}_k^{ai}(x_{ik,a},u_i)\rangle \tag{3.125}$$

  in the soft and collinear limits and the relation

$$\frac{2\tilde{p}_kp_a}{2p_ap_i} = \frac{1}{u_i} \tag{3.126}$$

  the $(m+1)$-parton fully differential cross section reads

$$\mathrm{d}\hat{\sigma}_{m+1} = \mathrm{d}\hat{\sigma}_m\sum_{ai}\sum_k\frac{\mathrm{d}u_i}{u_i}\,\mathrm{d}x_{ik,a}\,\frac{\mathrm{d}\phi}{2\pi}\,\frac{\alpha_\mathrm{s}}{2\pi}\,\frac{1}{\mathcal{N}_{ai}^{spec}}\,\frac{1}{x_{ik,a}}\,\langle\mathbf{V}_k^{ai}(x_{ik,a},u_i)\rangle\,. \tag{3.127}$$

  The integration range of the variables u_i and $x_{ik,a}$ is $[0,u_+]$ and $[0,1]$, respectively, and $[0,2\pi]$ for ϕ. The Jacobian

$$J(x_{ik,a}) = \frac{1}{x_{ik,a}} \tag{3.128}$$

  for the parton matrix element again is changed in hadronic interactions to include the effect of the PDFs, such that

$$\tilde{J}(x_{ik,a};\mu_F^2) = \frac{1}{x_{ik,a}}\,\frac{f_a(\eta_{ai}/x_{ik,a},\mu_F^2)}{f_{ai}(\eta_{ai},\mu_F^2)}\,, \tag{3.129}$$

  where again, in the implementation here the choice for the factorisation scale is $\mu_F = \mathbf{k}_\perp$, cf. Sec. 3.2.3. Note that the Jacobian takes into account not only a change in Bjørken-x but also a possible flavour change in the process' initial state.

- Sudakov form factor:
  The integration over u_i in Eq. (3.127) can be replaced by an integration over $\mathbf{k}_\perp^2$ according to

$$\frac{\mathrm{d}u_i}{u_i} = \frac{1-u_i}{1-2u_i}\,\frac{\mathrm{d}\mathbf{k}_\perp^2}{\mathbf{k}_\perp^2}\,. \tag{3.130}$$

The arising Jacobian is combined with the function $\tilde{J}(x_{ik,a};\mu_F^2)$ to

$$\tilde{J}(x_{ik,a},u_i;\mu_F^2) = \frac{1-u_i}{1-2u_i}\,\frac{1}{x_{ik,a}}\,\frac{f_a(\eta_{ai}/x_{ik,a},\mu_F^2)}{f_{ai}(\eta_{ai},\mu_F^2)}\,. \tag{3.131}$$

With $\mathbf{k}_\perp^2 > 0$ as the evolution variable and its cut-off being $\mathbf{k}_{\perp,0}^2$ the $x_{ik,a}$ phase-space boundaries are

$$x_{ik,a} \in \left[\frac{\eta_{ai}}{\eta_{\max}}\,,\frac{Q^2}{Q^2+4\mathbf{k}_{\perp,0}^2}\right]\,, \tag{3.132}$$

with $\eta_{\max}$ the maximal allowed Bjørken-x of the PDF. With $\mathbf{k}_\perp^2$ and $x_{ik,a}$ given, u_i can be calculated and yields

$$u_i = \frac{1}{2}\left(1-\sqrt{1-\frac{4\mathbf{k}_\perp^2 x_{ik,a}}{Q^2(1-x_{ik,a})}}\right)\,. \tag{3.133}$$

When $u_i \leq u_+$ an allowed branching is found. Thus the Sudakov form factor for having no emission from an initial-state parton accompanied by a final-state spectator between scales $\mathbf{k}_{\perp,\max}^2$ and $\mathbf{k}_{\perp,0}^2$ can be written down,

$$\begin{aligned}&\Delta_{\mathrm{IF}}(\mathbf{k}_{\perp,\max}^2,\mathbf{k}_{\perp,0}^2)\\ &\quad=\exp\left(-\sum_{ai}\sum_k \frac{1}{\mathcal{N}_{ai}^{spec}}\int_{\mathbf{k}_{\perp,0}^2}^{\mathbf{k}_{\perp,\max}^2}\frac{\mathrm{d}\mathbf{k}_\perp^2}{\mathbf{k}_\perp^2}\int_{x_-}^{x_+}\mathrm{d}x_{ik,a}\frac{\alpha_{\mathrm{s}}(\mathbf{k}_\perp^2/4)}{2\pi}\,\tilde{J}(x_{ik,a},u_i;\mathbf{k}_\perp^2)\langle\mathbf{V}_k^{ai}(x_{ik,a},u_i)\rangle\right)\,.\end{aligned} \tag{3.134}$$

- Physical kinematics:
  The new initial-state particle a remains parallel to the original initial-state parton, and is just rescaled by the splitting variable $x_{ik,a}$ such that

$$p_a = \frac{1}{x_{ik,a}}\,\tilde{p}_{ai}\,. \tag{3.135}$$

The two final-state momenta are most conveniently evaluated in the rest-frame of $Q+p_a$ with p_a pointing along the positive z-axis. The corresponding light-cone momenta read

$$Q+p_a = (M,M,\vec{0}) \quad\text{and}\quad p_a = (2E_a,0,\vec{0})\,. \tag{3.136}$$

Note that the massless vector p_a only has a light-cone +-component, given by twice the energy of the parton. For p_i and p_k the ansatz

$$p_i = (l_\perp\,e^y, l_\perp\,e^{-y},\vec{l}_\perp)\,,\quad p_k = (m_{k,\perp}\,e^z, m_{k,\perp}\,e^{-z},-\vec{l}_\perp)\,, \tag{3.137}$$

is used, with $m_\perp$ being the transverse mass. Besides the energy- and momentum--conservation requirement the momenta are constrained by the splitting variables,

$$u_i = \frac{p_i p_a}{(p_i + p_k) p_a} = \frac{l_\perp e^{-y}}{M} . \tag{3.138}$$

yielding

$$\vec{l}_\perp^{\,2} = (M^2 - m_k^2) u_i - M^2 u_i^2 , \tag{3.139}$$

for the transverse momentum squared. This equals the physical transverse momentum squared of parton i, $\mathbf{k}_\perp^2$. Employing the relations

$$\cosh y = \frac{M^2 - m_k^2}{2 M l_\perp} , \quad \sinh y = \frac{1}{2} \left(\frac{l_\perp}{M u_i} - \frac{M u_i}{l_\perp} \right) , \tag{3.140}$$

$$\cosh z = \frac{M^2 + m_k^2}{2 M m_{k,\perp}} , \quad \sinh z = \frac{1}{2} \left(\frac{m_{k,\perp}}{M(1-u_i)} - \frac{M(1-u_i)}{m_{k,\perp}} \right) , \tag{3.141}$$

the four-momenta of the final-state partons, in the frame specified above, read

$$p_i = (l_\perp \cosh y, l_\perp \cos\phi, l_\perp \sin\phi, l_\perp \sinh y) , \tag{3.142}$$

$$p_k = (m_{k,\perp} \cosh z, -l_\perp \cos\phi, -l_\perp \sin\phi, m_{k,\perp} \sinh z) . \tag{3.143}$$

Again, ϕ has been uniformly distributed in the transverse plane. The kinematics is completed by rotating and boosting the momenta p_a, p_i and p_k back in the laboratory frame.

Massless case

The massless limit of the scenario above, initial-state splittings accompanied by final-state spectators, $\{\widetilde{ai}, \tilde{k}\} \to \{a, i, k\}$, corresponds to neglecting the spectator mass, $\tilde{p}_k^2 = p_k^2 = 0$. Apart from that, the splitting variables remain unchanged and the dependence on m_k, of course, disappears in the corresponding phase-space boundaries.

Dropping the explicit mass terms present in $\langle \mathbf{V}_k^{\mathrm{q}_a \mathrm{q}_i}(x_{ik,a}) \rangle$ and $\langle \mathbf{V}_k^{\mathrm{g}_a \mathrm{g}_i}(x_{ik,a}, u_i) \rangle$ given in Eqs. (3.118) and (3.119), respectively, the factorised form of the fully differential cross section can completely be taken over.

Neglecting the finite spectator masses the splitting kinematics is significantly simplified. In the emitter–spectator Breit-frame

$$p_a = \frac{1}{x_{ik,a}} \tilde{p}_{ai} , \tag{3.144}$$

$$p_i = (1 - u_i) \frac{1 - x_{ik,a}}{x_{ik,a}} \tilde{p}_{ai} + u_i \tilde{p}_k + k_\perp , \tag{3.145}$$

$$p_k = u_i \frac{1 - x_{ik,a}}{x_{ik,a}} \tilde{p}_{ai} + (1 - u_i) \tilde{p}_k - k_\perp , \tag{3.146}$$

with $k_\perp$ perpendicular to both the emitter and the spectator.

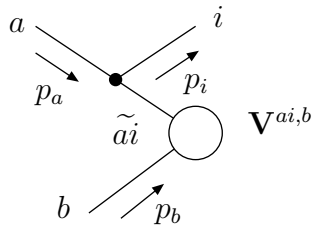

Figure 3.4: Schematical view of the splitting of an initial-state parton with an initial-state parton as spectator. The blob denotes the m-parton matrix element. Incoming and outgoing lines label the initial- and final-state partons, respectively.

3.3.4 Initial-state emitter and initial-state spectator

The last scenario to be studied is the splitting of an initial-state particle $\widetilde{ai}$, with the spectator b being an initial-state parton as well, cf. Fig. 3.4. This type of branching occurs when considering hadron-hadron collisions, where both the initial-state particles are colour charged and therefore can be colour connected. The simplest example for this configuration is the lowest order Drell-Yan process, where both the incoming quark and anti-quark can serve as emitter and spectator.
In contrast to all other cases discussed before, as the new incoming particles shall finally be aligned with the beam axes, it turns out to be convenient to preserve the spectator momentum p_b in this branching. Since also the emitter momentum remains parallel to p_a,

$$\tilde{p}_{ai} = x_{i,ab}\, p_a\,, \quad \text{with} \quad x_{i,ab} = \frac{p_a p_b - p_i p_a - p_i p_b}{p_a p_b}\,, \tag{3.147}$$

the transverse momentum of the emitted parton, p_i, has to be balanced by *all* other final-state momenta k_j. This does not only include the QCD partons, but all non-QCD particles, *e.g.* leptons, as well.

- Kinematics:
  Defining the variable

  $$\tilde{v}_i = \frac{p_i p_a}{p_a p_b} \tag{3.148}$$

  the transverse momentum squared of parton i is given by

  $$\mathbf{k}_\perp^2 = 2\tilde{p}_{ai} p_b\, \tilde{v}_i\, \frac{1 - x_{i,ab} - \tilde{v}_i}{x_{i,ab}}\,. \tag{3.149}$$

  The four-momenta of the m-parton ensemble fulfil

  $$\tilde{p}_{ai} + p_b - \sum_{j=1}^{m} \tilde{k}_j = 0\,, \tag{3.150}$$

correspondingly the full set of $m+1$ particles has to satisfy

$$p_a + p_b - \sum_{j=1}^{m} k_j - p_i = 0\,. \tag{3.151}$$

- Splitting kernels:
  The polarisation-averaged splitting kernels $\langle \mathbf{V}^{ai,b} \rangle$ depend on $x_{i,ab}$ only and read

$$\langle \mathbf{V}^{\mathrm{q_a g_i},b}(x_{i,ab}) \rangle = C_\mathrm{F} \left\{ \frac{2}{1-x_{i,ab}} - (1+x_{i,ab}) \right\}, \tag{3.152}$$

$$\langle \mathbf{V}^{\mathrm{q_a q_i},b}(x_{i,ab}) \rangle = C_\mathrm{F} \left\{ x_{i,ab} + 2\frac{1-x_{i,ab}}{x_{i,ab}} \right\}, \tag{3.153}$$

$$\langle \mathbf{V}^{\mathrm{g_a g_i},b}(x_{i,ab}) \rangle = 2C_\mathrm{A} \left\{ \frac{1}{1-x_{i,ab}} + \frac{1-x_{i,ab}}{x_{i,ab}} - 1 + x_{i,ab}(1-x_{i,ab}) \right\}, \tag{3.154}$$

$$\langle \mathbf{V}^{\mathrm{g_a q_i},b}(x_{i,ab}) \rangle = T_\mathrm{R} \left\{ 1 - 2x_{i,ab}(1-x_{i,ab}) \right\}. \tag{3.155}$$

- Phase space:
  The final-state phase space can be written as follows [98]

$$\mathrm{d}\Phi(p_i, k_1, \ldots; p_a + p_b) = \int_0^1 \mathrm{d}x\, \mathrm{d}\Phi(\tilde{k}_1, \ldots; x p_a + p_b)\, [\mathrm{d}p_i(p_a, p_b, x)]\,, \tag{3.156}$$

  with

$$[\mathrm{d}p_i(p_a, p_b, x)] = \frac{2p_a p_b}{16\pi^2}\, \frac{\mathrm{d}\phi}{2\pi}\, \mathrm{d}x_{i,ab}\, \mathrm{d}\tilde{v}_i\, \Theta(x(1-x))\, \Theta(\tilde{v}_i)\, \Theta\left(1 - \frac{\tilde{v}_i}{1-x}\right)\, \delta(x - x_{i,ab})\,, \tag{3.157}$$

  where ϕ is the polar angle in the plane perpendicular to p_a and p_b.

- Matrix element:
  Combining this with the expression for the $(m+1)$-parton matrix element

$$|\mathcal{M}_{m+1}|^2 = |\mathcal{M}_m|^2 \sum_{ai} \sum_{b \neq ai} \frac{1}{2p_a p_i}\, \frac{1}{\mathcal{N}_{ai}^{spec}}\, \frac{1}{x_{i,ab}}\, 8\pi\alpha_\mathrm{s}\, \langle \mathbf{V}^{ai,b}(x_{i,ab}) \rangle\,, \tag{3.158}$$

  the differential cross section becomes

$$\mathrm{d}\hat{\sigma}_{m+1} = \mathrm{d}\hat{\sigma}_m \sum_{ai} \sum_{b \neq ai} \frac{\mathrm{d}\tilde{v}_i}{\tilde{v}_i}\, \mathrm{d}x_{i,ab}\, \frac{\mathrm{d}\phi}{2\pi}\, \frac{\alpha_\mathrm{s}}{2\pi}\, \frac{1}{\mathcal{N}_{ai}^{spec}}\, \frac{1}{x_{i,ab}}\, \langle \mathbf{V}^{ai,b}(x_{i,ab}) \rangle\,, \tag{3.159}$$

  where $1 - x_{i,ab} - \tilde{v}_i > 0$ has to hold. The Jacobian can be read off as

$$J(x_{i,ab}) = \frac{1}{x_{i,ab}}\,, \tag{3.160}$$

  or, including again the PDFs,

$$\tilde{J}(x_{i,ab}; \mu_F^2) = \frac{1}{x_{i,ab}}\, \frac{f_a(\eta_{ai}/x_{i,ab}, \mu_F^2)}{f_{ai}(\eta_{ai}, \mu_F^2)}\,. \tag{3.161}$$

- Sudakov form factor:

  Regarding the transverse momentum given by Eq. (3.149) the identity

$$\frac{\mathrm{d}\tilde{v}_i}{\tilde{v}_i} = \frac{1-x_{i,ab}-\tilde{v}_i}{1-x_{i,ab}-2\tilde{v}_i}\frac{\mathrm{d}\mathbf{k}_\perp^2}{\mathbf{k}_\perp^2}\,, \tag{3.162}$$

  can be employed to replace the $\tilde{v}_i$ integration with a $\mathbf{k}_\perp^2$-integral. The resulting Jacobian, combined with $\tilde{J}(x_{i,ab};\mu_F^2)$, amounts to

$$\tilde{J}(x_{i,ab},\tilde{v}_i;\mu_F^2) = \frac{1-x_{i,ab}-\tilde{v}_i}{1-x_{i,ab}-2\tilde{v}_i}\,\frac{1}{x_{i,ab}}\,\frac{f_a(\eta_{ai}/x_{i,ab},\mu_F^2)}{f_{ai}(\eta_{ai},\mu_F^2)}\,. \tag{3.163}$$

  When evolving in $\mathbf{k}_\perp^2$ the dependence of the $x_{i,ab}$-integration boundaries on the cut-off $\mathbf{k}_{\perp,0}^2$ read

$$x_{i,ab} \in \left[\frac{\eta_{ai}}{\eta_{\max}}\,,\frac{2\tilde{p}_a p_b}{2\tilde{p}_a p_b + 4\mathbf{k}_{\perp,0}^2}\right]\,. \tag{3.164}$$

  $\tilde{v}_i$ can be calculated from $\mathbf{k}_\perp^2$ and $x_{i,ab}$,

$$\tilde{v}_i = \frac{1-x_{i,ab}}{2}\left(1-\sqrt{1-\frac{2\mathbf{k}_\perp^2 x_{i,ab}}{\tilde{p}_a p_b(1-x_{i,ab})^2}}\right)\,. \tag{3.165}$$

  The Sudakov form factor then reads

$$\begin{aligned}&\Delta_{\mathrm{II}}(\mathbf{k}_{\perp,\max}^2,\mathbf{k}_{\perp,0}^2)\\ &\quad= \exp\left(-\sum_{ai}\sum_{b\neq ai}\frac{1}{\mathcal{N}_{ai}^{spec}}\int\limits_{\mathbf{k}_{\perp,0}^2}^{\mathbf{k}_{\perp,\max}^2}\frac{\mathrm{d}\mathbf{k}_\perp^2}{\mathbf{k}_\perp^2}\int\limits_{x_-}^{x_+}\mathrm{d}x_{i,ab}\frac{\alpha_{\mathrm{s}}(\mathbf{k}_\perp^2/4)}{2\pi}\tilde{J}(x_{i,ab},\tilde{v}_i;\mathbf{k}_\perp^2)\langle\mathbf{V}^{ai,b}(x_{i,ab})\rangle\right)\,.\end{aligned} \tag{3.166}$$

- Physical kinematics:

  The momenta of the $(m+1)$-parton ensemble, expressed through the emitter and spectator momentum and the momenta of all other final-state particles of the m-parton process, read

$$p_a = \frac{1}{x_{i,ab}}\,\tilde{p}_{ai}\,, \tag{3.167}$$

$$p_i = \frac{1-x_{i,ab}-\tilde{v}_i}{x_{i,ab}}\,\tilde{p}_{ai} + \tilde{v}_i\,p_b + k_\perp\,, \tag{3.168}$$

$$k_j = \Lambda(\tilde{p}_{ai}+p_b, p_a+p_b-p_i)\,\tilde{k}_j\,, \tag{3.169}$$

  with $k_\perp/\sqrt{\mathbf{k}_\perp^2}$ uniformly distributed in the transverse plane and $\Lambda(\tilde{p}_{ai}+p_b, p_a+p_b-p_i) = \Lambda(\tilde{K},K)$ being a proper Lorentz transformation given by

$$\Lambda^\mu{}_\nu(\tilde{K},K) = g^\mu{}_\nu - \frac{2\,(\tilde{K}+K)^\mu\,(\tilde{K}+K)_\nu}{(\tilde{K}+K)^2} + \frac{2\,K^\mu\tilde{K}_\nu}{\tilde{K}^2}\,. \tag{3.170}$$

  Accordingly, the full set of final-state momenta compensates for the transverse momentum of p_i, although they do not participate in the splitting.

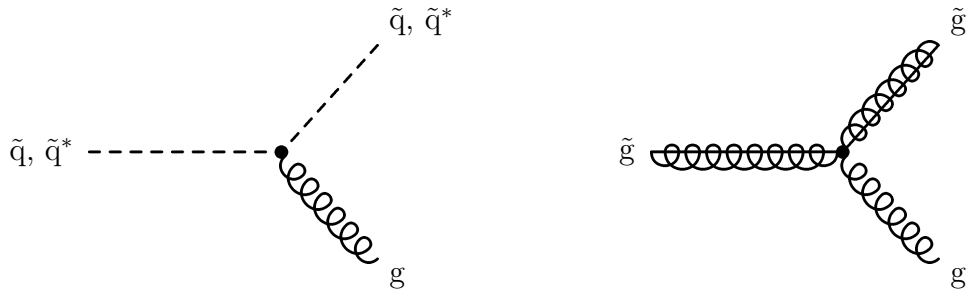

Figure 3.5: The SUSY QCD vertices corresponding to gluon emission off (anti-)squarks and gluinos.

3.3.5 SUSY QCD splitting functions

In the minimal supersymmetric extension of the Standard Model the sector of strongly interacting particles is extended by the superpartners of the ordinary quark- and gluon-fields [123]. The new particles participating in the strong interaction are the scalar-quarks, called squarks and the gluino. While the former are colour-triplets the gluino is a Majorana fermion in the adjoint representation, a colour-octet.

In order to be consistent with todays experimental (non-)observations the assumed SUSY particles have to be rather heavy. This renders the massless limit for these fields not applicable when describing their QCD interactions at the energies of the forthcoming colliders. Based on that argument it is beyond the present scope to describe possible branchings like $g \to \tilde{q}\tilde{q}^*$, $g \to \tilde{g}\tilde{g}$ in a quasi-collinear limit. Rather, they are appropriately described using exact matrix-element methods, as discussed in chapter 4 or Ref. [130, 131].

Since the spin and the flavour of the spectator parton do not enter the splitting functions, the branchings of the Standard Model particles are not altered in supersymmetric extensions. The only SUSY QCD splittings that appear to be relevant in the context of a parton-shower formulation are related to the emission of a gluon off a squark or anti-squark and off a gluino, cf. Fig. 3.5. Further, assuming that supersymmetric particles do not appear as partonic initial states those are solely final-state splittings. The associated spectator, however, can be either in the final state or in the initial state.

Due to its fermionic nature the splitting functions involving gluinos are equal to the corresponding splittings of massive quarks, cf. Eq. (3.37) and Eq. (3.86), only the colour factors have to be adapted from C_F to C_A.

The kernel of the branching $\tilde{q} \to \tilde{q}g$ with the spectator also in the final state reads

$$\langle \mathbf{V}_{\tilde{\mathrm{q}}_i \mathrm{g}_j, k}(\tilde{z}_i, y_{ij,k}) \rangle = C_{\mathrm{F}} \left\{ \frac{2}{1 - \tilde{z}_i + \tilde{z}_i y_{ij,k}} - \frac{\tilde{v}_{ij,k}}{v_{ij,k}} \left(2 + \frac{m_i^2}{p_i p_j} \right) \right\} , \tag{3.171}$$

where all the variables have been defined in Sec. 3.3.1. If the spectator is in the initial state

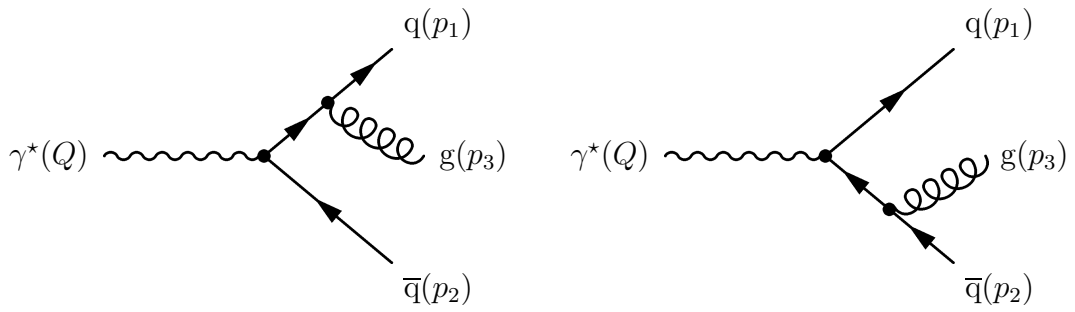

Figure 3.6: The two first order α_s Feynman diagrams contributing to $\gamma^\star \to q\overline{q}g$.

this becomes

$$\langle \mathbf{V}^a_{\tilde{q}_i g_j}(\tilde{z}_i, x_{ij,a}) \rangle = C_F \left\{ \frac{2}{1-\tilde{z}_i+(1-x_{ij,a})} - 2 - \frac{m_i^2}{p_i p_j} \right\} , \tag{3.172}$$

for the definitions of the variables used see Sec. 3.3.2.
Apart from the splitting kernels all the results derived in the corresponding sections describing the branchings of massive final-state partons with spectators in the final- or initial state can be taken over without any alteration. This includes the exact phase-space factorisation as well as the parton kinematics defined there.

3.4 Comparing the hardest emission with matrix elements

In the following, the predictions for the hardest (first) emission of the parton shower algorithm will be worked out for different processes and compared with corresponding exact tree-level matrix-element calculations. The set of processes to be considered covers three-jet production in e^+e^- collisions, cf. Sec. 3.4.1, the first order real correction process to DIS, cf. Sec. 3.4.2, and the production of a weak gauge boson accompanied by a light jet at hadron colliders, cf. Sec. 3.4.3. These three examples constitute a full set of generic processes to reliably test the first emission of the proposed parton-shower approach.

3.4.1 Three-jet production at lepton-colliders

In this example the production of three jets at a lepton-collider is investigated. Jet production proceeds via the s-channel exchange of a colour-singlet particle, namely a $\gamma^\star$ or Z^0-boson. The latter will be ignored in the discussion here. At first perturbative order in α_s, two Feynman diagrams contribute to the matrix element $\gamma^\star \to q\overline{q}g$, corresponding to the emission of a gluon from either the final-state quark or the anti-quark, cf. Fig. 3.6.

For convenience, the centre-of mass energy

$$E_{\text{c.m.}} \equiv \sqrt{Q^2} , \tag{3.173}$$

and the momentum fractions

$$x_i \equiv \frac{2p_iQ}{Q^2}\,. \tag{3.174}$$

are introduced. Neglecting the masses of the final-state particles the Lorentz-invariant Mandelstam variables for the $1 \to 3$ process become

$$\hat{s} \equiv (p_1+p_3)^2 = 2p_1p_3 = Q^2(1-x_2)\,, \tag{3.175}$$

$$\hat{t} \equiv (p_2+p_3)^2 = 2p_2p_3 = Q^2(1-x_1)\,, \tag{3.176}$$

$$\hat{u} \equiv (p_1+p_2)^2 = 2p_1p_2 = Q^2(1-x_3)\,. \tag{3.177}$$

Energy-momentum conservation implies that

$$x_1+x_2+x_3 = 2 \quad \text{and} \quad \hat{s}+\hat{t}+\hat{u} = Q^2\,. \tag{3.178}$$

The partonic differential decay rate with respect to the quark and anti-quark momentum fractions $x_{1,2}$ reads

$$\left.\frac{\mathrm{d}\hat{\Gamma}}{\mathrm{d}x_1\mathrm{d}x_2}\right|_{\mathrm{ME}} = \hat{\Gamma}_0\,\frac{\alpha_\mathrm{s}}{2\pi}\,C_\mathrm{F}\left[\frac{x_1^2+x_2^2}{(1-x_1)(1-x_2)}\right]\,, \tag{3.179}$$

where $\hat{\Gamma}_0$ denotes the total decay rate for $\gamma^\star \to \mathrm{q}\overline{\mathrm{q}}$,

$$\hat{\Gamma}_0 = 2\alpha_\mathrm{qed}e_\mathrm{q}^2E_\mathrm{c.m.}\,, \tag{3.180}$$

see for instance [132].

In the parton-shower approach, two contributions occur as well. They correspond to the timelike splitting of either the quark or the anti-quark, and the total result is just the incoherent sum of the two pieces. To work this out, consider the case of the quark splitting with the anti-quark being the spectator parton. Then, the shower variables are, cf. Sec. 3.3.1,

$$y_{13,2} = \frac{p_1p_3}{p_1p_3+p_1p_2+p_2p_3} = \frac{\hat{s}}{\hat{s}+\hat{u}+\hat{t}} = \frac{\hat{s}}{Q^2}\,, \tag{3.181}$$

$$\tilde{z}_1 = \frac{p_1p_2}{p_1p_2+p_3p_2} = \frac{\hat{u}}{\hat{u}+\hat{t}}\,, \tag{3.182}$$

which, expressed in terms of the x_i, translate into

$$y_{13,2} = 1-x_2 \quad \text{and} \quad \tilde{z}_1 = \frac{1-x_3}{x_2} = 1-\frac{1-x_1}{x_2}\,. \tag{3.183}$$

Accordingly, the decay rate for the emission off the quark can be cast into the form

$$\left.\frac{\mathrm{d}\hat{\Gamma}}{\mathrm{d}x_1\mathrm{d}x_2}\right|_{\mathrm{PSq}} = \hat{\Gamma}_0\,\frac{\alpha_\mathrm{s}}{2\pi}\,C_\mathrm{F}\left[\frac{1}{1-x_2}\left(\frac{2}{2-x_1-x_2}-(1+x_1)\right)+\frac{1-x_1}{x_2}\right]\,. \tag{3.184}$$

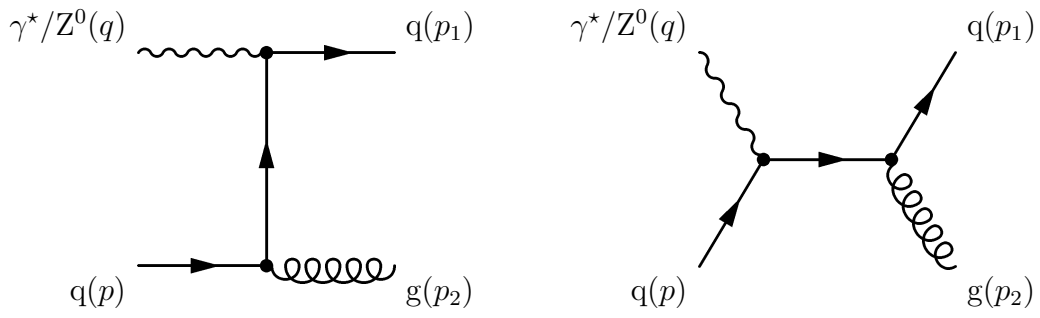

Figure 3.7: The two leading-order Feynman diagrams contributing to $\gamma^\star \mathrm{q} \to \mathrm{qg}$.

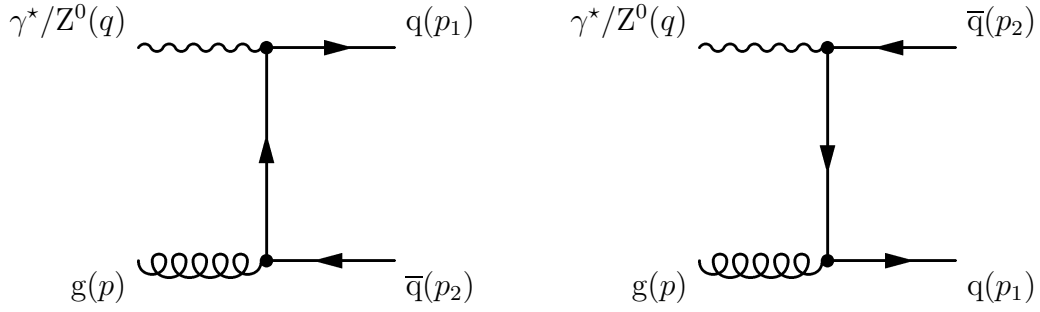

Figure 3.8: The two possible Feynman diagrams for $\gamma^\star \mathrm{g} \to \mathrm{q}\overline{\mathrm{q}}$.

The result for the emission of a gluon off the anti-quark can be obtained from Eq. (3.184) by $1 \leftrightarrow 2$. Taken together, the parton shower decay rate yields

$$\begin{aligned} \left.\frac{\mathrm{d}\hat{\Gamma}}{\mathrm{d}x_1\mathrm{d}x_2}\right|_{\mathrm{PS}} &= \left.\frac{\mathrm{d}\hat{\Gamma}}{\mathrm{d}x_1\mathrm{d}x_2}\right|_{\mathrm{PSq}} + \left.\frac{\mathrm{d}\hat{\Gamma}}{\mathrm{d}x_1\mathrm{d}x_2}\right|_{\mathrm{PS}\overline{\mathrm{q}}} \\ &= \hat{\Gamma}_0 \frac{\alpha_\mathrm{s}}{2\pi} C_\mathrm{F} \left[\frac{x_1^2 + x_2^2}{(1-x_1)(1-x_2)} + \frac{1-x_1}{x_2} + \frac{1-x_2}{x_1}\right] . \end{aligned} \tag{3.185}$$

Obviously, the parton-shower reproduces the matrix-element calculation in both the soft and the collinear limit. The only difference between the two results are two non-singular terms in the parton shower result that vanish as $x_{1,2} \to 1$.

3.4.2 Real corrections to leading-order DIS

The simplest physical process involving initial-state hadrons is deep-inelastic lepton-nucleon scattering (DIS), *i.e.* $e^\pm p \to e^\pm + X$. At leading order, two partonic processes contribute, namely $e^\pm \mathrm{q} \to e^\pm \mathrm{q}$ and $e^\pm \overline{\mathrm{q}} \to e^\pm \overline{\mathrm{q}}$, both of which must be convoluted with the initial hadron's PDF to obtain the hadronic cross section. The interaction is mediated by virtual-photon and Z^0-boson exchange. In the following, however, only the $\gamma^\star$ channel is taken into account, for which the two partonic cross sections are equal.

At next-to-leading-order the quark can radiate a gluon before or after its interaction with the virtual photon, cf. Fig. 3.7. Beyond this, at NLO the incoming quark may originate from a gluon in the initial hadron that produces a quark–anti-quark pair which the $\gamma^\star$ then couples to, cf. Fig. 3.8. The real emission matrix elements can be expressed through the kinematic variables

$$Q^2 = -q^2\,, \quad x = \frac{Q^2}{2pq}, \quad z_i = \frac{p_i p}{pq}\,, \tag{3.186}$$

where q denotes the four-momentum of the off-shell photon, p the incoming parton momentum and the p_i label the momenta of the final-state partons. The Mandelstam variables for the $2 \to 2$ processes $\gamma^\star(q)\mathrm{q}(p) \to \mathrm{q}(p_1)\mathrm{g}(p_2)$ and $\gamma^\star(q)\mathrm{g}(p) \to \mathrm{q}(p_1)\overline{\mathrm{q}}(p_2)$ are

$$\hat{s} \equiv (q+p)^2 = 2pq - Q^2 = Q^2\,\frac{1-x}{x}\,, \tag{3.187}$$

$$\hat{t} \equiv (p_1 - q)^2 = -2p_1 q - Q^2 = -Q^2\,\frac{1-z_1}{x}\,, \tag{3.188}$$

$$\hat{u} \equiv (p_2 - q)^2 = -2p_2 q - Q^2 = -Q^2\,\frac{1-z_2}{x}\,. \tag{3.189}$$

Momentum conservation implies that $q + p = p_1 + p_2$ and

$$\hat{s} + \hat{t} + \hat{u} + Q^2 = 0\,. \tag{3.190}$$

In the following, the two real emission processes will be discussed in detail.

The gluon emission process

The matrix element of the gluon emission channel $\gamma^\star(q)\mathrm{q}(p) \to \mathrm{q}(p_1)\mathrm{g}(p_2)$ reads [97, 132]

$$|\mathcal{M}_{2,\mathrm{q}}(p_1,p_2;p)|^2_{\mathrm{ME}} = \frac{8\pi\alpha_\mathrm{s}}{Q^2} C_\mathrm{F} \left[\frac{x^2+z_1^2}{(1-x)(1-z_1)} + 2(1-3xz_1)\right] \cdot |\mathcal{M}_{1,\mathrm{q}}(q+xp;xp)|^2\,, \tag{3.191}$$

with $\mathcal{M}_{1,\mathrm{q}}(q+p;p)$ the matrix element of the lowest order process.
In the parton-shower approach two contributions to this final state emerge. First, the emission of the gluon from the initial-state quark with the final-state parton serving as spectator (IF) has to be considered. Second, the initial-state parton acts as the spectator of the final-state splitting $\mathrm{q} \to \mathrm{qg}$ (FI).

- IF:
  The "parton-shower"-matrix element of the initial-state splitting with final-state spectator is obtained from Eq. (3.125) and is given by

$$|\mathcal{M}_{2,\mathrm{q}}(p_1,p_2;p)|^2_{\mathrm{PSif}} = \frac{1}{2pp_2}\,\frac{1}{x_{21,p}}\,8\pi\alpha_\mathrm{s}\,C_\mathrm{F} \left[\frac{2}{1-x_{21,p}+u_2} - (1+x_{21,p})\right] \cdot |\mathcal{M}_{1,\mathrm{q}}(q+xp;xp)|^2\,, \tag{3.192}$$

where the appropriate splitting function, Eq. (3.117) with $\mu_k^2 = 0$, has been inserted. Employing the identities

$$x_{21,p} = \frac{p_1p + p_2p - p_2p_1}{p_1p + p_2p} = \frac{\hat{u} + \hat{t} + \hat{s}}{\hat{u} + \hat{t}} = \frac{Q^2}{\hat{s} + Q^2} = x\,, \tag{3.193}$$

$$u_2 = \frac{p_2p}{p_2p + p_1p} = \frac{\hat{t}}{\hat{u} + \hat{t}} = z_2 = 1 - z_1\,, \tag{3.194}$$

$$\frac{1}{2pp_2x} = \frac{1}{Q^2pp_2/pq} = \frac{1}{Q^2(1 - z_1)}\,, \tag{3.195}$$

the expression above becomes

$$|\mathcal{M}_{2,\mathrm{q}}(p_1, p_2; p)|^2_{\mathrm{PSif}} = \frac{8\pi\alpha_\mathrm{s}}{Q^2(1 - z_1)}\, C_\mathrm{F} \left[\frac{2}{2 - x - z_1} - (1 + x)\right] \cdot |\mathcal{M}_{1,\mathrm{q}}(q + xp; xp)|^2\,. \tag{3.196}$$

- FI:
  In full analogy the shower expression for the final-state emission process yields

$$|\mathcal{M}_{2,\mathrm{q}}(p_1, p_2; p)|^2_{\mathrm{PSfi}} = \frac{1}{2p_1p_2}\,\frac{1}{x_{12,p}}\, 8\pi\alpha_\mathrm{s}\, C_\mathrm{F} \left[\frac{2}{1 - \tilde{z}_1 + (1 - x_{12,p})} - (1 + \tilde{z}_1)\right] \cdot |\mathcal{M}_{1,\mathrm{q}}(q + xp; xp)|^2\,.$$

  With

$$x_{12,p} = \frac{p_1p + p_2p - p_1p_2}{p_1p + p_2p} = x \quad \text{and} \quad \tilde{z}_1 = \frac{p_1p}{p_1p + p_2p} = z_1\,, \tag{3.197}$$

  this can be cast into the form

$$|\mathcal{M}_{2,\mathrm{q}}(p_1, p_2; p)|^2_{\mathrm{PSfi}} = \frac{8\pi\alpha_\mathrm{s}}{Q^2(1 - x)}\, C_\mathrm{F} \left[\frac{2}{2 - x - z_1} - (1 + z_1)\right] \cdot |\mathcal{M}_{1,\mathrm{q}}(q + xp; xp)|^2\,, \tag{3.198}$$

  where in addition

$$2p_1p_2 = Q^2\frac{1 - x}{x} \tag{3.199}$$

  has been employed.

Combining the two parton-shower contributions yields the final result, namely

$$\begin{aligned} |\mathcal{M}_{2,\mathrm{q}}(p_1, p_2; p)|^2_{\mathrm{PS}} &= |\mathcal{M}_{2,\mathrm{q}}(p_1, p_2; p)|^2_{\mathrm{PSif}} + |\mathcal{M}_{2,\mathrm{q}}(p_1, p_2; p)|^2_{\mathrm{PSfi}} \\ &= \frac{8\pi\alpha_\mathrm{s}}{Q^2}\, C_\mathrm{F} \left[\frac{x^2 + z_1^2}{(1 - x)(1 - z_1)}\right] \cdot |\mathcal{M}_{1,\mathrm{q}}(q + xp; xp)|^2\,. \end{aligned} \tag{3.200}$$

When comparing this with the exact perturbative result of Eq. (3.191), it can be inferred that the parton shower exactly reproduces the soft and collinear singular structure of the matrix element as $z_1 \to 1$ or $x \to 1$. The only difference is an additional finite non-singular term present in the exact result.

The initial-state gluon channel

Expressed in terms of the leading-order matrix element the exact real emission next-to-leading-order result for the process $\gamma^\star(q)\mathrm{g}(p) \to \mathrm{q}(p_1)\overline{\mathrm{q}}(p_2)$ reads [97, 132]

$$\begin{aligned}&|\mathcal{M}_{2,\mathrm{g}}(p_1,p_2;p)|^2_{\mathrm{ME}}\\ &\quad= \frac{8\pi\alpha_\mathrm{s}}{Q^2}\,T_\mathrm{R}\left[\frac{(z_1^2+(1-z_1)^2)(x^2+(1-x)^2)}{z_1(1-z_1)}+8x(1-x)\right]\cdot|\mathcal{M}_{1,\mathrm{q}}(q+xp;xp)|^2\ .\end{aligned} \tag{3.201}$$

Starting from the leading-order matrix element $\gamma^\star(q)\mathrm{q}(p) \to \mathrm{q}(p_1)$ there is only one possibility in the parton shower to reach the $2 \to 2$ process, the splitting of an initial-state gluon into $\mathrm{q}\overline{\mathrm{q}}$ and the q interacting with the off-shell photon. The second matrix-element diagram, corresponding to the interaction of the anti-quark with the $\gamma^\star$, here has no parton-shower counterpart. However, when starting the shower from the charge conjugated leading-order process, namely $\gamma^\star(q)\overline{\mathrm{q}}(p) \to \overline{\mathrm{q}}(p_1)$, this contribution will occur while the $\gamma^\star\mathrm{q}$ interaction will be missing instead. The two terms are evaluated separately and then added incoherently.

- Emission off the quark:
  The case of an internal quark propagator is discussed first. According to Eqs. (3.125) and (3.120) the parton-shower approximation to the matrix element reads

$$\begin{aligned}&|\mathcal{M}_{2,\mathrm{g}}(p_1,p_2;p)|^2_{\mathrm{PSq}}\\ &\quad= \frac{1}{2pp_2}\,\frac{1}{x_{21,p}}\,8\pi\alpha_\mathrm{s}\,T_\mathrm{R}\,[1-2x_{21,p}(1-x_{21,p})]\cdot|\mathcal{M}_{1,\mathrm{q}}(q+xp;xp)|^2\\ &\quad= \frac{8\pi\alpha_\mathrm{s}}{Q^2(1-z_1)}\,T_\mathrm{R}\,[1-2x(1-x)]\cdot|\mathcal{M}_{1,\mathrm{q}}(q+xp;xp)|^2\ .\end{aligned} \tag{3.202}$$

- Emission off the anti-quark:
  Starting instead the shower from the $\overline{\mathrm{q}}$ initiated process, and emitting the quark into the final state yields, correspondingly,

$$\begin{aligned}&|\mathcal{M}_{2,\mathrm{g}}(p_1,p_2;p)|^2_{\mathrm{PS}\overline{\mathrm{q}}}\\ &\quad= \frac{1}{2pp_1}\,\frac{1}{x_{12,p}}\,8\pi\alpha_\mathrm{s}\,T_\mathrm{R}\,[1-2x_{12,p}(1-x_{12,p})]\cdot|\mathcal{M}_{1,\overline{\mathrm{q}}}(q+xp;xp)|^2\\ &\quad= \frac{8\pi\alpha_\mathrm{s}}{Q^2 z_1}\,T_\mathrm{R}\,[1-2x(1-x)]\cdot|\mathcal{M}_{1,\overline{\mathrm{q}}}(q+xp;xp)|^2\ .\end{aligned} \tag{3.203}$$

Due to the charge conjugation invariance of the leading-order matrix element,

$$|\mathcal{M}_{1,\overline{\mathrm{q}}}(q+xp;xp)|^2 = |\mathcal{M}_{1,\mathrm{q}}(q+xp;xp)|^2\ , \tag{3.204}$$

the two parton-shower contributions can directly be combined and yield

$$\begin{aligned}|\mathcal{M}_{2,\mathrm{g}}(p_1,p_2;p)|^2_{\mathrm{PS}} &= |\mathcal{M}_{2,\mathrm{g}}(p_1,p_2;p)|^2_{\mathrm{PSq}}+|\mathcal{M}_{2,\mathrm{g}}(p_1,p_2;p)|^2_{\mathrm{PS}\overline{\mathrm{q}}}\\ &= \frac{8\pi\alpha_\mathrm{s}}{Q^2}\,T_\mathrm{R}\left[\frac{x^2+(1-x)^2}{z_1(1-z_1)}\right]\cdot|\mathcal{M}_{1,\mathrm{q}}(q+xp;xp)|^2\ .\end{aligned} \tag{3.205}$$

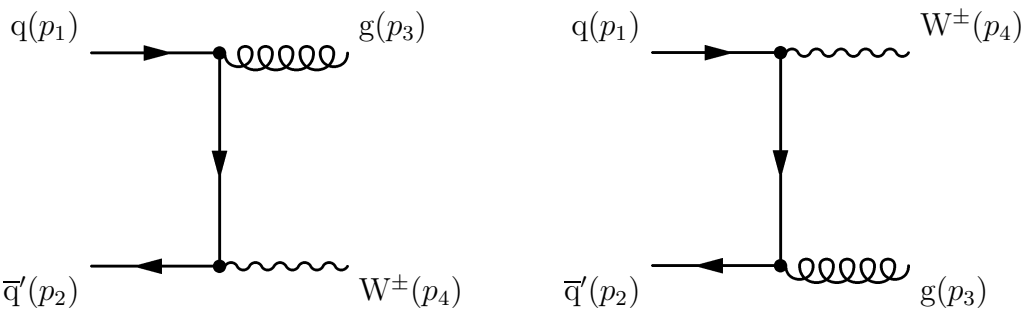

Figure 3.9: The leading-order Feynman diagrams contributing to the process $\text{q}\overline{\text{q}}' \to \text{W}^\pm\text{g}$.

Again the parton shower matches the soft and collinear behaviour of the matrix element given in Eq. (3.201) and reproduces the exact result up to non-singular terms.

3.4.3 Associated production of a weak gauge boson and a light parton

The lowest order production process of weak gauge bosons ($\text{W}^\pm$, Z^0, $\gamma^\star$) at a hadron collider proceeds via the s-channel fusion of two initial-state quarks. Without losing generality $\text{W}^\pm$ boson production will be investigated in the following. The leading-order process then simply reads $\text{q}\overline{\text{q}}' \to \text{W}^\pm$. At order α_s there are three processes emerging: $\text{q}\overline{\text{q}}' \to \text{W}^\pm\text{g}$, $\text{g}\overline{\text{q}}' \to \text{W}^\pm\overline{\text{q}}$ and $\text{qg} \to \text{W}^\pm\text{q}'$. Considering on-shell $\text{W}^\pm$ bosons for simplicity[5], only $2 \to 2$ processes have to be discussed, which can be described using the Mandelstam variables

$$\hat{s} \equiv (p_1 + p_2)^2 = 2p_1p_2\,, \tag{3.206}$$

$$\hat{t} \equiv (p_1 - p_3)^2 = -2p_1p_3\,, \tag{3.207}$$

$$\hat{u} \equiv (p_2 - p_3)^2 = -2p_2p_3\,. \tag{3.208}$$

Momentum conservation then implies that

$$\hat{s} + \hat{t} + \hat{u} = m_\text{W}^2\,, \tag{3.209}$$

where m_W denotes the $\text{W}^\pm$-boson mass.

The gluon emission channel

The first channel to be discussed is the gluon emission process $\text{q}\overline{\text{q}}' \to \text{W}^\pm\text{g}$. At tree-level, there are two Feynman diagrams contributing to the matrix element, cf. Fig. 3.9. The

[5]This corresponds to neglecting the off-shell gauge boson decays which, however, do not affect the QCD dynamics of the processes under consideration. The decay products of the gauge boson can be introduced into the process using the narrow-width-approximation, or by incorporating the full off-shell $\text{W}^\pm$ propagator.

partonic differential cross section can be written as [132]

$$\left.\frac{\mathrm{d}\hat{\sigma}}{\mathrm{d}\hat{t}}\right|_{ME} = \frac{\hat{\sigma}_0}{\hat{s}}\,\frac{\alpha_\mathrm{s}}{2\pi}\,C_\mathrm{F}\left[\frac{\hat{t}^2+\hat{u}^2+2m_\mathrm{W}^2\hat{s}}{\hat{t}\hat{u}}\right], \tag{3.210}$$

with $\hat{\sigma}_0$ the cross section of the leading-order process $\mathrm{q}\overline{\mathrm{q}}' \to \mathrm{W}^\pm$

$$\hat{\sigma}_0 = \frac{\pi}{3\hat{s}}\frac{g_\mathrm{W}^2}{4}, \tag{3.211}$$

where CKM-effects have been ignored. In the parton-shower approach there are two ways to produce the final-state gluon, which have to be added incoherently: either the gluon can be emitted from the initial-state quark or from the anti-quark.

- Emission off the quark:
  As a first step, the kinematical variables used in the parton-shower approximation should be related to the Mandelstam variables. In the first case, the initial quark as emitter and the initial anti-quark as spectator, the parton-shower variables become, cf. Sec. 3.3.4,

$$\tilde{v}_3 = \frac{p_3p_1}{p_1p_2} = -\frac{\hat{t}}{\hat{s}} \quad \text{and} \quad x_{3,12} = \frac{p_1p_2-p_3p_1-p_3p_2}{p_1p_2} = \frac{\hat{s}+\hat{t}+\hat{u}}{\hat{s}} = \frac{m_\mathrm{W}^2}{\hat{s}}. \tag{3.212}$$

  Using the appropriate splitting function of Eq. (3.152), the parton shower differential cross section

$$\left.\frac{\mathrm{d}\hat{\sigma}}{\mathrm{d}\tilde{v}_3}\right|_{\mathrm{PSq}} = \hat{\sigma}_0\,\frac{\alpha_\mathrm{s}}{2\pi}\,\frac{1}{\tilde{v}_3}\,C_\mathrm{F}\left[\frac{2}{1-x_{3,12}}-(1-x_{3,12})\right] \tag{3.213}$$

  can be cast into

$$\left.\frac{\mathrm{d}\hat{\sigma}}{\mathrm{d}\hat{t}}\right|_{\mathrm{PSq}} = \hat{\sigma}_0\,\frac{\alpha_\mathrm{s}}{2\pi}C_\mathrm{F}\frac{1}{-\hat{t}}\left[\frac{2}{1-x_{3,12}}-(1-x_{3,12})\right]. \tag{3.214}$$

  Using the relation

$$(1-x_{3,12}) = -\frac{\hat{t}+\hat{u}}{\hat{s}} \tag{3.215}$$

  and multiplying with $\hat{s}/\hat{s}$ yields

$$\left.\frac{\mathrm{d}\hat{\sigma}}{\mathrm{d}\hat{t}}\right|_{\mathrm{PSq}} = \frac{\hat{\sigma}_0}{\hat{s}}\,\frac{\alpha_\mathrm{s}}{2\pi}\,C_\mathrm{F}\left[\frac{\hat{s}^2+m_\mathrm{W}^4}{\hat{t}(\hat{t}+\hat{u})}\right]. \tag{3.216}$$

- Emission off the anti-quark:
  Swapping the rôle of the emitter and the spectator parton amounts to only interchanging $\hat{t}$ and $\hat{u}$ in the results above. Accordingly, the differential cross section in this case is given by

$$\left.\frac{\mathrm{d}\hat{\sigma}}{\mathrm{d}\hat{t}}\right|_{\mathrm{PS}\overline{\mathrm{q}}} = \frac{\hat{\sigma}_0}{\hat{s}}\,\frac{\alpha_\mathrm{s}}{2\pi}\,C_\mathrm{F}\left[\frac{\hat{s}^2+m_\mathrm{W}^4}{\hat{u}(\hat{t}+\hat{u})}\right]. \tag{3.217}$$

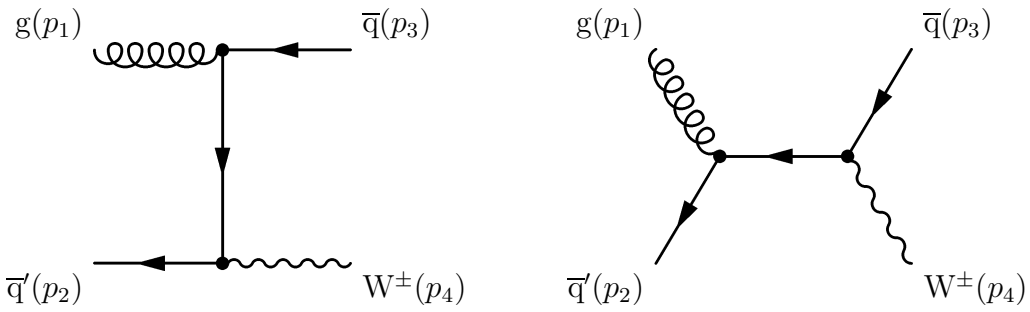

Figure 3.10: The leading-order Feynman diagrams contributing to the process $\mathrm{g}\overline{\mathrm{q}}' \to \mathrm{W}^{\pm}\overline{\mathrm{q}}$.

The full parton-shower result is the sum of the two contributions and reads

$$\left.\frac{\mathrm{d}\hat{\sigma}}{\mathrm{d}\hat{t}}\right|_{\mathrm{PS}} = \left.\frac{\mathrm{d}\hat{\sigma}}{\mathrm{d}\hat{t}}\right|_{\mathrm{PSq}} + \left.\frac{\mathrm{d}\hat{\sigma}}{\mathrm{d}\hat{t}}\right|_{\mathrm{PS}\overline{\mathrm{q}}} = \frac{\hat{\sigma}_0}{\hat{s}}\,\frac{\alpha_{\mathrm{s}}}{2\pi}\,C_{\mathrm{F}}\left[\frac{\hat{s}^2+m_{\mathrm{W}}^4}{\hat{t}\hat{u}}\right]. \tag{3.218}$$

Again, the parton-shower approach provides the correct description for soft and collinear phase-space configurations but misses non-singular terms. The difference of the parton shower and the exact result can be quantified by the ratio

$$\frac{\mathrm{d}\hat{\sigma}/\mathrm{d}\hat{t}\big|_{\mathrm{ME}}}{\mathrm{d}\hat{\sigma}/\mathrm{d}\hat{t}\big|_{\mathrm{PS}}} = \frac{\hat{t}^2+\hat{u}^2+2m_{\mathrm{W}}^2\hat{s}}{\hat{s}^2+m_{\mathrm{W}}^4} = 1-\frac{2\hat{t}\hat{u}}{\hat{s}^2+m_{\mathrm{W}}^4}, \tag{3.219}$$

which can take values between 0.5 and 1 in full agreement with the result of the parton-shower algorithm implemented in PYTHIA [133]. This indicates that the parton-shower approximation tends to overestimate the matrix element - a feature also present in $e^+e^- \to q\bar{q}g$, but not in the deep inelastic scattering processes.

The initial-state gluon case

There are two Feynman diagrams, cf. Fig. 3.10, contributing to the channel with an initial-state gluon, *i.e.* to the process $\mathrm{g}\overline{\mathrm{q}}' \to \mathrm{W}^{\pm}\overline{\mathrm{q}}$. The result of the full matrix-element calculation reads [132]

$$\left.\frac{\mathrm{d}\hat{\sigma}}{\mathrm{d}\hat{t}}\right|_{\mathrm{ME}} = \frac{\hat{\sigma}_0}{\hat{s}}\,\frac{\alpha_{\mathrm{s}}}{2\pi}\,T_{\mathrm{R}}\left[\frac{\hat{s}^2+\hat{u}^2+2m_{\mathrm{W}}^2\hat{t}}{-\hat{s}\hat{t}}\right]. \tag{3.220}$$

In the parton-shower approach only one emission process contributes to this channel, corresponding to the t-channel diagram. The s-channel contribution is not realised in the shower ansatz. Using the definitions of the shower variables as given above and the corresponding splitting function, cf. Eq. (3.155), the parton-shower cross section reads

$$\begin{aligned}\left.\frac{\mathrm{d}\hat{\sigma}}{\mathrm{d}\hat{t}}\right|_{\mathrm{PS}} &= \frac{\hat{\sigma}_0}{\hat{s}}\,\frac{\alpha_{\mathrm{s}}}{2\pi}\,T_{\mathrm{R}}\frac{\hat{s}}{-\hat{t}}\left[1-2x_{3,12}(1-x_{3,12})\right] \\ &= \frac{\hat{\sigma}_0}{\hat{s}}\,\frac{\alpha_{\mathrm{s}}}{2\pi}\,T_{\mathrm{R}}\left[\frac{\hat{s}^2+2m_{\mathrm{W}}^2(\hat{t}+\hat{u})}{-\hat{s}\hat{t}}\right],\end{aligned} \tag{3.221}$$

where

$$(1 - x_{3,12}) = -\frac{\hat{t} + \hat{u}}{\hat{s}} \quad \text{and} \quad x_{3,12} = m_{\mathrm{W}}^2/\hat{s} \tag{3.222}$$

has been used. The ratio of the parton-shower and the matrix-element result is

$$\frac{\mathrm{d}\hat{\sigma}/\mathrm{d}\hat{t}\big|_{\mathrm{ME}}}{\mathrm{d}\hat{\sigma}/\mathrm{d}\hat{t}\big|_{\mathrm{PS}}} = \frac{\hat{s}^2 + \hat{u}^2 + 2m_{\mathrm{W}}^2\hat{t}}{\hat{s}^2 + m_{\mathrm{W}}^4(\hat{t} + \hat{u})} = 1 + \frac{\hat{u}(\hat{u} - 2m_{\mathrm{W}}^2)}{(\hat{s} - m_{\mathrm{W}}^2)^2 + m_{\mathrm{W}}^4}\,, \tag{3.223}$$

varying between 1 and 3 [133]. Accordingly, the parton-shower ansatz tends to undershoot the exact matrix element. However, the shower is constructed to give the correct answer in the logarithmically enhanced phase-space regions and thus has the correct limiting behaviour in the soft and collinear limits. The differences identified here are a result of differences in the non-singular terms, contributing only in hard regions of phase space. The process $\mathrm{qg} \to \mathrm{W}^{\pm}\mathrm{q}'$ closely follows the above example solely $\hat{t}$ and $\hat{u}$ have to be exchanged. This leads to the same qualitative results and the same conclusions.

3.5 Applications

In this section, the abilities of the newly developed parton-shower formulation in describing QCD dynamics will be highlighted by comparing its results for various physics processes with experimental data and other calculations: In Sec. 3.5.1, the predictions for hadron production in e^+e^- collisions as measured at LEP will be studied and some results related to a future machine operated at $\sqrt{s} = 500$ GeV will be discussed. In Sec. 3.5.2, emphasis is put on the capabilities of the shower to describe particle production at hadron colliders such as the Tevatron or the upcoming LHC.

3.5.1 Jet production at e^+e^- colliders

Measurements of hadronic final states produced in e^+e^- collisions provide a very precise probe of QCD dynamics in the final state and an excellent means to deduce its fundamental parameters such as the value of $\alpha_S(m_Z)$, see for instance [134], and the colour charges C_F and C_A in three- and four-jet events as discussed *e.g.* in [134]-[137]. Therefore it is not surprising that in the past years calculations for relevant three-jet observables, such as thrust, have become available at NNLO [138] and that full parton-level Monte Carlo codes for four-jet final states at NLO have been constructed [139, 140]. Obviously such observables also provide a critical test of the corresponding final-state radiation piece of a parton-shower model. However, due to the fragmentation of partons into hadrons, which at the moment can be simulated with phenomenological models only, the parton-shower predictions can not directly be compared with experimental data but rather have to be supplemented with a hadronisation model. The new parton shower presented here therefore has been interfaced

to the Lund string fragmentation routines of PYTHIA version 6.2 [39] in the framework of the SHERPA event generator. The large number of very precisely measured observables at various energies allows tuning the intrinsic parameters of the parton shower in conjunction with the phenomenological parameters of the fragmentation model. Such a procedure has been performed, for instance, for the new parton-shower and fragmentation code in HERWIG++ [5]. In principle, such a tuning is a very time-consuming and delicate procedure, see for instance [141], deserving a publication in its own right. Recent developments to automatise the task of generator tuning and validation to a large extend are reported in [142]. Here, only a very limited tuning based on few parameters and observables only has been performed. The results of this tuning are presented in Sec. 3.5.1. In Sec. 3.5.1 the focus is on heavy-quark production at LEP1 and ILC energies to validate the treatment of finite parton masses in the shower model.

Comparison with LEP1 data

The most extensive data set available to validate QCD Monte Carlo predictions are LEP measurements at the Z^0 pole. A selection of event shape variables, multiplicity distributions, differential jet rates, four-jet angle measurements and various particle momentum distributions have been used to select values for the unconstrained, phenomenological parameters of the simulation, namely the value of the strong coupling constant at m_Z, the infrared shower cut-off $\mathbf{k}_{\perp,0}$ and the three Lund string hadronisation parameters a (`PARP(41)`), b (`PARP(42)`) and σ_q (`PARP(21)`). For the results presented in the following, they have been fixed to $\alpha_s(m_Z) = 0.125$, $\mathbf{k}_{\perp,0} = 0.63$ GeV, $a = 0.33$, $b = 0.75$ GeV^{-2}, and $\sigma_q = 0.358$ GeV, respectively. This yields a mean charged multiplicity per event of $\langle N_{ch}\rangle = 20.87$ at $\sqrt{s} = m_Z$, in good agreement with the experimentally found value of $\langle N_{ch}\rangle = 20.92 \pm 0.24$ [143].

Figures 3.11 to 3.14 show some exemplary results obtained with the new shower implementation compared to DELPHI LEP1 data at $\sqrt{s} = 91.2$ GeV [143].

In Fig. 3.11 the new algorithm, denoted as "CS shower" in the following, is compared with some event-shape measurements by DELPHI [143]. The distributions of thrust, thrust-major, thrust-minor and aplanarity are displayed. The lower panel of each plot contains the bin-wise ratio (MC-data)/data, and the yellow bands show the statistical plus systematic error of the respective measurements. All the observables are sensitive to the pattern of QCD radiation probing both soft and hard emissions off the shower initiating $q\bar{q}$ pair. The Monte Carlo predictions agree very well with the event-shape data. There is some slight excess at very low $1 - T$ corresponding to two-jet like events. This region of phase space, however, is very sensitive to hadronisation corrections and therefore dominated by non-perturbative physics. The same reasoning holds for the major and minor distributions at low M or m.

The transverse-momentum distribution within and out of the event plane defined by the

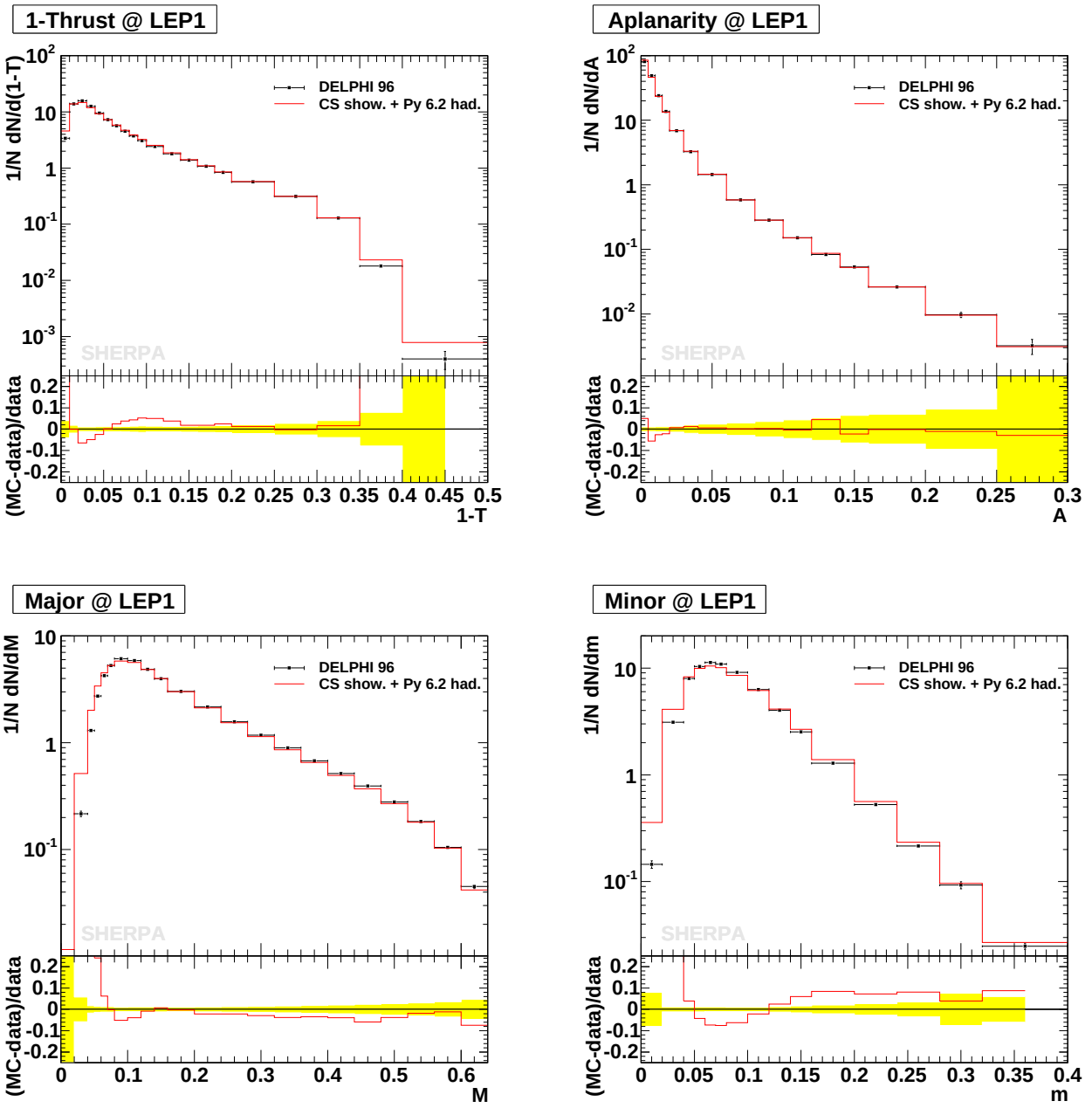

Figure 3.11: The event-shape variables 1−Thrust $(1-T)$, Aplanarity (A), Major (M) and Minor (m) in comparison with DELPHI data [143].

thrust and thrust-major axes, (p_T^{in}) and (p_T^{out}), respectively, are presented in Fig. 3.12. While p_T^{in} is quite well modelled by the Catani–Seymour shower, p_T^{out} is significantly underestimated for values above 1 GeV. This tendency, however, is observed in other QCD Monte Carlo simulations as well [143].

In Fig. 3.13 the predictions for the exclusive two-, three-, four- and five-jet rates in the Durham algorithm [53] as a function of the jet resolution $y_{\text{cut}}^{\text{Durham}}$ are compared with data

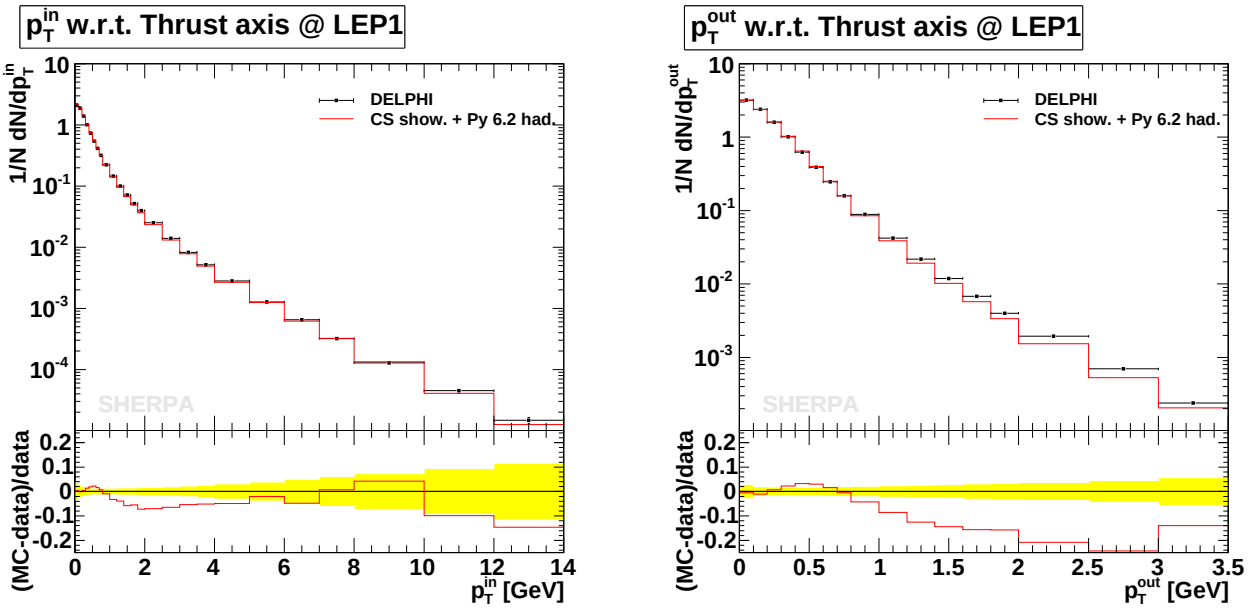

Figure 3.12: The p_T^{in} and p_T^{out} observables measured with respect to the thrust axis compared to a DELPHI measurement [143].

taken by the DELPHI experiment [144]. They all exhibit a sufficient agreement with data within the experimental uncertainty bands. For the four- and five-jet rate the shower seems to underestimate the region of $y_{\text{cut}}^{\text{Durham}} \approx 0.001$, however, this region is also affected by hadronisation effects and a more sophisticated tuning may provide an even better agreement with data here. The dependence on the choice of hadronisation parameters is even more pronounced for jet resolutions smaller than 0.001 where the results for the new shower preferably lie on the upper side of the experimental uncertainty band.

The last observables to be considered are jet angular distributions in events with four jets. These observables can not be expected to be too well described by a pure parton shower as they should probe spin correlations of the produced partons. Such correlations, however, are not taken into account in conventional showers but require full matrix-element calculations (eventually combined with a parton shower) to be completely taken into account [28, 145]. In Fig. 3.14, the predictions for the Bengtsson–Zerwas [146] and the Nachtmann–Reiter [147] angle are compared with DELPHI data [144] for events with four jets at a jet resolution $y_{\text{cut}}^{\text{Durham}} = 0.008$. Both results agree surprisingly well with data. A similar level of agreement is observed for the other two prominent four-jet angles, α_{34} and the Körner–Schierholz–Willrodt angle, that are not shown here.

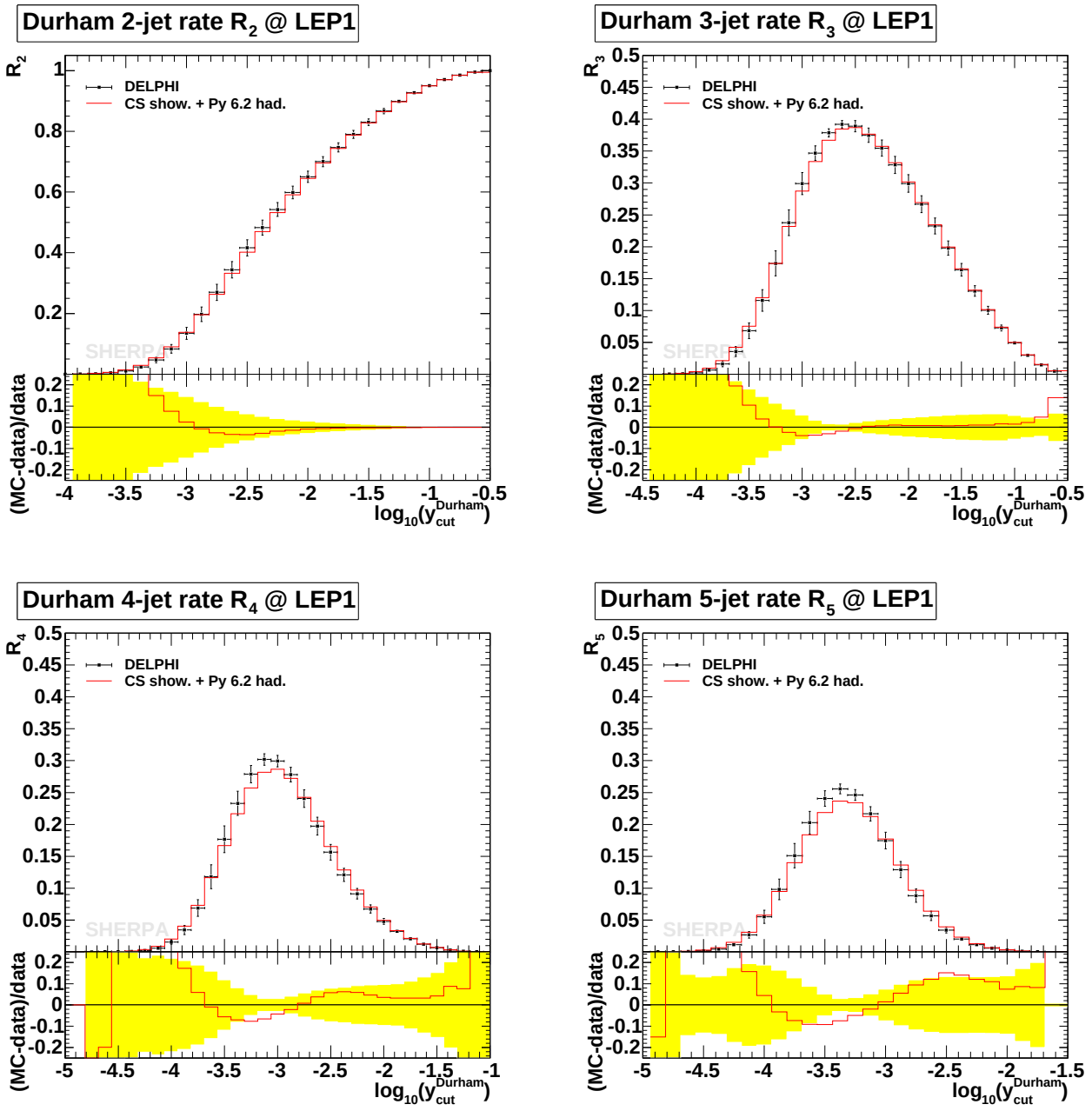

Figure 3.13: The n-jet rates R_n for the Durham jet algorithm as a function of the jet-resolution parameter $y_{\text{cut}}^{\text{Durham}}$. Data taken from [144].

Jet rates in heavy-quark production

The leading order of heavy-quark production at lepton colliders also proceeds through an intermediate γ^* or Z^0 in the s-channel. Since pair production of top-quarks was outside the kinematical reach of LEP, only the production of bottom-quarks is available at these energies to discuss the treatment of heavy quarks in the new parton-shower algorithm. At a future international linear collider (ILC), operating at or around $\sqrt{s} = 500$ GeV, pair

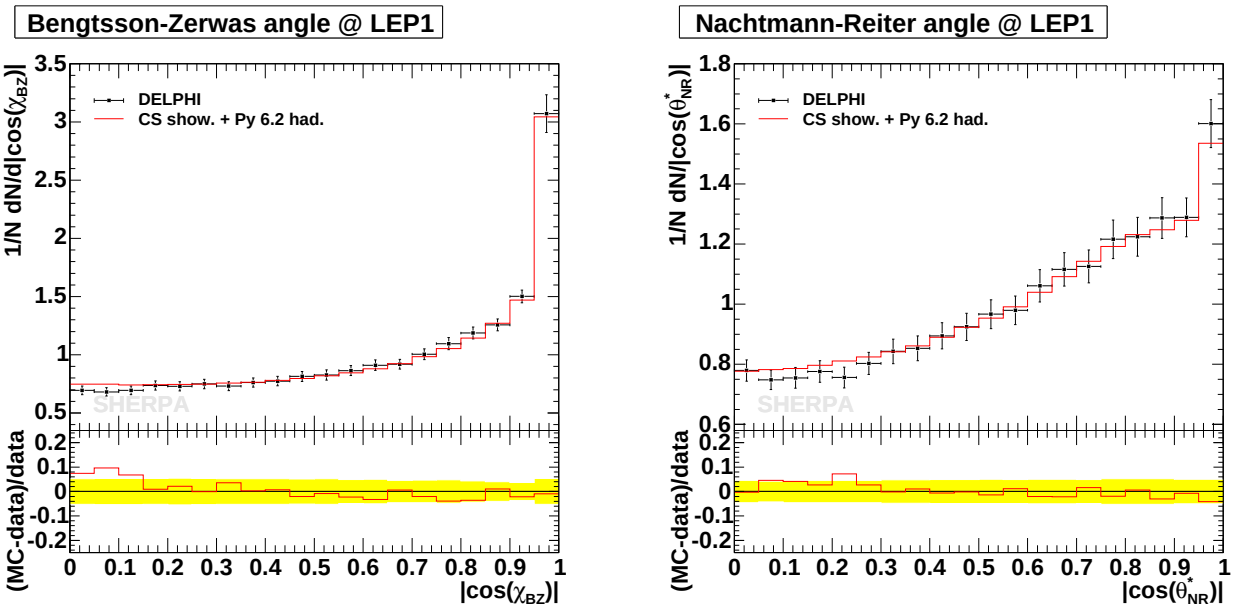

Figure 3.14: The Bengtsson–Zerwas and Nachtmann–Reiter four-jet angles compared with DELPHI data [144].

production of top-quarks will play a key rôle in the physics programme. This is also true for the LHC where top-quarks will copiously be produced and constitute a major background in nearly all searches for new physics. Therefore, a correct description of the radiation pattern of heavy quarks will be of enormous importance. As already hinted at in Sec. 3.3.1, radiation off massive quarks is suppressed with respect to the case $m_Q = 0$, also known as "dead-cone"-effect [114]. The impact is however rather small when considering b-quark masses of 4.8 GeV at collider energies that are much larger. To illustrate the impact of the finite b-quark mass in the shower approach the Durham two- and three-jet rates for $b\bar{b}$-production at LEP1 are presented in the left panel of Fig. 3.15. There, results are shown for the fully massive case (*i.e.* the mass has fully been taken into account in the splitting kernels, the phase-space boundaries and the splitting kinematics) and for the massless case are depicted. As expected, in the massive case both R_2 and R_3 are slightly enhanced at low values of $y_{\text{cut}}^{\text{Durham}}$, corresponding to the suppressions of additional radiation that turns a two-jet event into three-jet and a three-jet into a four-jet event at the scale of the emission.

In the right panel of Fig. 3.15 the same observables are presented, but this time for the pair-production of 175 GeV top-quarks at a 500 GeV ILC. Obviously, the finite mass has to be taken into account in the description of QCD radiation off top-quarks, since the differences with respect to the massless case can exceed an order of magnitude for the two-jet rate.

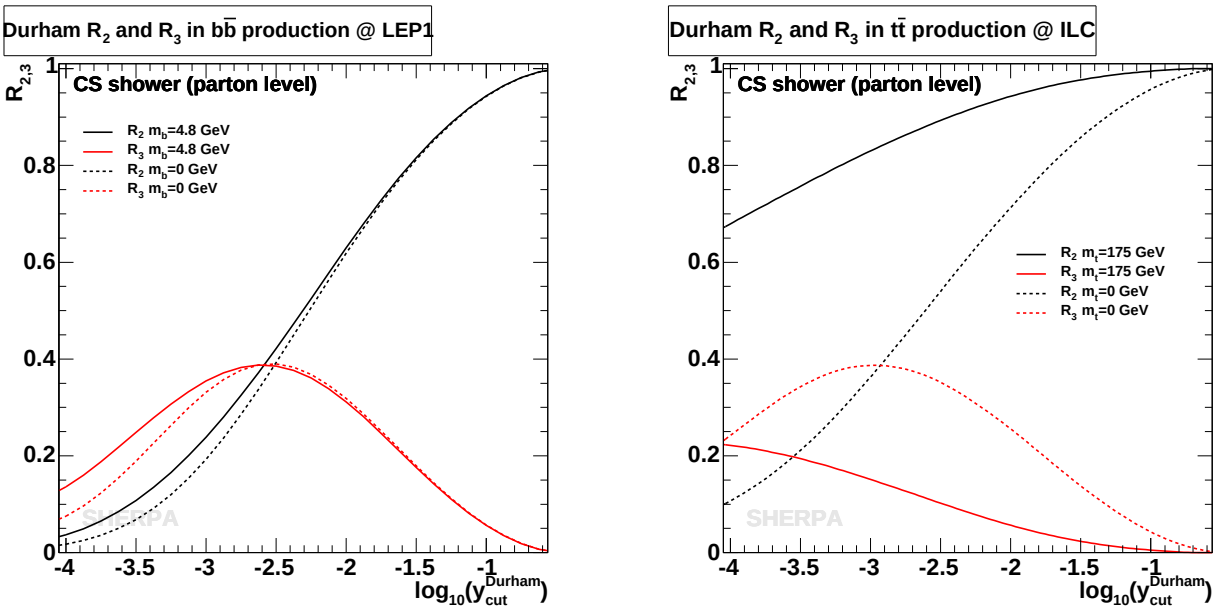

Figure 3.15: The exclusive Durham two- and three-jet rates in inclusive $b\bar{b}$ production at LEP1 (left panel) and $t\bar{t}$ production at a 500 GeV linear collider (right panel). The solid curves correspond to fully taking into account the quark masses in the parton-shower simulation while for the dashed predictions the finite masses have been neglected.

3.5.2 Particle production in hadron collisions

With the advent of the LHC era, the description and simulation of particle production processes at hadron colliders gained even more relevance. Due to the colour-charged partonic initial states, *every* hard process at hadron colliders is accompanied by initial- and subsequent final-state radiation. In the following, only two examples shall be considered to highlight the performance of the new parton-shower model in such situations. First, the inclusive production of Drell-Yan lepton pairs, the simplest process that features initial-state emitter – initial-state spectator dipoles, and, second, QCD jet production are discussed. For the latter, besides looking at some inclusive two-jet distributions, three-jet observables sensitive to the inclusion of QCD colour coherence are considered and qualitatively compared with data.

For all the predictions presented below, the CTEQ6L set of PDFs [148] has been used, the strong coupling constant has been fixed to $\alpha_s(m_Z) = 0.118$ with its running taken at two-loop level, in accordance with the choice in the PDF, and the infrared cut-off of the shower is chosen to be $\mathbf{k}_{\perp,0} = 2$ GeV. Hadronisation of the partonic shower final states is again accomplished by an interface to the Lund string routines of PYTHIA 6.2 [39].

Inclusive gauge boson production

The production of electroweak gauge bosons, *e.g.* $W^{\pm}$ and Z^0 bosons, and their subsequent decay into leptonic final states, is one of the most prominent processes at hadron colliders due to their clean signature. Although very interesting in their own right, their inclusive production, *i.e.* their production together with additional QCD jets, represents a serious background to many other interesting processes, like, *e.g.* the production and decay of top-quarks or SUSY particles. Therefore, many theoretical efforts have been undertaken to predict gauge boson production as precisely as possible, both at fixed order in the strong coupling, see for instance [149]-[153], or focusing on the analytical resummation of large logarithms from soft gluon emissions, see for example [154]-[158]. An important ingredient in all cases have been parametrisations of the PDFs and a good perturbative control over their scaling behaviour, which by now is known at the three-loop level [159]. In addition, in the past few years, Drell-Yan production formed the testbed for approaches aiming at the combination of tree-level matrix elements with parton-shower Monte Carlos [43, 30, 46, 73, 84]. Parton-shower Monte Carlos thereby have to deliver the correct description for the bulk of the events where the bosons are accompanied by rather soft emissions only.

In the following, Drell-Yan production of γ^*/Z^0 at Tevatron Run I energies is considered with the bosons decaying into e^+e^--pairs. They are constrained to fall into a mass-window of 66 GeV $< M_{e^+e^-} <$ 116 GeV. The predictions of the new shower algorithm will directly be compared to results obtained with the matrix-element–parton-shower merging approach as implemented in SHERPA. To this end, an inclusive sample combining matrix elements for no extra emission and one extra final-state QCD parton has been generated with SHERPA version 1.0.10. In the figures this sample will be denoted by "SHERPA 1.0.10 CKKW (0+1 jet ME)".

The discussion of the results starts with the rapidity- and pseudo-rapidity distributions of the produced lepton-pair, see Fig. 3.16. As the shape of the former is already described well at the leading order, *i.e.* without any radiation, there is hardly any difference visible for the two results. The gauge boson pseudo-rapidity distribution however, only emerges when there is some additional QCD radiation. The radiation pattern, and especially the hardest emission, determines this leptonic observable. The pure shower result is in good agreement with the merged result, which contains the exact tree-level matrix element for the first hard emission. However, the shower distribution is somewhat lower at central pseudo-rapidity and slightly exceeds the merged SHERPA result for the two maxima around $\eta_{e^+e^-} \approx \pm 4$. These differences can be traced back to the lack of sufficiently hard radiation in the shower, which is constrained from above through the default shower start scale for this process, namely the invariant mass squared of the initial dipoles, $M^2_{e^+e^-}$. Below that scale, however, the parton shower can be expected to deliver reliable results, and in order to fill the phase space above that scale, matrix-element–parton-shower merging techniques should be added.

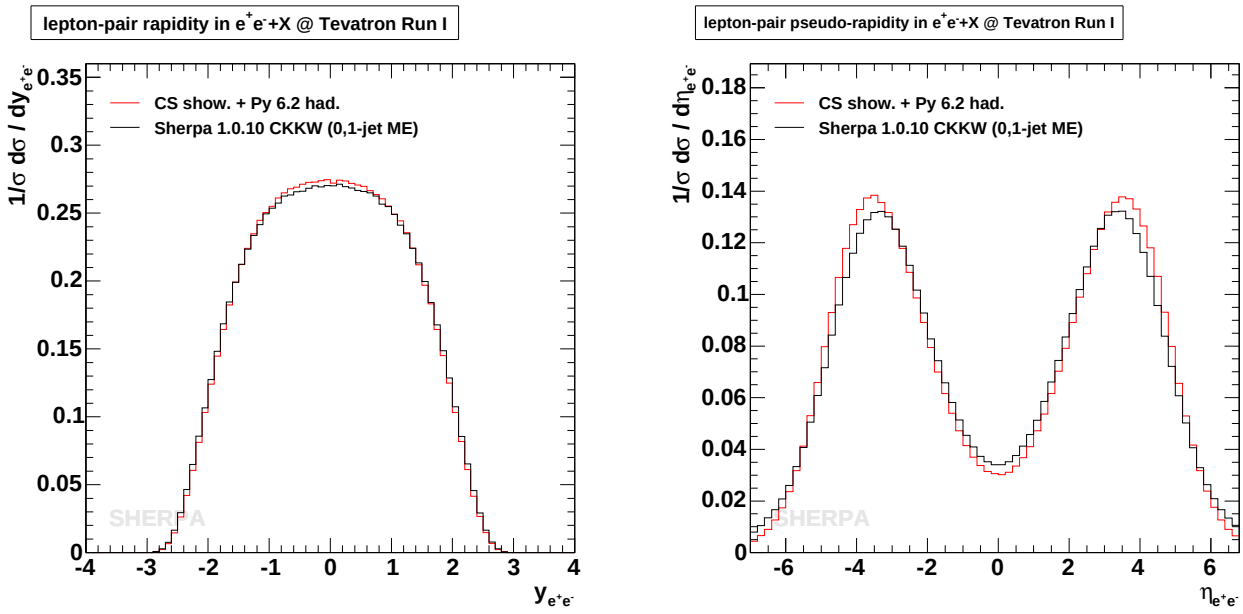

Figure 3.16: The rapidity- (left panel) and pseudo-rapidity (right panel) distribution of e^+e^- Drell-Yan pairs produced in $p\bar{p}$ collisions at $\sqrt{s} = 1800$ GeV.

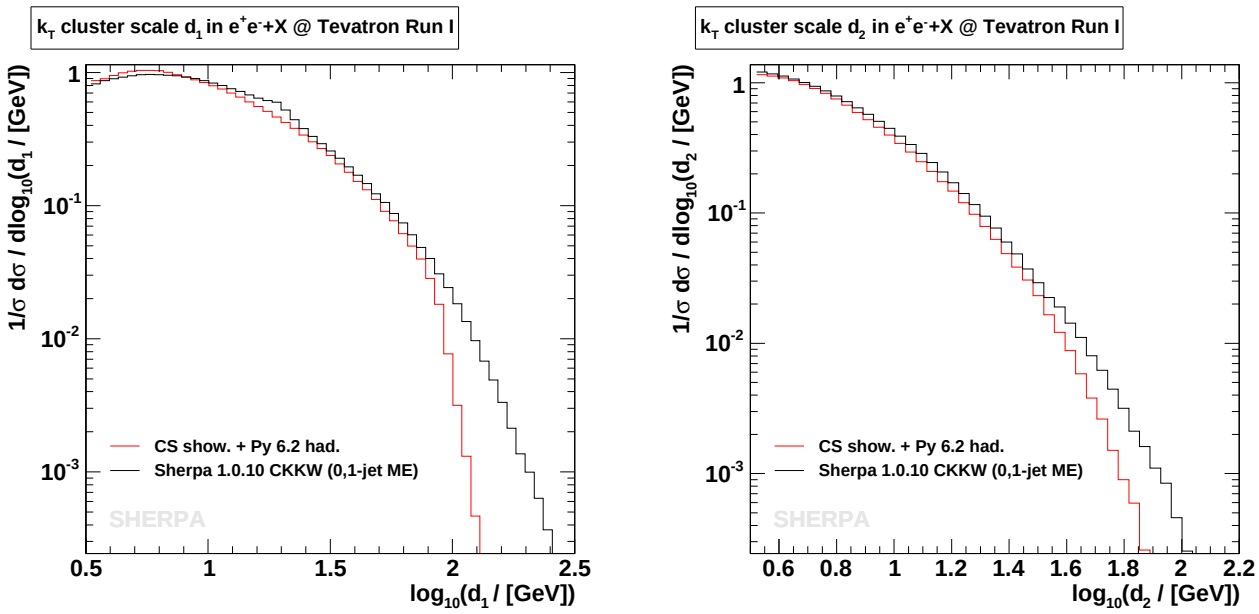

Figure 3.17: The $k_\perp$ differential jet rates d_1 and d_2 in $e^+e^- + X$ at Tevatron Run I.

The smaller amount of hard radiation can be further quantified by looking at the differential jet rates d_1 and d_2 for the $k_\perp$-jet algorithm [55], displayed in Fig. 3.17. These observables determine the scales where the first (d_1) and second (d_2) additional parton gets resolved as a jet from the core process. The results for the Catani–Seymour based shower and the merged SHERPA sample agree well for small cluster scales but, as can be expected, the shower is significantly lower for values of $d_i > m_Z$.

The last observable to be considered is the transverse momentum distribution of the lepton-pair. This distribution has been measured with high precision by the Tevatron experiments. Like the Drell-Yan pseudo-rapidity it is very sensitive to both soft and hard radiation accompanying the produced boson. Fig. 3.18 contains a comparison of the prediction from the new shower model with a CDF measurement [76] [6]. The agreement between data and simulation is quite good up to p_T's of approximately 80 GeV. The upper-right part of Fig. 3.18 contains a blow-up of the low transverse-momentum region of $p_T < 20$ GeV, this time, however, on a linear scale. There, the parton shower describes the turn-on of the distribution quite nicely, the actual peak, however, is slightly higher and a bit broader than seen in data. To describe the very low transverse-momentum region a Gaussian-smeared intrinsic $k_\perp$ was introduced, with a mean of 0.52 GeV and a width of 0.8 GeV. A more detailed tuning of these values combined with the shower cut-off $\mathbf{k}_{\perp,0}$ may yield an even better description of the distribution's peak. Above 80 GeV the parton shower dies off very rapidly due to its phase space being constrained by the choice of the starting scale, $\mathbf{k}^2_{\perp,\max} = M^2_{e^+e^-}$. For illustrative purposes a prediction has been added where the start scale has been enhanced to $4M^2_{e^+e^-}$. While the results at low p_T do not change significantly, the distribution continues in the tail, thereby following the experimental data. But, of course, with this choice of parton-shower starting scale, there is a similar drop-off of the distribution at scales of around $4M^2_{e^+e^-}$. However, since there is no guarantee that the parton-shower kernels do perform well enough at large scales, *i.e.* outside the soft- and collinear phase-space regions, it seems to be overly optimistic to stretch its predictions to such high scales. Instead, the parton-shower description should consistently be improved by incorporating exact higher-order corrections.

[6] A comparison of the merged SHERPA prediction with this data has been presented Sec. 2.3.1.

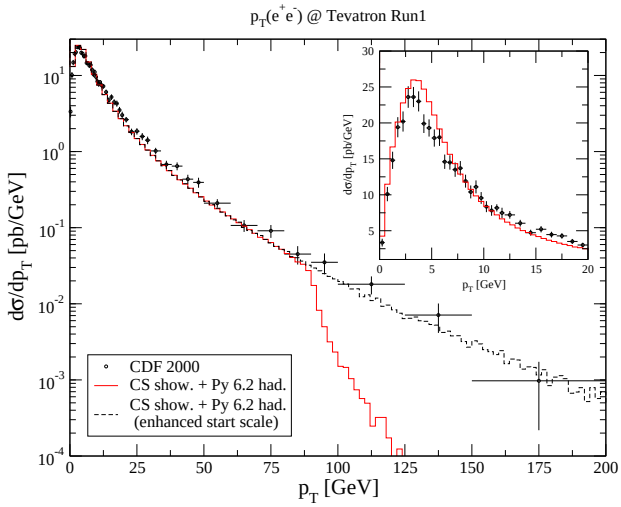

Figure 3.18: The p_T distribution of e^+e^- Drell-Yan pairs in comparison with data from CDF at the Tevatron, Run I [76].

Inclusive jet production

The most obvious QCD production process to look for at hadron colliders is inclusive jet production. However, from a theoretical point of view this is quite a complicated process. Besides tree-level calculations for up-to six final-state jets, so far, there merely exist full next-to-leading-order results up-to three-jet production [107], [160]-[163]. Despite of strong efforts, culminating in evaluating the complete set of necessary matrix elements [164]-[168] and in developing methods to isolate the infrared divergences in the real correction part [169] a full NNLO calculation for inclusive jet production has not been finished yet. Also, from the point of view of the parton shower presented here, jet production at hadron colliders is rather involved. This is because the $2 \to 2$ hard process will contain all possible colour connections between initial-state and final-state partons. Hence, QCD jet production constitutes a severe test of the entire shower algorithm. The input parameters for the simulations have been chosen as specified above. The starting scale of the shower, however, is related to the transverse momentum of the $2 \to 2$ core process' outgoing partons, namely $\mathbf{k}^2_{\perp,\max} = p^2_{\perp,j}$.

The first thing to be looked at is a very inclusive quantity, the dijet invariant mass. This has been measured by DØ during Run I [170]. The jets considered there have been reconstructed using a jet-cone algorithm with a cone opening angle of $R = 0.7$ in the $\eta - \phi$ space and with jet transverse energies above 30 GeV. Dijet candidates have then been subjected to the requirement that both jets satisfy $|\eta_j| < 1.0$. Fig. 3.19 exhibits the resulting dijet-mass distribution starting at $M_{\text{dijet}} > 200$ GeV. It is a very steeply falling spectrum spanning six orders of magnitude in the mass range under consideration. To compare with data the

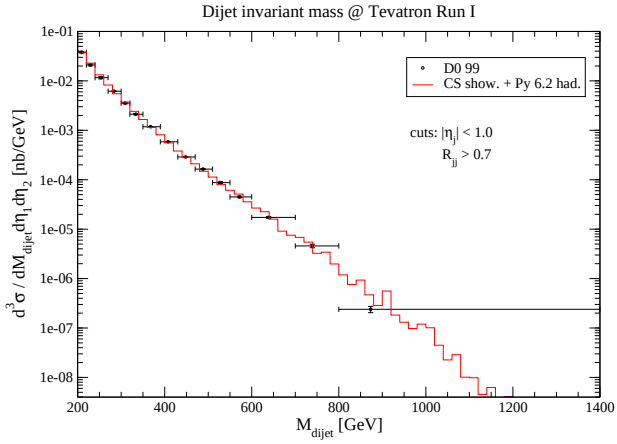

Figure 3.19: Dijet mass M_{dijet} measured by DØ at Tevatron Run I [170].

result of the (leading-order) simulation has been normalised to the cross section observed in experiment. In fact, the prediction of the proposed shower algorithm then is in very good agreement with the data and almost everywhere exactly hits the weighted bin centers.

Another interesting observable when studying dijet events is the azimuthal angle between the two highest-p_T jets. If there is no additional QCD radiation the two jets have equal transverse momenta and they are oriented back-to-back. Thus, in this case, their azimuthal separation $\Delta\phi_{\text{dijet}} = |\phi_1 - \phi_2|$ equals π. In the presence of merely soft radiation the azimuthal angles remain strongly correlated, the strength of the decorrelation rises with the presence of additional hard radiation. Therefore, the dijet decorrelation provides a testbed for soft- and hard QCD emissions without the necessity to reconstruct further jets. Fig. 3.20 contains the results of a recent DØ measurement for cone jets found for $R = 0.7$ [171]. The data fall into different ranges of the leading-jet transverse momentum and are then multiplied with different constant prefactors in order to display them in one plot. In all cases, the second-leading jet was required to have a transverse momentum $p_T > 40$ GeV and both jets are constrained to the central-rapidity region, $|y_j| < 0.5$. The data are overlayed with the respective predictions of the Catani–Seymour dipole shower approach. The simulation agrees very well with the data over the whole interval of $\Delta\phi_{\text{dijet}}$ spanned by the experimental measurements. This is a very satisfying result as it proves that the proposed shower formulation not only correctly accounts for phase-space regions related to soft and collinear radiation but also yields qualitatively and quantitatively correct estimates for rather hard emissions as well. Furthermore, since this observable is quite sensitive to model-intrinsic scale choices such as the shower start scale and scales entering the running coupling constant and parton density functions, this agreement proves that the defaults have been chosen correctly.

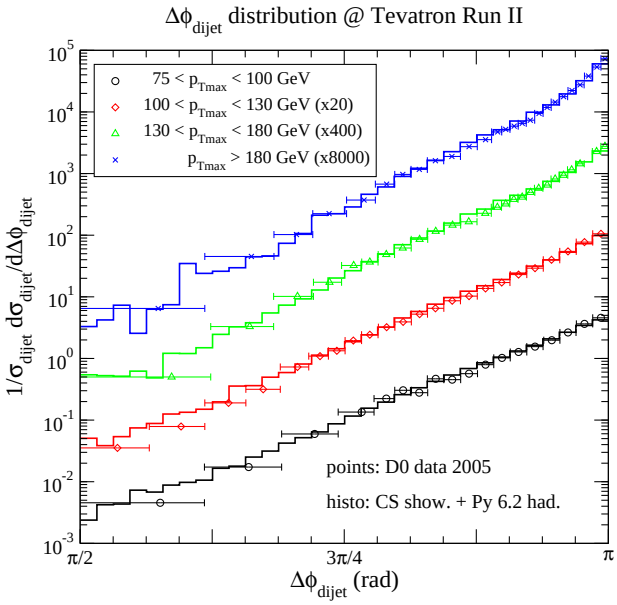

Figure 3.20: Dijet azimuthal decorrelation measured by DØ at Tevatron Run II [171].

The last item to be discussed are observables in QCD jet production at hadron colliders that are known to be sensitive to the correct treatment of QCD soft colour coherence in the parton-shower simulation. Colour-coherence effects have been widely studied for e^+e^- collisions, for an early review see e.g. [172]. They manifest themselves in the fact that soft emissions are forbidden outside a certain angular cone around the emitting particle's direction, known as angular ordering [114, 118]. To account for this in shower Monte Carlos the phase space for allowed emissions has to be properly constrained. Within the HERWIG Monte Carlo for instance this is realised by evolving the shower in terms of cone-opening angles. While the situation for pure final-state showers is quite clear, in hadronic collisions the situation is slightly more complicated due to the presence of more colour flows, among them those that connect initial- and final-state partons. As colour-coherence here already influences the first emission from the initial- and final-state partons QCD three-jet events are the best place to look for the pattern of these phenomena at hadron colliders.

In one of the pioneering studies [173] three-jet events that feature a hard leading jet and a rather soft third jet have been considered. Observables potentially sensitive to colour coherence are spatial correlations between the third jet and the leading ones. In [173] such discriminating variables have been found and by comparison with Monte Carlo simulations evidence for the observation of colour coherence in hadron collisions has been provided. This ultimately has led to a refinement of the PYTHIA shower algorithm in order to appropriately model colour coherence in the spirit of [174]. In the CDF study [173] jets have been defined through a cone algorithm with a cone radius of $R = 0.7$ and the following event selection

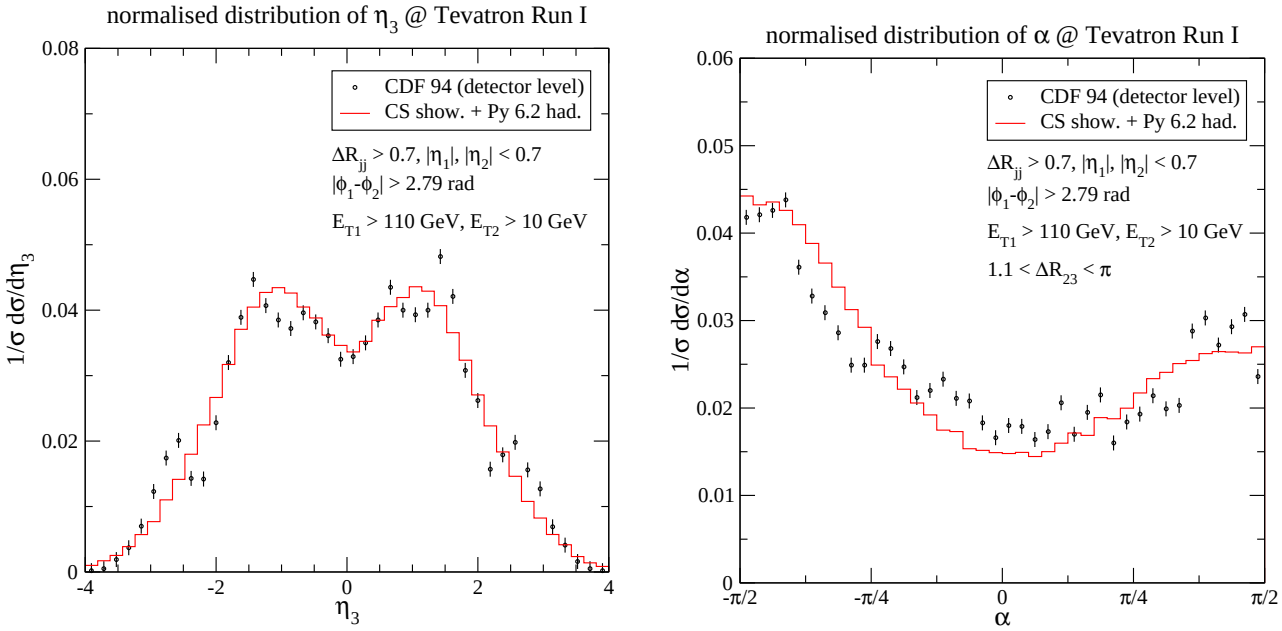

Figure 3.21: The pseudo-rapidity distribution of the third-hardest jet (left panel) and the distribution of the angle α (right panel) in inclusive QCD three-jet production in comparison with CDF data taking during Tevatron Run I. Experimental errors are statistical only. Histograms are normalised to one.

criteria have been applied:

- For the two leading jets the pseudo-rapidity is constrained to $|\eta_1| < 0.7$ and $|\eta_2| < 0.7$;
- they have to be back-to-back within 20 degrees in the transverse plane, corresponding to $|\phi_1 - \phi_2| > 2.79$ radian;
- and the transverse energy of the leading jet, E_{T1}, has to exceed 110 GeV, the third jet is required to have $E_{T3} > 10$ GeV.
- Only for the study of the α variable defined below the additional cut $1.1 < \Delta R_{23} < \pi$, where $\Delta R_{23} = \sqrt{(\eta_2 - \eta_3)^2 + (\phi_2 - \phi_3)^2}$, is imposed.

A number of observables has been considered, the two most convenient and discriminating ones have been the pseudo-rapidity distribution of the third jet, η_3, and the polar angle in the space parametrised by $\Delta\phi = \phi_3 - \phi_2$ and $\Delta H = \text{sign}(\eta_2)(\eta_3 - \eta_2)$, namely $\alpha = \arctan(\Delta H/|\Delta\phi|)$ [7]. It should be stressed that the published results, used for the com-

[7] A further observable considered in the CDF study is the spatial separation of the second- and third jet in the $\eta-\phi$ space, ΔR_{23}. This observable, however, seems to be less discriminatory between theoretical models. In addition, and more importantly, detector effects seem to have a larger impact on its discriminating power. Therefore it is not taken into account here.

parison, are not corrected for detector effects, such as finite resolution and uninstrumented regions, and therefore can only qualitatively be compared with theoretical calculations. The results of the Monte Carlo simulations exhibited in [173] have passed the full chain of the CDF detector simulation. In Fig. 3.21 the measurements are compared with simulated events at the hadron level. In the left panel the η_3 distribution is shown and the right panel contains the comparison of the α distribution. Both predictions agree well with the data. The η_3 distribution tends to be broader in models that take into account colour-coherence effects and only then theoretical calculations show the significant dip around $\eta_3 \approx 0$ seen in data [8]. The α variable is also very sensitive to the inclusion of colour coherence. It decreases from $\alpha = -\pi/2$ to $\alpha = 0$ but then the slope changes and the distribution rises as $\alpha \to \pi/2$. This trend is clearly seen for the simulation with the new shower algorithm. Models not taking into account coherence fail to describe the distribution's rise towards $\alpha \to \pi/2$ and have a clear excess of events at small $|\alpha|$. Concerning the interpretation of these results the missing detector smearing for the shower simulation has to be kept in mind. However, in Ref. [173] estimates for the size of the detector effects are given, showing that the impact of the finite detector resolution is much smaller than the size of the physical effects. The generic features of the two observables presented here are not dependent on detector effects, and they are well described by the new shower formulation.

The conclusion of this is that the proposed parton-shower algorithm with its notion of emitter–spectator dipoles associated with the color flow of the event and using transverse momenta as evolution variable accounts for soft colour coherence and yields a very satisfying description, both on the qualitative and the quantitative level. It can be anticipated that such non-trivial quantum phenomena are of large importance at the LHC, since the phase space for jet production is much larger and hard jets are produced copiously. For a solid description of QCD therefore the systematic and correct inclusion of these effects is paramount.

3.6 Summary and conclusions

A new parton-shower model based on Catani–Seymour dipole subtraction kernels has been presented, which was sketched for the first time in [100, 101]. In the present implementation, the original proposal is extended to cover also initial-state splittings, finite parton masses, and QCD radiation off SUSY particles.

Choices concerning the evolution parameter of the parton shower and the various scales entering running coupling constants, PDFs, etc. have been detailed, fixing the full algorithm. The kinematics of massive splittings has been presented in some detail, and the

[8] The HERWIG Monte Carlo, incorporating colour coherence through explicit angular ordering, describes the data very well. Switching on the approximate version of angular ordering in PYTHIA, realised by a veto on rising opening angles during shower evolution, significantly improves PYTHIA's agreement with data.

corresponding massless limits have been discussed. By direct comparison with some benchmark processes, at first order in α_s, the differences of the parton-shower approximation with respect to exact results have been worked out. It has been shown that indeed the parton-shower algorithm presented here reproduces the soft and collinear limits of the exact matrix elements and that differences between both results are non-singular terms only. Some first results with this new parton-shower formulation have been presented and show very encouraging agreement with other models and with experimental data.

In the near future, this new algorithm will be fully incorporated into the SHERPA framework and it will be made publicly available in the next releases of the code. This will also involve a more careful tuning of the shower parameters and the inputs of the hadronisation models provided by or linked to SHERPA, which surely will further improve the agreement with data. Planned is a detailed comparison against another new shower ansatz that is based on splitting colour dipoles [175], and that is also being developed in the SHERPA framework at present. In addition, a full merging with multi-leg matrix elements in the spirit of [28] will be implemented. It can furthermore be anticipated that this new shower implementation will lend itself to incorporation of MC@NLO-techniques [12, 16].

4 Simulation of supersymmetric processes

4.1 Introduction

The discoveries of the electroweak gauge bosons and the top-quark more than a decade ago established perturbative quantum field theory as a common description of electromagnetic, weak, and strong interactions, universally applicable for energies above the hadronic GeV scale. The subsequent measurements of QCD and electroweak observables in high-energy collision experiments at the SLAC SLC, CERN LEP, and Fermilab Tevatron have validated this framework to an unprecedented precision. Nevertheless, the underlying mechanism of electroweak symmetry breaking remains undetermined. It is not clear how the theory should be extrapolated beyond the electroweak scale $v = 246$ GeV to the TeV scale or even higher energies [176].

At the LHC (and an ILC) this energy range will be directly probed for the first time. If the perturbative paradigm holds, it is expected to see fundamental scalar Higgs particles, as predicted by the Standard Model. Weak-scale supersymmetry (SUSY) is a leading possible solution to theoretical problems in electroweak symmetry breaking, and predicts many additional new states. The minimal supersymmetric extension of the Standard Model (MSSM) is a model of softly-broken SUSY. The supersymmetric particles (squarks, sleptons, charginos, neutralinos and the gluino) can be massive in comparison to their SM counterparts. Previous and current high-energy physics experiments have put stringent lower bounds on supersymmetric particle masses, while fine-tuning arguments lead us to believe they do not exceed a few TeV. Therefore, a discovery in Run II at the Tevatron is not unlikely [177], and it will fall to the LHC to perform a conclusive search for SUSY, starting in 2008. Combining the energy reach of the LHC with precision measurements at a possible future electron–positron collider ILC, a thorough quantitative understanding of the SUSY particles and interactions would be possible [178].

Most realistically, SUSY will produce a plethora of particle production and decay channels that need to be disentangled and separated from the SM background. To uncover the nature of electroweak symmetry breaking not only have multi-particle production and decay

signatures to be analysed experimentally, an accurate simulation of the model predictions is also needed on the theory side.
Much SUSY phenomenology has been performed over the years in preparation for LHC and ILC, nearly all of it based on relatively simple $2 \to 2$ processes [179, 180] or their next-to-leading-order corrections. These approximations are useful for highly inclusive analyses and convenient for analytical calculations, but should be dropped once interested in precise measurements and their theoretical understanding. Furthermore, for a proper description of data, Monte-Carlo event generators are needed that fully account for high-energy collider environments. Examples for necessary improvements include: consideration of spin correlations [181] and finite-width effects in supersymmetric particle decays [182]; SUSY-electroweak and Yukawa interferences to some SUSY-QCD processes; exact rather than common virtual squark masses; and $2 \to 3$ or $2 \to 4$ particle production processes such as the production of hard jets in SUSY-QCD processes [183] or SUSY particles produced in weak-boson fusion (WBF) [184].
The structure of this chapter is as follows: In Sec. 4.2 the basic requirements for realistic SUSY simulations are considered, in particular a consistent setup of calculational rules and conventions for obtaining correct and reproducible results has to be defined. In the following the event generator AMEGIC++/SHERPA for SUSY processes is presented, cf. Sec. 4.3. It properly takes into account various physics aspects which are usually approximated in the literature, such as those listed above. It is build upon new methods and algorithms for automatic tree-level matrix-element calculation and phase-space generation that have successfully been applied to SM phenomenology. The involved structure of the MSSM requires very extensive and advanced tests of an actual implementation of the theory's Lagrangian into a calculational tool. Accordingly, Sec. 4.4 is devoted to detailed checks of the generator's numerical results. Therefore, predictions for various hundred processes have been compared with the two other existing approaches for calculating multi-particle production processes in the MSSM, namely MADGRAPH/MADEVENT [48, 49, 50] and O'MEGA/WHIZARD [185, 186]. Secs. 4.5 and 4.6 cover one particular application, the physics of sbottom-quarks at the LHC and ILC, respectively. The emphasis thereby lies on off-shell effects of various kinds which for the first time are accurately described using the tools presented here. These phenomenological studies as well as the technical comparison of the three available approaches have been published in [130].

4.2 The calculational framework

Throughout this chapter, it is assumed that the R-parity quantum number is conserved in the MSSM. This assumption constrains both the physical spectrum of the theory and the allowed interactions of the supersymmetric states. The SUSY particle content then consists of the SM particles, the five Higgs bosons, and their superpartners, namely six sleptons,

three sneutrinos, six up-type and six down-type squarks, two charginos, four neutralinos, and the gluino. The MSSM is defined as the general TeV/weak-scale Lagrangian for the SM particles with two Higgs doublets, with gauge- and Lorentz-invariant, R-parity-conserving, renormalisable couplings, and softly-broken supersymmetry. Unfortunately, while this completely fixes the physics, it leaves a considerable freedom in choosing phase conventions. The large number of Lagrangian terms leaves ample room for errors in deriving Feynman rules, coding them in a computer program, and relating the input parameters to a standard convention, cf. Secs. 4.2.1 and 4.2.2. Apart from that, building tools for the simulation of multi-particle production in the MSSM, one is has to deal with Majorana fermions, not present in the SM, and a multitude of unstable heavy particles that can decay through several intermediate steps. The first problem necessitates the introduction of generalised fermionic Feynman rules as discussed in Sec. 4.2.3, while the later requires careful considerations on the treatment of off-shell effects in corresponding calculations, cf. Sec. 4.2.4

4.2.1 Parameters and conventions

As already indicated above no assumptions about the SUSY breaking mechanism shall be made. The MSSM is just defined through a set of weak-scale parameters that serve as inputs for the calculations of production and decay processes of relevance for future collider experiments.

Since only recently there exists now a common format for the definition of a unique set of conventions for inputs to supersymmetric calculations, the so-called SUSY Les Houches Accord (SLHA) [187]. Associated with that is a generic file structure to pass

- supersymmetric model specifications and input parameters,
- electroweak scale supersymmetric mass and coupling spectra, and
- decay information like total and partial widths of supersymmetric particles,

between spectrum calculation programs, codes concerned with the calculation of SUSY decays, and actual event generators. Here the focus shall be only on the last member in the chain, the event generators, that use the output of highly specialised spectrum codes, such as [188, 189], as input for the evaluation of cross sections or the generation of SUSY production and decay events.

Since the SLHA defines weak-scale parameters in a particular renormalisation scheme, it has to be specified how to use them for a tree-level calculations: the electroweak parameters are fixed via the Fermi constant G_μ, m_Z, and α_{qed}. Using the tree-level relations (as required for gauge-invariant matrix elements at tree level) parameters such as $\sin^2\theta_w$ and m_W are obtained as derived quantities; m_W and m_Z are defined as pole masses.

The SLHA uses pole masses for all the MSSM particles, while mixing matrices and Yukawa couplings are given as loop-improved $\overline{\text{DR}}$ values. From this input a set of mass and coupling

parameters suitable for tree-level matrix-element calculations needs to be derived. This can lead to violation of electroweak gauge invariance as discussed in Sec. 4.2.2. However, numerically this is a minor problem, relevant only for very few processes (*e.g.* SUSY particle production in weak-boson fusion [184]) at asymptotically high energies. Accordingly, in practice the loop-improved SLHA masses and mixing matrices are used at face value also in tree-level calculations.

For the bottom- and top-quarks the (running) Yukawa couplings and the masses are identified, as required by gauge invariance. The weak scale as the renormalisation point yields realistic values for the Yukawa couplings. One might be concerned that the kinematical masses are then off from their actual values. However, since the tree-level production cross section should be regarded as the leading contribution to the inclusive cross section, the relevant scale is the energy scale of the whole process rather than the scale of individual heavy quarks. This necessitates the use of running masses to make reliable estimates.

Another delicate issue is related to the possible appearance of negative gaugino mass eigenvalues. Those can be treated on two distinct ways: the negative mass values can directly be used in corresponding propagators and wave functions or the gaugino fields can be rotated to positive masses, what yields complex mixing matrices, even in the case CP is conserved in the SUSY sector.

4.2.2 Unitarity constraints

The MSSM is a renormalisable quantum field theory [190]. To any fixed order in perturbation theory, a partial-wave amplitude calculated from the Feynman rules, renormalised properly, is bounded from above. Cross sections with a finite number of partial waves (*e.g.* s-channel processes) asymptotically fall off like $1/s$, while massless particle exchange must not lead to more than a logarithmic increase with energy. This makes unitarity a convenient check for the Feynman rules used in a matrix-element calculator.

As an example, individual diagrams that contribute to $2 \to 2$ weak boson scattering rise like the fourth power of the energy, but the two leading terms of the energy expansion cancel among diagrams to ameliorate this to a constant. This property connects the three- and four-boson vertices, and predicts the existence and couplings of a Higgs boson, assuming the theory is weakly interacting to high energies [191]. For example, for weak boson fusion to neutralinos and charginos, these unitarity cancellations can be neatly summarised in a set of sum rules for the SUSY masses and couplings [184]. For generic Higgs sectors, the unitarity relations were worked out in [192].

Many, but not all, terms in the Lagrangian can be checked by requiring unitarity. For instance, gauge cancellations in WW scattering to two SUSY particles need not happen if the final-state particle has an $SU(2) \times U(1)$ invariant mass term. In the softly-broken SUSY Lagrangian, this property holds for the gauginos and higgsinos as well as for the

second Higgs doublet in the MSSM. For these particles, it can be expected that unitarity relations impose some restrictions on their couplings, but not a complete set of equations, so some couplings remain unconstrained.

As mentioned above, although doing tree-level calculations often renormalisation-group improved SUSY spectra are used in practice. In principle, these spectra then would need to be adopted for the Higgs sector, where gauge invariance (or unitarity) relates masses, trilinear and quartic couplings. While at tree-level all unitarity relations are automatically satisfied, any improved spectrum will violate unitarity constraints unless the Higgs trilinear couplings are computed in the same scheme. However, not all couplings are known to the same accuracy as the Higgs masses [193]. Following the standard approach of computing the trilinear Higgs couplings from effective mixing angles α and β unitarity violation can be expected. Luckily, this only occurs in $2 \to 3$ processes of the type $WW \to WWH$ [192], while in $2 \to 2$ processes of the type $WW \to HH$ where one might naively expect unitarity violation, the values of the Higgs trilinear couplings change the value of total high-energy asymptotic cross section but do not affect unitarity.

A similar problem arises in the neutralino and chargino sector. Unitarity is violated at high energies in processes of the type $VV \to \tilde{\chi}\tilde{\chi}$ ($V = \mathrm{W}, \mathrm{Z}$) [184]. If using renormalisation-group improved $\overline{\mathrm{DR}}$ neutralino and chargino mass matrices (or equivalently the masses and mixing matrices) the gaugino–higgsino mixing entries which are equivalent to the Higgs couplings of the neutralinos and the charginos implicitly involve $m_{W,Z}$, also in the $\overline{\mathrm{DR}}$ scheme. To ensure proper gauge cancellations which guarantee unitarity, these gauge boson masses must be identical to the kinematical masses of the gauge bosons in the scattering process, which are usually defined in the on-shell scheme. One possible solution would be to extract a set of gauge boson masses that satisfies all tree-level relations from the mass matrices. This scheme has the disadvantage that while it works for the leading corrections, it will likely not be possible to derive a consistent set of weak parameters in general. Moreover, the higher-order corrections included in the renormalisation-group improved neutralino and chargino mass matrices will not be identical to the leading corrections to, for example, the s-channel propagator mass. However, an artificial spectrum that is specifically designed to fulfill the tree-level relations can be used for technical tests of high-energy unitarity. Such detailed checks have been performed for the MadGraph MSSM implementation [184].

4.2.3 Feynman rules for Majorana fermions

Majorana spinors are the crucial new ingredient for calculating helicity amplitudes in supersymmetric field theories. The complication which arises can easily be seen for the process $e^+e^- \to \tilde{\chi}_i^0\tilde{\chi}_j^0$ with $i, j = 1, 2, 3, 4$. There are three types of Feynman diagrams contributing, an s-channel graph where a virtual Z^0 is propagating, and t- and u-channels mediated through scalar-electron exchange, cf. Fig. 4.1. If one naïvely follows the fermion number

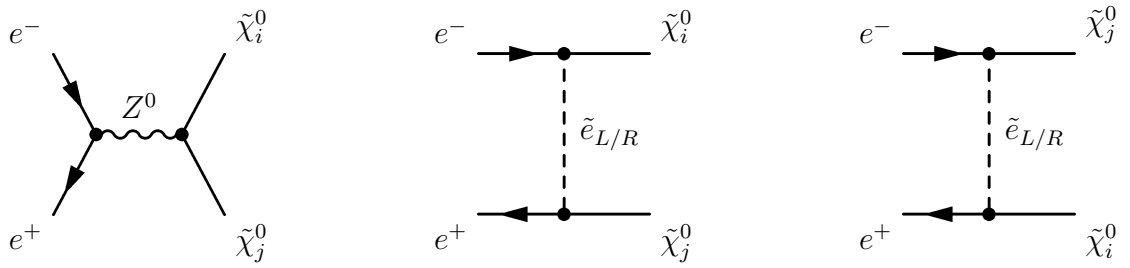

Figure 4.1: Feynman diagrams contributing to the process $e^+e^- \to \tilde{\chi}_i^0\tilde{\chi}_j^0$ $(i,j = 1,2,3,4)$.

flow of the incoming fermions, the t-channel and u-channel amplitudes would require different external spinors for the final-state fermions. Apart from that, using conventional Feynman rules the Relative Signs of Interfering Feynman graphs (RSIF) can not be read off the diagrams but need to be determined using Wick's theorem.
The most elegant algorithm known for evaluating amplitudes of fermion number violating processes is presented in Ref. [194]. These Feynman rules are close to the rules for Dirac fermions. They are based on the introduction of an (arbitrary) orientation for each fermion line. Based on this fermion flow chains of Dirac matrices can be formed and the RSIF is determined as done for Dirac fermions. Besides the well known expression for the Dirac propagator only two analytical expressions for each vertex involving fermions have to be introduced. The method shall be briefly reviewed here.

The basics

Consider a typical interaction term $\mathcal{L}_I = \bar{\chi}\,\Gamma\,\chi$ where each χ can be either a Dirac or a Majorana fermion and Γ denotes a generic fermion interaction including Dirac matrices, coupling constants g^i_{abc} and boson fields Φ:

$$\bar{\chi}\,\Gamma\,\chi = g^i_{abc}\bar{\chi}_a\,\Gamma_i\,\chi_b\Phi_c. \tag{4.1}$$

The field Φ might denote scalar or vector fields and for Γ_i the sixteen matrices of the Clifford algebra can be considered

$$\Gamma_i = 1, i\gamma_5, \gamma_\mu\gamma_5, \gamma_\mu, \sigma_{\mu\nu}. \tag{4.2}$$

Consider a matrix element with fermionic interactions,

$$\left\langle 0 \left| b_{i_1} \dots d_{i_m}\, T\left[(\bar{\chi}\,\Gamma\,\chi)\dots(\bar{\chi}\,\Gamma\,\chi)\right]\, b^\dagger_{i_{m+1}} \dots d^\dagger_{i_n} \right| 0 \right\rangle. \tag{4.3}$$

Here $b_i^\dagger$, $d_i^\dagger$ are the creation operators of fermions and anti-fermions, respectively, and b_i, d_i the corresponding annihilation operators. The index i summarises momentum p_i, spin s_i and possible further quantum numbers. To a specific Feynman graph uniquely correspond certain equivalent sets of contractions of the matrix element.

In the case of Dirac fermions the continuous fermion number flow guarantees that the interaction Lagrangians and the annihilation and creation operators of the external particles can be reordered in such a way that two operators of a contraction are adjacent to each other, e.g.

$$\ldots \underbrace{(\bar{\chi}\,\Gamma\,\chi)}(\bar{\chi}\,\Gamma\,\chi) \ldots . \tag{4.4}$$

For self-conjugated fields the contractions $\underbrace{\chi\,\chi}$ and $\underbrace{\bar{\chi}\,\bar{\chi}}$ are non-vanishing and the fermion number flow is no longer maintained. Nevertheless the interaction Lagrangians and annihilation and creation operators can be reordered such that fields which are contracted are in adjacent interaction Lagrangians. But now the contracted fields in general do not stand next to each other. For instance the following contraction can occur

$$\ldots \underbrace{(\bar{\chi}\,\Gamma\,\chi}\ldots\underbrace{)\ldots} \tag{4.5}$$

It is possible to reverse the interaction Lagrangian $\bar{\chi}\,\Gamma\,\chi$ by introducing the charge-conjugated fields

$$\tilde{\chi} = C\bar{\chi}^T\,, \qquad \bar{\tilde{\chi}} = -\chi^T C^\dagger, \tag{4.6}$$

and the "reversed" vertex Γ',

$$\Gamma' = C\,\Gamma^T\,C^\dagger. \tag{4.7}$$

Using the properties of the charge conjugation matrix C,

$$C^\dagger = C^{-1}\,, \qquad C^T = -C\,, \qquad C\,\Gamma_i^T\,C^{-1} = \eta_i\,\Gamma_i\,, \tag{4.8}$$

with

$$\eta_i = \left\{ \begin{array}{rl} 1 & : \ \Gamma_i = 1, i\gamma_5, \gamma_\mu\gamma_5 \\ -1 & : \ \Gamma_i = \gamma_\mu, \sigma_{\mu\nu}. \end{array} \right. \tag{4.9}$$

one obtains

$$\begin{aligned} \bar{\chi}\,\Gamma\,\chi &= g^i_{abc}\bar{\chi}_a\,\Gamma_i\,\chi_b\Phi_c = g^i_{abc}\,(\bar{\chi}_a\,\Gamma_i\,\chi_b)^T\,\Phi_c = (-1)\,g^i_{abc}\chi_b^T\,\Gamma_i^T\,\bar{\chi}_a^T\Phi_c \\ &= g^i_{abc}\bar{\tilde{\chi}}_b\,C\,\Gamma_i^T\,C^{-1}\tilde{\chi}_a\Phi_c = g^i_{abc}\bar{\tilde{\chi}}_b\,\eta_i\,\Gamma_i\,\tilde{\chi}_a\Phi_c \equiv \bar{\tilde{\chi}}\,\Gamma'\,\tilde{\chi}. \end{aligned} \tag{4.10}$$

Note that the factor of (-1) originating from the anti-commutation of the fermion fields is contained in the definition of Γ'. If both χ's at an interaction vertex are Majorana fermions, namely $\tilde{\chi} = \chi$, Eq. (4.10) implies that $\eta_i\,g^i_{abc} = g^i_{bac}$ for all i, i.e. $\Gamma = \Gamma'$. Using Eq. (4.10) each of the interaction Lagrangians within a fermion chain can be rearranged such that all contracted fields stand next to each other (apart from the first and last field in a closed fermion loop). This procedure replaces the fermion number flow by the more general fermion flow that is equivalent to the orientation of a complete fermion chain. As usual the total sign

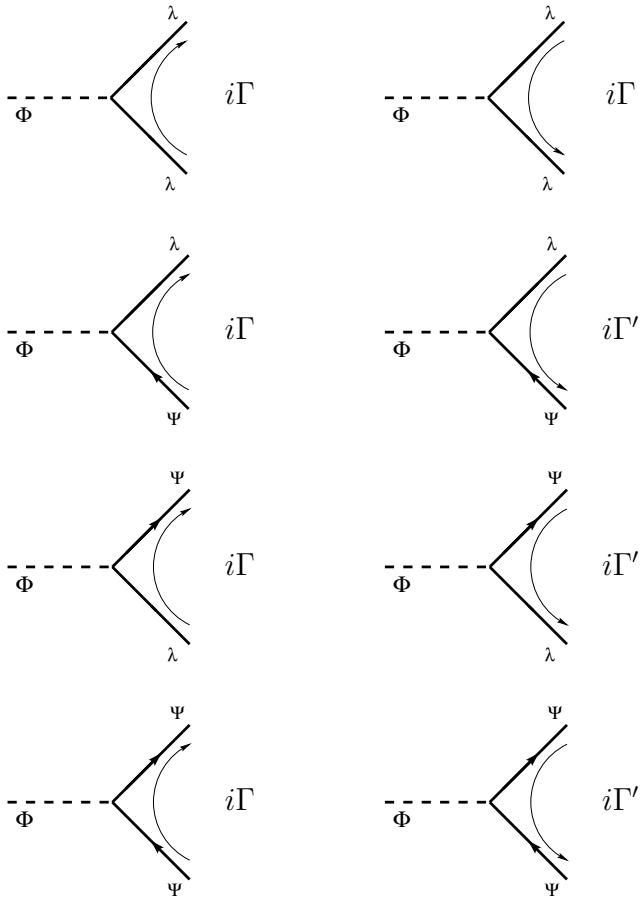

Figure 4.2: The Feynman rules for fermionic vertices with orientation (thin arrows).

of an amplitude is obtained from the permutation of the external creation and annihilation operators.

Using Eq. (4.8) the propagator for the charge-conjugate fermion fields can be derived

$$\langle 0\,|T(\tilde{\chi}\bar{\tilde{\chi}})|\,0\rangle = C\ \langle 0\,|T(\chi\bar{\chi})|\,0\rangle^T\ C^{-1} \tag{4.11}$$

$$\longrightarrow\ C\,S^T(p)\,C^{-1} = C\,\frac{1}{\not{p}-m}\,C^{-1} = \frac{1}{-\not{p}-m} = S(-p) \equiv S'(p). \tag{4.12}$$

For the spinors the following relations hold true

$$u(p,\lambda) = C\,\overline{v}^T(p,\lambda)\,, \qquad v(p,\lambda) = C\,\overline{u}^T(p,\lambda)\,. \tag{4.13}$$

The rules

With the language of the last paragraph the new Feynman rules can be formulated. Fermions are denoted by solid lines and Dirac fermions carry an arrow indicating the fermion number flow. Majorana lines do not carry an arrow. Beside the direct expression of a fermionic vertex obtained from the Lagrangian (Γ) the "reversed" one (Γ') is needed as well, cf. Fig. 4.2.

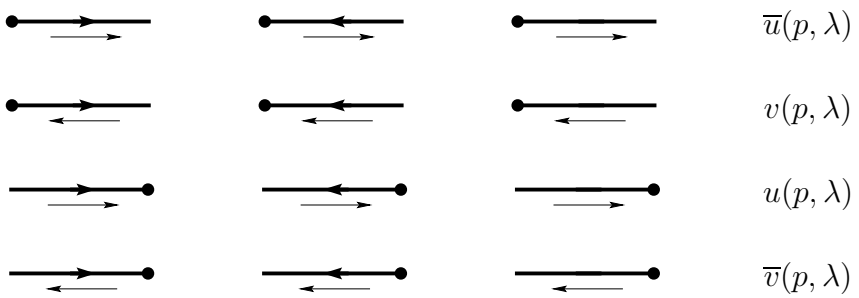

Figure 4.3: The Feynman rules for external fermion lines with orientation (thin arrows). In all cases the flow of the momentum p is from left to right.

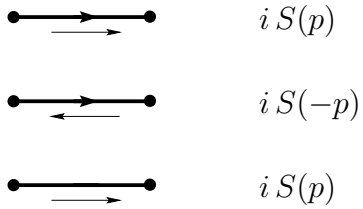

Figure 4.4: The Feynman rules for fermionic propagators with orientation (thin arrows). Again, the momentum p flows from left to right.

For a pure Majorana fermion vertex only one expression is obtained since $\Gamma = \Gamma'$. Reflecting the fermion number flow of Dirac fermions there exists the usual propagator $S(p)$ and the "reversed" one $S'(p) = S(-p)$. Similarly the usual spinors and their "reversed" counterparts are needed for Dirac fermions. Majorana fermions possess only the usual propagator and spinors. There is no need for reversed spinors. This is illustrated in Figs. 4.3 and 4.4.

The algorithm

Algorithmically, Feynman diagrams and their relative signs are constructed via:

- Draw all possible Feynman diagrams for a given process.
- Fix an arbitrary orientation (fermion flow) for each fermion chain.
- Start at any external leg (for closed loops at some arbitrary propagator) and write down the Dirac matrices proceeding opposite to the chosen orientation through the chain.
- For each internal propagator, external line and vertex insert the appropriate analytic expression as given in Figs. 4.2 -4.4, corresponding to the chosen fermion flow. Accordingly, if the orientation is opposite to the fermion number flow the reversed propagators $S(-p)$, spinors and vertices Γ' have to be used.

- Multiply by (-1) for every closed fermion loop.
- Multiply with the permutation parity of the spinors in the obtained analytical expression with respect to some reference order (e.g. the first amplitude that has been evaluated).
- Concerning the determination of combinatorial factors, Majorana fermions need to be treated like real scalar or vector fields.

It should be noted that the analytical expressions are independent of the chosen orientation (fermion flow). Therefore this set of rules guarantees that all sign ambiguities disappear and the RSIF is determined exactly as in the case of Dirac fermions. In Appendix A.2 the application of these Feynman rules is illustrated for the example given above, namely neutralino production at an e^+e^- machine.
The algorithm as presented above is easily applicable for an automated generation of Feynman graphs and corresponding helicity amplitudes and has consequently been implemented in e.g. AMEGIC++/SHERPA, MADGRAPH/MADEVENT and O'MEGA/WHIZARD.

4.2.4 Intermediate heavy states

During the initial phase of the LHC, narrow resonances can be described by simple $2 \to 2$ production cross sections and subsequent cascade decays. However, establishing that these resonances are indeed the long-sought SUSY partners would call for more sophisticated methods.
The identification of resonances as SUSY partners would require determination of their spin and parity quantum numbers [181]. This in turn requires a proper description of the spin correlations among the particles in the production and the decay cascades. The simplest consistent approximation calculates the resonant Feynman diagrams for the $2 \to n$ process and forces narrow intermediate states on the mass shell without affecting spin correlations. For fermions the leading term can be written in the (small) expansion parameter Γ/m as:

$$\frac{1}{|s - m + \mathrm{i}\Gamma|^2} \to \frac{\pi}{m\Gamma}\,\delta(s - m^2)\,. \tag{4.14}$$

The alternative approach of manually inserting the appropriate density matrices for production and decay is more error-prone due to the need for consistent phase conventions.
The width of the heavy resonances are themselves observables predicted by SUSY for a given set of soft breaking parameters and should be taken into account. A naïve Lorentzian smearing of Eq. (4.14) will not yield a theoretically consistent description of finite-width effects. Gauge and SUSY Ward identities are immediately violated once amplitudes are continued off-shell. Since scattering amplitudes in gauge theories and SUSY theories exhibit strong numerical cancellations, the violation of the corresponding Ward identities can result

in numerically large effects. Therefore a proper description of a resonance with a finite width requires a complete gauge invariant set of diagrams, the simplest of which is the set of all diagrams contributing to the $2 \to n$ process [195]. In Secs. 4.5 and 4.6 the numerical impact of finite-width effects for the concrete example of sbottom production at high-energy colliders is studied.
Intermediate charged particles with finite widths present additional gauge invariance issues, which were studied at LEP2 in great detail for W boson production processes [196]. There exist several prescriptions for introducing widths in matrix-element calculations the most prominent one, the fixed-width scheme, is used in all what is described below. A careful analysis on the impact of different choices, as done for SM four- and six-fermion production in [197, 198], is beyond the scope of this work.

4.3 The MSSM implementation in SHERPA

SHERPA [7] is a new complete Monte Carlo event generator for collider physics including hard matrix elements, parton showers, hadronisation and other soft physics aspects, written from scratch in C++. As discussed in chapter 2, the key feature of SHERPA is the implementation of an algorithm [28, 29, 30, 31], which allows for a consistent combination of tree-level matrix elements for the hard production of particles with the subsequent parton showers that model softer bremsstrahlung.
The simulation of supersymmetry with event generators such as SHERPA mainly concerns the evaluation of corresponding partonic production processes and the description of the decays of the produced rather heavy states. For strongly-interacting SUSY particles a parton-shower simulation may sometimes need to be invoked. Some details on parton shower simulations for supersymmetric particles have already been presented in chapter 3. It has to be noted here, that for processes involving strongly-interacting SUSY particles the advanced methods of merging matrix elements with parton showers are not yet realised but remain subject of future research. In SUSY scenarios with R-parity conservation all the SUSY states decay into SM particles and a number of the stable lightest supersymmetric particle that, in order to be consistent with experimental observations, has to be weakly interacting. Accordingly, no modifications to the hadronisation routines are necessary in the physical framework considered here.
Due to the shear multitude of possible SUSY signatures and their calculational complexity automatised tools for matrix-element calculations in the framework of the MSSM are highly desirable. Especially when considering multi-particle final states, that need to be evaluated to separate SUSY from other possible extensions of the SM, sophisticated tools for exact multi-leg tree-level calculations are needed. These codes, called matrix-element generators, are able to calculate nearly arbitrary processes from a given set of Feynman rules for a certain physics model. In Sec. 4.3.1 SHERPA's built-in matrix-element generator,

AMEGIC++, will be briefly introduced. The Feynman rules for the MSSM, that have been incorporated in the program, are discussed in Sec. 4.3.2. Sec. 4.3.3 gives some details about the translation of the SLHA inputs to the parameter convention used for SUSY interactions in AMEGIC++/SHERPA.

4.3.1 Introducing AMEGIC++

AMEGIC++ [21], acronym for (A Matrix Element Generator in C++), is a multi-purpose parton-level generator. It provides a convenient tool for the calculation of cross sections for nearly arbitrary scattering processes at the tree-level in the framework of the Standard Model, the extension of the SM by a general set of anomalous triple- and quartic gauge couplings [22, 23], the Two-Higgs-Doublet Model, the Minimal Supersymmetric Standard Model, and the ADD model of large extra dimensions [24, 25]. Besides calculating production and decay rates AMEGIC++ is used to generate single parton-level events within the event simulation framework of SHERPA. With the help of SHERPA the partonic events can consistently be supplemented with parton showers and linked to hadronisation, leading to realistic hadronic final states.

Specifying a physics model and a certain process AMEGIC++ can automatically generate the corresponding full set of tree-level Feynman diagrams from the complete set of interaction vertices the model possesses. These Feynman diagrams then get translated into helicity amplitudes relying on a formalism similar to the one described in [199, 200]. An extension of the helicity amplitude techniques to incorporate also spin-2 particles has been presented in Ref. [201]. The diagrams then get grouped into sets of amplitudes with a common colour structure. Based on them, the exact matrix of colour factors between amplitudes is calculated using the $SU(3)$ algebra. A number of refinements of the helicity method have been implemented within the code to speed up the matrix-element evaluation or to cope with problems that arise when considering extensions of the SM [202, 203].

Concerning the latter the general set of fermion Feynman rules given in [194] and discussed in Sec. 4.2.3 has been implemented, to unambiguously fix the relative signs amongst Feynman diagrams involving Majorana spinors. Furthermore, explicite polarisations for massive or massless external spin-one bosons are enabled, allowing to consider polarised cross sections. Similar considerations help to replace numerators of spin-one propagators by summing over suitably defined polarisations for off-shell particles, thereby disentangling nested Lorentz structures emerging for amplitudes with many internal spin-one bosons. As a result, the only basic helicity amplitude building blocks AMEGIC++ needs to construct arbitrary processes, are the generic Lorentz structures present in the physics model under consideration. Using the helicity formalism allows to accelerate the matrix-element evaluation by making use of symmetries amongst different Feynman graphs. One example are diagrams with equal colour structure, that possess common factors, as it is illustrated in Fig. 4.5. Accordingly the

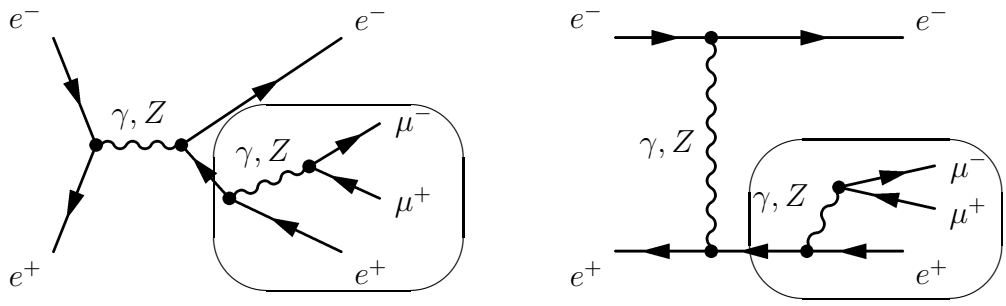

Figure 4.5: Factoring out common pieces of amplitudes with identical colour structure. In the example above, the parts within the boxes are identical, hence terms inside the box can be factored out and the two amplitudes can be added.

identical parts can be factored out and the cutted graphs can be added, thereby reducing the number of complex multiplications to be carried out. Finally, the resulting helicity amplitudes for the process under consideration are stored in library files.
Within AMEGIC++ unstable particles are treated in the fixed-width-scheme (FWS). Defining the complex mass parameters of vector bosons, scalar particles and fermions in terms of the real masses and the constant widths through

$$M_V^2 = m_V^2 - i\Gamma_V\, m_V\,, \quad M_S^2 = m_S^2 - i\Gamma_S\, m_S\,, \quad M_F = m_F - i\Gamma_F/2\,, \tag{4.15}$$

the corresponding propagators can be written as

$$D_F^{\mu\nu}(q) = \frac{-g^{\mu\nu} + q^\mu q^\nu / M_V^2}{q^2 - M_V^2}\,, \quad D_F(q) = \frac{1}{q^2 - M_S^2}\,, \quad S_F(q) = \frac{\not{q} + M_F}{q^2 - M_F^2}\,. \tag{4.16}$$

For the integration over the phase space of the incoming and outgoing particles AMEGIC++ employs an adaptive multi-channel method according to [204, 205]. Correspondingly, generic elements for phase-space mappings such as for instance propagator-like structures or decays are provided. The individual Feynman diagrams are analysed individually, and one or more suitable phase-space parametrisations for each diagram are automatically created and stored in library files. As an example consider Fig. 4.6, which exhibits a diagram and its translation into propagator- and decay-parametrisations. To further improve the efficiency of the dominant integration channels VEGAS [206] is used to further optimised the found phase-space mappings.
Both, the amplitude and the phase-space parametrisations need to be compiled and linked to the code before the actual integration and event generation starts.

4.3.2 MSSM Feynman rules and conventions

In this paragraph the conventions used for specifying the MSSM interaction vertices in AMEGIC++/SHERPA are presented, they follow closely those used in Ref. [207]. This includes

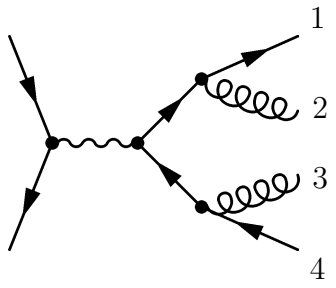

$$D_s(12,34) \times D_a(1,2) \times D_a(4,3) \times P_0(12) \times P_0(34)$$

Figure 4.6: Translation of a Feynman diagram into a phase-space parametrisation. $D_{s,a}$ denote symmetric or asymmetric decays - the latter ones reproduce the typical feature of collinear emission of particles notorious for gauge theories with massless spin-one bosons. The propagator terms for massless particles P_0 peak at the minimal allowed invariant mass.

the definition of the theory's field content, the specification of the possible interactions in a supersymmetric extension of the SM, supplemented with a general set of terms that explicitly break supersymmetry at the electroweak scale.

To account for the observed masses of the electroweak gauge bosons, and to establish finite masses for the SM matter fields, the electroweak symmetry has to be broken. The principles and consequences of the Higgs mechanism in the MSSM are briefly discussed in Sec. 4.3.2.

This paragraph concludes with considerations on the actual particle spectrum in the MSSM, thereby focusing on the definition of the occurring mixing matrices in the various sectors of the model. Having established the mass eigenstates of the theory a complete list of all their interaction vertices can be specified. In Ref. [207] such a full set of Feynman rules is given, and it is this set of vertices, that has been implemented in the AMEGIC++/SHERPA generator.

The field content of the MSSM

As already stated above the MSSM field content consists of the SM fields, extended by a second $SU(2)_L$ Higgs doublet with weak-hypercharge $Y_W = -1$, plus their superpartners that differ in spin by one-half unit. In the following these fields shall be introduced explicitly, to fix the notation used to write down the MSSM Lagrangian later on.

The gauge group structure of the Standard Model before electroweak symmetry breaking, namely $SU(3)_c \otimes SU(2)_L \otimes U(1)_Y$, is reflected by the massless gauge fields of the strong, weak, and electromagnetic interaction. Each of these vector fields gets equipped with a fermionic superpartner called gaugino, that is represented by a two-component Weyl spinor. The resulting fields are listed in Tab. 4.1.

For the SM matter fermions new bosonic fields have to be introduced, the sfermions. The gauge eigenstates of the MSSM matter fields are summarised in Tab. 4.2. The $SU(2)_L$

spin 1/2	spin 1	gauge group	coupling
$\tilde{B}$	B_μ	$U(1)_Y$	g_1
$\tilde{W}^i$	W_μ^i	$SU(2)_L$	g_2
$\tilde{G}^A$	G_μ^A	$SU(3)_c$	g_3

Table 4.1: The gauge and gaugino field content of the MSSM.

spin 0	spin 1/2
$\tilde{Q} = \begin{pmatrix} \tilde{u}_L \\ \tilde{d}_L \end{pmatrix}$	$Q = \begin{pmatrix} u_L \\ d_L \end{pmatrix}$
$\tilde{U} = \tilde{u}_R^*$	$U = (u_R)^c$
$\tilde{D} = \tilde{d}_R^*$	$D = (d_R)^c$
$\tilde{L} = \begin{pmatrix} \tilde{\nu} \\ \tilde{e}_L \end{pmatrix}$	$L = \begin{pmatrix} \nu \\ e_L \end{pmatrix}$
$\tilde{E} = \tilde{e}_R^*$	$E = (e_R)^c$

Table 4.2: The matter fields of the MSSM, expressed in terms of the interaction eigenstates. The $SU(3)_c$ and generation indices are not written explicitly.

singlets are written in terms of the charge conjugated states. For the fermions charge conjugation is denoted by the index c for the scalar superpartner a star is used.
The Higgs fields and their associated partners, the higgsinos, are summarised in Tab. 4.3. Each higgsino doublet contains two Weyl spinors summing up to eight fermionic degrees of freedom (dof) in total and therefore exactly compensating for the scalar dof associated to the Higgs sector, as required by supersymmetry.

The supersymmetric Lagrangian

Having identified the field content of the MSSM its Lagrangian can be introduced. As stated above its construction is guided by requiring invariance under gauge- and SUSY transformations supplemented with the conservation of R-parity.

Kinetic terms

Employing a very compact notation the kinetic terms of the MSSM Lagrangian can be

spin 0	spin 1/2	Y_W
$H^1 = \begin{pmatrix} H_1^0 \\ H_1^- \end{pmatrix}$	$\tilde{H}^1 = \begin{pmatrix} \tilde{H}_1^0 \\ \tilde{H}_1^- \end{pmatrix}$	-1
$H^2 = \begin{pmatrix} H_2^+ \\ H_2^0 \end{pmatrix}$	$\tilde{H}^2 = \begin{pmatrix} \tilde{H}_2^+ \\ \tilde{H}_2^0 \end{pmatrix}$	1

Table 4.3: The MSSM Higgs fields and their superpartners, the fermionic higgsino fields.

condensed to

$$\mathcal{L}_{\text{kin}} = \sum_i \left\{ (D_\mu \Phi_i^*)(D^\mu \Phi_i) + i\bar{\psi}_i \not{D} \psi_i \right\} + \sum_A \left\{ -\frac{1}{4} F^A_{\mu\nu} F_A^{\mu\nu} + \frac{i}{2} \bar{\lambda}_A \not{D} \lambda_A \right\} , \tag{4.17}$$

with D^μ the covariant derivatives of the three SM gauge groups. All scalar fields are denoted by Φ, whereas the fermion fields are summarised by ψ. The only exception are the Majorana gauginos, denoted by λ, and $\lambda^A = (\tilde{B}, \tilde{W}^i, \tilde{G}^A)$. The sum i has to be understood as a sum over all SM fermion fields and their scalar superpartners plus the Higgs fields and their fermionic partners. The sum over A accounts for the gauge fields.

Gauge-type interactions

Not yet included are interactions of the gaugino fields with pairs of associated fermions and scalars, these interactions are generated by the first term of Eq. (4.18),

$$\mathcal{L}_{\text{int}} = -\sqrt{2} \sum_{i,A} g_A \left\{ \Phi_i^* T^A \bar{\psi}_i \lambda_A + h.c. \right\} - \frac{1}{2} \sum_A \left\{ \sum_i g_A \Phi_i^* T^A \Phi_i \right\}^2 . \tag{4.18}$$

Here T^A are the generators of the corresponding gauge group. The second term is equivalent to interactions of four scalars, the interaction strengths are given in terms of the gauge couplings.

Non-gauge interactions, the superpotential

Finally, the superpotential W incorporates non-gauge interactions, like, for instance, Yukawa interactions of the Higgs and matter fields. It is a fully supersymmetric, gauge invariant Lorentz scalar, that has the additional constraint to be analytic in the scalar fields Φ. Conserving R-parity the superpotential is given by

$$W = \epsilon^{ij} \left(\mu H_i^1 H_j^2 + l^{IJ} H_i^1 \tilde{L}_j^I \tilde{E}^J + d^{\text{IJ}} H_i^1 \tilde{Q}_j^I \tilde{D}^J + u^{IJ} H_i^2 \tilde{Q}_j^I \tilde{U}^J \right) , \tag{4.19}$$

where $\epsilon_{ij} = -\epsilon_{ji}$ (with $\epsilon_{12} = 1$) contracts the $SU(2)_L$ doublets. The capital letters I and J are generation indices and μ is the Higgs-mass parameter. The matrices u^{IJ}, d^{IJ}

and l^{IJ} denote the ordinary SM Yukawa couplings. From the superpotential the remaining interaction Lagrangian can be derived

$$\mathcal{L}_W = -\sum_i \left|\frac{\delta W}{\delta \Phi_i}\right|^2 - \frac{1}{2}\sum_{ij}\left\{\bar{\psi}_i \frac{\delta^2 W}{\delta\Phi_i \delta\Phi_j}\psi_j + h.c.\right\}. \tag{4.20}$$

The first term represents quartic scalar interactions, *i.e.* four-squark- and four-slepton interactions as well as interactions of two Higgs fields and two sfermion fields. Furthermore, it provides mass contributions of the scalar Higgs fields and Yukawa-type interactions of the scalar fields. The second term of Eq. (4.20) generates, apart from the SM Yukawa interactions, mass terms for the fermionic higgsino fields and fermion–sfermion–higgsino interactions. For the SM Yukawa interactions it is apparent that the field H_1^0 couples (and later on and gives masses) to down-type quarks and leptons only, while H_2^0 solely couples to the up-type quarks. These two tasks cannot be accomplished by a single Higgs doublet, as the superpotential has to be analytic in the scalar fields.

Explicit supersymmetry breaking

Exact weak-scale supersymmetry can't be realised in nature but must be broken. Breaking scenarios that preserve the desired cancellation of quadratic divergencies in the perturbative expansion of the theory are denoted as soft. Since the underlying dynamics of SUSY breaking is unknown, the most general set of such soft, R-parity conserving effective terms with adjustable free parameters is introduced and defines the most general form of the MSSM. The MSSM soft-breaking Lagrangian can be divided into four parts

$$\mathcal{L}_{\text{soft}} = \mathcal{L}_{\text{soft}}^{\text{g.m.}} + \mathcal{L}_{\text{soft}}^{\text{s.m.}} + \mathcal{L}_{\text{soft}}^{\text{Yuk.}} + \mathcal{L}_{\text{soft}}^{\text{Higgs}}. \tag{4.21}$$

In detail the contributions signify

- Majorana gaugino mass terms,

$$\mathcal{L}_{\text{soft}}^{\text{g.m.}} = -(\frac{1}{2}M_1\tilde{B}\tilde{B} + h.c.) - (\frac{1}{2}M_2\tilde{W}^i\tilde{W}^i + h.c.) - (\frac{1}{2}M_3\tilde{G}^A\tilde{G}^A + h.c.), \tag{4.22}$$

- Mass terms for the scalar fields,

$$\begin{aligned}\mathcal{L}_{\text{soft}}^{\text{s.m.}} = \quad & -(m^2_{\tilde{\text{L}}})^{\text{IJ}}\tilde{L}_i^{\text{I}*}\tilde{L}_i^{\text{J}} - (m^2_{\tilde{\text{E}}})^{\text{IJ}}\tilde{E}^{\text{I}*}\tilde{E}^{\text{J}} \\ & -(m^2_{\tilde{\text{Q}}})^{\text{IJ}}\tilde{Q}_i^{\text{I}*}\tilde{Q}_i^{\text{J}} - (m^2_{\tilde{\text{D}}})^{\text{IJ}}\tilde{D}^{\text{I}*}\tilde{D}^{\text{J}} - (m^2_{\tilde{\text{U}}})^{\text{IJ}}\tilde{U}^{\text{I}*}\tilde{U}^{\text{J}},\end{aligned} \tag{4.23}$$

- Additional Yukawa-type couplings of the scalar fields,

$$\mathcal{L}_{\text{soft}}^{\text{Yuk.}} = \epsilon^{ij}\left(l_S^{\text{IJ}}H_i^1\tilde{L}_j^I\tilde{E}^J + d_S^{\text{IJ}}H_i^1\tilde{Q}_j^I\tilde{D}^J - u_S^{\text{IJ}}H_i^2\tilde{Q}_j^I\tilde{U}^J + h.c.\right), \tag{4.24}$$

- Masses for the Higgs fields

$$\mathcal{L}_{\text{soft}}^{\text{Higgs}} \;=\; - m_{\text{H}^1}^2 H_i^1 H_i^1 - m_{\text{H}^2}^2 H_i^2 H_i^2 - \epsilon^{ij} \left(h_S \, H_i^1 \, H_j^2 + h.c. \right) . \tag{4.25}$$

M_1, M_2, M_3 are the complex bino, wino and gluino masses, respectively. In the second item the $m_{\tilde{L}}^2$ *etc.* are the slepton and squark hermitian 3×3 mass matrices in family space.
The most general form of the soft-breaking Lagrangian allows for a possible fifth kind of contributions, namely Yukawa-type interactions different from that obtained by the superpotential,

$$\mathcal{L}_{\text{soft}}^{\text{n.anal.}} = k_S^{\text{IJ}} \, H_i^{2*} \, \tilde{L}_i^{\text{I}} \, \tilde{E}^{\text{J}} + e_S^{\text{IJ}} \, H_i^{2*} \, \tilde{Q}_i^{\text{I}} \, \tilde{D}^{\text{J}} + w_S^{\text{IJ}} \, H_i^{1*} \, \tilde{Q}_i^{\text{I}} \, \tilde{U}^{\text{J}} + h.c. \, . \tag{4.26}$$

Usually such couplings are not considered since in the case of extending SUSY to supergravity (the local version of SUSY) they must be excluded [208]. If such terms are truly absent once measurements are analysed, their absence provides a clue about how SUSY is broken and how the breaking is transmitted to the low-energy theory.
In contrast to the Standard Model, the masses, flavour rotation angles or phases of the SUSY fields have not yet been measured. So all of the new parameters introduced to accomplish SUSY breaking are *a priori* unknown. However, just the absence of observations of superpartners provides useful information about some of them.

The MSSM particle spectrum

To generate masses for the theory's gauge bosons the electroweak symmetry has to be broken, providing mass terms for the matter fields as well. Out of the derived Lagrangian the mass eigenstates of the theory have to be calculated, leading to the physical spectrum of the model. This is not a trivial task, since any set of sparticles of a given spin, baryon number, lepton number and $SU(3)_c \otimes U(1)_Q$ quantum number can mix and the Feynman rules involving these particles have to be inferred in terms of the corresponding mixing matrices. An exception is the gluino. It is the only colour octet fermion, therefore it can not mix with any other MSSM field even if R-parity is violated. In four-component notation there are eight gluinos $\tilde{G}^A$, which are Majorana fermions with a tree-level mass of M_3.

Electroweak symmetry breaking and the MSSM Higgs bosons

As in the SM the minimum of the scalar potential of the Higgs fields has to break the electroweak gauge symmetry, $SU(2)_L \otimes U(1)_Y \rightarrow U(1)_Q$. This can be accomplished by assigning finite vacuum expectations value (*vev*) to each of the fields H_1^0 and H_2^0, namely

$$\langle H_1^0 \rangle = \frac{1}{\sqrt{2}} \, v_1 \; , \quad \langle H_2^0 \rangle = \frac{1}{\sqrt{2}} \, v_2 \, . \tag{4.27}$$

If instead one of the scalar-squark or slepton fields would aquire a non-zero *vev* this would directly lead to the breaking of colour or lepton number. Note also that even though using

two Higgs doublets, without introducing soft SUSY breaking terms into the Lagrangian it would be impossible to break spontaneously the electroweak gauge symmetry in the MSSM. The ratio

$$\tan\beta \equiv v_2/v_1 \tag{4.28}$$

is a parameter of the theory whose value is not yet fixed by experiment. However, both the *vev*s cannot be chosen freely, instead they are fixed by the following tree-level condition,

$$m_Z = \frac{g_2}{2\,\cos\theta_W}\sqrt{v_1^2+v_2^2} \quad\Longrightarrow\quad \sqrt{v_1^2+v_2^2} = v \approx 246\ \text{GeV}\,, \tag{4.29}$$

where θ_W denotes the Weinberg angle. The Higgs mechanism works in the same manner as in the Standard Model. Before the symmetry is broken, the two complex $SU(2)_L$ doublets have eight real scalar degrees of freedom. Choosing the unitary gauge, after the electroweak symmetry breakdown, three of them are the would-be Nambu–Goldstone bosons $G^0, G^\pm$, that become the longitudinal polarisation modes of the now massive Z^0 and $\mathrm{W}^\pm$ vector bosons. The remaining five degrees of freedom form five physical Higgs particles, one CP-odd neutral scalar A^0, two charged scalars $H^\pm$, and two CP-even neutral scalars h^0 and H^0. The mass eigenstates are obtained by diagonalising the Higgs mass matrix

$$M_{ij}^2 = \frac{1}{2}\,\frac{\partial^2 V}{\partial\phi_i\partial\phi_j}\,, \tag{4.30}$$

that is calculated from the Higgs scalar potential V. In Eq. (4.30) ϕ_i and ϕ_j denote the eight real scalar degrees of freedom of the theory's Higgs sector. M_{ij}^2 splits into four 2×2 block-diagonal factors. The respective mass eigenstates read

$$\begin{pmatrix} G^- \\ H^- \end{pmatrix} = Z_H^{-1}\begin{pmatrix} H_2^{+*} \\ H_1^- \end{pmatrix}, \tag{4.31}$$

$$\begin{pmatrix} G^+ \\ H^+ \end{pmatrix} = Z_H^{-1}\begin{pmatrix} H_2^{+} \\ H_1^{-*} \end{pmatrix}, \tag{4.32}$$

$$\begin{pmatrix} G^0 \\ A^0 \end{pmatrix} = \sqrt{2}\,Z_H^{-1}\begin{pmatrix} \mathrm{Im}[H_2^0] \\ \mathrm{Im}[H_1^0] \end{pmatrix}, \tag{4.33}$$

$$\begin{pmatrix} h^0 \\ H^0 \end{pmatrix} = Z_R^{-1}\begin{pmatrix} \sqrt{2}\,\mathrm{Re}[H_1^0]-v_1 \\ \sqrt{2}\,\mathrm{Re}[H_2^0]-v_2 \end{pmatrix}, \tag{4.34}$$

with

$$Z_H = \begin{pmatrix} \sin\beta & -\cos\beta \\ \cos\beta & \sin\beta \end{pmatrix}, \qquad Z_R = \begin{pmatrix} \cos\alpha & -\sin\alpha \\ \sin\alpha & \cos\alpha \end{pmatrix}. \tag{4.35}$$

The factors for the charged states and the neutral one in the basis $(\mathrm{Im}[\mathrm{H}_2^0], \mathrm{Im}[H_1^0])$ each have one zero eigenvalue, the mentioned would-be Nambu–Goldstone bosons. The tree-level

masses of the physical particles are

$$m^2_{h^0,H^0} = \frac{1}{2}\left(m^2_{A^0} + m^2_Z \mp \sqrt{(m^2_{A^0} + m^2_Z)^2 - 4m^2_{A^0} m^2_Z \cos^2(2\beta)}\right), \tag{4.36}$$

$$m^2_{A^0} = m^2_{H^1} + m^2_{H^2} + 2|\mu|^2, \tag{4.37}$$

$$m^2_{H^\pm} = m^2_W + m^2_{A^0}\,. \tag{4.38}$$

Per definition h^0 is the lighter of two neutral CP-even mass eigenstates. In terms of the tree-level masses, the mixing angle α appearing in Eq. (4.35) is determined by

$$\tan 2\alpha = \tan 2\beta \, \frac{m^2_{A^0} + m^2_Z}{m^2_{A^0} - m^2_Z}\,. \tag{4.39}$$

To obtain the mass eigenstates of the SM quarks, leptons and gauge bosons the same steps as in the SM have to be performed. The quark mixing is parametrised by the known CKM-matrix, V_{CKM}. Assuming neutrinos as massless the charged lepton interaction- and mass eigenstates coincide. The masses of the SM matter fermions expressed in terms of the diagonalised Yukawa couplings and the Higgs *vev*s read

$$m^I_\nu = 0\,, \quad m^I_l = -\frac{v_1 l^I}{\sqrt{2}}\,, \quad m^I_u = \frac{v_2 u^I}{\sqrt{2}}\,, \quad m^I_d = -\frac{v_1 d^I}{\sqrt{2}}\,, \tag{4.40}$$

where l^I and d^I are defined as negative. The neutral gauge boson interaction eigenstates mix to form the physical Z^0 and γ bosons.

Neutralinos and charginos

Once the $SU(2)_L \otimes U(1)_Y$ symmetry is broken the higgsinos and the electroweak gauginos mix with each other and form two mass eigenstates with charge ± 1, the charginos, and four neutral Majorana fermions, the neutralinos.

The neutralinos

In the fermion sector, the neutral fermionic partners of the B and W^3 gauge bosons, $\tilde{B}$ and $\tilde{W}^3$, can mix with the neutral fermion partners of the Higgs bosons, $\tilde{H}^0_1$ and $\tilde{H}^0_2$, to form four Majorana fermion mass eigenstates, the neutralinos. Working in the basis $\tilde{\psi}^0 = (-i\tilde{B},\ -i\tilde{W}^3,\ \tilde{H}^0_1,\ \tilde{H}^0_2)$, the neutralino mass contributions are found to be

$$\mathcal{L}^{\text{neut.}}_{\text{mass}} = -\frac{1}{2}\,(\tilde{\psi}^0)^T\, Y\, \tilde{\psi}^0 + h.c. \tag{4.41}$$

At tree-level the corresponding 4×4 mass matrix reads

$$Y = \begin{pmatrix} M_1 & 0 & -m_Z \cos\beta \sin\theta_W & m_Z \sin\beta \sin\theta_W \\ 0 & M_2 & m_Z \cos\beta \cos\theta_W & -m_Z \sin\beta \cos\theta_W \\ -m_Z \cos\beta \sin\theta_W & m_Z \cos\beta \cos\theta_W & 0 & -\mu \\ m_Z \sin\beta \sin\theta_W & -m_Z \sin\beta \cos\theta_W & -\mu & 0 \end{pmatrix}, \tag{4.42}$$

where the elements M_1 and M_2 originate from the soft-breaking Lagrangian, see Eq. (4.22), and the entries $-\mu$ are the higgsino mass terms from the superpotential, see Eq. (4.20). The terms proportional to m_Z result from the Higgs–higgsino–gaugino interactions, Eq. (4.18). The physical states are found by diagonalising the 4×4 matrix with the help of the unitary matrix Z_N, such that

$$[Z_N^T Y Z_N]_{ij} = \eta_i \, m_{\tilde{\chi}_i^0} \, \delta_{ij} \, . \tag{4.43}$$

The obtained mass eigenvalues can be either positive or negative. The sign of the mass eigenvalues ($\eta_i = \pm 1$) is physically relevant and corresponds to the CP eigenvalue of the neutralino state. The physical masses $m_{\tilde{\chi}_i^0}$ are defined to be positive and fulfill $m_{\tilde{\chi}_1^0} < m_{\tilde{\chi}_2^0} < m_{\tilde{\chi}_3^0} < m_{\tilde{\chi}_4^0}$. Within AMEGIC++/SHERPA, however, the signed masses are used within propagators and spinors, instead of rotating the fields and using a complex mixing matrix.

The charginos

The charginos are a mixture of the charged higgsinos, $\tilde{H}_1^-$ and $\tilde{H}_2^+$, and the fermionic superpartners of the $W^\pm$ gauge bosons, $\tilde{W}^\pm = (\tilde{W}^1 \mp i\tilde{W}^2)/\sqrt{2}$. In the basis $\tilde{\psi}^\pm = (-i\tilde{W}^+, \, \tilde{H}_2^+ \, - i\tilde{W}^-, \, \tilde{H}_1^-)$ terms in the Lagrangian can be rearranged into

$$\mathcal{L}_{\text{mass}}^{\text{char.}} = -\frac{1}{2} \, (\tilde{\psi}^\pm)^T \begin{pmatrix} 0 & X^T \\ X & 0 \end{pmatrix} \tilde{\psi}^\pm + h.c. \, . \tag{4.44}$$

At leading order the 2×2 chargino mass matrix X reads

$$X = \begin{pmatrix} M_2 & \sqrt{2} m_W \sin\beta \\ \sqrt{2} m_W \cos\beta & \mu \end{pmatrix} . \tag{4.45}$$

The diagonal chargino mass matrix is found employing two independent unitary matrices Z^- and Z^+,

$$[(Z^-)^T X Z^+]_{ij} = \eta_i \, m_{\tilde{\chi}_i^+} \, \delta_{ij} \, . \tag{4.46}$$

Again the mass eigenvalues can be positive or negative ($\eta_i = \pm 1$). The physical masses are chosen such that χ_1^+ is lighter than χ_2^+.

The squark and slepton mass matrices

In principle any pair of scalars with identical quantum numbers can mix. Accordingly, when assuming completely arbitrary soft-breaking terms, the mass eigenstates of the squarks and sleptons have to be obtained by diagonalising three 6×6 matrices, for the up-type squarks ($\tilde{u}_L$, $\tilde{c}_L$, $\tilde{t}_L$, $\tilde{u}_R$, $\tilde{c}_R$, $\tilde{t}_R$), the down-type squarks ($\tilde{d}_L$, $\tilde{s}_L$, $\tilde{b}_L$, $\tilde{d}_R$, $\tilde{s}_R$, $\tilde{b}_R$), and the charged sleptons ($\tilde{e}_L$, $\tilde{\mu}_L$, $\tilde{\tau}_L$, $\tilde{e}_R$, $\tilde{\mu}_R$, $\tilde{\tau}_R$). The sneutrino eigenstates are obtained by diagonalisation of the appropriate 3×3 mass matrix. Most often only the mutual mixing of the third generation charged sfermions is important, due to their large Yukawa couplings. However, in

AMEGIC++/SHERPA generation mixing is implemented in the most general form and therefore the complete matrices will be presented here.

The up-type squarks

The fields $\tilde{Q}_1^{\mathrm{I}}$ and $\tilde{U}^{\mathrm{I}}$ with the generation index $I = 1, 2, 3$ form six up-type scalar squarks $\tilde{U}_i$. Diagonalisation of the up-type squark mass matrix is realised by the unitary matrix Z_U, that connects the interaction and mass eigenstates,

$$Z_U^\dagger M_U Z_U = Z_U^\dagger \begin{pmatrix} A^\dagger & D^* \\ D^T & B^* \end{pmatrix} Z_U = \mathrm{diag}\{m^2_{\tilde{U}_1}, \cdots, m^2_{\tilde{U}_6}\}\,, \tag{4.47}$$

$$\tilde{Q}_1^{\mathrm{I}} = Z_U^{\mathrm{Ii}}\, \tilde{U}_i^+\,, \quad \tilde{U}^{\mathrm{I}} = Z_U^{(\mathrm{I}+3)\mathrm{i}*} \tilde{U}_i^-\,. \tag{4.48}$$

At lowest order the elements of the mass matrix are given by

$$A^{IJ} = m_Z^2 \cos(2\beta) \left(\frac{1}{2} - Q_u \sin^2\theta_W\right) \delta^{IJ} + (m_u^I)^2\, \delta^{IJ} + (m^2_{\tilde{Q}})^{KL}\, V_{CKM}^{KI*}\, V_{CKM}^{LJ}\,, \tag{4.49}$$

$$B^{IJ} = Q_u\, m_Z^2\, \sin^2\theta_W\, \delta^{IJ} + (m_u^I)^2\, \delta^{IJ} + (m^2_{\tilde{U}})^{IJ}\,, \tag{4.50}$$

$$D^{IJ} = -\frac{1}{\sqrt{2}} \left[v_1 (u^I\, \mu^*\, \delta^{IJ} + w_S^{IJ}) + v_2\, u_S^{IJ} \right], \tag{4.51}$$

where $Q_u = 2/3$ is the $U(1)_Q$ charge of the up-type squarks and V_{CKM}^{IJ} are elements of the CKM matrix. Note that the most general form of soft-breaking terms has been considered and therefore contributions originating from Eq. (4.26) are taken into account as well.

The down-type squarks

For the case of the down-type squarks the procedure is simular. The six down-type squarks are composed from the fields $\tilde{Q}_2^{\mathrm{I}}$ and $\tilde{D}^{\mathrm{I}}$. The diagonalisation matrix is denoted Z_D and it follows

$$Z_D^\dagger M_D Z_D = Z_D^\dagger \begin{pmatrix} A^T & C \\ C^\dagger & B \end{pmatrix} Z_D = \mathrm{diag}\{m^2_{\tilde{D}_1}, \cdots, m^2_{\tilde{D}_6}\}\,, \tag{4.52}$$

$$\tilde{Q}_2^{\mathrm{I}} = Z_D^{\mathrm{Ii}*}\, \tilde{D}_i^-\,, \quad \tilde{D}^{\mathrm{I}} = Z_D^{(\mathrm{I}+3)\mathrm{i}}\, \tilde{D}_i^+\,, \tag{4.53}$$

with

$$A^{IJ} = -m_Z^2 \cos(2\beta) \left(\frac{1}{2} + Q_d \sin^2\theta_W\right) \delta^{IJ} + (m_d^I)^2\, \delta^{IJ} + (m^2_{\tilde{Q}})^{IJ}\,, \tag{4.54}$$

$$B^{IJ} = Q_d\, m_Z^2\, \sin^2\theta_W\, \delta^{IJ} + (m_d^I)^2\, \delta^{IJ} + (m^2_{\tilde{D}})^{IJ}\,, \tag{4.55}$$

$$C^{IJ} = \frac{1}{\sqrt{2}} \left[v_2 (d^I\, \mu^*\, \delta^{IJ} - e_S^{IJ}) + v_1 d_S^{IJ} \right], \tag{4.56}$$

at tree-level. Again $Q_d = -1/3$ denotes the electric charge of the down-type squarks.

The charged sleptons

The six charged sleptons $\tilde{L}_i$ are mixtures of the fields $\tilde{L}_2^{\rm I}$ and $\tilde{E}^I$. The mass matrix is diagonalised by the 6×6 matrix Z_L,

$$Z_L^\dagger M_L Z_L = Z_L^\dagger \begin{pmatrix} A^T & C \\ C^\dagger & B \end{pmatrix} Z_L = \mathrm{diag}\{m^2_{\tilde{L}_1}, \cdots, m^2_{\tilde{L}_6}\}\,, \tag{4.57}$$

with the mass matrix elements at leading order given by

$$\begin{aligned} A^{IJ} &= -m_Z^2 \cos(2\beta) \left(\frac{1}{2} - \sin^2\theta_W\right) \delta^{IJ} + (m_l^I)^2\,\delta^{IJ} + (m^2_{\tilde{L}})^{IJ}\,, & (4.58)\\ B^{IJ} &= -m_Z^2\, \sin^2\theta_W\, \delta^{IJ} + (m_l^I)^2\,\delta^{IJ} + (m^2_{\tilde{E}})^{IJ}\,, & (4.59)\\ C^{IJ} &= \frac{1}{\sqrt{2}}\left[v_2(l^I\,\mu^*\,\delta^{IJ} - k_S^{IJ}) + v_1 l_S^{IJ}\right]\,. & (4.60) \end{aligned}$$

Here it has been used that the electric charge of the charged sleptons is -1. The relation between the interaction eigenstates and the mass eigenstates is

$$\tilde{L}_2^{\rm I} = Z_L^{\rm Ii*}\,\tilde{L}_i^-\,, \quad \tilde{E}^{\rm I} = Z_L^{\rm (I+3)i}\tilde{L}_i^+. \tag{4.61}$$

The sneutrinos

Out of the three complex scalar fields $\tilde{L}_1^{\rm I}$ one obtains three sneutrino mass eigenstates $\tilde{\nu}_{\rm I}$. Their masses are the eigenvalues of the 3×3 mass matrix M_ν,

$$M_\nu^{IJ} = \frac{1}{2} m_Z^2 \cos(2\beta)\,\delta^{\rm IJ} + (m^2_{\tilde{L}})^{\rm IJ}\,. \tag{4.62}$$

The diagonalisation matrix is called Z_ν and it provides

$$Z_\nu^\dagger M_\nu Z_\nu = \mathrm{diag}\{m^2_{\tilde{\nu}_1}, m^2_{\tilde{\nu}_2}, m^2_{\tilde{\nu}_3}\}\,, \quad \tilde{L}_1^{\rm I} = Z_\nu^{\rm IJ}\,\tilde{\nu}^{\rm J}. \tag{4.63}$$

Most often the slepton soft-breaking masses are considered as diagonal. In that case the sneutrino mixing matrix is diagonal as well and the interaction eigenstates and the mass eigenstates coincide.

4.3.3 Relating to the SLHA inputs

The inclusion of explicite supersymmetry breaking terms in the weak-scale MSSM Lagrangian introduces a wealth of new parameters that actually specify the model and its particle spectrum, and that finally determine its phenomenology. It is the large number of input parameters and the complexity of the MSSM Lagrangian that render setting up a consistent framework for calculations in the MSSM a complicated task. To be able to calculate arbitrary cross sections or decay rates in a certain SUSY scenario, the corresponding set of particle masses, model parameters and mixing matrices needs to be specified beforehand. There exist now various spectrum generator programs that determine the full

set of weak-scale MSSM input parameters from a given high-scale physics supersymmetry breaking scenario [189]. All of those codes use the SUSY Les Houches Accord format to output their calculated spectra, such that they can then easily be used as inputs for cross section calculations or event generation, cf. Sec. 4.2.1. However, in order to be able to make use of the SLHA interface the conventions used there have to be translated to the ones used in the actual calculation. In the following the conversion of the SLHA conventions to the nomenclature used within AMEGIC++/SHERPA is worked out. This corresponds to translating the SLHA output to the conventions used in Ref. [207].
In its present form the SLHA is limited to the case of supersymmetric extensions of the Standard Model, where R-parity and CP are conserved. Apart from that, further assumptions on the structure of the MSSM Lagrangian made are: sfermion mixing is restricted to left-right mixing of the third generation scalar-quarks and scalar-leptons, and the flavour structure of the soft-breaking terms is trivial. Accordingly, the terms given in Eq. (4.26) are not considered, and the slepton, and squark mass matrices $(m_i^2)^{IJ}$ with $i = \tilde{L}$, $\tilde{E}$, $\tilde{Q}$, $\tilde{D}$, $\tilde{U}$ do not introduce additional sources of flavour violation.

Standard Model parameters

As mentioned in Sec. 4.2.1, the SLHA provides the electroweak parameters of the Standard Model in the G_μ-scheme. From G_μ, the Fermi constant from muon decay, m_Z, the Z^0 boson pole mass, and $\alpha_{\mathrm{qed}}(m_Z)$ in the $\overline{MS}$-scheme, the remaining two parameters can be derived, according to

$$m_W = \sqrt{\frac{m_Z^2}{2} + \sqrt{\frac{m_Z^4}{4} - \frac{m_Z^2 \alpha_{\mathrm{qed}}(m_Z)\pi}{\sqrt{2} G_\mu}}}\,, \quad \text{and} \quad \sin^2\theta_W = 1 - \frac{m_W^2}{m_Z^2}\,. \tag{4.64}$$

The strong interaction strength is fixed by $\alpha_{\mathrm{s}}(m_Z)$ in the five-flavour $\overline{MS}$-scheme.

Parameters defining the Higgs sector

The conventions for the parameters specifying the Higgs sector are almost identical for the SLHA and Ref. [207]. The two fields $H_{1,2}^0$ aquire non-zero vacuum expectation values as given in Eq. (4.27), and the relevant parameter $\tan\beta$ is again defined as

$$\tan\beta \equiv v_2/v_1\,, \tag{4.65}$$

fixing the mixing matrix Z_H of the charged and pseudo-scalar Higgs states. To guarantee consistency with tree-level calculations, per default the running of $\tan\beta$ is not taken into account within AMEGIC++/SHERPA. Instead the parameter is fixed to its value at scale m_Z. The convention used for the Higgs mass parameter μ is same in both versions of the MSSM Lagrangian. The last issue to be resolved for the Higgs sector is the parametrisation of the

neutral scalar Higgs mixing. The SLHA defines the corresponding mixing angle α by the mixing matrix

$$\begin{pmatrix} H^0 \\ h^0 \end{pmatrix} = \begin{pmatrix} \cos\alpha & \sin\alpha \\ -\sin\alpha & \cos\alpha \end{pmatrix} \begin{pmatrix} \sqrt{2}\mathrm{Re}[H_1^0] - v_1 \\ \sqrt{2}\mathrm{Re}[H_2^0] - v_2 \end{pmatrix} . \tag{4.66}$$

Accordingly, the matrix elements of the mixing matrix Z_R, defined in Eq. (4.34), are then given by

$$Z_R = \begin{pmatrix} -\sin\alpha & \cos\alpha \\ \cos\alpha & -\sin\alpha \end{pmatrix} . \tag{4.67}$$

Neutralino and chargino mixing

Neutralino mixing

The spinor basis used to describe the mixing in the neutral fermion sector is the same for the SLHA conventions and what is used in the Sec. 4.3.2, namely $\tilde{\psi}^0 = (-i\tilde{B},\ -i\tilde{W}^3,\ \tilde{H}_1^0,\ \tilde{H}_2^0)$. The corresponding neutralino mass matrix defined by

$$\mathcal{L}_{\mathrm{mass}}^{\mathrm{neut.}} = -\frac{1}{2}\,(\tilde{\psi}^0)^T\,\mathcal{M}_{\tilde{\psi}^0}\,\tilde{\psi}^0 + h.c. \tag{4.68}$$

is diagonalised by the 4×4 matrix N according to

$$[N^*\mathcal{M}_{\tilde{\psi}^0}N^\dagger]_{ij} = \eta_i\, m_{\tilde{\chi}_i^0}\,\delta_{ij}\,. \tag{4.69}$$

In case the mixing matrix is found to be complex, the phase gets absorbed into the definition of the corresponding eigenvector. When CP violation is absent the mixing matrix can be chosen strictly real, for the price of having signed masses. Comparing Eq. (4.69) with the corresponding expression for the Feynman rules introduced above, cf. Eq. (4.43), the simple relation

$$Z_N = N^T \tag{4.70}$$

can be inferred.

Chargino mixing

As for the neutralinos the spinor basis state used to describe the mixing in the charged fermion sector coincides for the AMEGIC++/SHERPA rules and the SLHA, namely $\tilde{\psi}^+ = (-i\tilde{W}^+,\ \tilde{H}_2^+)$ and $\tilde{\psi}^- = (-i\tilde{W}^-,\ \tilde{H}_1^-)$. In the SLHA nomenclature the un-symmetric chargino mass matrix gets diagonalised by the 2×2 matrices U and V according to

$$[U^*\mathcal{M}_{\tilde{\psi}^+}V^\dagger]_{ij} = \eta_i\, m_{\tilde{\chi}_i^+}\,\delta_{ij}\,, \tag{4.71}$$

where in the absence of CP violation U and V can be chosen strictly real. Comparing Eq. (4.71) and the corresponding relation for the Feynman rules of Ref. [207], cf. Eq. (4.46), one can read off

$$Z^- = U^T \quad \text{and} \quad Z^+ = V^T\,. \tag{4.72}$$

Sfermion mixing

As stated above, at present sfermion mixing in the SLHA is restricted to the left-right mixing of the third generation sfermion sector only. In contrast, the mixing matrices implemented in AMEGIC++/SHERPA allow for a general mixing of all the slepton, up-type squark and down-type squark states, respectively. Accordingly the charged sfermion mixing matrices are 6×6 instead of 2×2 only. In the SLHA the interaction eigenstates are labeled by $\tilde{f}_{L/R}$ for the $SU(2)_L$ doublet and singlet states, respectively, with $\tilde{f} \in \{t, b, \tau\}$. The resulting mass eigenstates $\tilde{f}_{1/2}$ then refer to the lighter and heavier physical particle, respectively. The mixing is parametrised by the mixing matrix

$$\begin{pmatrix} \tilde{f}_1 \\ \tilde{f}_2 \end{pmatrix} = \begin{pmatrix} F_{11} & F_{12} \\ F_{21} & F_{22} \end{pmatrix} \begin{pmatrix} \tilde{f}_L \\ \tilde{f}_R \end{pmatrix}, \tag{4.73}$$

whose determinant should be ± 1. Comparing this with Ref. [207], this results in $Z_{L/U/D}$ having the form

$$Z_{L/U/D} = \begin{pmatrix} 1 & 0 & 0 & 0 & 0 & 0 \\ 0 & 1 & 0 & 0 & 0 & 0 \\ 0 & 0 & F_{11} & 0 & 0 & F_{21} \\ 0 & 0 & 0 & 1 & 0 & 0 \\ 0 & 0 & 0 & 0 & 1 & 0 \\ 0 & 0 & F_{12} & 0 & 0 & F_{22} \end{pmatrix}. \tag{4.74}$$

As sneutrino mixing is not supported by the SLHA the general mixing matrix present in the Feynman rules of Ref. [207], allowing for non-diagonal soft-breaking terms $(m^2_{\tilde{L}})^{IJ}$, is set to

$$[Z_\nu]_{ij} = \delta_{ij}\,. \tag{4.75}$$

4.4 Comparison with other approaches

Besides AMEGIC++/SHERPA, at present, there exist only two more program packages that can carry out exact tree-level calculations for multi-particle processes in the framework of the MSSM, – MADGRAPH/MADEVENT and O'MEGA/WHIZARD. As AMEGIC++/SHERPA they consist of two more or less independent programs, an automated matrix-element generator, that generates helicity amplitudes for a chosen process, and a library for adaptive phase-space integration and event generation, that produces integrated cross sections and weighted or unweighted event samples.

Beneath these common general features, the similarities of the three tools quickly disappear: they use independently derived Feynman rules with distinct conventions, different algorithms for matrix-element generation, phase-space setup, and integration. Successfully testing these vastly different programs against each other, with a Lagrangian as complex as that of the

TeV-scale MSSM, should give confidence in the predictive power of these programs for SUSY physics at the LHC and later at an ILC.

In Secs. 4.4.1 and 4.4.2 the generators MadGraph/MadEvent and O'mega/Whizard are briefly introduced. For the comparison of the three codes the MSSM with R-parity conservation is considered. A general set of TEV-scale MSSM input parameters is allowed for, with a few simplifying restrictions: (i) CP conservation is assumed, *i.e.* all soft-breaking terms in the Lagrangian are real (cf. also (iii) below); (ii) masses and Yukawa couplings for the first two fermion generations are neglected , *i.e.* left-right mixing occurs only for third-generation squarks and sleptons [1]; (iii) correspondingly, the SM flavour structure is assumed to be trivial, $V_{\rm CKM} = V_{\rm MNS} = 1$; (iv) likewise it is assumed that the flavour structure of the SUSY-breaking terms is trivial. In Sec. 4.4.3 an extensive set of $2 \to 2$ scattering processes is considered, that involves and thereby tests all Feynman rules, that could be of any relevance at the LHC and a future ILC. Sec. 4.4.4 focuses on the residual effects that emerge when the above restrictions concerning the MSSM flavour sector are partially lifted.

4.4.1 MadGraph II and MadEvent

MadGraph [48] was the first program allowing fully automated calculations of squared helicity amplitudes in the Standard Model and has been applied to many physics calculations. MadGraph ii is implemented in fortran77. It generates all Feynman diagrams for a given process, performs the colour algebra and translates the result into a fortran77 procedure with calls to the Helas library [210]. During this translation, redundant subexpressions are recognised and computed only once. While the complexity continues to grow asymptotically with the number of Feynman diagrams, this approach generates efficient code for typical applications.

The correct implementation of colour flows for hadron collider physics was an important objective for the very first version of MadGraph, while the implementation of extensions of the SM remained nontrivial for users. MadGraph ii reads the model information from two files and supports Majorana fermions, allowing fully automated calculations in the MSSM. The MSSM implementation makes use and extends the list of Feynman rules that have been derived in the context of [211, 212, 213].

MadEvent [49, 50] uses phase-space mappings based on single squared Feynman diagrams for adaptive multi-channel sampling [205]. The MadGraph/MadEvent package has a web-based user interface and supports shortcuts such as summing over initial-state partons, summing over jet flavours and restricting intermediate states. Interfaces to parton-shower and hadronisation Monte Carlos [214] are available.

[1] This includes neglecting light fermion masses in the neutralino and chargino sector, which would otherwise appear via Yukawa-higgsino couplings. Physically, this is motivated by flavour constraints which forbid large deviations from universality in the first and second generations [209].

4.4.2 O'MEGA and WHIZARD

O'MEGA [185] and WHIZARD [186] were initially designed for e^+e^- linear colliders studies. O'MEGA constructs numerically stable and optimally factorised scattering amplitudes and allows the study of physics beyond the Standard Model. A general treatment of colour was added to O'MEGA only recently and is currently available only in conjunction with WHIZARD. O'MEGA constructs an expression for the scattering matrix element from a description of the Feynman rules and the target programming language. The complexity of these expressions grows only exponentially with the number of external particles, unlike the factorial growth of the number of Feynman diagrams. Optionally, O'MEGA can calculate cascades: long-lived intermediate particles can be forced on the mass shell in order to obtain gauge invariant approximations with full spin correlations.

O'MEGA is implemented in the functional programming language Objective Caml [215], but the compiler is portable and no knowledge of Objective Caml is required for using O'MEGA with the supported models. The tables describing the Lagrangians can be extended by users. Its set of MSSM Feynman rules was derived in accordance with Ref. [216].

WHIZARD builds a Monte Carlo event generator on the library VAMP [217] for adaptive multi-channel sampling. It uses heuristics to construct phase-space parameterisations corresponding to the dominant time- and space-like singularities for each process. For processes with many identical particles in the final state, symmetries are used extensively to reduce the number of independent channels.

WHIZARD is written in FORTRAN95, with some Perl glue code. It is particularly easy to simulate multiple processes (*i.e.* reducible backgrounds) with the correct relative rates simultaneously. It has an integrated interface to PYTHIA [80] that follows the Les Houches Accord [214] for parton showers and hadronisation.

4.4.3 Pair production of SUSY particles

The setup

As long as R-parity is conserved, SUSY particles are only produced in pairs. Therefore, SUSY phenomenology at the LHC and ILC amounts to essentially searching for all accessible supersymmetric pair-production channels with subsequent (cascade) decays. Proper simulations need to describe this type of processes as accurately as possible. This requires a careful treatment of many-particle final states, off-shell effects and SUSY as well as SM backgrounds. The complexity of this task and the variety of conventions and schemes commonly used require careful cross-checks at all levels of the calculation.

As a first step, a comprehensive list of total cross sections for on-shell supersymmetric pair production processes is presented in Appendix A.4. These results give a rough overview of the possible SUSY phenomenology at future colliders, at least for the chosen point in SUSY

parameter space. The second purpose of this computation is a careful check of the used sets of Feynman rules and their numerical implementation. After testing the tools it is moved on to a proper treatment beyond naïve $2 \to 2$ production processes. All numbers are computed independently with MadGraph, Whizard, and Sherpa, using identical input parameters. The MSSM parameter set used corresponds to the point SPS1a [218]. This point assumes gravity mediated supersymmetry breaking with the universal GUT-scale parameters:

$$m_0 = 100 \text{ GeV} , \quad m_{1/2} = 250 \text{ GeV} , \quad A_0 = -100 \text{ GeV} , \quad \tan\beta = 10 , \quad \mu > 0 . \quad (4.76)$$

The TeV-scale physical spectrum has been computed with SoftSusy [188]. For the purpose of evaluating $2 \to 2$ cross sections, all SUSY particle widths have been set to zero. The final states are all possible combinations of two SUSY partners or two Higgs bosons. The initial states required to test all the SUSY vertices are:

$$e^+e^-,\ e^-\bar{\nu}_e,\ e^-e^-,\ \tau^+\tau^-,\ \tau^-\bar{\nu}_\tau,\ u\bar{u},\ d\bar{d},\ uu,\ dd,\ b\bar{b},\ t\bar{t},$$
$$\mathrm{W}^+\mathrm{W}^-,\ \mathrm{W}^-\mathrm{Z}^0,\ \mathrm{W}^-\gamma,\ \mathrm{Z}^0\mathrm{Z}^0,\ \mathrm{Z}^0\gamma,\ \gamma\gamma,\ g\mathrm{W}^-,\ g\mathrm{Z}^0,\ g\gamma,\ gg,\ ug,\ dg\,.$$

The (partonic) initial-state energy is always fixed. This allows for a comparison of cross sections without dependence on parton structure functions, and with much-improved numerical efficiency. Clearly, some of these initial states cannot be realised on-shell or are even impossible to realise at a collider. They serve only as tests of the Feynman rules. Any MSSM Feynman rule relevant for an observable collider process is involved in at least one of the considered processes. For SM processes, comprehensive checks and comparisons were performed in the past [198, 219].

The complete list of input parameters is given in Appendix A.3. The input is specified in the SLHA format [187]. This ensures compatibility of the input conventions, even though different conventions for the Lagrangian and Feynman rules are used by the different programs.

In Appendix A.4, the results for two partonic c.m. energies $\sqrt{s} = 500$ GeV and 2 TeV are listed and compared. All results agree within a Monte Carlo statistical uncertainty of 0.1% or less. These errors reflect neither the accuracy nor the efficiency of any of the programs; the number of matrix element calls or the amount of CPU time required in the computation is not specified. To obtain a precise $2 \to 2$ total cross section, Monte Carlo integration is not a good choice. On the other hand these simple processes serve as the most efficient framework to test the numerical implementation of Feynman rules and the MSSM spectrum. It has to be emphasised that the three programs MadGraph, Whizard, and Sherpa, and their SUSY implementation are completely independent. They use different conventions, signs and phase choices for the MSSM Feynman rules; have independent algorithms and helicity amplitude libraries; and use different methods for parameterising and sampling the phase space. The results presented can be considered as a strong check that covers all practical aspects of MSSM calculations, from the model setup to the numerical details.

Specifically, the Feynman rules in Ref. [207] can be confirmed as they are used in SHERPA. These Feynman rules do not use the SLHA format, so translating them is a non-trivial part of the implementation. For MADGRAPH and WHIZARD, the Feynman rules were derived independently.

Sample cross sections

The cross section results and their physical interpretation are briefly discussed. While the numbers are specific for the chosen SUSY parameter point SPS1a [218] and its associated mass spectrum, many features of the results are rather generic in one-scale SUSY breaking models and depend only on the structure of the TeV-scale MSSM.

e^+e^- processes

All e^+e^-–induced SUSY production cross sections receive contributions from s-channel Z^0 and (for charged particles) photon exchange. The couplings of the supersymmetric particles to Z^0 and photon are determined by the $SU(2)_L \times U(1)_Y$ gauge couplings and mixing angle. As expected from perturbative unitarity, all s-channel-process cross sections asymptotically fall off like $1/s$. If the process in question includes t-channel exchange, all partial waves have to be summed

$$\frac{m^2}{2p\cdot k + m^2} = \sum_{n=0}^{\infty}\left(\frac{-2p\cdot k}{m^2}\right)^n \Longrightarrow \quad \sigma \propto \frac{1}{s} \times \begin{cases} \log\frac{s}{m^2} & \text{for no vector boson exchange,} \\ \frac{s}{m^2} & \text{for vector boson exchange.} \end{cases} \tag{4.77}$$

The implication of the second line is that Coulomb scattering, WBF, and in some sense all hadronic cross sections, do not decrease with s.

The e^+e^- cross sections are listed in A.4.1. The largest, of up to a few hundred fb at $\sqrt{s} = 500$ GeV, correspond to sneutrino and selectron production, $\tilde{\chi}_1^0$ and $\tilde{\chi}_2^0$, and chargino pair production. These are the processes with a dominant t-channel slepton contribution. In SPS1a the heavier neutralinos $\tilde{\chi}_3^0, \tilde{\chi}_4^0$ are almost pure higgsinos. Higgsinos couple only to the s-channel Z^0, and diagonal pair production of $\tilde{\chi}_3^0\tilde{\chi}_3^0, \tilde{\chi}_4^0\tilde{\chi}_4^0$ is suppressed because of the inherent cancellation between the two higgsino fractions h_u and h_d; *i.e.* the amplitudes are proportional to $|h_u|^2 - |h_d|^2$, which vanishes in the limit where they have the same higgsino masses. Only mixed $\tilde{\chi}_3^0\tilde{\chi}_4^0$ production has a significant cross section, because it is proportional to the sum $|h_u|^2 + |h_d|^2$.

In the Higgs sector, SPS1a realises the decoupling limit where the light Higgs h^0 closely resembles the SM Higgs. The production channels Z^0h, AH^0, and H^+H^- dominate if kinematically accessible, while the reduced coupling of the Z^0 to heavy Higgses strongly suppresses the Z^0H^0 and A^0h^0 channels.

For completeness, the $e^-\bar{\nu}_e$ set of cross sections are also shown in A.4.3, even though such a collider is infeasible.

W^+W^- and WZ^0 processes

The cross sections for weak boson fusion processes, listed in A.4.6 and A.4.7, are generically of the same order of magnitude as their fermion-initiated counterparts, with a few notable differences. In addition to gauge boson exchange, s- and t-channel Higgs exchange contributes to WBF production of third-generation sfermions, neutralinos, charginos, and Higgs/vector bosons. These processes are sensitive to a plethora of Higgs couplings to supersymmetric particles. Furthermore, the longitudinal polarisation components of the external vector bosons approximate, in the high-energy limit, the pseudo-Goldstone bosons of electroweak symmetry breaking. This results in a characteristic asymptotic behaviour (that can be checked by inserting $\sqrt{s}$ values of several TeV, not shown in the tables): the total cross sections for vector-boson and CP-even Higgs pair production in WBF approach a constant at high energy, corresponding to t-channel gauge boson exchange between two scalars. Production cross sections that contain the CP-odd Higgs or the charged Higgs instead decrease like $1/s$, because no scalar-Goldstone-gauge boson vertices exist for these particles.
In the cases involving first and second generation sfermions, t-channel sfermion exchange with an initial-state W contributes only to left-handed sfermions, so the $\tilde{f}_L\tilde{f}_L^*$ cross sections dominate over $\tilde{f}_R\tilde{f}_R^*$. In the neutralino sector, $\tilde{\chi}_1^0$ is dominantly bino and does not couple to neutral Higgs bosons, so $\tilde{\chi}_1^0$ production in W^+W^- fusion is suppressed. The other neutralinos and charginos, being the SUSY partners of massive vector bosons and Higgses, are produced with cross sections up to 100 pb. The largest neutralino rates occur for mixed gaugino and higgsino production, because the Yukawa couplings are given by the gaugino–higgsino mixing entry in the neutralino mass matrix. In the Higgs sector, the decoupling limit ensures that only $W^+W^- \to Z^0h^0$, $WZ^0 \to Wh^0$ (almost 100 pb), and $W^+W^- \to h^0h^0$ (6 pb) are important, while the production of heavy Higgses is suppressed. For $W^+W^- \to A^0h^0$ and $W^-Z^0 \to H^-h^0$ the decoupling suppression applies twice.
In reality, $WW \to XX$ and $WZ^0 \to XY$ scattering occurs only as a subprocess of $2 \to 6$ multi-particle production. The initial vector bosons are emitted as virtual states from a pair of incoming fermions. The measurable cross sections are phase-space suppressed by a few orders of magnitude. A rough estimate can be made by folding the energy-dependent WW/WZ^0 cross sections with weak-boson structure functions. Reliable calculations require the inclusion of all Feynman diagrams, as can be done with the three programs under investigation — the production rates rarely exceed $\mathcal{O}$(ab) at the LHC [184].

Other processes

For the remaining lists of processes with vector-boson or fermion initial states, similar considerations apply. In particular, the photon has no longitudinal component, so γ-induced electroweak processes (Secs. A.4.8, A.4.10 and A.4.11) are not related to Goldstone-pair scattering. Even rather unrealistic fermionic initial states such as $\tau^+\tau^-$, $\tau^-\bar{\nu}_\tau$ and $b\bar{t}$ are

listed in reference tables, cf. Secs. A.4.2, A.4.4 and A.4.5, because they involve Feynman rules that do not occur in other production processes, but are relevant for decays.
Finally, the set of processes studied contains several lists with the coloured fermionic initial states $u\bar{u}$, $d\bar{d}$ and $b\bar{b}$ (Secs. A.4.16–A.4.18, plus Sec. A.4.20 for same-flavour fermions); gg-fusion (Sec. A.4.15); qg-fusion (Sec. A.4.19); and mixed QCD-electroweak processes $\mathrm{g}A^0$, $\mathrm{g}\mathrm{Z}^0$ and gW (Secs. A.4.12, A.4.13 and A.4.14). These (as full hadronic processes) are accessible at hadron colliders, and comparing their cross sections completes the check of Feynman rules of the SUSY-QCD sector and its interplay with the electroweak interactions. Note that for a transparent comparison the quark- and gluon-induced processes are not folded with structure functions.
The only Feynman rules not checked by any process in this list are the four-scalar couplings. It is expected, and has explicitly been verified for the four-Higgs coupling in particular [220], that these contact interactions are not accessible at any collider in the foreseeable future. They have therefore been neglected for the comparison.

4.4.4 Flavour mixing

For most of this comparison the quark masses and the mixings of the first two squark and slepton/sneutrino generations have been neglected . With very few exceptions, these effects are numerically rather unimportant or irrelevant for the simulation of SUSY scattering and decay processes. Here a brief account of the consequences of using a non-diagonal CKM matrix shall be given. Full CKM mixing is available as an option for the WHIZARD and SHERPA event generators. For MADGRAPH, it is straightforward to modify the model definition file accordingly.
The CKM mixing matrix essentially drops out from most processes when summing over all quark intermediate and final states. This is due to CKM unitarity, violated only by terms proportional to the quark mass squared over $\sqrt{s}$ in high energy scattering processes. For the first two generations, such corrections are negligible at the energies considered here.
At hadron colliders, summation over initial-state flavours does not lead to cancellation because the parton densities are flavour-dependent. In the SM, CKM structure matters only for charged-current processes where a $\mathrm{q}\bar{\mathrm{q}}'$ pair annihilates into a W boson. For instance, the cross section for $u\bar{d} \to \mathrm{W}^{+*} \to X$ is multiplied by $|V_{ud}|^2$, and the cross section for $u\bar{s} \to \mathrm{W}^{+*} \to X$ is proportional to $|V_{us}|^2$.
In the partonic final state, CKM unitarity ensures that a cross section does not depend on flavour mixing. However, jet hadronisation depends on the jet quark flavour. Neglecting CKM mixing can result in a wrong jet-flavour decomposition. In practice, this is not relevant since jet-flavour tagging (except for b quarks, and possibly for c quarks) is impossible. In cases where it is relevant, *e.g.* charm tagging in Higgs decay backgrounds at an ILC, the problem may be remedied either by reverting to the full CKM treatment, or by rotating the

CKM diagonal	
$u\bar{u} \to \tilde{d}_L \tilde{d}_L^*$	166.621(8)
$u\bar{u} \to \tilde{s}_L \tilde{s}_L^*$	175.686(9)
$d\bar{d} \to \tilde{u}_L \tilde{u}_L^*$	174.678(9)
$d\bar{d} \to \tilde{c}_L \tilde{c}_L^*$	178.113(9)

with CKM	
$u\bar{u} \to \tilde{d}_L \tilde{d}_L^*$	160.547(8)
$u\bar{u} \to \tilde{s}_L \tilde{s}_L^*$	168.733(8)
$d\bar{d} \to \tilde{u}_L \tilde{u}_L^*$	167.875(8)
$d\bar{d} \to \tilde{c}_L \tilde{c}_L^*$	170.984(9)

Table 4.4: Squark production cross sections computed using SHERPA/WHIZARD with and without non-trivial CKM mixing.

outgoing quark flavours before hadronisation on an event-by-event basis.

To estimate the impact of CKM mixing on SUSY processes, the electroweak production of two light-flavour squarks at the LHC: $q\bar{q} \to \tilde{q}'\tilde{q}'^*$ is considered. Adopting the input of Appendix A.3 and standard values for the CKM mixing parameters reduces the cross section by about 4%, Tab. 4.4. This is negligible for LHC phenomenology, but ensures a correct implementation of CKM mixing in the codes.

Finally, there can be nontrivial flavour effects in the soft SUSY-breaking parameters. That is, if squark mixing differs from quark mixing, in the case of flavour-dependent SUSY breaking [209]. Non-minimal flavour violation predicts large signals for physics beyond the Standard Model, in particular flavour-changing neutral currents, in low-energy precision observables like kaon mixing. Their absence is a strong indication of flavour universality in a SUSY breaking mechanism. The MSSM implementation in SHERPA allows for nontrivial SUSY flavour effects, provided the SLHA input routines are adopted correspondingly (cf. Sec. 4.3). In principle, these effects can be also be included in MADGRAPH and WHIZARD with some minor modifications.

4.5 Sbottom production at the LHC

A SUSY process of primary interest at the LHC is bottom squark production. For this specific discussion, a SUSY parameter point with rather light sbottoms and a rich low-energy phenomenology is adopted. The complete parameter set is listed in Appendix A.5. The sbottom masses are

$$m_{\tilde{b}_1} = 295.36\,\text{GeV}, \qquad m_{\tilde{b}_2} = 399.92\,\text{GeV}. \tag{4.78}$$

In the following the focus shall be on the decay $\tilde{b}_1 \to b\tilde{\chi}_1^0$ with a branching ratio of 43.2%. The lightest Higgs boson is near the LEP limit, but decays invisibly to neutralinos with a branching ratio of 44.9%. The heavy Higgses are at 300 GeV. The lightest neutralino mass is $m_{\tilde{\chi}_1^0} = 46.84\,\text{GeV}$, while the other neutralinos and charginos are between 106 and 240 GeV. Sleptons are around 200 GeV. The squark mass scale is 430 GeV (except for $m_{\tilde{t}_2}$),

and the gluino mass is 800 GeV. For all the LHC calculations presented in the following the CTEQ5l parton distribution functions [221] have been employed.

A spectacular signal at this SUSY parameter point would of course be the light Higgs. Apart from SUSY decays, the light MSSM Higgs sits in the decoupling region, which means it is easily covered by the MSSM No-Lose theorem at the LHC [222]: for large pseudo-scalar Higgs masses a light Higgs will be seen by the Standard Model searches in the WBF $\tau\tau$ channel. Unfortunately, in most scenarios it would be challenging to distinguish a SUSY Higgs boson from its SM counterpart, after properly including systematic errors. Here, the SUSY parameter point used predicts a large light Higgs boson invisible branching fraction, which would also be visible in the WBF channel [223]. There would be little doubt that this light Higgs is not part of the SM Higgs sector.

It has been checked that the SUSY parameter point under consideration satisfies the low-energy constraints for $\Delta\rho$ [224, 225], $g_\mu - 2$ [226, 227], $b \to s\gamma$ [228, 229] and $B_s \to \mu^+\mu^-$ [230, 231], as well as the exclusion limits for Higgs and SUSY particles. The relic neutralino density [232] is below the observed dark-matter density [233] and therefore allowed.

While this point might look slightly exceptional, in particular because of the large invisible light Higgs branching ratio, the only parameters which matter for sbottom searches at the LHC are the fairly small sbottom masses. The current direct experimental limits come from the Tevatron search for jets plus missing energy, where at least for CDF the jets include bottom quark tags [177]. However, for sbottom production the Tevatron limit has to be regarded as a limit on cross section times branching ratio. The mass limits derived in the light-flavour squark and gluino mass plane assume squark pair production including diagrams with a t-channel gluino, which is strongly reduced for final-state sbottoms. Moreover, strong mass limits arise from associated squark–gluino production, which is also largely absent in the case of sbottoms [211].

Searching for squark and gluino signatures at the LHC as a sign of physics beyond the Standard Model (such as SUSY) has one distinct advantage: once asking for a large amount of missing energy, the typical SM background will involve a W or Z^0 boson. Because squarks and gluinos are strongly interacting, the signal-to-background ratio S/B is automatically enhanced by a factor $\alpha_\mathrm{s}/\alpha_\mathrm{qed}$. This means that for typical squark and gluino masses below $\mathcal{O}$(TeV) it is expected to see signs of new physics right before a light-Higgs signal. Most SUSY mass spectrum information is carried by the squark and gluino cascade decay kinematics [181, 182], and though non-negligible, it can be assumed that QCD effects will not alter these results dramatically [183]. The most dangerous backgrounds to cascade decay analyses may not be SM Z^0+jets events, but SUSY backgrounds, for example simple combinatorics with two decay chains in the same event. The (less likely) case that SUSY particles are produced at the LHC, but do not decay within the detector, is an impressive show of the power of the LHC detectors — finding and studying these particles does not pose a serious problem at either ATLAS or CMS [234].

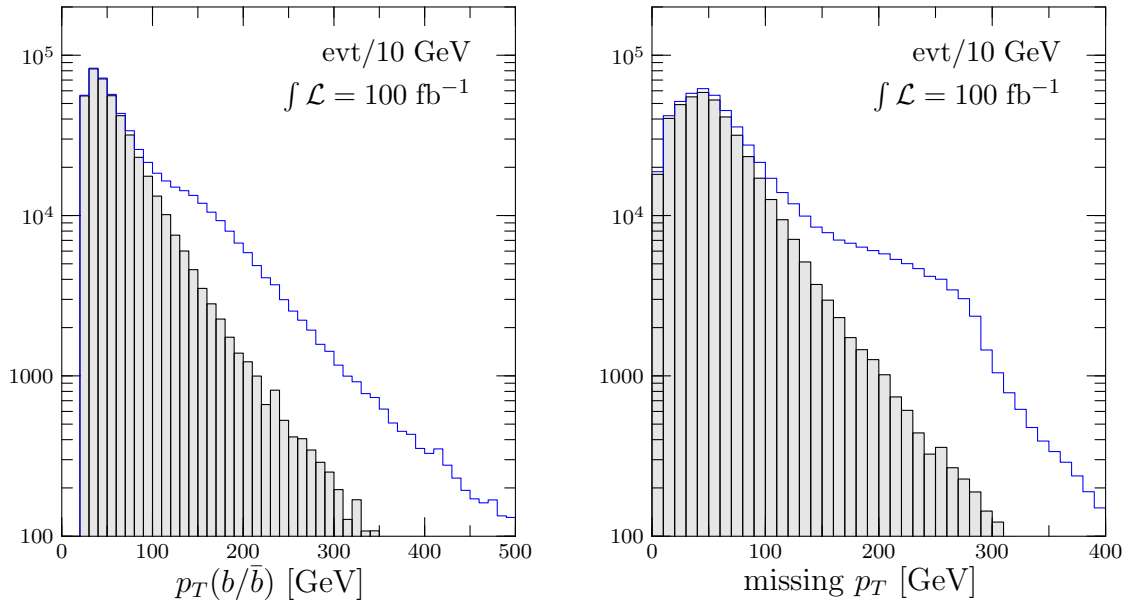

Figure 4.7: The $p_{T,b}^{\max}$ (left) and $\not{p}_T$ (right) distributions for the signal process $gg \to b\bar{b}\tilde{\chi}_1^0\tilde{\chi}_1^0$ and the main SM background $pp \to b\bar{b}\nu\bar{\nu}$, at the LHC. The missing transverse momentum $\not{p}_T$ is defined as the transverse momentum of the $\tilde{\chi}_1^0\tilde{\chi}_1^0$ or $\nu\bar{\nu}$ pair and does not include b decay products. Both processes are evaluated including all off-shell diagrams.

4.5.1 Off-shell effects in sbottom decays

From a theoretical point of view, the production process $pp \to \tilde{b}_1\tilde{b}_1^*$ with subsequent dual decays $\tilde{b}_1 \to b\tilde{\chi}_1^0$ can be described using two approximations. Because the sbottoms are scalars, their production and decay matrix elements can be separated by an approximate Breit-Wigner propagator. Furthermore, the sbottom width $\Gamma_{\tilde{b}_1} = 0.53$ GeV is sufficiently small to safely assume that even extending the Breit-Wigner approximation to a narrow-width description should result in percent-level effects, unless cuts force the sbottoms to be off-shell.

For this entire LHC section basic cuts for the bottom quark are required, whether it arises from sbottom decays or from QCD jet radiation: $p_{T,b} > 20$ GeV and $|\eta_b| < 4$. Any two bottom jets have to be separated by $\Delta R_{bb} > 0.4$. There are no additional cuts, for example on missing transverse energy, because not a full signal vs. background analysis shall be attempted. Instead, the focus is on the approximations which enter the signal process calculation.

To stress the importance of properly understanding the signal process' distributions, the $p_{T,b}^{\max}$ and $\not{p}_T$ for the signal process gg $\to b\bar{b}\tilde{\chi}_1^0\tilde{\chi}_1^0$ and for the main SM background $pp \to b\bar{b}\nu\bar{\nu}$ are depicted in Fig. 4.7. As expected, all final-state particles are considerably harder for the signal process. This is due to heavy intermediate sbottoms in the final state. These kinds of distributions for QCD backgrounds have played an important role illustrating progress

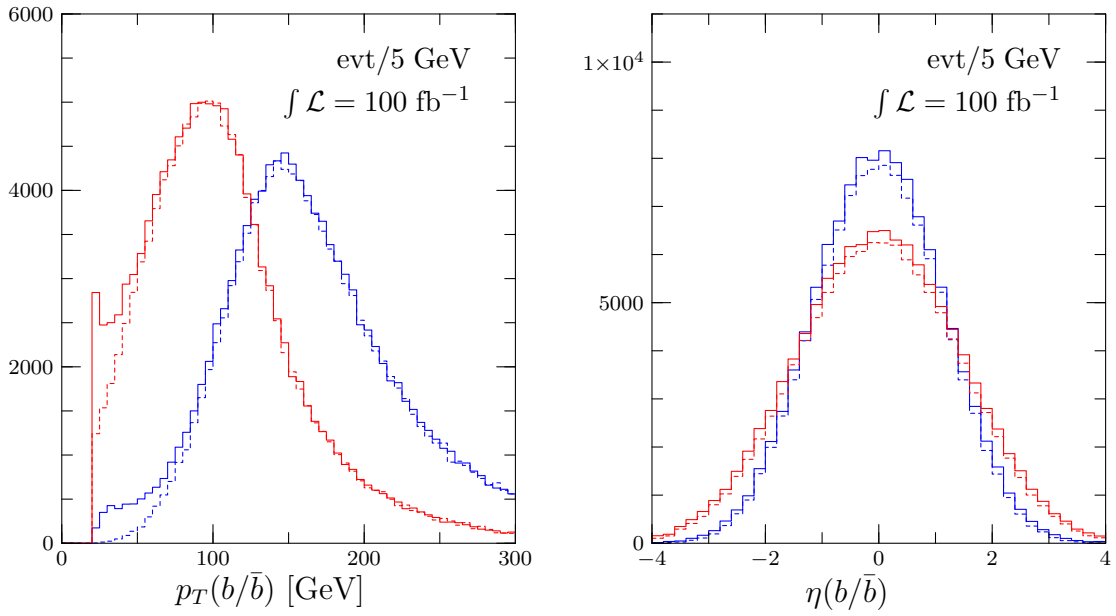

Figure 4.8: The $p_{T,b}$ (left) and η_b (right) distributions for $gg \to b\bar{b}\tilde{\chi}_1^0\tilde{\chi}_1^0$ at the LHC. The blue (red) curves correspond to the harder (softer) of the two b-jets. The dashed lines show the Breit-Wigner approximation for sbottoms; solid lines include all off-shell effects.

in the proper description of jet radiation, a discussion turned to in the next section. The $\not{p}_T$ distribution is only a parton-level approximation, *i.e.* the transverse momentum of the $\tilde{\chi}_1^0\tilde{\chi}_1^0$ or $\nu\bar{\nu}$ pair and does not include b decays. However, the b-decay contributions can be expected to be comparably small and largely balanced between the two sbottom decays.

The effects of the Breit-Wigner approximation compared to the complete set of off-shell diagrams are shown in Fig. 4.8. After basic cuts the cross section for the process gg $\to$ $\tilde{b}_1\tilde{b}_1^* \to b\bar{b}\tilde{\chi}_1^0\tilde{\chi}_1^0$ is 1120 fb. Because of the roughly 250 GeV mass difference between the decaying sbottom and the final-state neutralino, even the softer b-jet p_T distribution peaks at 100 GeV. As expected from phase-space limitations, the harder of the b-jets is considerably more central, but for both of the final-state bottom jets an additional tagging-inspired cut $|\eta_b| < 2.5$ would capture most events. Including all off-shell contributions, *i.e.* studying the complete process gg $\to b\bar{b}\tilde{\chi}_1^0\tilde{\chi}_1^0$, leads to a small cross section increase, to 1177 fb after basic cuts. The additional events are concentrated at softer jet transverse momenta ($p_{T,b} \lesssim$ 60 GeV) and alter the shape of the distributions sizeably. The diagrams which can contribute to off-shell effects are, for example, bottom quark pair production in association with a slightly off-shell Z^0, where the Z^0 decays to two neutralinos. The remaining QCD process gg $\to b\bar{b}$ produces much softer b-jets, because of the lack of heavy resonances. Luckily, this considerable distribution shape change is mostly in a phase-space region plagued by large background, as shown in Fig. 4.7, therefore will be removed in an analysis. On the other hand, there is no guarantee that off-shell effects will always lie in this kind of phase-space

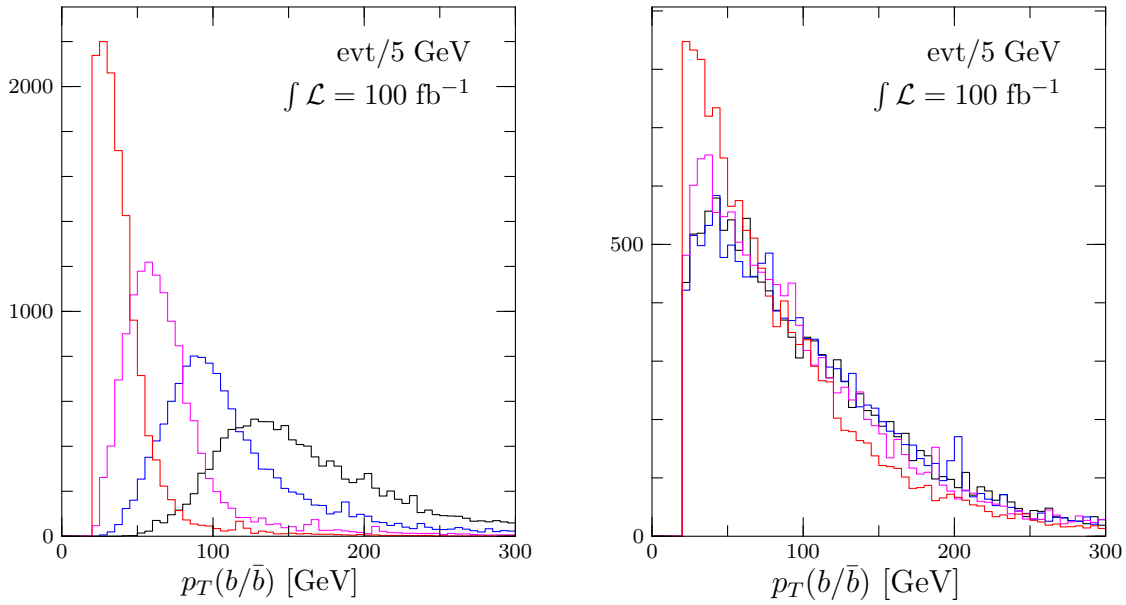

Figure 4.9: The $p_{T,b}$ distributions for the LHC process $gg \to b\bar{b}b\bar{b}\tilde{\chi}_1^0\tilde{\chi}_1^0$. The left panel orders the jets according to their $p_{T,b}$, while in the right panel they are ordered by $|\eta_b|$. These peaks from left to right correspond to more central jets.

region, and from Fig. 4.8 it can be read off that the Breit-Wigner approximation is by no means perfect.

4.5.2 Bottom-jet radiation

Just as with light-flavour squarks in $q\bar{q}$ scattering, LHC could produce sbottom pairs from a $b\bar{b}$ initial state. Bottom densities [235] and SUSY signatures at the LHC are presently undergoing careful study [236]. However, for heavy Higgs production it was shown that bottom densities are the proper description for processes involving initial-state bottom quarks. The comparison between gluon-induced [237] and bottom-induced [238] processes backs the bottom-parton approach, as long as the bottom partons are defined consistently [127, 239]. The bottom-parton picture for Higgs production becomes more convincing the heavier the final-state particles are [240], *i.e.* precisely the kinematic configuration one is interested in for SUSY particles [236].

Sbottom pair production is the ideal process for a first attempt to study the effects of bottom jet radiation on SUSY-QCD signatures. In the fixed-flavour scheme (only light-flavour partons) the leading-order production process for sbottom pairs is $2 \to 2$ gluon fusion. Following fixed-order perturbation theory, the radiation of a jet is part of the NLO corrections [211]. This jet is likely to be an initial-state gluon, radiated off the gg or $q\bar{q}$ initial states. Crossing the final- and initial-state partons, qg scattering would contribute to sbottom pair production at NLO, adding a light-flavour quark jet to the final state. The

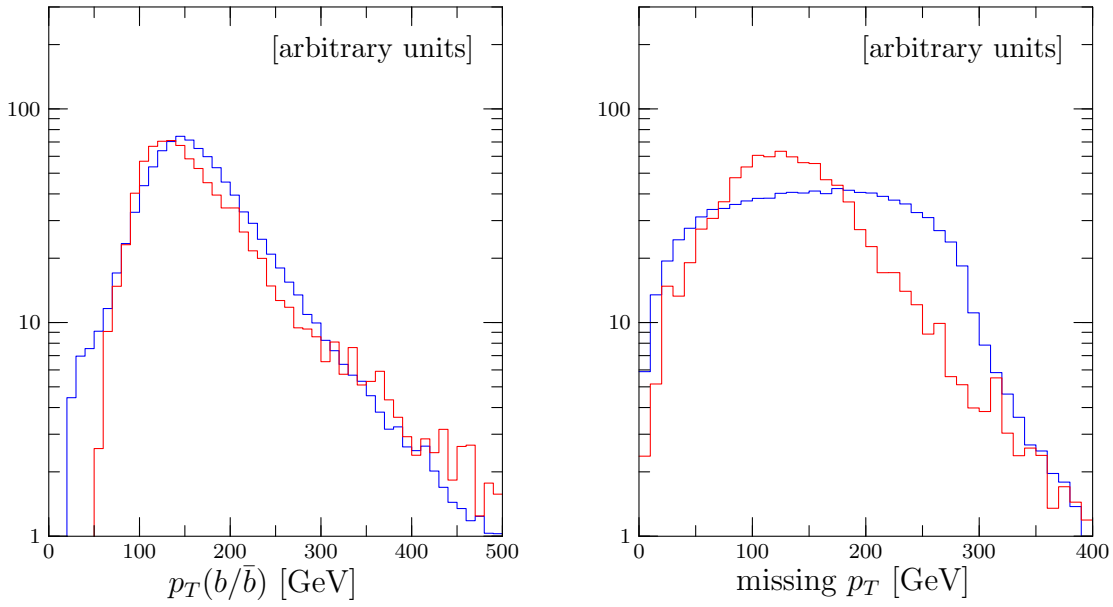

Figure 4.10: The $p_{T,b}^{\max}$ (left) and $\not{p}_T$ (right) distributions for $gg \to b\bar{b}b\bar{b}\tilde{\chi}_1^0\tilde{\chi}_1^0$ (red) and $gg \to b\bar{b}\tilde{\chi}_1^0\tilde{\chi}_1^0$ (blue) at the LHC.

perturbative series for the total rate is stable, and as long as the additional jet is sufficiently hard ($p_{T,j} \gtrsim 50$ GeV), the ratio of the inclusive cross sections is small: $\sigma_{\tilde{b}\tilde{b}j}/\sigma_{\tilde{b}\tilde{b}} \sim 1/3$ [183]. With the radiation of two jets (at NNLO in the fixed-flavour scheme), the situation becomes more complicated. It is known that QCD jet radiation at the LHC is not necessarily softer than jets from SUSY cascade decays [183]. This jet radiation can manifest itself as a combinatorial background in a cascade analysis. Here the energy spectrum of bottom jets from the decay $\tilde{b}_1 \to b\tilde{\chi}_1^0$ is investigated, so additional bottom jets from the initial state lead to combinatorial background. Once radiating two jets from the dominant gg initial state, bottom jets appear as initial-state radiation (ISR). In the total rate this process can be included just by using the variable-flavour scheme in the leading-order cross section, as discussed above.

As expected, the rate for the production process gg $\to b\bar{b}b\bar{b}\tilde{\chi}_1^0\tilde{\chi}_1^0$ of 130.7 fb is considerably suppressed compared to the 1177 fb for inclusive (off-shell) sbottom pair production. Again, $p_{T,b} > 20$ GeV is required. The b-jet multiplicity is expected to decrease once asking for harder b-jets in a proper analysis.

From a more conceptual point of view, the crucial question is how to identify the decay b-jets, which carry information on the SUSY mass spectrum [182]. Because the ISR b-jets arise from gluon splitting, they are predominantly soft and forward in the detector. To identify the decay b quarks one can try to exclude the most forward and softest of the four b-jets in the event, to reduce the combinatorial background. In Fig. 4.9 the ordered $p_{T,b}$ spectra of the four final-state sbottoms are presented. Because of kinematics one may expect that it should not matter if one orders the sbottoms according to $p_{T,b}$ or $|\eta_b|$, at least for

grouping into initial-state and decay jet pairs. However, it is observed, that this kinematical argument is not well suited to remove combinatorial backgrounds. Only the most forward b-jet is indeed slightly softer than the other three, but the remaining three $p_{T,b}$ distributions ordered according to $|\eta_b|$ are indistinguishable.

After discussing the combinatorial effects of additional b-jets in the final state, the important question is whether additional b-jet radiation alters the kinematics of sbottom production and decay. In Fig. 4.10 the $p_{T,b}^{\max}$ and the $\not{p}_T$ distributions for $b\bar{b}\tilde{\chi}_1^0\tilde{\chi}_1^0$ and $b\bar{b}b\bar{b}\tilde{\chi}_1^0\tilde{\chi}_1^0$ production at the LHC are shown; those most likely to be useful in suppressing SM backgrounds. The soft ends of the $p_{T,b}$ distributions do not scale because in the $4b$ case the hardest b-jet becomes less likely to be a decay b-jet. Instead, a soft decay b quark will be replaced with a harder initial-state b-jet. The $4b$ distribution peaks at lower $p_{T,b}$ because the minimum cut on $p_{T,b}$ of the initial-state b-jets eats into the steep gluon densities. At very large values of $p_{T,b}$ this effect becomes relatively less important, and the two distributions scale with each other.

The $\not{p}_T$ distributions, however, are sensitive to $\sum p_{T,b}$. If both b-jets come from heavy particle decays, the decay can alter their back-to-back kinematics. In contrast, additional light particle production balances out the event, leading to generally smaller $\not{p}_T$ values. The situation in the final analysis may be better, because a proper analysis after background rejection cuts will be biased toward small $\not{p}_T$, thus will be less sensitive to b-jet radiation and combinatorial backgrounds.

4.6 Sbottom production at an ILC

At an ILC it would be possible to obtain more accurate mass and cross section measurements, provided the collider energy is sufficient to produce sbottom pairs. This is due to the much cleaner lepton collider environment, relative to a hadron collider – even though the lower rate can statistically limit measurements. For this study again the parameter point described in Appendix A.5 is chosen. There, the sbottom mass is low, but the appearance of various Higgs and neutralino backgrounds complicates the analysis.

With sbottom production a process is encountered where multiple channels and their interferences contribute to the total signal rate; this is more typical than not. Off-shell effects have to be well understood to perform a sensible precision analysis. Assuming 800 GeV collider energy, the production channels $\tilde{b}_1\tilde{b}_1^*$ and $\tilde{b}_1\tilde{b}_2^*$ are open. From the squark-mixing matrix it can be seen that the lighter of the two sbottoms, $\tilde{b}_1$, predominantly is right-handed. Its main decay mode is to $b\tilde{\chi}_1^0$. Therefore, as with sbottom production at the LHC, the principal final state to be studied is $b\bar{b}$ plus missing energy.

At the LHC, sbottom pair production dominates this final state because it is the only strongly-interacting production channel. In contrast, sbottom pair production at an ILC would proceed via electroweak interactions. Hence, all electroweak SUSY and SM processes

Channel	$\sigma_{2\to2}$ [fb]	$\sigma \times$ BR [fb]	σ_{BW} [fb]
Z^0h^0	20.574	1.342	1.335
Z^0H^0	0.003	0.000	0.000
h^0A^0	0.002	0.001	0.000
H^0A^0	5.653	0.320	0.314
$\tilde{\chi}_1^0\tilde{\chi}_2^0$	69.109	13.078	13.954
$\tilde{\chi}_1^0\tilde{\chi}_3^0$	24.268	3.675	4.828
$\tilde{\chi}_1^0\tilde{\chi}_4^0$	19.337	0.061	0.938
$\tilde{b}_1\tilde{b}_1$	4.209	0.759	0.757
$\tilde{b}_1\tilde{b}_2$	0.057	0.002	0.002
Sum		19.238	22.129
Exact			19.624
w/ISR			22.552

Channel	$\sigma_{2\to2/3}$ [fb]	$\sigma \times$ BR [fb]	σ_{BW} [fb]
$\mathrm{Z}^0\mathrm{Z}^0$	202.2	12.6	13.1
Z^0h^0	20.6	1.9	1.9
Z^0H^0	0.0	0.0	0.0
$\mathrm{Z}^0\bar{\nu}\nu$	626.1	109.9	111.4
$h^0\bar{\nu}\nu$	170.5	76.5	76.4
$H^0\bar{\nu}\nu$	0.0	0.0	0.0
Sum		186.5	187.7
Exact			190.1
w/ISR			174.2

Table 4.5: SUSY cross sections contributing to $e^+e^- \to b\bar{b}\tilde{\chi}_1^0\tilde{\chi}_1^0$ (left) and the SM background $e^+e^- \to b\bar{b}\nu\bar{\nu}$ (right). The columns assume: on-shell production; same, including the branching ratio into $b\bar{b}\tilde{\chi}_1^0\tilde{\chi}_1^0$ and $b\bar{b}\nu\bar{\nu}$; and with a Breit-Wigner propagator. The incoherent sum is shown at the bottom. In the SM case, only the $2 \to 3$ processes are summed, to avoid double-counting. The exact tree-level result includes all Feynman diagrams and interferences. The last line shows the effect of initial-state radiation (ISR) and beamstrahlung.

that contribute to the same final state need to be considered. In particular, the following $2 \to 2$ production processes contribute to $e^+e^- \to b\bar{b}\tilde{\chi}_1^0\tilde{\chi}_1^0$:

$$e^+e^- \to \mathrm{Z}^0h^0,\ \mathrm{Z}^0H^0,\ A^0h^0,\ A^0H^0,\ \tilde{\chi}_1^0\tilde{\chi}_2^0,\ \tilde{\chi}_1^0\tilde{\chi}_3^0,\ \tilde{\chi}_1^0\tilde{\chi}_4^0,\ \tilde{b}_1\tilde{b}_1^*,\ \tilde{b}_1\tilde{b}_2^*\,. \tag{4.79}$$

All cross sections, in different approximations as well as in a complete calculation including all interferences, are displayed in Table 4.5. Once folding in the branching ratios, fewer processes contribute significantly, namely:

$$e^+e^- \to \mathrm{Z}^0h^0,\ A^0H^0,\ \tilde{\chi}_1^0\tilde{\chi}_2^0,\ \tilde{\chi}_1^0\tilde{\chi}_3^0,\ \tilde{b}_1\tilde{b}_1^*,\ \tilde{b}_1\tilde{b}_2^*\,. \tag{4.80}$$

The SM process $e^+e^- \to b\bar{b}\nu_i\bar{\nu}_i$ $(i = e, \mu, \tau)$ is dominated by WW fusion to Z^0/h^0 (followed by $\mathrm{Z}^0/h^0 \to b\bar{b}$) and by $\mathrm{Z}^0h^0/\mathrm{Z}^0\mathrm{Z}^0$ pair production. It represents a significant irreducible background, as a neutrino cannot be distinguished from the lightest neutralino in high-energy collisions. Thus, this final state with neutrinos is referred to as SM background.

4.6.1 Numerical approximations

It is instructive to compare various levels of approximation found in the literature before moving to a complete treatment of the process. The simplest approximation for resonant production and decay is to multiply the production cross section by the appropriate branching fraction. This narrow width approximation (NWA) is expected to hold as long as $\Gamma/m \ll 1$. In traditional Monte Carlos, angular correlations are lost for scalar resonances unless spin correlations along the lines of Ref. [241] are included.
It can be improved upon this by constraining the intermediate state to resonances (in the case considered the two sbottoms) and inserting Breit-Wigner propagators. Such an approach takes into account off-shell corrections that originate from the nontrivial resonance kinematics. However, the Breit-Wigner amplitude is not gauge-invariant off-resonance, thus the precise result depends on the choice of gauge (here unitarity gauge). Both, this approximation and the NWA neglect interferences with off-resonant diagrams.
To obtain the full tree-level result, all Feynman graphs and their interferences must be taken into account, and an unambiguous breakdown into resonance channels is no longer possible. Perturbation theory breaks down at the poles of intermediate on-shell states. The emerging divergences have to be regularised, for example via finite particle widths which unitarise the amplitude. Not surprisingly, naïvely including particle widths violates gauge invariance, but schemes exist which properly address this problem [196]. Here the fixed-width scheme shall be used, which includes the finite width even in the spacelike region and avoids problems of gauge invariance in the processes considered here.
Finally, in many cases the effects of initial-state radiation (ISR) and beamstrahlung are numerically of the same order of magnitude as the full resonance and interference corrections, or even larger, and therefore need to be addressed.

4.6.2 Particle widths

As discussed before, the finite widths for all intermediate particles that can become on-shell must be included. For the processes discussed here this includes the neutral Higgs and Z^0 bosons, the neutralinos, and the sbottoms. It is tempting to merely treat the widths as externally fixed numerical parameters. This, however, can lead to a mismatch: consider a tree-level process with an intermediate resonance with mass M and total width Γ. The tree-level cross section contains a factor

$$\frac{1}{(p^2 - M^2)^2 + M^2\Gamma^2} \,.$$

In the vicinity of the pole a factor $1/\Gamma$ is picked up. If $\Gamma \ll M$, this contribution to the cross section can be approximated by the on-shell production cross section multiplied by the branching ratio for resonance decay into the desired final state X, *i.e.* $\mathrm{BR}_X = \Gamma_X/\Gamma$ (cf. Sec. 4.2.4). While the total width Γ is an external numerical parameter, the partial width

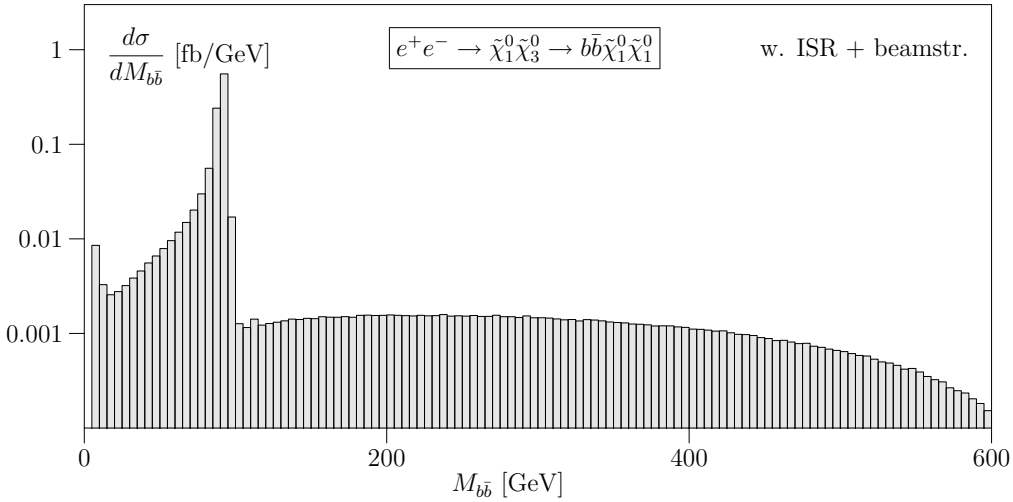

Figure 4.11: The $b\bar{b}$ invariant mass distribution for the $\tilde{\chi}_1^0\tilde{\chi}_3^0$ contribution to $e^+e^- \to b\bar{b}\tilde{\chi}_1^0\tilde{\chi}_1^0$.

Γ_X is implicitly computed by the integration program at tree-level during cross section evaluation. This can lead to a noticeable mismatch, especially if the external full width is calculated with higher-order corrections. Formally, the use of loop-improved widths induces an order mismatch in any leading-order calculation, which, in principle, is allowed. However, in reality, dominant corrections might reside in both the decay (width) calculation and the production process, canceling each other in the full result. The NLO corrections to the full process that would remedy the problem are generally unavailable, at least in a form suitable for event generation [242]. To illustrate this reasoning, consider a case where the resonance has only one decay channel. Then, in the narrow-width limit, the factorised result is reproduced only if the tree-level width is taken as an input computed from exactly the same parameters as the complete process.

While this looks like a trivial requirement, it should be stressed that most MSSM decay codes return particle widths that include higher orders, either explicitly or implicitly through the introduction of running couplings and mass parameters. Similarly, for the Z^0 boson width one is tempted to insert the measured value, which in the best of all worlds corresponds to the all-orders perturbative result. To avoid the problems mentioned above, the relevant particle widths are calculated in the same tree-level framework used for the full process. For completeness, they are listed in Tab. A.1 of Appendix A.5, corresponding to the SLHA input file used for the collider calculation. The corresponding leading-order widths agree with those of SDECAY [243].

4.6.3 Testing the Narrow Width Approximation

An estimate of the effects of the NWA and of Breit-Wigner propagators is shown in Tab. 4.5. In replacing on-shell intermediate states by Breit-Wigner functions in the SUSY processes

(left panel) the total cross section increases by 15%. Breaking the cross section down into individual contributions, it becomes apparent that this increase is mainly due to the heavy neutralino channels. In contrast, the Z^0, Higgs and sbottom channels are fairly well-described by the on-shell approximation of Eq. (4.14). Including the complete set of all tree-level Feynman diagrams with all interferences results in a decrease of 11%. Obviously, continuum and interference effects are non-negligible and must be properly taken into account.

Similar considerations apply to the SM background, $e^+e^- \to b\bar{b}\nu\bar{\nu}$, shown in the right panel of Tab. 4.5. At a collider energy of 800 GeV, the SM process is dominated by weak boson fusion, while pair production (Z^0Z^0/Z^0H^0) borders on negligible. For the total cross section, the NWA works well: inserting Breit-Wigner propagators for the intermediate Z^0, h states increases the rate by a mere 0.6%, and including all diagrams with interferences leads to a further increase of only 1.3%.

Finally, the effect of ISR and beamstrahlung is calculated: the SUSY cross section increases by 15% — a general effect seen for processes dominated by particle pair production well above threshold. (In that range the cross sections are proportional to $1/\hat{s}$ and therefore profit from the reduction in effective energy due to photon radiation.) In contrast, for the SM background, adding ISR and beamstrahlung amounts to a reduction by 8%. This is expected for a t-channel-dominated process with asymptotically flat energy dependence.

Apart from total cross sections, it is crucial to understand off-shell effects in distributions. They are significant in the neutralino channels $e^+e^- \to \tilde{\chi}_1^0\tilde{\chi}_i^0$ ($i = 2, 3, 4$), the dominant SUSY backgrounds to the sbottom signal. For this mass spectrum, the $\tilde{\chi}_2^0$ has a three-body decay to $q\bar{q}\tilde{\chi}_1^0$; here the focus is on $q = b$. The higgsino-like $\tilde{\chi}_3^0$ has a two-body decay $\tilde{\chi}_3^0 \to Z^0\tilde{\chi}_1^0$ with a branching fraction close to 100% [243].

In the complete calculation, neither the decaying $\tilde{\chi}_3^0$ nor the intermediate Z^0 is forced on-shell. Continuum effects play a role. This explains the differences in the decay spectrum between the full calculation and the approximation using Breit-Wigner propagators, as seen in Fig. 4.11. There, neutralino pair production, $e^+e^- \to \tilde{\chi}_1^0\tilde{\chi}_3^0$, is included. In Fig. 4.11 the $b\bar{b}$ invariant mass spectrum for the process $e^+e^- \to \tilde{\chi}_1^0\tilde{\chi}_3^0 \to b\bar{b}\tilde{\chi}_1^0\tilde{\chi}_1^0$ is depicted. Assuming a two-body $\tilde{\chi}_3^0$ decay, a sharp Breit-Wigner Z^0 resonance at 91.18 GeV may be expected. Instead, the resonance is not Breit-Wigner-like and is surrounded by a nearly flat continuous distribution at both high and low masses. Clearly, this would not be accounted for by a factorised production–decay approximation. In fact, it stems from a highly off-shell three-body decay $\tilde{\chi}_3^0 \to b\bar{b}\tilde{\chi}_1^0$ via an intermediate sbottom. As a background to sbottom pair production, this process gives the dominant contribution, because it can be easily cutted against on-shell neutralino production. The significant low-mass tail explains the 30% enhancement for this channel seen in Tab. 4.5. Similar reasoning holds for other channels.

The results in Tab. 4.5 also demonstrate that photon radiation, both in the elementary process (ISR) and as a semi-classical interaction of the incoming beams (beamstrahlung),

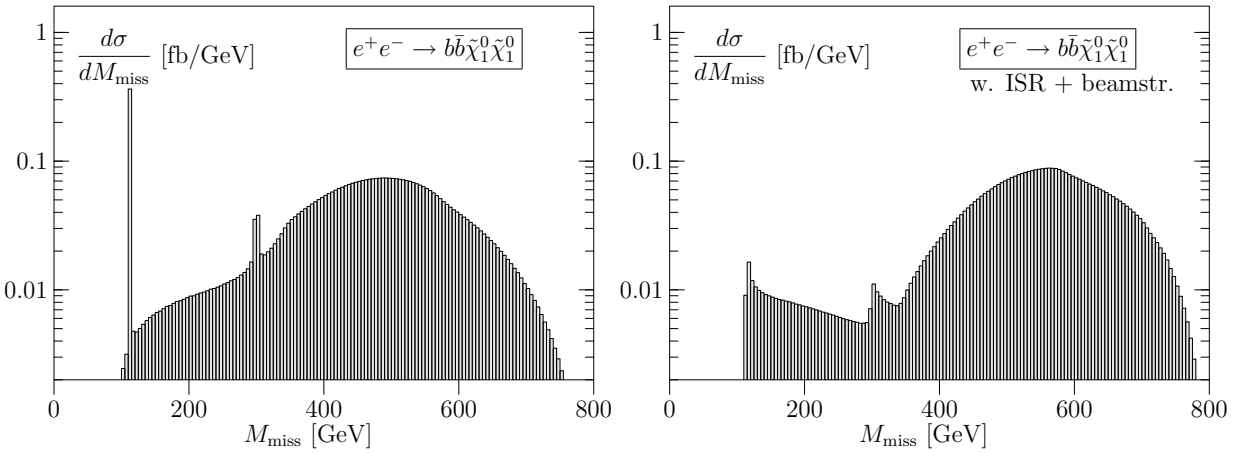

Figure 4.12: Missing invariant mass spectrum for the full process $e^+e^- \to b\bar{b}\tilde{\chi}_1^0\tilde{\chi}_1^0$: on the left for the partonic process, on the right including ISR and beamstrahlung.

cannot be neglected. For the numerical results, ISR is included using the third-order leading-logarithmic approximation [244], and beamstrahlung using the TESLA 800 parameterisation in CIRCE [245]. In both cases the photon radiation is predominantly collinear with the incoming beams and therefore invisible. Therefore, all distributions depending on missing momentum, *i.e.* the momentum of the final-state neutralinos, are distorted by such effects. In the left panel of Fig. 4.12 the missing invariant-mass spectrum for the full process $e^+e^- \to b\bar{b}\tilde{\chi}_1^0\tilde{\chi}_1^0$ without ISR and beamstrahlung is shown. Two narrow peaks are clearly visible, corresponding to the one light and two (unresolved) heavy Higgs bosons. These peaks sit on top of a continuum reaching a maximum around 500 GeV, dominantly stemming from neutralino and sbottom pairs. ISR and beamstrahlung are included in the right panel of Fig. 4.12. They tend to wash out the two sharp peaks, with a long tail to higher invariant masses. Without explicitly showing it, it shall be emphasised that the same happens to the SM background, where the Z^0 boson decays invisibly into $\nu\bar{\nu}$.

4.6.4 Isolating the sbottom-pair signal

According to Tab. 4.5, the dominant contribution to the $b\bar{b}\tilde{\chi}_1^0\tilde{\chi}_1^0$ final state at an ILC is neutralino pair production. To study the sbottom sector, its contribution needs to be isolated with kinematic cuts. In addition, vector boson fusion into Z^0 and Higgs bosons represent non-negligible backgrounds, and have to be reduced accordingly. It can be observed that Higgs boson and heavy sbottom production are of minor importance.

An obvious cut for background reduction is on the reconstructed $b\bar{b}$ invariant mass. Fig. 4.13 shows the distribution for the full process, with all Feynman diagrams and including ISR and beamstrahlung. SM contributions (light gray) and the MSSM (dark) must be superimposed to obtain the complete signal and background result, since neutrinos cannot be distinguished from neutralinos. The spectrum depicted in Fig. 4.13 has several distinct features: there

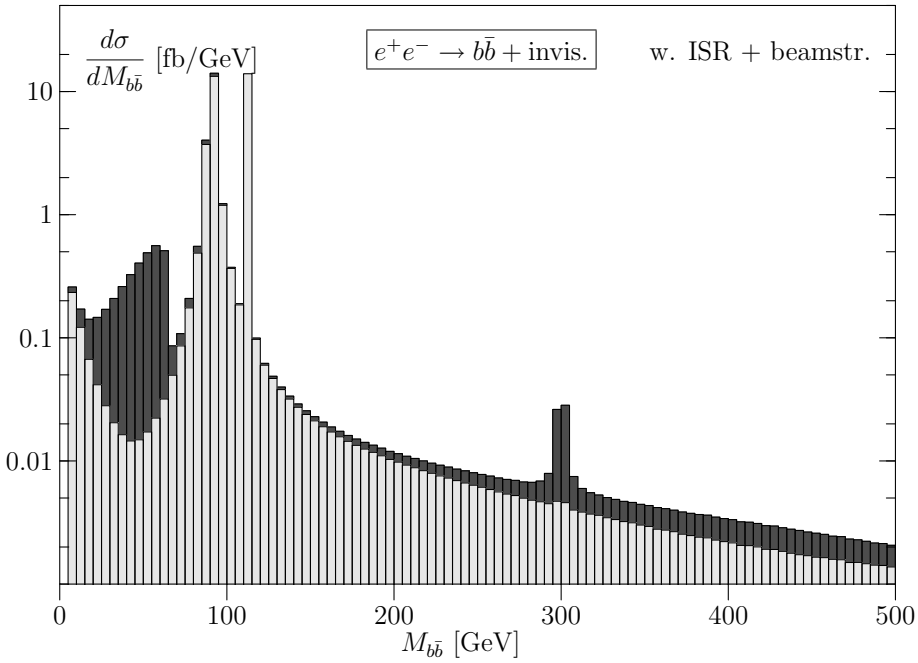

Figure 4.13: The $b\bar{b}$ invariant mass spectrum for the full process $e^+e^- \to b\bar{b}+\not{E}$ with ISR and beamstrahlung. The SM background ($\mathrm{Z}^0 \to \nu\bar{\nu}$) with the Z^0, h^0 peaks is light gray. Dark gray represents all MSSM processes, with two peaks from heavy neutralino and heavy Higgs decays.

are narrow peaks at the h, Z^0 and H/A boson masses, as well as a broader enhancement around 50 GeV, associated with the $\tilde{\chi}_2^0$ three-body decay. (The $\tilde{b}_1\tilde{b}_1^*$ signal does not have any resonance structure and populates the continuum at high invariant $b\bar{b}$ masses.) To remove all resonances certain invariant mass windows are cutted out:

$$M_{b\bar{b}} < 150 \text{ GeV} , \qquad 250 \text{ GeV} < M_{b\bar{b}} < 350 \text{ GeV} . \tag{4.81}$$

This cut retains mostly sbottom-pair signal events, with some continuum background. In the crude NWA (just the simple production channels $\tilde{b}_1\tilde{b}_1^*$, $\tilde{\chi}_1^0\tilde{\chi}_2^0$, $\tilde{\chi}_1^0\tilde{\chi}_3^0$ and $\mathrm{W}^+\mathrm{W}^- \to \mathrm{Z}^0/h^0$, $\mathrm{Z}^0\mathrm{Z}^0$, Z^0h^0, H^0A^0, ...; times decay matrix elements), these cuts would remove the entire background, while only marginally affecting the signal.

The effect of applying this cut is shown in Tab. 4.6 using the various approximations. In the full calculation 60% of the signal rate is retained. While in the on-shell approximation this cut would remove 100% of the peaked backgrounds, the complete calculation including Breit-Wigner propagators retains a whopping 2.3 fb (SUSY) and 2.1 fb (SM). Surprisingly, the exact tree-level cross section without ISR is considerably smaller than that: 0.5 fb (SUSY, signal+background) and 1.8 fb (SM). Obviously, for the background SUSY processes the Breit-Wigner approximation is misleadingly wrong if forcing the phase space into the sbottom-signal region. Only the full calculation gives a reliable result.

In the absence of backgrounds, the b-jet energy spectrum from sbottom decays exhibits a box-like shape corresponding to the decay kinematics of $\tilde{b}_1 \to b\tilde{\chi}_1^0$. Assuming that $m_{\tilde{\chi}_1^0}$ is

Channel	σ_{BW} [fb]	$\sigma_{\mathrm{BW}}^{\mathrm{cut}}$ [fb]
$\mathrm{Z}^0 h^0$	1.335	0.009
$\mathrm{Z}^0 H^0$	0.000	0.000
$h^0 A^0$	0.000	0.000
$H^0 A^0$	0.314	0.003
$\tilde{\chi}_1^0\tilde{\chi}_2^0$	13.954	0.458
$\tilde{\chi}_1^0\tilde{\chi}_3^0$	4.828	0.454
$\tilde{\chi}_1^0\tilde{\chi}_4^0$	0.938	0.937
$\tilde{b}_1\tilde{b}_1$	0.757	0.451
$\tilde{b}_1\tilde{b}_2$	0.002	0.001
Sum	22.129	2.314
Exact	19.624	0.487
w/ISR	22.552	0.375

Channel	σ_{BW} [fb]	$\sigma_{\mathrm{BW}}^{\mathrm{cut}}$ [fb]
$\mathrm{Z}^0\bar{\nu}\nu$	111.4	2.114
$h^0\bar{\nu}\nu$	76.4	0.002
$H^0\bar{\nu}\nu$	0.0	0.000
Sum	187.7	2.117
Exact	190.1	1.765
w/ISR	174.2	1.609

Table 4.6: SUSY cross sections contributing to $e^+e^- \to b\bar{b}\tilde{\chi}_1^0\tilde{\chi}_1^0$ (left) and the SM background $e^+e^- \to b\bar{b}\nu\bar{\nu}$ (right). The left column is the Breit-Wigner approximation without cuts. The right column is after the $M_{b\bar{b}}$ cuts of Eq. (4.81). Shown are the results for the incoherent sum of channels, the complete result with all interferences, and the same with ISR and beamstrahlung.

known from a threshold scan, the edges of the box would allow a simple kinematical fit to yield a precise determination of $m_{\tilde{b}_1}$. The realistic E_b distribution appears in Fig. 4.14. In the left panel the E_b spectrum for the full process without cuts is presented, including all interferences, and taking ISR and beamstrahlung into account. The large background precludes any identification of a box shape. The right panel displays the same distribution after the $M_{b\bar{b}}$ cuts of Eq. (4.81) and compares it with the ideal case (no background, no ISR, no cuts) in the same normalisation.

The SUSY contribution after cuts (dark area) shows the same kinematical limits as the ideal box, but the edges are washed out by the combined effects of cuts, ISR/beamstrahlung, and continuum background. However, the signal sits atop a sizable leftover SM background. As argued above, this background cannot be realistically simulated by simply concatenating particle production and decays. Without going into detail, it shall be noted that for further improvement of the signal-to-background ratio, one could use beam polarisation (reducing the $\mathrm{W}^+\mathrm{W}^- \to b\bar{b}$ continuum) or a cut on missing invariant mass (to suppress $\mathrm{Z}^0 \to \nu\bar{\nu}$). For a final verdict on the measurement of sbottom properties in this decay channel, a realistic analysis must also consider fragmentation and hadronisation effects. NLO corrections to the signal process must be taken into account to gain some idea about realistic event rates.

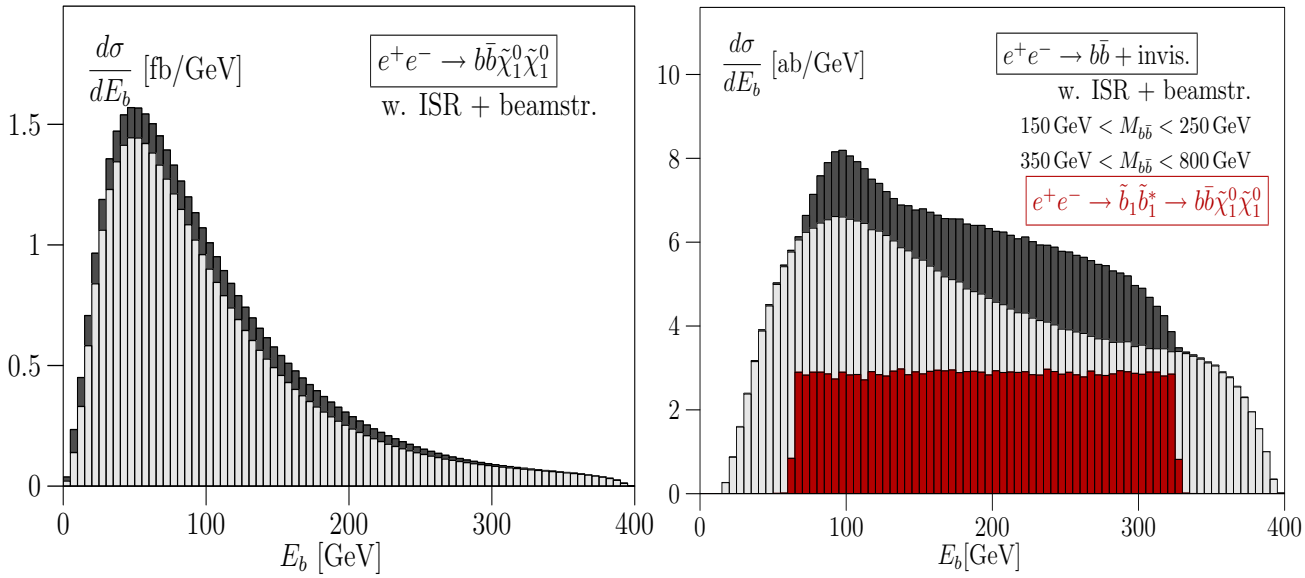

Figure 4.14: The E_b spectrum of the full process $e^+e^- \to b\bar{b}+\not{E}$, including all interferences and off-shell effects, plus ISR and beamstrahlung. The light gray histogram is the SM background, dark gray the sum of SUSY processes. The left panel is before the cut of Eq. (4.81), while the right panel includes the cut. Also in the right panel the idealised case (red) of on-shell sbottom production without ISR or beamstrahlung is shown. The SM background is again shown in light gray, while the dark gray shows the sbottom contribution alone.

4.7 Summary and conclusions

Phenomenological and experimental (Monte Carlo) analyses for new physics at colliders are usually approached at a level of sophistication which does not match the know-how available for the Standard Model. For supersymmetric signals at the LHC and an ILC effects which occur beyond simple $2 \to 2$ cross section analyses have been carefully studied, using sbottom pair production as a simple example process.

At the LHC, the reconstruction of decay kinematics is the source of essentially all information on heavy new particles. Any observable linked to cross sections instead of kinematical features is bound to suffer from much larger QCD uncertainties. Typical experimental errors from jet energy scaling are of the same order as finite-width effects in the total cross section. However, in relevant distributions, off-shell effects can easily be larger.

QCD off-shell effects also include additional jet radiation from the incoming state. Usually, jet radiation is treated by parton showers in the collinear approximation. For processes with bottom jets in the final state this approximation has been tested by computing the effects of two additional bottom jets created through gluon splitting in the initial state. The effects on the rate are typically below 10%, and kinematical distributions do indeed change. In the considered case, distinguishing between initial-state bottom jets and decay bottom jets via

rapidity and transverse momentum characteristics does not look promising.
Sbottom pair production at the LHC has the fortunate feature that most of these off-shell effects and combinatorial backgrounds can be removed together with the SM backgrounds, but this feature is by no means guaranteed for general SUSY processes.
At an ILC, the extraction of parameters from kinematic distributions is usually more precise compared to more inclusive measurements. In contrast to the LHC, the typical size Γ/M of off-shell effects exceeds the present ILC design experimental precision. It is therefore mandatory for multi-particle final states to include the complete set of off-shell Feynman diagrams in ILC studies, since they can alter signal distributions drastically. This was impressively demonstrated by the study of sbottom pair production where corrections up to 400% to production rates from off-shell effects have been found after standard cuts.
Irreducible SM backgrounds to missing energy signals can strongly distort the shapes of energy and invariant mass distributions. Hence, if trying to attempt to extract masses and mass differences from invariant mass distributions at an ILC, one finds that off-shell effects and additional many-particle intermediate states must be taken into account which can change cross sections dramatically. Simulation of initial-state radiation and beamstrahlung is mandatory to describe shapes of resonances and distributions in a realistic linear collider environment.
To be able to compute the effects described above the MSSM Lagrangian and the proper description of Majorana particles have to be incorporated into event generators. The implementation in the AMEGIC++/SHERPA Monte Carlo has been discussed in some detail and the two other available solutions to the problem, the generators MADGRAPH/MADEVENT and O'MEGA/WHIZARD, have been briefly introduced. To carefully check these tools several hundred SUSY production processes have been compared numerically, as well as a number of unitarity and gauge invariance checks were performed. All results, as well as the SLHA input file, are given in the Appendix — this list of processes might serve as a standard reference to check MSSM implementations in collider physics or phenomenology tools.

5 Summary

In this thesis new theoretical tools for the accurate simulation of scattering processes at present and future collider experiments have been developed. Especially the next generation of accelerators, the CERN LHC and a future e^+e^- machine, will set new standards for the number and the complexity of final states to be studied and will allow for particle physics measurements with an unprecedented precision. Accordingly, they provide a great challenge for theorists concerned with the description of the scattering events to be observed.

Besides a precise modelling of Standard Model physics various scenarios of physics beyond the Standard Model must be considered. Tools are needed for realistic studies of the signatures for new physics and for the development of strategies to find these signals in the presence of Standard Model or even new physics backgrounds. Special emphasis has thereby to be given to multi-particle/multi-jet final states that often constitute signals for interesting (new) physics.

Considering final states with a number of hard jets, there seems to be enough evidence that the traditional simulation tools HERWIG and PYTHIA cannot fully accomplish their description. Starting from a $2 \to 2$ core process, they account only for soft and collinear QCD emissions through parton-shower models. Only recently, theoretical prescriptions have been found to consistently combine tree-level matrix-element calculations with the existing parton-shower algorithms. These methods avoid double counting of phase-space configurations present in the matrix-element calculations and the parton-shower approach. They can be understood as the automatic resummation of leading logarithms for the tree-level matrix elements. The gain of such methods is that phase-space regions covered by hard and by soft parton kinematics are simultaneously well described. In Chapter 2 of this thesis the working principles of such prescriptions have been discussed with special attention being paid to the merging scheme implemented in the SHERPA Monte Carlo. This algorithm, known as CKKW, has carefully been tested for single gauge boson production in hadron–hadron collisions. Direct comparison with exact next-to-leading-order calculations and experimental data confirmed that the CKKW merging prescription yields an improved description of jet observables. To gain some more insight into the systematics of approaches for combining matrix element calculations with parton showers, an extensive comparison of all the presently available implementations of such prescription has been carried out for

W+jets production at hadron colliders. It has been found that all the calculations reasonably agree when taking into account systematic uncertainties. The systematics could be reduced through a detailed tuning of the generators on current Tevatron data to yield reliable predictions for the LHC.

To consistently match QCD higher-order calculations (at one-loop or tree-level) with parton showers, a good analytical control over the perturbative terms present in the latter is required. This has triggered the demand for improved parton-shower models that facilitate the inclusion of exact matrix elements. In this line a completely new shower algorithm has been presented in Chapter 3. It is based on the Catani–Seymour dipole subtraction formalism, a universal method for calculating arbitrary processes at next-to-leading order in QCD. The splitting kernels used in the shower are justified approximations of the Catani–Seymour dipole functions. The kinematics of the individual splittings is accomplished such that exact four-momentum conservation can be ensured for each single branching. Accordingly, the shower can be stopped and started again at each intermediate stage of the evolution. The model incorporates emissions from final- and initial-state partons and finite parton masses are taken into account in a very general way. As ordering parameter for subsequent emissions transverse momenta are used. The implementation of the new shower formulation has been tested against a large set of experimental data. A very satisfactory agreement with the measurements is observed and the model is apparently capable of describing QCD colour coherence effects seen in three-jet events at the Tevatron collider. It can be anticipated that this new shower implementation will be well suited for matching with higher-order calculations.

In order to be adequately equipped for searches of phenomena beyond the Standard Model in the experimental data, the theoretical models for their simulation also need to be improved. One prime example is the supersymmetric extension of the Standard Model, the MSSM, that yields rather complex signal topologies that will be hard to disentangle from the Standard Model anyway. However, to be able to extract enough information from the measurements to gain some confidence about the nature of the new physics, like masses, spins and other quantum numbers of the new states, these multi-particle final states need to be simulated quite precisely. So far, the description of SUSY production processes has relied on simple $2 \to 2$ matrix elements with possible decays of the new unstable particles modelled rather crudely. To improve on that, only recently a new generation of Monte Carlo generators has emerged that accomplish exact tree-level matrix-element calculations for multi-particle final states in the framework of the MSSM. With these new tools it can correctly be accounted for all kinds of off-shell effects, quantum interferences and angular correlations by calculating the entire set of Feynman diagrams for a given final state. In Chapter 4 the framework for consistent matrix-element calculations within the MSSM has been specified and the incorporation of the theory's most general Lagrangian into the generator SHERPA has been discussed in detail. Extensive tests of the implementation have been carried out, all proving

the correctness of the Feynman rules used. As an illustrative example for the importance of off-shell effects in the simulation of SUSY particle production sbottom pair production at the LHC and an ILC has been considered. While the impact of off-shell effects in the considered SUSY scenario was found to be rather small at the LHC, for the corresponding ILC analysis their inclusion is absolutely mandatory to get reasonable results, both for production rates after selection cuts and differential distributions.
It can finally be concluded that the SHERPA generator in its present form is well prepared for the challenges provided by the LHC, and that the course is set towards further improvements of the simulation of final states as observed at collider experiments.

Acknowledgments

First of all, I would like to thank Frank Krauss for guidance and inspiration, his continuous support and lots of coffee.

I would like to thank Michael Kobel for taking responsibility for this thesis and his support.

I thank all the former and current members of the SHERPA-team for a successful collaboration, lots of help and numberless discussions. Special thanks go to Jan Winter, Andreas Schälicke, Tanju Gleisberg, Stefan Höche and Frank Siegert.

I am deeply thankful to my collaborators on the various projects I have dealt with over the past years, especially I would like to mention here Michelangelo L. Mangano, Tilman Plehn, and Kaoru Hagiwara.

It is a pleasure to thank all the users of SHERPA who have helped to get the project so far. Personally I am greatly indebted to Henrik Nilsen who became a good friend of mine.

I thank the whole Dresden ATLAS group, and especially Markus Warsinsky and Wolfgang Mader, for lots of fruitful discussions and inputs.

I would like to thank the staff of the Institute for Theoretical Physics for the pleasant atmosphere, especially I want to thank my favourite secretary Gundula Schädlich, and Jürgen Weißbarth for many discussions related to teaching.

Finally, I want to express my deepest gratitude to my wife for her enormous patience and support, and for giving me this cute little son. I thank Leander for making me laugh *every* day.

Appendix A

A.1 Input parameters and phase-space cuts for $W^{\pm}/Z^0$+jets at Tevatron

The PDF set used for all analyses is CTEQ6l [148]. The value of α_s is chosen according to the value taken for the PDF, namely $\alpha_s(m_Z) = 0.118$. For the running of the strong coupling the corresponding two-loop equation is used. Jets or initial partons are restricted to the light flavour sector, namely g, u, d, s, c. In fact these flavours are taken to be massless and the Yukawa couplings of the quarks are neglected throughout the entire analysis.

A.1.1 SM input parameters

The SM parameters are given in the G_μ scheme:

$$\begin{aligned} &m_W = 80.419 \text{ GeV}\,, \quad \Gamma_W = 2.06 \text{ GeV}, \\ &m_Z = 91.188 \text{ GeV}\,, \quad \Gamma_Z = 2.49 \text{ GeV}, \\ &G_\mu = 1.16639 \times 10^{-5} \text{ GeV}^{-2}, \\ &\sin^2\theta_W = 1 - m_W^2/m_Z^2, \\ &\alpha_s = 0.118\,. \end{aligned} \tag{A.1}$$

The electromagnetic coupling is derived from the Fermi constant G_μ according to

$$\alpha_{\text{qed}} = \frac{\sqrt{2}\, G_\mu\, M_W^2\, \sin^2\theta_W}{\pi}\,. \tag{A.2}$$

The constant widths of the electroweak gauge bosons are introduced via the fixed-width scheme. CKM mixing of the quark generations is neglected.

A.1.2 Cuts and jet criteria

The analyses of jet quantities the Run II $k_\perp$-clustering algorithm defined in [56] have been used. The parameter of this jet algorithm is a pseudo-cone of size D given below for the

Tevatron analysis. For the charged leptons the following cuts have been applied:

$$p_\perp^{\text{lepton}} > 20 \text{ GeV}, \quad |\eta^{\text{lepton}}| < 1, \quad m^{ll} > 15 \text{ GeV}. \tag{A.3}$$

For the case of W production an additional cut on missing transverse momentum according to the neutrino has been required, namely

$$p_\perp^{\text{miss}} > 20 \text{ GeV}. \tag{A.4}$$

For the jet definition a pseudo-cone size of $D = 0.7$ has been used in addition to cuts on pseudo-rapidity and transverse momentum:

$$p_\perp^{\text{jet}} > 15 \text{ GeV}, \quad |\eta^{\text{jet}}| < 2. \tag{A.5}$$

A.2 Feynman rules for Majorana fermions: neutralino production

The usage of the Feynman rules presented in Sec. 4.2.3 is exemplified for the production of two Majorana fermions, namely two neutralinos, in the process $e^- e^+ \to \chi_i^0 \chi_j^0$ with $i,j = 1,2,3,4$. There are three types of diagrams contributing to the total amplitude, an s-channel graph with Z^0 boson exchange and two t-channel and u-channel diagrams, respectively, where both types of selectrons are exchanged, see Fig. 4.1. The s-channel diagram and one of the t-channel contributions will be evaluated. Besides the determination of the relative sign of the two graphs it will be shown that the expression for each diagram is independent of the chosen orientation.

The s-channel diagram

Choosing the fermion flow within the s-channel graph according to Fig. A.1a the amplitude reads

$$\mathcal{M}_a^s = \bar{v}(p_{e^+})\,\Gamma_i\,u(p_{e^-})\,D_{Z^0}\,\bar{u}(p_{\tilde{\chi}_i^0})\,\Gamma_j\,v(p_{\tilde{\chi}_j^0})\,. \tag{A.6}$$

Evaluating the same diagram but inverting the fermion flows, cf. Fig. A.1b, leads to the expression

$$\mathcal{M}_b^s = \bar{v}(p_{e^-})\,\Gamma_i'\,u(p_{e^+})\,D_{Z^0}\,\bar{u}(p_{\tilde{\chi}_j^0})\,\Gamma_j\,v(p_{\tilde{\chi}_i^0})\,. \tag{A.7}$$

The coupling of the Z^0 boson to the leptons has thereby been denoted by $\Gamma_i^{(\prime)}$ whereas Γ_j represents the appropriate coupling of the neutralinos to the Z^0. The equivalence of Eq. (A.6) and Eq. (A.7) can be shown employing the transposed fermion-boson interactions and applying Eqs. (4.8) and (4.13),

$$\begin{aligned}
\mathcal{M}_a^s &= u^T(p_{e^-})\,\Gamma_i^T\,\bar{v}^T(p_{e^+})\,D_{Z^0}\,v^T(p_{\tilde{\chi}_j^0})\,\Gamma_j^T\,\bar{u}^T(p_{\tilde{\chi}_i^0}) \\
&= \bar{v}(p_{e^-})\,C^T\,\Gamma_i^T\,C^\dagger\,u(p_{e^+})\,D_{Z^0}\,\bar{u}(p_{\tilde{\chi}_j^0})\,C^T\,\Gamma_j^T\,C^\dagger\,v(p_{\tilde{\chi}_i^0}) \\
&= \bar{v}(p_{e^-})\,\Gamma_i'\,u(p_{e^+})\,D_{Z^0}\,\bar{u}(p_{\tilde{\chi}_j^0})\,\Gamma_j\,v(p_{\tilde{\chi}_i^0}) \\
&= \mathcal{M}_b^s.
\end{aligned} \tag{A.8}$$

Both choices of the fermion flow lead to the same result. The value of the amplitude is uniquely fixed and no sign ambiguities appear. According to the orientation of diagram (a) the permutation of the fermion fields is found to be (e^+, e^-, $\tilde{\chi}_i^0$, $\tilde{\chi}_j^0$).

The t- and u-channel diagrams

As an example for the t- and u-channel contributions the diagram depicted in Fig. A.2a is considered. There the choice for the fermion flow leads to

$$\mathcal{M}_a^t = \bar{u}(p_{\tilde{\chi}_i^0})\,\Gamma_k\,u(p_{e^-})\,D_{\tilde{e}_L}\,\bar{v}(p_{e^+})\,\Gamma_l\,v(p_{\tilde{\chi}_j^0})\,. \tag{A.9}$$

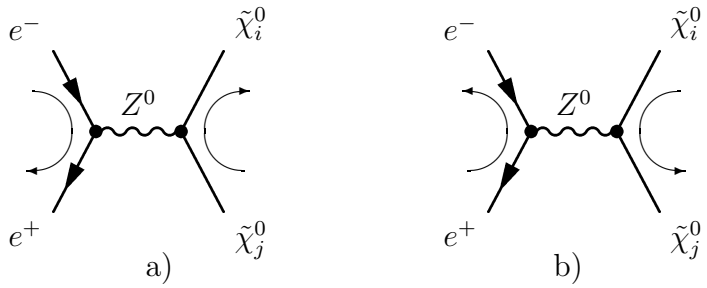

Figure A.1: The s-channel diagram of the production of two neutralinos, depicted for the two choices of the orientation.

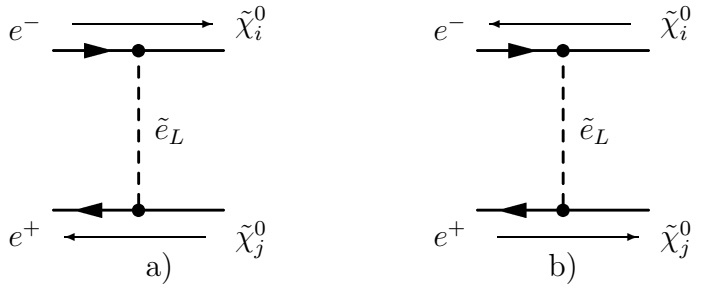

Figure A.2: The t-channel contribution to the production of two neutralinos, depicted for the two choices of the orientation.

The coupling $e^-\,\tilde{\chi}_i^0\,\tilde{e}_L$ is denoted by Γ_k, Γ_l represents the $\tilde{e}_L\,\tilde{\chi}_j^0\,e^-$ coupling and $D_{\tilde{e}_L}$ is the propagator of the scalar electron. Inverting the fermion flow as displayed in Fig. A.2b leads to the expression

$$\mathcal{M}_b^t = \bar{v}(p_{e^-})\,\Gamma_k'\,v(p_{\tilde{\chi}_i^0})\,D_{\tilde{e}_L}\,\bar{u}(p_{\tilde{\chi}_j^0})\,\Gamma_l\,u(p_{e^+})\,. \tag{A.10}$$

To show that both equations yield the same, Eq. (A.9) is transformed similarly to Eq. (A.6),

$$\begin{aligned}
\mathcal{M}_a^t &= u^T(p_{e^-})\,\Gamma_k^T\,\bar{u}^T(p_{\tilde{\chi}_i^0})\,D_{\tilde{e}_L}\,v^T(p_{\tilde{\chi}_j^0})\,\Gamma_l^T\,\bar{v}^T(p_{e^+}) \\
&= \bar{v}(p_{e^-})\,C^T\,\Gamma_k^T\,C^\dagger\,v(p_{\tilde{\chi}_i^0})\,D_{\tilde{e}_L}\,\bar{u}(p_{\tilde{\chi}_j^0})\,C^T\,\Gamma_l^T\,C^\dagger\,u(p_{e^+}) \\
&= \bar{v}(p_{e^-})\,\Gamma_k'\,v(p_{\tilde{\chi}_i^0})\,D_{\tilde{e}_L}\,\bar{u}(p_{\tilde{\chi}_j^0})\,\Gamma_l'\,u(p_{e^+}) \\
&= \mathcal{M}_b^t.
\end{aligned} \tag{A.11}$$

Again the amplitude is independent of the fermion lines orientation. The permutations of the fermion fields are either $(\tilde{\chi}_i^0, e^-, e^+, \tilde{\chi}_j^0)$ or $(e^-, \tilde{\chi}_i^0, \tilde{\chi}_j^0, e^+)$. Comparing this with the permutation for the s-channel diagram always an odd permutation parity is found. Accordingly the two diagrams possess a negative interference. For the u-channel diagrams where the final-state neutralinos are exchanged an additional minus sign is obtained such that the total sign equals the one of the s-channel graph.

A.3 Input parameters used in the SUSY comparison

Here the SLHA output of the SoftSusy program specifying the input parameters used is listed:

```
# SOFTSUSY1.9
# B.C. Allanach, Comput. Phys. Commun. 143 (2002) 305-331, hep-ph/0104145
Block SPINFO         # Program information
     1   SOFTSUSY    # spectrum calculator
     2   1.9         # version number
Block MODSEL  # Select model
     1    1   # sugra
Block SMINPUTS   # Standard Model inputs
#     1    1.27934000e+02   # alpha_em^(-1)(MZ) SM MSbar
     2    1.16639000e-05   # G_Fermi
#     3    1.17200000e-01   # alpha_s(MZ)MSbar
#     4    9.11876000e+01   # MZ(pole)
#     5    4.25000000e+00   # Mb(mb)
#     6    1.74300000e+02   # Mtop(pole)
     7    1.77700000e+00   # Mtau(pole)
Block MINPAR  # SUSY breaking input parameters
     3    1.00000000e+01   # tanb
     4    1.00000000e+00   # sign(mu)
     1    1.00000000e+02   # m0
     2    2.50000000e+02   # m12
     5   -1.00000000e+02   # A0
# Low energy data in SOFTSUSY: MIXING=-1 TOLERANCE=1.00000000e-03
# mgut=2.46245508e+16 GeV
Block MASS   # Mass spectrum
#PDG code      mass              particle
        24     8.04194155e+01   # MW
        25     1.10762900e+02   # h0
        35     4.00615086e+02   # H0
        36     4.00247030e+02   # A0
        37     4.08528577e+02   # H+
   1000001     5.72715810e+02   # ~d_L
   1000002     5.67266777e+02   # ~u_L
   1000003     5.72715810e+02   # ~s_L
   1000004     5.67266777e+02   # ~c_L
   1000005     5.15224253e+02   # ~b_1
   1000006     3.95930570e+02   # ~t_1
   1000011     2.04280587e+02   # ~e_L
   1000012     1.88661921e+02   # ~nue_L
   1000013     2.04280587e+02   # ~mu_L
   1000014     1.88661921e+02   # ~numu_L
   1000015     1.36227332e+02   # ~stau_1
   1000016     1.87777460e+02   # ~nu_tau_L
```

```
   1000021     6.07618238e+02   # ~g
   1000022     9.72807171e+01   # ~neutralino(1)
   1000023     1.80959888e+02   # ~neutralino(2)
   1000024     1.80377023e+02   # ~chargino(1)
   1000025    -3.64450624e+02   # ~neutralino(3)
   1000035     3.83149239e+02   # ~neutralino(4)
   1000037     3.83385634e+02   # ~chargino(2)
   2000001     5.46084642e+02   # ~d_R
   2000002     5.47013902e+02   # ~u_R
   2000003     5.46084642e+02   # ~s_R
   2000004     5.47013902e+02   # ~c_R
   2000005     5.43980537e+02   # ~b_2
   2000006     5.85709387e+02   # ~t_2
   2000011     1.45527209e+02   # ~e_R
   2000013     1.45527209e+02   # ~mu_R
   2000015     2.08226705e+02   # ~stau_2
# Higgs mixing
Block alpha   # Effective Higgs mixing parameter
          -1.13731924e-01   # alpha
Block stopmix  # stop mixing matrix
   1  1     5.38076009e-01   # O_{11}
   1  2     8.42896322e-01   # O_{12}
   2  1     8.42896322e-01   # O_{21}
   2  2    -5.38076009e-01   # O_{22}
Block sbotmix  # sbottom mixing matrix
   1  1     9.47748557e-01   # O_{11}
   1  2     3.19018296e-01   # O_{12}
   2  1    -3.19018296e-01   # O_{21}
   2  2     9.47748557e-01   # O_{22}
Block staumix  # stau mixing matrix
  1  1     2.80949722e-01   # O_{11}
  1  2     9.59722488e-01   # O_{12}
  2  1     9.59722488e-01   # O_{21}
  2  2    -2.80949722e-01   # O_{22}
Block nmix  # neutralino mixing matrix
  1  1     9.86069014e-01   # N_{1,1}
  1  2    -5.46217310e-02   # N_{1,2}
  1  3     1.47637908e-01   # N_{1,3}
  1  4    -5.37346696e-02   # N_{1,4}
  2  1     1.02047560e-01   # N_{2,1}
  2  2     9.42730347e-01   # N_{2,2}
  2  3    -2.74969181e-01   # N_{2,3}
  2  4     1.58863895e-01   # N_{2,4}
  3  1    -6.04553550e-02   # N_{3,1}
  3  2     8.97014273e-02   # N_{3,2}
  3  3     6.95501771e-01   # N_{3,3}
  3  4     7.10335196e-01   # N_{3,4}
```

```
  4  1    -1.16616232e-01   # N_{4,1}
  4  2     3.16590608e-01   # N_{4,2}
  4  3     6.47203433e-01   # N_{4,3}
  4  4    -6.83592537e-01   # N_{4,4}
Block Umix  # chargino U mixing matrix
  1  1     9.15543496e-01   # U_{1,1}
  1  2    -4.02218978e-01   # U_{1,2}
  2  1     4.02218978e-01   # U_{2,1}
  2  2     9.15543496e-01   # U_{2,2}
Block Vmix  # chargino V mixing matrix
  1  1     9.72352114e-01   # V_{1,1}
  1  2    -2.33519522e-01   # V_{1,2}
  2  1     2.33519522e-01   # V_{2,1}
  2  2     9.72352114e-01   # V_{2,2}
Block hmix Q= 4.64241862e+02  # Higgs mixing parameters
     1     3.58355327e+02   # mu(Q)MSSM DRbar
#     2     9.75144517e+00   # tan beta(Q)MSSM DRbar
     3     2.44921676e+02   # higgs vev(Q)MSSM DRbar
     4     1.69588951e+04   # mA^2(Q)MSSM DRbar
Block au Q= 4.64241862e+02
  1  1     0.00000000e+00   # Au(Q)MSSM DRbar
  2  2     0.00000000e+00   # Ac(Q)MSSM DRbar
  3  3    -5.04528807e+02   # At(Q)MSSM DRbar
Block ad Q= 4.64241862e+02
  1  1     0.00000000e+00   # Ad(Q)MSSM DRbar
  2  2     0.00000000e+00   # As(Q)MSSM DRbar
  3  3    -7.97132778e+02   # Ab(Q)MSSM DRbar
Block ae Q= 4.64241862e+02
  1  1     0.00000000e+00   # Ae(Q)MSSM DRbar
  2  2     0.00000000e+00   # Amu(Q)MSSM DRbar
  3  3    -2.56155534e+02   # Atau(Q)MSSM DRbar
```

Parameters used with a different value than specified in the above SLHA file are $m_W = 80.419\,\text{GeV}$, $m_Z = 91.188\,\text{GeV}$. All SUSY particle widths are set to zero, since there are no SUSY particles in the s-channel. The only widths used in the comparison are set by hand, $\Gamma_W = 2.048\,\text{GeV}$ and $\Gamma_Z = 2.446\,\text{GeV}$. All Higgs widths have been set to zero, as well as the electron mass. The third generation quark masses have been given the values $m_t = 178.0\,\text{GeV}$ and $m_b = 4.6\,\text{GeV}$. For the strong coupling $\alpha_s(m_Z) = 0.118$ is used and all remaining SM input parameters are calculated in the $G_\mu - m_Z - \alpha_{\text{qed}}$ scheme.

A.4 Cross section values for $2 \to 2$ SUSY processes

The following tables are also maintained at the web page
`http://www.sherpa-mc.de/susy_comparison/susy_comparison.html`.

A.4.1 e^+e^- processes

$\mathbf{e^+e^- \to X}$						
Final	MadGraph/Helas		O'mega/Whizard		Amegic++/Sherpa	
state	0.5 TeV	2 TeV	0.5 TeV	2 TeV	0.5 TeV	2 TeV
$\tilde{e}_L\tilde{e}_L^*$	54.687(2)	78.864(6)	54.687(3)	78.866(4)	54.6890(7)	78.8670(8)
$\tilde{e}_R\tilde{e}_R^*$	274.69(2)	91.776(8)	274.682(1)	91.776(5)	274.695(3)	91.778(1)
$\tilde{e}_L\tilde{e}_R^*$	75.168(5)	7.237(1)	75.167(3)	7.2372(4)	75.1693(7)	7.23744(7)
$\tilde{\mu}_L\tilde{\mu}_L^*$	22.5471(7)	6.8263(2)	22.5478(9)	6.8265(3)	22.5482(2)	6.82638(7)
$\tilde{\mu}_R\tilde{\mu}_R^*$	51.839(2)	5.8107(2)	51.837(2)	5.8105(2)	51.8401(5)	5.81085(6)
$\tilde{\tau}_1\tilde{\tau}_1^*$	55.582(2)	5.7139(2)	55.580(2)	5.7141(2)	55.5835(6)	5.71399(6)
$\tilde{\tau}_2\tilde{\tau}_2^*$	19.0161(6)	6.5047(2)	19.0174(7)	6.5045(3)	19.0163(2)	6.50473(7)
$\tilde{\tau}_1\tilde{\tau}_2^*$	1.4118(4)	0.21406(1)	1.41191(5)	0.214058(8)	1.41187(1)	0.214067(2)
$\tilde{\nu}_e\tilde{\nu}_e^*$	493.35(2)	272.15(2)	493.38(2)	272.15(1)	493.358(5)	272.155(3)
$\tilde{\nu}_\mu\tilde{\nu}_\mu^*$	14.8632(4)	2.9231(1)	14.8638(6)	2.9232(1)	14.8633(1)	2.92309(3)
$\tilde{\nu}_\tau\tilde{\nu}_\tau^*$	15.1399(5)	2.9246(1)	15.1394(8)	2.9245(1)	15.1403(2)	2.92465(3)
$\tilde{u}_L\tilde{u}_L^*$	—	7.6185(2)	—	7.6188(3)	—	7.61859(8)
$\tilde{u}_R\tilde{u}_R^*$	—	4.6933(1)	—	4.6935(2)	—	4.69342(5)
$\tilde{c}_L\tilde{c}_L^*$	—	7.6185(2)	—	7.6182(3)	—	7.61859(8)
$\tilde{c}_R\tilde{c}_R^*$	—	4.6933(1)	—	4.6933(2)	—	4.69342(5)
$\tilde{t}_1\tilde{t}_1^*$	—	5.9845(4)	—	5.9847(2)	—	5.98459(6)
$\tilde{t}_2\tilde{t}_2^*$	—	5.3794(3)	—	5.3792(2)	—	5.37951(6)
$\tilde{t}_1\tilde{t}_2^*$	—	1.2427(1)	—	1.24264(5)	—	1.24270(1)
$\tilde{d}_L\tilde{d}_L^*$	—	5.2055(1)	—	5.2059(2)	—	5.20563(2)
$\tilde{d}_R\tilde{d}_R^*$	—	1.17588(2)	—	1.17595(5)	—	1.17591(1)
$\tilde{s}_L\tilde{s}_L^*$	—	5.2055(1)	—	5.2058(2)	—	5.20563(2)
$\tilde{s}_R\tilde{s}_R^*$	—	1.17588(2)	—	1.17585(5)	—	1.17591(1)
$\tilde{b}_1\tilde{b}_1^*$	—	4.9388(3)	—	4.9387(2)	—	4.93883(5)
$\tilde{b}_2\tilde{b}_2^*$	—	1.1295(1)	—	1.12946(4)	—	1.12953(1)
$\tilde{b}_1\tilde{b}_2^*$	—	0.51644(3)	—	0.516432(9)	—	0.516447(6)

$\mathbf{e^+e^- \to X}$						
Final	MadGraph/Helas		O'mega/Whizard		Amegic++/Sherpa	
state	0.5 TeV	2 TeV	0.5 TeV	2 TeV	0.5 TeV	2 TeV
$\tilde{\chi}_1^0\tilde{\chi}_1^0$	240.631(4)	26.3082(2)	240.636(7)	26.3087(9)	240.638(2)	26.3086(3)
$\tilde{\chi}_1^0\tilde{\chi}_2^0$	62.377(1)	9.9475(1)	62.374(2)	9.9475(4)	62.3785(6)	9.94778(1)
$\tilde{\chi}_1^0\tilde{\chi}_3^0$	7.78117(2)	0.64795(1)	7.78131(4)	0.64796(1)	7.78121(8)	0.647969(6)
$\tilde{\chi}_1^0\tilde{\chi}_4^0$	1.03457(3)	1.36561(1)	1.03460(3)	1.36564(5)	1.03460(1)	1.36568(1)
$\tilde{\chi}_2^0\tilde{\chi}_2^0$	70.730(2)	18.6841(3)	70.730(3)	18.6845(8)	70.7310(7)	18.6843(2)
$\tilde{\chi}_2^0\tilde{\chi}_3^0$	—	1.85588(2)	—	1.85590(4)	—	1.85594(2)
$\tilde{\chi}_2^0\tilde{\chi}_4^0$	—	3.03946(4)	—	3.03951(9)	—	3.03949(3)
$\tilde{\chi}_3^0\tilde{\chi}_3^0$	—	4.2214(1)e-3	—	4.2214(2)e-3	—	4.22147(4)e-3
$\tilde{\chi}_3^0\tilde{\chi}_4^0$	—	9.93621(8)	—	9.9362(3)	—	9.93637(1)
$\tilde{\chi}_4^0\tilde{\chi}_4^0$	—	0.135479(1)	—	0.135482(5)	—	0.135479(1)
$\tilde{\chi}_1^+\tilde{\chi}_1^-$	162.786(6)	45.079(2)	162.788(7)	45.080(2)	162.786(2)	45.0808(5)
$\tilde{\chi}_2^+\tilde{\chi}_2^-$	—	26.9854(3)	—	26.9864(6)	—	26.9857(3)
$\tilde{\chi}_1^+\tilde{\chi}_2^-$	—	4.01053(5)	—	4.01053(9)	—	4.01066(4)
Z^0h^0	59.377(2)	3.1148(2)	59.376(1)	3.11492(9)	59.3789(6)	3.11491(3)
Z^0H^0	6.17904(1)e-4	5.5060(3)e-4	6.179180(5)e-4	5.5058(2)e-4	6.17919(6)e-4	5.50607(6)e-4
A^0h^0	—	5.3434(2)e-4	—	5.3433(2)e-4	—	5.34350(5)e-4
A^0H^0	—	2.37418(7)	—	2.37434(9)	—	2.37422(2)
H^+H^-	—	5.5335(2)	—	5.5339(2)	—	5.53374(6)

A.4.2 $\tau^+\tau^-$ processes

$\tau^+\tau^- \to \mathbf{X}$						
Final	MadGraph/Helas		O'mega/Whizard		Amegic++/Sherpa	
state	0.5 TeV	2 TeV	0.5 TeV	2 TeV	0.5 TeV	2 TeV
$\tilde{\tau}_1\tilde{\tau}_1^*$	257.31(5)	79.63(4)	257.32(1)	79.636(4)	257.30(1)	79.638(4)
$\tilde{\tau}_2\tilde{\tau}_2^*$	46.368(6)	66.86(2)	46.368(2)	66.862(3)	46.372(2)	66.862(3)
$\tilde{\tau}_1\tilde{\tau}_2^*$	81.72(2)	18.96(1)	81.720(3)	18.9588(8)	81.726(4)	18.960(1)
$\tilde{\nu}_\tau\tilde{\nu}_\tau^*$	502.26(7)	272.01(8)	502.27(2)	272.01(1)	502.30(3)	272.01(1)
$\tilde{\chi}_1^0\tilde{\chi}_1^0$	249.94(2)	26.431(1)	249.954(9)	26.431(1)	249.96(1)	26.431(1)
$\tilde{\chi}_1^0\tilde{\chi}_2^0$	69.967(3)	9.8940(3)	69.969(2)	9.8940(4)	69.968(3)	9.8937(5)
$\tilde{\chi}_1^0\tilde{\chi}_3^0$	17.0387(3)	0.7913(1)	17.0394(1)	0.79136(2)	17.040(1)	0.79137(5)
$\tilde{\chi}_1^0\tilde{\chi}_4^0$	7.01378(4)	1.50743(3)	7.01414(6)	1.5075(5)	7.0141(4)	1.50740(8)
$\tilde{\chi}_2^0\tilde{\chi}_2^0$	82.351(7)	18.887(1)	82.353(3)	18.8879(9)	82.357(4)	18.8896(1)
$\tilde{\chi}_2^0\tilde{\chi}_3^0$	—	1.7588(1)	—	1.75884(5)	—	1.7588(1)
$\tilde{\chi}_2^0\tilde{\chi}_4^0$	—	2.96384(7)	—	2.9640(1)	—	2.9639(1)
$\tilde{\chi}_3^0\tilde{\chi}_3^0$	—	0.046995(4)	—	0.0469966(9)	—	0.046999(2)
$\tilde{\chi}_3^0\tilde{\chi}_4^0$	—	8.5852(4)	—	8.5857(3)	—	8.5856(4)
$\tilde{\chi}_4^0\tilde{\chi}_4^0$	—	0.26438(2)	—	0.264389(5)	—	0.26437(1)
$\tilde{\chi}_1^+\tilde{\chi}_1^-$	185.09(3)	45.15(1)	185.093(6)	45.147(2)	185.10(1)	45.151(2)
$\tilde{\chi}_2^+\tilde{\chi}_2^-$	—	26.515(1)	—	26.5162(6)	—	26.515(1)
$\tilde{\chi}_1^+\tilde{\chi}_2^-$	—	4.2127(4)	—	4.21267(9)	—	4.2125(2)
h^0h^0	0.3533827(3)	1.242(2)e-4	0.35339(2)	1.2422(3)e-4	0.35340(2)	1.24218(6)e-4
h^0H^0	—	5.167(4)e-3	—	5.1669(3)e-3	—	5.1671(3)e-3
H^0H^0	—	0.07931(3)	—	0.079301(6)	—	0.079311(4)
A^0A^0	—	0.07975(3)	—	0.079758(6)	—	0.079744(4)
Z^0h^0	59.591(3)	3.1803(8)	59.589(3)	3.1802(1)	59.602(3)	3.1829(2)
Z^0H^0	2.8316(3)	4.671(5)	2.83169(9)	4.6706(3)	2.8318(1)	4.6706(2)
Z^0A^0	2.9915(4)	4.682(5)	2.99162(9)	4.6821(3)	2.9917(2)	4.6817(2)
A^0h^0	—	5.143(4)e-3	—	5.1434(3)e-3	—	5.1440(3)e-3
A^0H^0	—	1.4880(2)	—	1.48793(9)	—	1.48802(8)
H^+H^-	—	5.2344(6)	—	5.2344(2)	—	5.2345(3)

A.4.3 $e^-\bar{\nu}_e$ processes

$\mathbf{e^-\bar{\nu}_e \to X^-}$						
Final	MadGraph/Helas		O'mega/Whizard		Amegic++/Sherpa	
state	0.5 TeV	2 TeV	0.5 TeV	2 TeV	0.5 TeV	2 TeV
$\tilde{e}_L\tilde{\nu}_e^*$	158.69(1)	67.096(5)	158.694(7)	67.095(3)	158.703(8)	67.100(3)
$\tilde{e}_R\tilde{\nu}_e^*$	68.51(1)	6.547(4)	68.513(3)	6.5470(4)	68.508(3)	6.5469(3)
$\tilde{\mu}_L\tilde{\nu}_\mu^*$	58.492(3)	13.894(1)	58.491(2)	13.8935(5)	58.492(3)	13.8931(7)
$\tilde{\tau}_1\tilde{\nu}_\tau^*$	8.5018(5)	1.1169(1)	8.5021(3)	1.11690(4)	8.5018(4)	1.11696(6)
$\tilde{\tau}_2\tilde{\nu}_\tau^*$	51.792(3)	12.784(1)	51.790(2)	12.7836(5)	51.795(3)	12.7844(6)
$\tilde{\chi}_1^-\tilde{\chi}_1^0$	137.414(5)	21.4202(6)	137.416(4)	21.4203(9)	137.426(8)	21.419(2)
$\tilde{\chi}_1^-\tilde{\chi}_2^0$	58.797(3)	21.284(2)	58.795(1)	21.283(1)	58.794(3)	21.282(2)
$\tilde{\chi}_1^-\tilde{\chi}_3^0$	—	2.2676(1)	—	2.26760(7)	—	2.2678(1)
$\tilde{\chi}_1^-\tilde{\chi}_4^0$	—	3.5104(2)	—	3.51046(6)	—	3.5105(2)
$\tilde{\chi}_2^-\tilde{\chi}_1^0$	1.16070(5)	1.73602(6)	1.16072(3)	1.73607(6)	1.16066(6)	1.73593(9)
$\tilde{\chi}_2^-\tilde{\chi}_2^0$	—	3.6111(3)	—	3.61122(6)	—	3.6113(2)
$\tilde{\chi}_2^-\tilde{\chi}_3^0$	—	26.9497(5)	—	26.9511(7)	—	26.952(1)
$\tilde{\chi}_2^-\tilde{\chi}_4^0$	—	24.022(1)	—	24.0223(8)	—	24.022(1)

A.4.4 $\tau^-\bar{\nu}_\tau$ processes

$\mathbf{\tau^-\bar{\nu}_\tau \to X^-}$						
Final	MadGraph/Helas		O'mega/Whizard		Amegic++/Sherpa	
state	0.5 TeV	2 TeV	0.5 TeV	2 TeV	0.5 TeV	2 TeV
$\tilde{\tau}_1\tilde{\nu}_\tau^*$	84.13(2)	12.272(7)	84.129(3)	12.2724(4)	84.124(4)	12.2719(6)
$\tilde{\tau}_2\tilde{\nu}_\tau^*$	139.86(1)	61.466(7)	139.852(6)	61.463(3)	139.858(7)	61.467(3)
$\tilde{\chi}_1^-\tilde{\chi}_1^0$	146.263(6)	21.386(1)	146.265(4)	21.3863(9)	146.27(1)	21.389(2)
$\tilde{\chi}_1^-\tilde{\chi}_2^0$	56.218(4)	21.338(3)	56.217(1)	21.336(1)	56.218(5)	21.339(2)
$\tilde{\chi}_1^-\tilde{\chi}_3^0$	—	2.2049(1)	—	2.2046(2)	—	2.2050(2)
$\tilde{\chi}_1^-\tilde{\chi}_4^0$	—	3.4436(3)	—	3.44365(7)	—	3.4434(3)
$\tilde{\chi}_2^-\tilde{\chi}_1^0$	7.5231(2)	1.9569(1)	7.52316(6)	1.95691(6)	7.5234(8)	1.9570(2)
$\tilde{\chi}_2^-\tilde{\chi}_2^0$	—	3.4953(3)	—	3.49538(6)	—	3.4955(3)
$\tilde{\chi}_2^-\tilde{\chi}_3^0$	—	25.867(1)	—	25.8690(7)	—	25.866(3)
$\tilde{\chi}_2^-\tilde{\chi}_4^0$	—	23.199(1)	—	23.1989(8)	—	23.201(2)
H^-h^0	—	0.002422(1)	—	0.0024223(1)	—	0.0024221(1)
H^-H^0	—	4.8560(5)	—	4.8560(3)	—	4.8564(2)
H^-A^0	—	4.8574(5)	—	4.8578(3)	—	4.8576(2)
W^-h^0	133.484(7)	7.537(1)	133.478(5)	7.5376(3)	133.476(7)	7.5377(4)
W^-H^0	57.988(7)	8.543(7)	57.989(2)	8.5432(4)	57.991(3)	8.5435(4)
W^-A^0	58.584(7)	8.567(7)	58.583(2)	8.5672(4)	58.586(3)	8.5679(4)
Z^0H^-	17.9854(1)	13.99(1)	17.9860(5)	13.9881(6)	17.986(1)	13.9881(7)

A.4.5 $b\bar{t}$ processes

$\mathbf{b\bar{t} \to X^-}$						
Final	MadGraph/Helas		O'mega/Whizard		Amegic++/Sherpa	
state	0.5 TeV	2 TeV	0.5 TeV	2 TeV	0.5 TeV	2 TeV
$\tilde{b}_1\tilde{t}_1^*$	—	667.4(2)	—	667.45(2)	—	667.53(4)
$\tilde{b}_1\tilde{t}_2^*$	—	609.5(1)	—	609.52(2)	—	609.53(3)
$\tilde{b}_2\tilde{t}_1^*$	—	692.7(1)	—	692.66(2)	—	692.73(4)
$\tilde{b}_2\tilde{t}_2^*$	—	775.7(2)	—	775.71(2)	—	775.69(4)
$\tilde{\chi}_1^-\tilde{\chi}_1^0$	37.7535(4)	0.58472(5)	37.75442(7)	0.584741(6)	37.7542(1)	0.58473(2)
$\tilde{\chi}_1^-\tilde{\chi}_2^0$	171.662(4)	6.1432(8)	171.6667(6)	6.1435(2)	171.6654(1)	6.1432(3)
$\tilde{\chi}_1^-\tilde{\chi}_3^0$	—	7.2061(7)	—	7.20626(9)	—	7.2057(4)
$\tilde{\chi}_1^-\tilde{\chi}_4^0$	—	9.7429(7)	—	9.7429(1)	—	9.7428(5)
$\tilde{\chi}_2^-\tilde{\chi}_1^0$	17.9155(5)	2.8972(3)	17.91595(4)	2.89723(3)	17.9159(1)	2.8972(1)
$\tilde{\chi}_2^-\tilde{\chi}_2^0$	—	8.1076(7)	—	8.10775(8)	—	8.1078(4)
$\tilde{\chi}_2^-\tilde{\chi}_3^0$	—	54.043(2)	—	54.046(1)	—	54.050(4)
$\tilde{\chi}_2^-\tilde{\chi}_4^0$	—	48.083(1)	—	48.0844(9)	—	48.083(2)
H^-h^0	—	26.660(8)	—	26.660(1)	—	26.666(4)
H^-H^0	—	2.0061(5)	—	2.00611(8)	—	2.0063(2)
H^-A^0	—	1.9083(5)	—	1.90817(8)	—	1.9084(2)
Z^0H^-	20.3530(1)	34.76(1)	20.3544(1)	34.766(1)	20.3543(1)	34.764(2)

A.4.6 W^+W^- processes

$\mathbf{W^+W^- \to X}$						
Final	MadGraph/Helas		O'mega/Whizard		Amegic++/Sherpa	
state	0.5 TeV	2 TeV	0.5 TeV	2 TeV	0.5 TeV	2 TeV
$\tilde{e}_L\tilde{e}_L^*$	192.14(2)	26.538(4)	192.145(1)	26.5380(6)	192.151(9)	26.538(1)
$\tilde{e}_R\tilde{e}_R^*$	14.215(3)	1.0297(3)	14.2151(4)	1.02966(4)	14.2153(7)	1.02968(5)
$\tilde{\mu}_L\tilde{\mu}_L^*$	192.14(2)	26.538(4)	192.146(1)	26.5380(6)	192.139(9)	26.540(1)
$\tilde{\mu}_R\tilde{\mu}_R^*$	14.215(3)	1.0297(3)	14.2145(4)	1.02972(4)	14.2153(7)	1.02975(5)
$\tilde{\tau}_1\tilde{\tau}_1^*$	7.926(2)	0.8328(3)	7.9266(2)	0.83284(3)	7.9269(4)	0.83286(4)
$\tilde{\tau}_2\tilde{\tau}_2^*$	168.05(2)	22.419(4)	168.046(1)	22.4195(5)	168.046(8)	22.419(1)
$\tilde{\tau}_1\tilde{\tau}_2^*$	17.852(3)	2.3294(4)	17.8521(1)	2.32935(5)	17.8518(9)	2.3293(1)
$\tilde{\nu}_e\tilde{\nu}_e^*$	157.80(4)	23.487(6)	157.809(3)	23.486(1)	157.803(8)	23.489(1)
$\tilde{\nu}_\mu\tilde{\nu}_\mu^*$	157.80(4)	23.487(6)	157.806(3)	23.487(1)	157.807(8)	23.488(1)
$\tilde{\nu}_\tau\tilde{\nu}_\tau^*$	152.51(4)	23.427(6)	152.509(3)	23.429(1)	152.520(8)	23.429(1)
$\tilde{u}_L\tilde{u}_L^*$	—	41.59(1)	—	41.590(1)	—	41.588(2)
$\tilde{u}_R\tilde{u}_R^*$	—	1.0761(3)	—	1.07608(3)	—	1.07605(5)
$\tilde{c}_L\tilde{c}_L^*$	—	41.59(1)	—	41.588(1)	—	41.599(2)
$\tilde{c}_R\tilde{c}_R^*$	—	1.0761(3)	—	1.07603(3)	—	1.07596(5)
$\tilde{t}_1\tilde{t}_1^*$	—	180.64(1)	—	180.637(4)	—	180.637(9)
$\tilde{t}_2\tilde{t}_2^*$	—	204.46(1)	—	204.461(3)	—	204.47(1)
$\tilde{t}_1\tilde{t}_2^*$	—	85.176(3)	—	85.178(2)	—	85.187(4)
$\tilde{d}_L\tilde{d}_L^*$	—	39.006(7)	—	39.0067(4)	—	39.007(2)
$\tilde{d}_R\tilde{d}_R^*$	—	0.26929(7)	—	0.269305(8)	—	0.26930(1)
$\tilde{s}_L\tilde{s}_L^*$	—	39.006(7)	—	39.0062(4)	—	39.007(2)
$\tilde{s}_R\tilde{s}_R^*$	—	0.26929(7)	—	0.269291(8)	—	0.26930(1)
$\tilde{b}_1\tilde{b}_1^*$	—	141.456(8)	—	141.457(2)	—	141.467(7)
$\tilde{b}_2\tilde{b}_2^*$	—	19.714(1)	—	19.7133(4)	—	19.715(1)
$\tilde{b}_1\tilde{b}_2^*$	—	61.090(4)	—	61.090(1)	—	61.093(3)
$\tilde{\chi}_1^0\tilde{\chi}_1^0$	3.8822(2)	1.2741(4)	3.8824(1)	1.27423(8)	3.8821(2)	1.2741(1)
$\tilde{\chi}_1^0\tilde{\chi}_2^0$	121.29(1)	24.47(1)	121.2925(7)	24.472(3)	121.296(6)	24.477(1)
$\tilde{\chi}_1^0\tilde{\chi}_3^0$	6.8936(7)	12.880(7)	6.8934(2)	12.8790(8)	6.8938(3)	12.8793(6)
$\tilde{\chi}_1^0\tilde{\chi}_4^0$	1.4974(1)	9.707(5)	1.4973(6)	9.7064(7)	1.49735(7)	9.7078(4)
$\tilde{\chi}_2^0\tilde{\chi}_2^0$	5996.5(4)	1.0415(6)e3	5996.57(2)	1.04150(5)e3	5996.4(3)	1.04148(5)e3
$\tilde{\chi}_2^0\tilde{\chi}_3^0$	—	365.6(2)	—	365.615(6)	—	365.63(2)
$\tilde{\chi}_2^0\tilde{\chi}_4^0$	—	467.8(2)	—	467.775(8)	—	467.77(2)
$\tilde{\chi}_3^0\tilde{\chi}_3^0$	—	82.35(3)	—	82.347(8)	—	82.352(4)
$\tilde{\chi}_3^0\tilde{\chi}_4^0$	—	138.20(5)	—	138.18(1)	—	138.205(7)
$\tilde{\chi}_4^0\tilde{\chi}_4^0$	—	117.78(4)	—	117.80(1)	—	117.786(6)
$\tilde{\chi}_1^+\tilde{\chi}_1^-$	3772(1)	944.3(8)	3771.6(4)	944.2(1)	3771.8(2)	944.32(5)
$\tilde{\chi}_2^+\tilde{\chi}_2^-$	—	258.3(2)	—	258.37(4)	—	258.36(1)
$\tilde{\chi}_1^+\tilde{\chi}_2^-$	—	131.0(1)	—	130.98(2)	—	130.966(7)

$\mathbf{W^+W^- \to X}$						
Final	MadGraph/Helas		O'mega/Whizard		Amegic++/Sherpa	
state	0.5 TeV	2 TeV	0.5 TeV	2 TeV	0.5 TeV	2 TeV
h^0h^0	6023.6(9)	6.057(3)e3	6024.7(4)	6.061(1)e3	6025.0(3)	6.0587(3)e3
h^0H^0	—	2.174(1)	—	2.1752(6)	—	2.1752(1)
H^0H^0	—	6.7515(1)	—	6.7509(11)	—	6.7517(3)
A^0A^0	—	6.7270(1)	—	6.7273(4)	—	6.7274(3)
Z^0h^0	75520(13)	8.617(4)e4	75539(7)	8.620(2)e4	75528(4)	8.6181(4)e4
Z^0H^0	1.70948(2)	16.390(8)	1.70944(8)	16.3939(37)	1.70971(9)	16.3933(8)
A^0h^0	—	6.0126(3)e-3	—	6.0123(7)e-3	—	6.0130(3)e-3
A^0H^0	—	3.4709(3)	—	3.4708(7)	—	3.4710(2)
H^+H^-	—	19.605(1)	—	19.6060(23)	—	19.605(1)

A.4.7 W^-Z^0 processes

$\mathbf{W^-Z^0 \to X^-}$						
Final	MadGraph/Helas		O'mega/Whizard		Amegic++/Sherpa	
state	0.5 TeV	2 TeV	0.5 TeV	2 TeV	0.5 TeV	2 TeV
$\tilde{e}_L\tilde{\nu}_e^*$	96.635(6)	15.726(1)	96.639(2)	15.728(2)	96.632(5)	15.7249(8)
$\tilde{\mu}_L\tilde{\nu}_\mu^*$	96.635(6)	15.726(1)	96.638(2)	15.727(2)	96.631(5)	15.7264(8)
$\tilde{\tau}_1\tilde{\nu}_\tau^*$	14.9542(8)	1.427(1)	14.952(1)	1.4268(2)	14.953(1)	1.42747(7)
$\tilde{\tau}_2\tilde{\nu}_\tau^*$	85.875(5)	14.479(1)	85.875(2)	14.478(2)	85.870(4)	14.4780(7)
$\tilde{d}_L\tilde{u}_L^*$	—	24.220(3)	—	24.220(1)	—	24.219(1)
$\tilde{s}_L\tilde{c}_L^*$	—	24.220(3)	—	24.221(1)	—	24.220(1)
$\tilde{b}_1\tilde{t}_1^*$	—	40.676(2)	—	40.676(4)	—	40.677(2)
$\tilde{b}_2\tilde{t}_2^*$	—	8.3717(5)	—	8.3706(7)	—	8.3722(4)
$\tilde{b}_1\tilde{t}_2^*$	—	63.596(3)	—	63.592(6)	—	63.591(3)
$\tilde{b}_2\tilde{t}_1^*$	—	3.9242(2)	—	3.9236(5)	—	3.9244(2)
$\tilde{\chi}_1^0\tilde{\chi}_1^-$	61.634(6)	16.389(5)	61.626(3)	16.389(1)	61.633(3)	16.391(1)
$\tilde{\chi}_2^0\tilde{\chi}_1^-$	2.8355(7)e3	668.2(4)	2.8350(3)e3	668.1(1)	2.8356(2)e3	668.34(3)
$\tilde{\chi}_3^0\tilde{\chi}_1^-$	—	278.5(1)	—	278.53(1)	—	278.58(2)
$\tilde{\chi}_4^0\tilde{\chi}_1^-$	—	270.9(1)	—	270.97(2)	—	271.02(2)
$\tilde{\chi}_1^0\tilde{\chi}_2^-$	11.7607(3)	12.379(4)	11.7619(7)	12.380(1)	11.7602(6)	12.380(1)
$\tilde{\chi}_2^0\tilde{\chi}_2^-$	—	218.3(1)	—	218.38(2)	—	218.40(1)
$\tilde{\chi}_3^0\tilde{\chi}_2^-$	—	76.50(3)	—	76.494(5)	—	76.497(4)
$\tilde{\chi}_4^0\tilde{\chi}_2^-$	—	97.70(4)	—	97.693(7)	—	97.693(4)
h^0H^-	—	4.439(6)e-3	—	4.4399(5)e-3	—	4.4395(2)e-3
H^0H^-	—	6.1592(6)	—	6.1592(2)	—	6.1589(3)
A^0H^-	—	5.9728(6)	—	5.9726(5)	—	5.9723(3)
W^-h^0	7.620(3)e4	8.29(1)e4	7.6213(6)e4	8.289(2)e4	7.6209(4)e4	8.2909(4)e4
W^-H^0	4.2446(2)	15.78(2)	4.2446(2)	15.783(3)	4.2445(2)	15.7848(8)
W^-A^0	1.07034(3)	0.24799(1)	1.07037(1)	0.24815(7)	1.07017(6)	0.24801(1)
Z^0H^-	0.177241(1)	0.25405(1)	0.17723(2)	0.25403(7)	0.17714(4)	0.25404(1)

A.4.8 $W^-\gamma$ processes

$\mathbf{W^-\gamma \to X^-}$						
Final	MadGraph/Helas		O'mega/Whizard		Amegic++/Sherpa	
state	0.5 TeV	2 TeV	0.5 TeV	2 TeV	0.5 TeV	2 TeV
$\tilde{e}_L\tilde{\nu}_e^*$	92.93(2)	14.478(3)	92.927(7)	14.477(3)	92.933(5)	14.4789(7)
$\tilde{\mu}_L\tilde{\nu}_\mu^*$	92.93(2)	14.478(3)	92.942(7)	14.479(3)	92.934(5)	14.4782(7)
$\tilde{\tau}_1\tilde{\nu}_\tau^*$	12.098(2)	1.2566(2)	12.100(1)	1.2566(3)	12.1035(6)	1.25669(6)
$\tilde{\tau}_2\tilde{\nu}_\tau^*$	85.17(1)	13.373(2)	85.167(7)	13.372(3)	85.174(4)	13.3731(7)
$\tilde{d}_L\tilde{u}_R^*$	—	6.260(2)	—	6.260(1)	—	6.2605(3)
$\tilde{s}_L\tilde{c}_R^*$	—	6.260(2)	—	6.262(1)	—	6.2605(3)
$\tilde{b}_1\tilde{t}_1^*$	—	5.527(1)	—	5.528(1)	—	5.5279(3)
$\tilde{b}_2\tilde{t}_2^*$	—	0.5418(1)	—	0.5417(1)	—	0.54182(3)
$\tilde{b}_1\tilde{t}_2^*$	—	6.267(1)	—	6.267(1)	—	6.2680(3)
$\tilde{b}_2\tilde{t}_1^*$	—	0.8593(2)	—	0.8595(2)	—	0.85928(4)
$\tilde{\chi}_1^0\tilde{\chi}_1^-$	15.824(4)	3.834(2)	15.821(2)	3.8332(6)	15.823(1)	3.8338(2)
$\tilde{\chi}_2^0\tilde{\chi}_1^-$	1.2235(2)e3	303.1(1)	1.2235(1)e3	303.04(5)	1.22335(6)e3	303.11(2)
$\tilde{\chi}_3^0\tilde{\chi}_1^-$	—	50.91(2)	—	50.902(8)	—	50.909(3)
$\tilde{\chi}_4^0\tilde{\chi}_1^-$	—	52.64(2)	—	52.648(8)	—	52.643(3)
$\tilde{\chi}_1^0\tilde{\chi}_2^-$	3.0373(3)	6.574(2)	3.03742(7)	6.5764(9)	3.0373(2)	6.5749(3)
$\tilde{\chi}_2^0\tilde{\chi}_2^-$	—	34.00(1)	—	34.003(5)	—	34.000(2)
$\tilde{\chi}_3^0\tilde{\chi}_2^-$	—	47.72(1)	—	47.719(7)	—	47.720(2)
$\tilde{\chi}_4^0\tilde{\chi}_2^-$	—	59.64(2)	—	59.636(8)	—	59.639(3)
h^0H^-	—	4.519(1)e-3	—	4.5192(8)e-3	—	4.5194(3)e-3
H^0H^-	—	4.961(1)	—	4.9610(9)	—	4.9611(2)
A^0H^-	—	4.966(1)	—	4.9671(9)	—	4.9668(2)
W^-h^0	1.2848(6)e4	1.580(2)e4	1.2855(3)e4	1.5811(4)e4	1.28512(7)e4	1.5801(1)e4
W^-H^0	0.5401(1)	3.016(4)	0.54011(6)	3.0172(7)	0.54016(3)	3.0170(2)

A.4.9 Z^0Z^0 processes

$\mathbf{Z^0Z^0 \to X}$						
Final	MadGraph/Helas		O'mega/Whizard		Amegic++/Sherpa	
state	0.5 TeV	2 TeV	0.5 TeV	2 TeV	0.5 TeV	2 TeV
$\tilde{e}_L\tilde{e}_L^*$	35.791(1)	3.78984(6)	35.7923(4)	3.8011(2)	35.792(2)	3.8009(2)
$\tilde{e}_R\tilde{e}_R^*$	22.9506(3)	1.92383(3)	22.9508(4)	1.9234(1)	22.950(1)	1.9239(1)
$\tilde{\mu}_L\tilde{\mu}_L^*$	35.791(1)	3.78984(6)	35.7920(4)	3.8008(2)	35.792(2)	3.8008(2)
$\tilde{\mu}_R\tilde{\mu}_R^*$	22.9506(3)	1.92383(3)	22.9509(4)	1.9239(1)	22.951(1)	1.9240(2)
$\tilde{\tau}_1\tilde{\tau}_1^*$	19.7282(2)	1.99982(4)	19.7282(3)	1.99985(8)	19.729(1)	1.9998(1)
$\tilde{\tau}_2\tilde{\tau}_2^*$	30.0569(7)	3.6161(1)	30.0574(2)	3.6161(1)	30.057(2)	3.6164(2)
$\tilde{\tau}_1\tilde{\tau}_2^*$	0.5145(1)	0.05745(1)	0.51455(2)	0.057456(2)	0.51455(3)	0.057455(3)
$\tilde{\nu}_e\tilde{\nu}_e^*$	232.51(1)	32.0348(7)	232.517(3)	32.037(2)	232.51(1)	32.035(2)
$\tilde{\nu}_\mu\tilde{\nu}_\mu^*$	232.51(1)	32.0348(7)	232.515(3)	32.037(2)	232.51(1)	32.036(2)
$\tilde{\nu}_\tau\tilde{\nu}_\tau^*$	233.33(1)	32.0709(7)	233.341(3)	32.072(2)	233.34(1)	32.073(2)
$\tilde{u}_L\tilde{u}_L^*$	—	15.6788(4)	—	15.6792(3)	—	15.6799(8)
$\tilde{u}_R\tilde{u}_R^*$	—	1.20947(1)	—	1.20948(2)	—	1.20948(6)
$\tilde{c}_L\tilde{c}_L^*$	—	15.6788(4)	—	15.6791(3)	—	15.6792(8)
$\tilde{c}_R\tilde{c}_R^*$	—	1.20947(1)	—	1.20949(2)	—	1.20950(2)
$\tilde{t}_1\tilde{t}_1^*$	—	262.15(1)	—	262.155(8)	—	262.15(1)
$\tilde{t}_2\tilde{t}_2^*$	—	475.11(2)	—	475.11(1)	—	475.14(2)
$\tilde{t}_1\tilde{t}_2^*$	—	10.7125(2)	—	10.7125(2)	—	10.7128(5)
$\tilde{d}_L\tilde{d}_L^*$	—	30.546(1)	—	30.5474(5)	—	30.547(2)
$\tilde{d}_R\tilde{d}_R^*$	—	0.238111(1)	—	0.238127(6)	—	0.23812(1)
$\tilde{s}_L\tilde{s}_L^*$	—	30.546(1)	—	30.5475(5)	—	30.545(2)
$\tilde{s}_R\tilde{s}_R^*$	—	0.238111(1)	—	0.238115(6)	—	0.23811(1)
$\tilde{b}_1\tilde{b}_1^*$	—	20.7326(7)	—	20.7329(2)	—	20.734(1)
$\tilde{b}_2\tilde{b}_2^*$	—	10.68655(1)	—	10.6865(2)	—	10.6870(5)
$\tilde{b}_1\tilde{b}_2^*$	—	18.6452(1)	—	18.6455(2)	—	18.6454(9)
h^0h^0	7886(1)	7800(5)	7887.5(1)	7802.5(3)	7887.7(4)	7801.3(4)
h^0H^0	—	2.772(2)	—	2.7726(2)	—	2.7727(2)
H^0H^0	—	11.5202(2)	—	11.5209(4)	—	11.5206(6)
A^0A^0	—	11.3523(2)	—	11.3528(4)	—	11.3528(6)
H^+H^-	—	3.17134(3)	—	3.17136(5)	—	3.1714(2)

A.4.10 $Z^0\gamma$ processes

$\mathbf{Z^0\gamma \to X}$						
Final	MadGraph/Helas		O'mega/Whizard		Amegic++/Sherpa	
state	0.5 TeV	2 TeV	0.5 TeV	2 TeV	0.5 TeV	2 TeV
$\tilde{e}_L\tilde{e}_L^*$	64.062(2)	8.7331(2)	64.0633(7)	8.7333(5)	64.062(3)	8.7336(3)
$\tilde{e}_R\tilde{e}_R^*$	50.727(1)	6.0452(1)	50.7284(7)	6.0451(4)	50.728(3)	6.0453(3)
$\tilde{\mu}_L\tilde{\mu}_L^*$	64.062(2)	8.7331(2)	64.0628(7)	8.7327(5)	64.064(3)	8.7329(4)
$\tilde{\mu}_R\tilde{\mu}_R^*$	50.727(1)	6.0452(1)	50.7284(7)	6.0455(4)	50.728(3)	6.0450(3)
$\tilde{\tau}_1\tilde{\tau}_1^*$	36.4564(6)	4.13408(5)	36.4567(6)	4.1336(3)	36.455(2)	4.1339(2)
$\tilde{\tau}_2\tilde{\tau}_2^*$	46.604(1)	6.3910(1)	46.6053(5)	6.3907(4)	46.603(2)	6.3909(3)
$\tilde{\tau}_1\tilde{\tau}_2^*$	24.0433(2)	2.31001(2)	24.0446(3)	2.3102(1)	24.043(1)	2.3100(1)
$\tilde{u}_L\tilde{u}_L^*$	—	10.1947(3)	—	10.1949(2)	—	10.1949(5)
$\tilde{u}_R\tilde{u}_R^*$	—	1.86038(5)	—	1.86042(3)	—	1.8603(1)
$\tilde{c}_L\tilde{c}_L^*$	—	10.1947(3)	—	10.1949(2)	—	10.1950(5)
$\tilde{c}_R\tilde{c}_R^*$	—	1.86038(5)	—	1.86039(3)	—	1.8604(1)
$\tilde{t}_1\tilde{t}_1^*$	—	0.00126511(2)	—	0.00126510(3)	—	0.00126512(6)
$\tilde{t}_2\tilde{t}_2^*$	—	3.44658(6)	—	3.44660(5)	—	3.4465(2)
$\tilde{t}_1\tilde{t}_2^*$	—	19.0977(4)	—	19.0982(7)	—	19.098(1)
$\tilde{d}_L\tilde{d}_L^*$	—	3.70757(7)	—	3.70773(5)	—	3.7077(2)
$\tilde{d}_R\tilde{d}_R^*$	—	0.116431(3)	—	0.116438(2)	—	0.116431(6)
$\tilde{s}_L\tilde{s}_L^*$	—	3.70757(7)	—	3.70774(6)	—	3.7076(2)
$\tilde{s}_R\tilde{s}_R^*$	—	0.116431(3)	—	0.116435(2)	—	0.116431(6)
$\tilde{b}_1\tilde{b}_1^*$	—	3.1278(1)	—	3.12782(6)	—	3.1276(2)
$\tilde{b}_2\tilde{b}_2^*$	—	0.0114499(3)	—	0.0114501(2)	—	0.0114507(6)
$\tilde{b}_1\tilde{b}_2^*$	—	0.53387(1)	—	0.533885(9)	—	0.53388(3)
H^+H^-	—	6.1846(2)	—	6.1849(1)	—	6.1848(3)

A.4.11 $\gamma\gamma$ processes

$\gamma\gamma \to \mathbf{X}$						
Final	MadGraph/Helas		O'mega/Whizard		Amegic++/Sherpa	
state	0.5 TeV	2 TeV	0.5 TeV	2 TeV	0.5 TeV	2 TeV
$\tilde{e}_L\tilde{e}_L^*$	210.00(1)	29.058(1)	210.005(7)	20.056(5)	210.00(1)	29.060(2)
$\tilde{e}_R\tilde{e}_R^*$	250.32(1)	31.376(1)	250.321(11)	31.381(6)	250.324(12)	31.379(2)
$\tilde{\mu}_L\tilde{\mu}_L^*$	210.00(1)	29.058(1)	209.979(7)	29.041(5)	210.008(12)	29.058(2)
$\tilde{\mu}_R\tilde{\mu}_R^*$	250.32(1)	31.376(1)	250.322(11)	31.379(6)	250.313(13)	31.376(2)
$\tilde{\tau}_1\tilde{\tau}_1^*$	263.35(1)	31.715(1)	263.362(13)	31.714(6)	263.360(13)	31.719(2)
$\tilde{\tau}_2\tilde{\tau}_2^*$	207.62(1)	28.895(1)	207.618(7)	28.897(5)	207.625(10)	28.896(2)
$\tilde{u}_L\tilde{u}_L^*$	—	9.4531(3)	—	9.4536(4)	—	9.4530(4)
$\tilde{u}_R\tilde{u}_R^*$	—	9.7241(3)	—	9.7244(5)	—	9.7236(5)
$\tilde{c}_L\tilde{c}_L^*$	—	9.4531(3)	—	9.4534(4)	—	9.4531(4)
$\tilde{c}_R\tilde{c}_R^*$	—	9.7241(3)	—	9.7230(5)	—	9.7244(5)
$\tilde{t}_1\tilde{t}_1^*$	—	12.5153(5)	—	12.5159(9)	—	12.5157(6)
$\tilde{t}_2\tilde{t}_2^*$	—	9.2289(3)	—	9.2298(4)	—	9.2287(5)
$\tilde{d}_L\tilde{d}_L^*$	—	0.58654(2)	—	0.58655(3)	—	0.58655(3)
$\tilde{d}_R\tilde{d}_R^*$	—	0.60857(2)	—	0.60853(3)	—	0.60857(3)
$\tilde{s}_L\tilde{s}_L^*$	—	0.58654(2)	—	0.58656(3)	—	0.58656(3)
$\tilde{s}_R\tilde{s}_R^*$	—	0.60857(2)	—	0.60863(3)	—	0.60860(3)
$\tilde{b}_1\tilde{b}_1^*$	—	0.63761(2)	—	0.63761(3)	—	0.63759(3)
$\tilde{b}_2\tilde{b}_2^*$	—	0.61043(2)	—	0.61045(3)	—	0.61049(3)
$\tilde{\chi}_1^+\tilde{\chi}_1^-$	1458.99(6)	274.0(1)	1459.04(6)	274.020(9)	1458.96(7)	274.01(1)
$\tilde{\chi}_2^+\tilde{\chi}_2^-$	—	181.54(3)	—	181.542(6)	—	181.549(9)
H^+H^-	—	20.650(1)	—	20.644(2)	—	20.649(1)

A.4.12 $g\gamma$ processes

$\mathbf{g}\gamma \to \mathbf{X}$						
Final	MadGraph/Helas		O'mega/Whizard		Amegic++/Sherpa	
state	0.5 TeV	2 TeV	0.5 TeV	2 TeV	0.5 TeV	2 TeV
$\tilde{u}_L\tilde{u}_L^*$	—	55.427(1)	—	55.4290(8)	—	55.428(3)
$\tilde{u}_R\tilde{u}_R^*$	—	57.017(1)	—	57.0184(9)	—	57.020(3)
$\tilde{c}_L\tilde{c}_L^*$	—	55.427(1)	—	55.4288(8)	—	55.430(3)
$\tilde{c}_R\tilde{c}_R^*$	—	57.017(1)	—	57.0175(9)	—	57.019(3)
$\tilde{t}_1\tilde{t}_1^*$	—	73.382(2)	—	73.382(2)	—	73.383(4)
$\tilde{t}_2\tilde{t}_2^*$	—	54.113(1)	—	54.1136(8)	—	54.113(3)
$\tilde{d}_L\tilde{d}_L^*$	—	13.7565(4)	—	13.7569(2)	—	13.7560(7)
$\tilde{d}_R\tilde{d}_R^*$	—	14.2733(4)	—	14.2737(2)	—	14.2740(7)
$\tilde{s}_L\tilde{s}_L^*$	—	13.7565(4)	—	13.7568(2)	—	13.7575(7)
$\tilde{s}_R\tilde{s}_R^*$	—	14.2733(4)	—	14.2735(2)	—	14.2731(7)
$\tilde{b}_1\tilde{b}_1^*$	—	14.9542(4)	—	14.9546(3)	—	14.9540(7)
$\tilde{b}_2\tilde{b}_2^*$	—	14.3169(4)	—	14.3171(2)	—	14.3183(7)

A.4.13 gZ^0 processes

$gZ^0 \to X$						
Final	MadGraph/Helas		O'mega/Whizard		Amegic++/Sherpa	
state	0.5 TeV	2 TeV	0.5 TeV	2 TeV	0.5 TeV	2 TeV
$\tilde{u}_L\tilde{u}_L^*$	—	59.776(2)	—	59.7774(9)	—	59.778(3)
$\tilde{u}_R\tilde{u}_R^*$	—	10.9082(3)	—	10.9085(2)	—	10.9079(5)
$\tilde{c}_L\tilde{c}_L^*$	—	59.776(2)	—	59.7772(9)	—	59.778(3)
$\tilde{c}_R\tilde{c}_R^*$	—	10.9082(3)	—	10.9084(2)	—	10.9088(5)
$\tilde{t}_1\tilde{t}_1^*$	—	0.0074179(2)	—	0.0074179(2)	—	0.0074182(4)
$\tilde{t}_2\tilde{t}_2^*$	—	20.2088(5)	—	20.2091(3)	—	20.208(1)
$\tilde{t}_1\tilde{t}_2^*$	—	111.978(3)	—	111.986(4)	—	111.980(6)
$\tilde{d}_L\tilde{d}_L^*$	—	86.956(2)	—	86.9615(1)	—	86.960(4)
$\tilde{d}_R\tilde{d}_R^*$	—	2.73075(7)	—	2.73090(4)	—	2.7308(1)
$\tilde{s}_L\tilde{s}_L^*$	—	86.956(2)	—	86.959(1)	—	86.956(4)
$\tilde{s}_R\tilde{s}_R^*$	—	2.73075(7)	—	2.73078(4)	—	2.7308(1)
$\tilde{b}_1\tilde{b}_1^*$	—	73.359(2)	—	73.360(1)	—	73.354(4)
$\tilde{b}_2\tilde{b}_2^*$	—	0.268544(7)	—	0.268554(4)	—	0.26857(1)
$\tilde{b}_1\tilde{b}_2^*$	—	12.5213(3)	—	12.5214(2)	—	12.5214(6)

A.4.14 gW^- processes

$gW^- \to X^-$						
Final	MadGraph/Helas		O'mega/Whizard		Amegic++/Sherpa	
state	0.5 TeV	2 TeV	0.5 TeV	2 TeV	0.5 TeV	2 TeV
$\tilde{d}_L\tilde{u}_L^*$	—	187.611(5)	—	187.616(3)	—	187.604(8)
$\tilde{s}_R\tilde{c}_R^*$	—	187.611(5)	—	187.617(3)	—	187.619(8)
$\tilde{b}_1\tilde{t}_1^*$	—	138.625(2)	—	138.625(4)	—	138.624(7)
$\tilde{b}_2\tilde{t}_2^*$	—	16.5094(3)	—	16.5095(3)	—	16.5088(8)
$\tilde{b}_1\tilde{t}_2^*$	—	195.686(1)	—	195.692(4)	—	195.701(9)
$\tilde{b}_2\tilde{t}_1^*$	—	20.7535(5)	—	20.7532(7)	—	20.753(1)

A.4.15 gg processes

$\mathbf{gg \to X}$						
Final	MadGraph/Helas		O'mega/Whizard		Amegic++/Sherpa	
state	0.5 TeV	2 TeV	0.5 TeV	2 TeV	0.5 TeV	2 TeV
$\tilde{g}\tilde{g}$	—	13575(2)	—	13575.6(1)	—	13575.8(7)
$\tilde{u}_L\tilde{u}_L^*$	—	185.60(2)	—	185.615(3)	—	185.61(1)
$\tilde{u}_R\tilde{u}_R^*$	—	191.58(2)	—	191.590(3)	—	191.59(1)
$\tilde{c}_L\tilde{c}_L^*$	—	185.60(2)	—	185.612(3)	—	185.61(1)
$\tilde{c}_R\tilde{c}_R^*$	—	191.58(2)	—	191.588(3)	—	191.59(1)
$\tilde{t}_1\tilde{t}_1^*$	—	250.70(2)	—	250.71(1)	—	250.70(1)
$\tilde{t}_2\tilde{t}_2^*$	—	180.54(2)	—	180.541(3)	—	180.54(1)
$\tilde{d}_L\tilde{d}_L^*$	—	184.07(2)	—	184.081(3)	—	184.09(1)
$\tilde{d}_R\tilde{d}_R^*$	—	191.87(2)	—	191.875(3)	—	191.87(1)
$\tilde{s}_L\tilde{s}_L^*$	—	184.07(2)	—	184.079(3)	—	184.08(1)
$\tilde{s}_R\tilde{s}_R^*$	—	191.87(2)	—	191.873(3)	—	191.86(1)
$\tilde{b}_1\tilde{b}_1^*$	—	201.88(2)	—	201.884(4)	—	201.90(1)
$\tilde{b}_2\tilde{b}_2^*$	—	192.52(2)	—	192.516(3)	—	192.53(1)

A.4.16 $u\bar{u}$ processes

$\mathbf{u\bar{u} \to X}$						
Final	MadGraph/Helas		O'mega/Whizard		Amegic++/Sherpa	
state	0.5 TeV	2 TeV	0.5 TeV	2 TeV	0.5 TeV	2 TeV
$\tilde{g}\tilde{g}$	—	1.1377(2)e3	—	1.1378(2)e3	—	1.1377(1)e3
$\tilde{e}_L\tilde{e}_L^*$	5.169(1)	1.5467(3)	5.1698(9)	1.5469(2)	5.1700(3)	1.54698(8)
$\tilde{e}_R\tilde{e}_R^*$	6.538(1)	0.7318(1)	6.538(1)	0.7318(1)	6.5379(3)	0.73179(4)
$\tilde{\mu}_L\tilde{\mu}_L^*$	5.169(1)	1.5467(3)	5.1687(9)	1.5466(3)	5.1693(3)	1.54679(8)
$\tilde{\mu}_R\tilde{\mu}_R^*$	6.538(1)	0.7318(1)	6.536(1)	0.7316(1)	6.5387(3)	0.73189(4)
$\tilde{\tau}_1\tilde{\tau}_1^*$	6.993(1)	0.7195(1)	6.992(1)	0.7194(1)	6.9935(3)	0.71949(4)
$\tilde{\tau}_2\tilde{\tau}_2^*$	4.1263(7)	1.3962(2)	4.1246(7)	1.3957(2)	4.1269(2)	1.39617(7)
$\tilde{\tau}_1\tilde{\tau}_2^*$	0.5420(1)	0.08218(1)	0.54193(9)	0.08217(1)	0.54199(3)	0.082184(4)
$\tilde{\nu}_e\tilde{\nu}_e^*$	5.7063(5)	1.1222(2)	5.706(1)	1.1222(2)	5.7064(3)	1.12224(6)
$\tilde{\nu}_\mu\tilde{\nu}_\mu^*$	5.7063(5)	1.1222(2)	5.704(1)	1.1217(2)	5.7070(3)	1.12237(6)
$\tilde{\nu}_\tau\tilde{\nu}_\tau^*$	5.812(1)	1.1228(2)	5.813(1)	1.1229(2)	5.8126(3)	1.12282(6)
$\tilde{u}_L\tilde{u}_L^*$	—	799.6(1)	—	799.6(1)	—	799.63(4)
$\tilde{u}_R\tilde{u}_R^*$	—	879.7(1)	—	879.7(1)	—	879.75(4)
$\tilde{u}_L\tilde{u}_R^*$	—	784.1(2)	—	784.16(3)	—	784.15(4)
$\tilde{c}_L\tilde{c}_L^*$	—	178.39(1)	—	178.39(2)	—	178.398(9)
$\tilde{c}_R\tilde{c}_R^*$	—	185.63(2)	—	185.62(2)	—	185.655(9)
$\tilde{t}_1\tilde{t}_1^*$	—	245.12(2)	—	245.11(3)	—	245.10(1)
$\tilde{t}_2\tilde{t}_2^*$	—	169.22(1)	—	169.22(2)	—	169.223(8)
$\tilde{t}_1\tilde{t}_2^*$	—	0.47708(4)	—	0.47714(8)	—	0.47712(2)
$\tilde{d}_L\tilde{d}_L^*$	—	166.63(2)	—	166.60(2)	—	166.621(8)
$\tilde{d}_R\tilde{d}_R^*$	—	185.58(2)	—	185.56(3)	—	185.60(1)
$\tilde{s}_L\tilde{s}_L^*$	—	175.69(1)	—	175.68(2)	—	175.686(9)
$\tilde{s}_R\tilde{s}_R^*$	—	185.58(2)	—	185.58(2)	—	185.578(9)
$\tilde{b}_1\tilde{b}_1^*$	—	200.37(2)	—	200.364(8)	—	200.38(1)
$\tilde{b}_2\tilde{b}_2^*$	—	186.50(2)	—	186.500(7)	—	186.51(1)
$\tilde{b}_1\tilde{b}_2^*$	—	0.19827(2)	—	0.198272(8)	—	0.19827(1)

$\mathbf{u\bar{u} \to X}$						
Final	MadGraph/Helas		O'mega/Whizard		Amegic++/Sherpa	
state	0.5 TeV	2 TeV	0.5 TeV	2 TeV	0.5 TeV	2 TeV
$\tilde{\chi}_1^0\tilde{\chi}_1^0$	2.2483(1)	1.2164(1)	2.24829(2)	1.2165(1)	2.2483(1)	1.2165(2)
$\tilde{\chi}_1^0\tilde{\chi}_2^0$	0.053855(3)	0.10850(1)	0.0538560(9)	0.10850(1)	0.053855(3)	0.108493(5)
$\tilde{\chi}_1^0\tilde{\chi}_3^0$	0.524518(4)	0.096758(1)	0.524526(3)	0.096752(5)	0.52450(3)	0.096763(5)
$\tilde{\chi}_1^0\tilde{\chi}_4^0$	9.8233(3)e-3	0.067303(3)	9.82339(8)e-3	0.067293(6)	9.8238(5)e-3	0.067308(3)
$\tilde{\chi}_2^0\tilde{\chi}_2^0$	3.66463(5)	4.2298(3)	3.66472(3)	4.2296(4)	3.6646(2)	4.2298(3)
$\tilde{\chi}_2^0\tilde{\chi}_3^0$	—	0.21148(3)	—	0.211458(8)	—	0.21147(1)
$\tilde{\chi}_2^0\tilde{\chi}_4^0$	—	0.55025(5)	—	0.55025(8)	—	0.55028(3)
$\tilde{\chi}_3^0\tilde{\chi}_3^0$	—	3.3843(1)e-4	—	3.3843(1)e-4	—	3.3844(2)e-4
$\tilde{\chi}_3^0\tilde{\chi}_4^0$	—	4.4435(3)	—	4.4433(2)	—	4.4436(2)
$\tilde{\chi}_4^0\tilde{\chi}_4^0$	—	0.016385(3)	—	0.016389(3)	—	0.016386(1)
$\tilde{\chi}_1^+\tilde{\chi}_1^-$	153.97(2)	10.732(5)	153.977(2)	10.734(2)	153.964(8)	10.7329(5)
$\tilde{\chi}_2^+\tilde{\chi}_2^-$	—	5.0402(5)	—	5.0401(2)	—	5.0400(3)
$\tilde{\chi}_1^+\tilde{\chi}_2^-$	—	1.5363(2)	—	1.5362(2)	—	1.5363(1)
Z^0h^0	22.795(2)	1.1958(1)	22.797(2)	1.1960(2)	22.798(1)	1.19582(6)
Z^0H^0	2.37220(1)e-4	2.1138(2)e-4	2.37224(1)e-4	2.1142(4)e-4	2.3723(1)e-4	2.1141(1)e-4

A.4.17 $d\bar{d}$ processes

$\mathbf{d\bar{d} \to X}$						
Final	MadGraph/Helas		O'mega/Whizard		Amegic++/Sherpa	
state	0.5 TeV	2 TeV	0.5 TeV	2 TeV	0.5 TeV	2 TeV
$\tilde{g}\tilde{g}$	—	1.1333(2)e3	—	1.1334(2)e3	—	1.13338(5)e3
$\tilde{e}_L\tilde{e}_L^*$	3.3467(6)	0.9844(2)	3.3472(6)	0.9845(2)	3.3473(2)	0.98453(5)
$\tilde{e}_R\tilde{e}_R^*$	2.0046(3)	0.21577(4)	2.0047(3)	0.21578(4)	2.0047(1)	0.21577(1)
$\tilde{\mu}_L\tilde{\mu}_L^*$	3.3467(6)	0.9844(2)	3.3465(6)	0.9843(2)	3.3469(2)	0.98435(5)
$\tilde{\mu}_R\tilde{\mu}_R^*$	2.0046(3)	0.21577(4)	2.0041(3)	0.21572(4)	2.0049(1)	0.21578(1)
$\tilde{\tau}_1\tilde{\tau}_1^*$	1.7274(3)	0.17266(3)	1.7271(3)	0.17264(3)	1.7273(1)	0.17265(1)
$\tilde{\tau}_2\tilde{\tau}_2^*$	2.4580(4)	0.8175(1)	2.4570(4)	0.8171(1)	2.4582(1)	0.81753(4)
$\tilde{\tau}_1\tilde{\tau}_2^*$	0.6951(1)	0.10539(2)	0.6950(1)	0.10538(2)	0.69505(4)	0.105383(5)
$\tilde{\nu}_e\tilde{\nu}_e^*$	7.3174(1)	1.4391(2)	7.318(1)	1.4391(2)	7.3177(4)	1.43913(7)
$\tilde{\nu}_\mu\tilde{\nu}_\mu^*$	7.3174(1)	1.4391(2)	7.314(1)	1.4385(3)	7.3186(4)	1.43930(7)
$\tilde{\nu}_\tau\tilde{\nu}_\tau^*$	7.454(1)	1.4398(2)	7.454(1)	1.4400(2)	7.4539(4)	1.43987(7)
$\tilde{u}_L\tilde{u}_L^*$	—	174.67(4)	—	174.67(2)	—	174.678(9)
$\tilde{u}_R\tilde{u}_R^*$	—	185.21(2)	—	185.19(3)	—	185.228(9)
$\tilde{c}_L\tilde{c}_L^*$	—	178.11(1)	—	178.10(2)	—	178.113(9)
$\tilde{c}_R\tilde{c}_R^*$	—	185.21(2)	—	185.21(2)	—	185.212(9)
$\tilde{t}_1\tilde{t}_1^*$	—	244.45(2)	—	244.45(3)	—	244.44(1)
$\tilde{t}_2\tilde{t}_2^*$	—	168.81(1)	—	168.80(2)	—	168.812(8)
$\tilde{t}_1\tilde{t}_2^*$	—	0.61179(5)	—	0.61183(8)	—	0.61184(3)
$\tilde{d}_L\tilde{d}_L^*$	—	790.4(1)	—	790.3(1)	—	790.38(4)
$\tilde{d}_R\tilde{d}_R^*$	—	927.1(1)	—	926.9(1)	—	927.11(5)
$\tilde{s}_L\tilde{s}_L^*$	—	175.92(1)	—	175.92(2)	—	175.920(9)
$\tilde{s}_R\tilde{s}_R^*$	—	185.48(2)	—	185.47(2)	—	185.474(9)
$\tilde{b}_1\tilde{b}_1^*$	—	200.54(2)	—	200.54(3)	—	200.57(1)
$\tilde{b}_2\tilde{b}_2^*$	—	186.38(2)	—	186.37(2)	—	186.384(9)
$\tilde{b}_1\tilde{b}_2^*$	—	0.25425(2)	—	0.25429(5)	—	0.25426(1)

$\mathbf{d\bar{d} \to X}$						
Final	MadGraph/Helas		O'mega/Whizard		Amegic++/Sherpa	
state	0.5 TeV	2 TeV	0.5 TeV	2 TeV	0.5 TeV	2 TeV
$\tilde{\chi}_1^0\tilde{\chi}_1^0$	0.118931(1)	0.079120(5)	0.1189331(7)	0.079125(4)	0.118938(5)	0.079118(5)
$\tilde{\chi}_1^0\tilde{\chi}_2^0$	0.249928(5)	0.34310(3)	0.249935(1)	0.34310(2)	0.24992(1)	0.34309(2)
$\tilde{\chi}_1^0\tilde{\chi}_3^0$	0.81721(1)	0.17387(1)	0.817225(4)	0.173875(3)	0.81722(5)	0.17387(1)
$\tilde{\chi}_1^0\tilde{\chi}_4^0$	0.0212680(5)	0.140018(3)	0.0212673(2)	0.140020(3)	0.021268(1)	0.14003(1)
$\tilde{\chi}_2^0\tilde{\chi}_2^0$	1.93986(1)	3.1013(3)	1.939907(9)	3.1011(2)	1.9399(1)	3.1012(2)
$\tilde{\chi}_2^0\tilde{\chi}_3^0$	—	1.07903(5)	—	1.07909(2)	—	1.07910(5)
$\tilde{\chi}_2^0\tilde{\chi}_4^0$	—	1.1685(1)	—	1.16852(6)	—	1.16868(5)
$\tilde{\chi}_3^0\tilde{\chi}_3^0$	—	2.66293(3)e-3	—	2.66298(4)e-3	—	2.6631(1)e-3
$\tilde{\chi}_3^0\tilde{\chi}_4^0$	—	4.7678(5)	—	4.76810(9)	—	4.7678(3)
$\tilde{\chi}_4^0\tilde{\chi}_4^0$	—	0.08799(1)	—	0.087994(6)	—	0.087993(5)
$\tilde{\chi}_1^+\tilde{\chi}_1^-$	137.16(2)	10.508(5)	137.161(3)	10.504(2)	137.17(1)	10.5073(5)
$\tilde{\chi}_2^+\tilde{\chi}_2^-$	—	4.4960(5)	—	4.4954(1)	—	4.49605(5)
$\tilde{\chi}_1^+\tilde{\chi}_2^-$	—	0.7742(2)	—	0.77407(5)	—	0.77420(5)
Z^0h^0	29.232(2)	1.5335(2)	29.235(3)	1.5337(3)	29.235(1)	1.53363(8)
Z^0H^0	3.04205(1)e-4	2.7107(3)e-4	3.0421(2)e-4	2.7112(5)e-4	3.0421(1)e-4	2.7109(1)e-4

A.4.18 $b\bar{b}$ processes

$\mathbf{b\bar{b} \to X}$						
Final	MadGraph/Helas		O'mega/Whizard		Amegic++/Sherpa	
state	0.5 TeV	2 TeV	0.5 TeV	2 TeV	0.5 TeV	2 TeV
$\tilde{b}_1\tilde{b}_1^*$	—	896.9(1)	—	896.92(3)	—	896.96(4)
$\tilde{b}_2\tilde{b}_2^*$	—	933.1(1)	—	933.08(3)	—	933.09(5)
$\tilde{b}_1\tilde{b}_2^*$	—	742.4(1)	—	742.46(2)	—	742.48(4)
$\tilde{t}_1\tilde{t}_1^*$	—	475.0(1)	—	475.02(2)	—	475.05(3)
$\tilde{t}_2\tilde{t}_2^*$	—	178.05(2)	—	178.057(7)	—	178.072(9)
$\tilde{t}_1\tilde{t}_2^*$	—	50.580(6)	—	50.581(2)	—	50.583(2)
$\tilde{\chi}_1^0\tilde{\chi}_1^0$	6.07876(2)	0.096781(3)	6.078898(4)	0.096786(2)	6.0788(3)	0.096782(4)
$\tilde{\chi}_1^0\tilde{\chi}_2^0$	27.5227(1)	0.44563(1)	27.52342(2)	0.445637(9)	27.523(1)	0.44564(2)
$\tilde{\chi}_1^0\tilde{\chi}_3^0$	11.19120(1)	0.13673(1)	11.191450(4)	0.1367346(7)	11.1909(6)	0.136730(7)
$\tilde{\chi}_1^0\tilde{\chi}_4^0$	4.487214(3)	0.106440(6)	4.487316(1)	0.1064429(7)	4.4876(2)	0.106455(6)
$\tilde{\chi}_2^0\tilde{\chi}_2^0$	31.52534(5)	3.5455(1)	31.52604(1)	3.54561(9)	31.525(1)	3.5458(2)
$\tilde{\chi}_2^0\tilde{\chi}_3^0$	—	0.92863(6)	—	0.928660(6)	—	0.92869(5)
$\tilde{\chi}_2^0\tilde{\chi}_4^0$	—	1.08817(1)	—	1.08823(1)	—	1.08829(6)
$\tilde{\chi}_3^0\tilde{\chi}_3^0$	—	0.26420(1)	—	0.264224(9)	—	0.26421(1)
$\tilde{\chi}_3^0\tilde{\chi}_4^0$	—	2.7853(2)	—	2.78541(3)	—	2.7856(1)
$\tilde{\chi}_4^0\tilde{\chi}_4^0$	—	0.46431(1)	—	0.46432(1)	—	0.46431(2)
$\tilde{\chi}_1^+\tilde{\chi}_1^-$	162.814(8)	13.912(2)	162.816(5)	13.9123(6)	162.802(8)	13.9123(7)
$\tilde{\chi}_2^+\tilde{\chi}_2^-$	—	104.770(3)	—	104.774(2)	—	104.784(5)
$\tilde{\chi}_1^+\tilde{\chi}_2^-$	—	6.7892(3)	—	6.78942(9)	—	6.7892(3)
h^0h^0	0.797127(4)	7.62(2)e-4	0.79711(4)	7.6246(1)e-4	0.79715(4)	7.6252(4)e-4
h^0H^0	—	0.06106(6)	—	0.061079(3)	—	0.061084(3)
H^0H^0	—	1.1850(5)	—	1.18500(9)	—	1.18503(6)
A^0A^0	—	1.1935(5)	—	1.19373(9)	—	1.19368(6)
A^0h^0	—	0.07681(6)	—	0.076825(4)	—	0.076823(4)
A^0H^0	—	2.406(1)	—	2.4064(1)	—	2.4066(1)
Z^0h^0	30.490(1)	1.782(1)	30.487(1)	1.78212(5)	30.492(2)	1.78209(9)
Z^0H^0	50.837(1)	16.98(2)	50.838(1)	16.9839(8)	50.840(3)	16.9849(8)
Z^0A^0	52.024(1)	17.01(2)	52.025(1)	17.0182(8)	52.023(3)	17.0163(9)
H^+H^-	—	2.3187(6)	—	2.31882(9)	—	2.3188(1)

A.4.19 qg processes

$\mathbf{qg \to X}$						
Process	MadGraph/Helas		O'mega/Whizard		Amegic++/Sherpa	
	0.5 TeV	2 TeV	0.5 TeV	2 TeV	0.5 TeV	2 TeV
$ug \to \tilde{u}_L\tilde{g}$	—	3405.0(5)	—	3405.2(3)	—	3404.8(2)
$ug \to \tilde{u}_R\tilde{g}$	—	3460.0(5)	—	3460.0(3)	—	3460.4(2)
$dg \to \tilde{d}_L\tilde{g}$	—	3390.0(5)	—	3390.5(3)	—	3390.0(2)
$dg \to \tilde{d}_R\tilde{g}$	—	3462.5(5)	—	3462.5(3)	—	3462.0(2)

A.4.20 Two identical fermions as initial state

$\mathbf{ff \to X}$						
Process	MadGraph/Helas		O'mega/Whizard		Amegic++/Sherpa	
	0.5 TeV	2 TeV	0.5 TeV	2 TeV	0.5 TeV	2 TeV
$e^-e^- \to \tilde{e}_L\tilde{e}_L$	520.30(4)	36.83(3)	520.31(3)	36.836(2)	520.32(3)	36.832(2)
$e^-e^- \to \tilde{e}_R\tilde{e}_R$	459.6(1)	28.65(3)	459.59(1)	28.650(3)	459.63(3)	28.651(2)
$e^-e^- \to \tilde{e}_L\tilde{e}_R$	160.04(1)	56.55(2)	159.96(2)	56.522(8)	160.04(2)	56.545(3)
$uu \to \tilde{u}_L\tilde{u}_L$	—	716.9(1)	—	716.973(4)	—	716.99(4)
$uu \to \tilde{u}_R\tilde{u}_R$	—	679.6(1)	—	679.627(4)	—	679.54(4)
$uu \to \tilde{u}_L\tilde{u}_R$	—	1212.52(6)	—	1212.52(5)	—	1212.60(6)
$dd \to \tilde{d}_L\tilde{d}_L$	—	712.6(1)	—	712.668(4)	—	712.68(4)
$dd \to \tilde{d}_R\tilde{d}_R$	—	667.4(1)	—	667.448(4)	—	667.38(3)
$dd \to \tilde{d}_L\tilde{d}_R$	—	1206.22(6)	—	1206.22(5)	—	1206.30(7)

A.5 Input parameters for the LHC and ILC simulations

```
BLOCK DCINFO  # Decay Program information
     1   SDECAY       # decay calculator
     2   1.1a         # version number
#
BLOCK SPINFO  # Spectrum calculator information
     1   SOFTSUSY     # spectrum calculator
     2   1.9          # version number
#
BLOCK MODSEL  # Model selection
     1     0   extSugra
#
BLOCK SMINPUTS  # Standard Model inputs
         1     1.27908957E+02   # alpha_em^-1(M_Z)^MSbar
         2     1.16637000E-05   # G_F [GeV^-2]
         3     1.18700000E-01   # alpha_S(M_Z)^MSbar
         4     9.11876000E+01   # M_Z pole mass
         5     2.50000000E+00   # mb(mb)^MSbar
         6     1.70000000E+02   # mt pole mass
         7     1.77699000E+00   # mtau pole mass
#
BLOCK MINPAR  # Input parameters - minimal models
         3     2.00000000E+01   # tanb
#
BLOCK EXTPAR  # Input parameters - non-minimal models
        34     5.68797374E+01   # meR(MX)
        35     1.89750900E+02   # mmuR(MX)
        36     8.00000000E+02   # mtauR(MX)
        45    -5.16238332E+02   # mcR(MX)
#
BLOCK MASS  # Mass Spectrum
# PDG code           mass       particle
        24     7.98256000E+01   # W+
        25     1.14451412E+02   # h
        35     3.00156029E+02   # H
        36     2.99997325E+02   # A
        37     3.10961504E+02   # H+
         5     2.50000000E+00   # b [running mass parameter]
   1000001     4.41227652E+02   # ~d_L
   2000001     4.37876121E+02   # ~d_R
   1000002     4.33747239E+02   # ~u_L
   2000002     4.35113863E+02   # ~u_R
   1000003     4.41227652E+02   # ~s_L
   2000003     4.37876121E+02   # ~s_R
   1000004     4.33747239E+02   # ~c_L
   2000004     4.35113863E+02   # ~c_R
```

```
   1000005     2.95364891E+02   # ~b_1
   2000005     3.99917523E+02   # ~b_2
   1000006     4.13841488E+02   # ~t_1
   2000006     9.78880993E+02   # ~t_2
   1000011     2.05024705E+02   # ~e_L
   2000011     2.05651082E+02   # ~e_R
   1000012     1.89267532E+02   # ~nu_eL
   1000013     2.05024705E+02   # ~mu_L
   2000013     2.05651082E+02   # ~mu_R
   1000014     1.89267532E+02   # ~nu_muL
   1000015     1.93593658E+02   # ~tau_1
   2000015     2.16389302E+02   # ~tau_2
   1000016     1.89240110E+02   # ~nu_tauL
   1000021     8.00886030E+02   # ~g
   1000022     4.68440180E+01   # ~chi_10
   1000023     1.12408563E+02   # ~chi_20
   1000025    -1.48090300E+02   # ~chi_30
   1000035     2.36766770E+02   # ~chi_40
   1000024     1.06599344E+02   # ~chi_1+
   1000037     2.37250120E+02   # ~chi_2+
#
BLOCK NMIX  # Neutralino Mixing Matrix
  1  1     8.95603865E-01   # N_11
  1  2    -9.72020087E-02   # N_12
  1  3     4.04193897E-01   # N_13
  1  4    -1.58343869E-01   # N_14
  2  1    -4.03047040E-01   # N_21
  2  2    -5.13608598E-01   # N_22
  2  3     5.77552867E-01   # N_23
  2  4    -4.90093846E-01   # N_24
  3  1    -1.49313892E-01   # N_31
  3  2     1.60265318E-01   # N_32
  3  3     6.53298812E-01   # N_33
  3  4     7.24721361E-01   # N_34
  4  1    -1.14682879E-01   # N_41
  4  2     8.37301025E-01   # N_42
  4  3     2.76153292E-01   # N_43
  4  4    -4.57727201E-01   # N_44
#
BLOCK UMIX  # Chargino Mixing Matrix U
  1  1    -3.90666525E-01   # U_11
  1  2     9.20532273E-01   # U_12
  2  1    -9.20532273E-01   # U_21
  2  2    -3.90666525E-01   # U_22
#
BLOCK VMIX  # Chargino Mixing Matrix V
  1  1    -6.55146178E-01   # V_11
```

```
  1  2     7.55502141E-01   # V_12
  2  1    -7.55502141E-01   # V_21
  2  2    -6.55146178E-01   # V_22
#
BLOCK STOPMIX  # Stop Mixing Matrix
  1  1     9.92937358E-01   # cos(theta_t)
  1  2     1.18639802E-01   # sin(theta_t)
  2  1    -1.18639802E-01   # -sin(theta_t)
  2  2     9.92937358E-01   # cos(theta_t)
#
BLOCK SBOTMIX  # Sbottom Mixing Matrix
  1  1     9.13760750E-02   # cos(theta_b)
  1  2     9.95816455E-01   # sin(theta_b)
  2  1    -9.95816455E-01   # -sin(theta_b)
  2  2     9.13760750E-02   # cos(theta_b)
#
BLOCK STAUMIX  # Stau Mixing Matrix
  1  1     7.16384593E-01   # cos(theta_tau)
  1  2     6.97705608E-01   # sin(theta_tau)
  2  1    -6.97705608E-01   # -sin(theta_tau)
  2  2     7.16384593E-01   # cos(theta_tau)
#
BLOCK ALPHA  # Higgs mixing
          -6.49713878E-02   # Mixing angle in the neutral Higgs boson sector
#
BLOCK HMIX Q=  6.12412338E+02  # DRbar Higgs Parameters
         1     1.33393949E+02   # mu(Q)MSSM
         2     1.94594998E+01   # tan
         3     2.43561981E+02   # higgs
         4     1.06061486E+05   # mA^2(Q)MSSM
#
BLOCK GAUGE Q=  6.12412338E+02  # The gauge couplings
     1     3.61902434E-01   # gprime(Q) DRbar
     2     6.48956611E-01   # g(Q) DRbar
     3     1.09052463E+00   # g3(Q) DRbar
#
BLOCK AU Q=  6.12412338E+02  # The trilinear couplings
  1  1     0.00000000E+00   # A_u(Q) DRbar
  2  2     0.00000000E+00   # A_c(Q) DRbar
  3  3    -5.80795469E+02   # A_t(Q) DRbar
#
BLOCK AD Q=  6.12412338E+02  # The trilinear couplings
  1  1     0.00000000E+00   # A_d(Q) DRbar
  2  2     0.00000000E+00   # A_s(Q) DRbar
  3  3    -1.84431338E+02   # A_b(Q) DRbar
#
BLOCK AE Q=  6.12412338E+02  # The trilinear couplings
```

```
  1  1     0.00000000E+00   # A_e(Q) DRbar
  2  2     0.00000000E+00   # A_mu(Q) DRbar
  3  3    -3.54951850E-01   # A_tau(Q) DRbar
#
BLOCK Yu Q=  6.12412338E+02  # The Yukawa couplings
  1  1     0.00000000E+00   # y_u(Q) DRbar
  2  2     0.00000000E+00   # y_c(Q) DRbar
  3  3     8.97145644E-01   # y_t(Q) DRbar
#
BLOCK Yd Q=  6.12412338E+02  # The Yukawa couplings
  1  1     0.00000000E+00   # y_d(Q) DRbar
  2  2     0.00000000E+00   # y_s(Q) DRbar
  3  3     2.73916822E-01   # y_b(Q) DRbar
#
BLOCK Ye Q=  6.12412338E+02  # The Yukawa couplings
  1  1     0.00000000E+00   # y_e(Q) DRbar
  2  2     0.00000000E+00   # y_mu(Q) DRbar
  3  3     2.03572357E-01   # y_tau(Q) DRbar
#
BLOCK MSOFT Q=  6.12412338E+02  # The soft SUSY breaking masses at the scale Q
         1     5.67130636E+01   # M_1(Q)
         2     1.89501347E+02   # M_2(Q)
         3     8.04258574E+02   # M_3(Q)
        21     7.62419102E+04   # mH1^2(Q)
        22    -2.17208514E+04   # mH2^2(Q)
        31     1.99736710E+02   # meL(Q)
        32     1.99736710E+02   # mmuL(Q)
        33     1.99710725E+02   # mtauL(Q)
        34     5.68797374E+01   # meR(MX)
        35     1.89750900E+02   # mmuR(MX)
        36     8.00000000E+02   # mtauR(MX)
        41     4.08231245E+02   # mqL1(Q)
        42     4.08231245E+02   # mqL2(Q)
        43     3.73390800E+02   # mqL3(Q)
        44     4.07778323E+02   # muR(Q)
        45    -5.16238332E+02   # mcR(MX)
        46     9.51532103E+02   # mtR(Q)
        47     4.08215309E+02   # mdR(Q)
        48     4.08215309E+02   # msR(Q)
        49     2.58317593E+02   # mbR(Q)
```

Particle	Γ [GeV]	Particle	Γ [GeV]
Z^0	2.4148	$\tilde{\chi}_2^0$	5.1100×10^{-5}
h^0	5.0080×10^{-3}	$\tilde{\chi}_3^0$	1.1622×10^{-2}
H^0	2.2924	$\tilde{\chi}_4^0$	1.0947
A^0	2.7750	$\tilde{b}_1$	0.53952
		$\tilde{b}_2$	3.4956

Table A.1: Relevant tree-level particle widths using the input of Appendix A.5.

Bibliography

[1] T. Sjöstrand, Comput. Phys. Commun. **82** (1994) 74.

[2] T. Sjöstrand, S. Mrenna and P. Skands, JHEP **0605** (2006) 026.

[3] G. Corcella *et al.*, JHEP **0101** (2001) 010.

[4] G. Corcella *et al.*, arXiv:hep-ph/0210213.

[5] S. Gieseke, A. Ribon, M. H. Seymour, P. Stephens and B. Webber, JHEP **0402** (2004) 005.

[6] `http://www.thep.lu.se/~torbjorn/pythiaaux/future.html`

[7] T. Gleisberg, S. Höche, F. Krauss, A. Schälicke, S. Schumann and J. C. Winter, JHEP **0402** (2004) 056.

[8] S. Gieseke, P. Stephens and B. Webber, JHEP **0312** (2003) 045.

[9] P. Stephens, arXiv:hep-ph/0408363.

[10] M. Gigg and P. Richardson, Eur. Phys. J. C **51** (2007) 989.

[11] T. Sjöstrand and P. Z. Skands, Eur. Phys. J. C **39** (2005) 129.

[12] S. Frixione and B. R. Webber, JHEP **0206** (2002) 029.

[13] S. Frixione, P. Nason and B. R. Webber, JHEP **0308** (2003) 007.

[14] P. Nason, JHEP **0411** (2004) 040.

[15] S. Frixione, P. Nason and C. Oleari, arXiv:0709.2092 [hep-ph].

[16] P. Nason and G. Ridolfi, JHEP **0608** (2006) 077.

[17] O. Latunde-Dada, S. Gieseke and B. Webber, JHEP **0702** (2007) 051.

[18] S. Frixione, P. Nason and G. Ridolfi, arXiv:0707.3088 [hep-ph].

[19] O. Latunde-Dada, arXiv:0708.4390 [hep-ph].

[20] S. Frixione and B. R. Webber, arXiv:hep-ph/0612272.

[21] F. Krauss, R. Kuhn and G. Soff, JHEP **0202** (2002) 044.

[22] T. Appelquist and C. W. Bernard, Phys. Rev. D **22** (1980) 200.

[23] T. Appelquist and G. H. Wu, Phys. Rev. D **48** (1993) 3235.

[24] N. Arkani-Hamed, S. Dimopoulos and G. R. Dvali, Phys. Lett. B **429** (1998) 263.

[25] I. Antoniadis, N. Arkani-Hamed, S. Dimopoulos and G. R. Dvali, Phys. Lett. B **436** (1998) 257.

[26] R. Kuhn, F. Krauss, B. Ivanyi and G. Soff, Comput. Phys. Commun. **134** (2001) 223.

[27] F. Krauss, A. Schälicke and G. Soff, Comput. Phys. Commun. **174** (2006) 876.

[28] S. Catani, F. Krauss, R. Kuhn and B. R. Webber, JHEP **0111** (2001) 063.

[29] F. Krauss, JHEP **0208** (2002) 015.

[30] F. Krauss, A. Schälicke, S. Schumann and G. Soff, Phys. Rev. D **70** (2004) 114009.

[31] A. Schälicke and F. Krauss, JHEP **0507** (2005) 018.

[32] see C. Buttar *et al.* in S. Alekhin *et al.*, arXiv:hep-ph/0601012; and Stefan Höche, Diploma thesis, Fakultät für Mathematik und Naturwissenschaften, Institut für Theoretische Physik, TU Dresden, 2004.

[33] T. Sjöstrand and M. van Zijl, Phys. Rev. D **36** (1987) 2019.

[34] S. Höche, F. Krauss and T. Teubner, arXiv:0705.4577 [hep-ph].

[35] B. Andersson, G. Gustafson, G. Ingelman and T. Sjöstrand, Phys. Rept. **97** (1983) 31.

[36] B. Andersson, Camb. Monogr. Part. Phys. Nucl. Phys. Cosmol. **7** (1997) 1.

[37] R. D. Field and R. P. Feynman, Nucl. Phys. B **136** (1978) 1.

[38] B. R. Webber, Nucl. Phys. B **238** (1984) 492.

[39] T. Sjöstrand, L. Lönnblad and S. Mrenna, arXiv:hep-ph/0108264.

[40] J. C. Winter, F. Krauss and G. Soff, Eur. Phys. J. C **36** (2004) 381.

[41] L. Lönnblad, JHEP **0205** (2002) 046.

[42] M. L. Mangano, M. Moretti and R. Pittau, Nucl. Phys. B **632** (2002) 343.

[43] S. Mrenna and P. Richardson, JHEP **0405** (2004) 040.

[44] M. L. Mangano, M. Moretti, F. Piccinini and M. Treccani, JHEP **0701** (2007) 013.

[45] L. Lönnblad, Comput. Phys. Commun. **71** (1992) 15.

[46] N. Lavesson and L. Lönnblad, JHEP **0507** (2005) 054.

[47] M. L. Mangano, M. Moretti, F. Piccinini, R. Pittau and A. D. Polosa, JHEP **0307** (2003) 001.

[48] T. Stelzer and W. F. Long, Comput. Phys. Commun. **81** (1994) 357.

[49] F. Maltoni and T. Stelzer, JHEP **0302** (2003) 027.

[50] J. Alwall *et al.*, arXiv:0706.2334 [hep-ph].

[51] A. Kanaki and C. G. Papadopoulos, Comput. Phys. Commun. **132** (2000) 306.

[52] C. G. Papadopoulos and M. Worek, Eur. Phys. J. C **50** (2007) 843.

[53] S. Catani, Y. L. Dokshitzer, M. Olsson, G. Turnock and B. R. Webber, Phys. Lett. B **269** (1991) 432.

[54] S. Catani, Y. L. Dokshitzer and B. R. Webber, Phys. Lett. B **285** (1992) 291.

[55] S. Catani, Y. L. Dokshitzer, M. H. Seymour and B. R. Webber, Nucl. Phys. B **406** (1993) 187.

[56] G. C. Blazey *et al.*, arXiv:hep-ex/0005012.

[57] S. Abachi *et al.* [D0 Collaboration], Phys. Rev. Lett. **75** (1995) 1456.

[58] T. Affolder *et al.* [CDF Collaboration], Phys. Rev. D **64** (2001) 052001.

[59] V. M. Abazov *et al.* [D0 Collaboration], Phys. Rev. D **66** (2002) 012001.

[60] W. Ashmanskas *et al.*, the Tevatron Electroweak Working Group, CDF and D0 Collaborations, arXiv:hep-ex/0311039.

[61] C. Albajar *et al.* [UA1 Collaboration], Phys. Lett. B **253** (1991) 503.

[62] J. Alitti *et al.* [UA2 Collaboration], Phys. Lett. B **276** (1992) 365.

[63] F. Abe *et al.* [CDF Collaboration], Phys. Rev. D **52** (1995) 2624.

[64] B. Abbott *et al.* [D0 Collaboration], Phys. Rev. D **61** (2000) 072001.

[65] T. Affolder *et al.* [CDF Collaboration], Phys. Rev. Lett. **85** (2000) 3347.

[66] V. M. Abazov *et al.* [D0 Collaboration], Phys. Rev. D **66** (2002) 032008.

[67] ATLAS Collaboration, "Detector and Physics Performance Technical Design Report", CERN/LHCC/99-15, vol. 2.

[68] S. Haywood *et al.*, arXiv:hep-ph/0003275.

[69] V. A. Khoze, A. D. Martin, R. Orava and M. G. Ryskin, Eur. Phys. J. C **19** (2001) 313.

[70] M. Dittmar, F. Pauss and D. Zurcher, Phys. Rev. D **56** (1997) 7284.

[71] A. D. Martin, R. G. Roberts, W. J. Stirling and R. S. Thorne, Eur. Phys. J. C **14** (2000) 133.

[72] W. T. Giele and S. A. Keller, arXiv:hep-ph/0104053.

[73] F. Krauss, A. Schälicke, S. Schumann and G. Soff, Phys. Rev. D **72** (2005) 054017.

[74] T. Gleisberg, F. Krauss, A. Schälicke, S. Schumann and J. C. Winter, Phys. Rev. D **72** (2005) 034028.

[75] B. Abbott *et al.* [D0 Collaboration], Phys. Lett. B **513** (2001) 292.

[76] T. Affolder *et al.* [CDF Collaboration], Phys. Rev. Lett. **84** (2000) 845.

[77] J. Campbell and R. K. Ellis, Phys. Rev. D **65** (2002) 113007.

[78] J. Campbell, R. K. Ellis and D. L. Rainwater, Phys. Rev. D **68** (2003) 094021.

[79] `http://www-d0.fnal.gov/Run2Physics/WWW/results/prelim/HIGGS/H15/`

[80] T. Sjöstrand, L. Lönnblad, S. Mrenna and P. Skands, arXiv:hep-ph/0308153.

[81] `http://www.phys.ufl.edu/~rfield/cdf/tunes/py_tuneA.html`

[82] Henrik Nilsen, private communication.

[83] D. L. Rainwater and D. Zeppenfeld, Phys. Rev. D **60** (1999) 113004 [Erratum-ibid. D **61** (2000) 099901].

[84] J. Alwall *et al.*, arXiv:0706.2569 [hep-ph].

[85] G. Gustafson, Phys. Lett. B **175** (1986) 453.

[86] G. Gustafson and U. Pettersson, Nucl. Phys. B **306** (1988) 746.

[87] B. Andersson, G. Gustafson and L. Lönnblad, Nucl. Phys. B **339** (1990) 393.

[88] B. Andersson, G. Gustafson, L. Lönnblad and U. Pettersson, Z. Phys. C **43** (1989) 625.

[89] L. Lönnblad, Nucl. Phys. B **458** (1996) 215.

[90] A. Aktas *et al.* [H1 Collaboration], Eur. Phys. J. C **46** (2006) 27.

[91] L. Lönnblad, Z. Phys. C **65** (1995) 285.

[92] F. Caravaglios, M. L. Mangano, M. Moretti and R. Pittau, Nucl. Phys. B **539** (1999) 215.

[93] J. Alwall *et al.*, Comput. Phys. Commun. **176** (2007) 300.

[94] C. G. Papadopoulos, Comput. Phys. Commun. **137** (2001) 247.

[95] C. Åberg, Diploma thesis, Lund University, 2004, Lund preprint LU-TP 04-25.

[96] S. Schumann and F. Krauss, arXiv:0709:1027 [hep-ph].

[97] S. Catani and M. H. Seymour, Nucl. Phys. B **485** (1997) 291 [Erratum-ibid. B **510** (1998) 503].

[98] S. Catani, S. Dittmaier, M. H. Seymour and Z. Trocsanyi, Nucl. Phys. B **627** (2002) 189.

[99] Michael Dinsdale, Marko Ternick and Stefan Weinzierl, arXiv:0709.1026 [hep-ph].

[100] Z. Nagy and D. E. Soper, JHEP **0510** (2005) 024.

[101] Z. Nagy and D. E. Soper, arXiv:hep-ph/0601021.

[102] D. A. Kosower, Phys. Rev. D **57** (1998) 5410.

[103] J. M. Campbell, M. A. Cullen and E. W. N. Glover, Eur. Phys. J. C **9** (1999) 245.

[104] W. T. Giele, D. A. Kosower and P. Z. Skands, arXiv:0707.3652 [hep-ph].

[105] J. M. Campbell and R. K. Ellis, Phys. Rev. D **60** (1999) 113006.

[106] W. Beenakker, S. Dittmaier, M. Kramer, B. Plumper, M. Spira and P. M. Zerwas, Phys. Rev. Lett. **87** (2001) 201805.

[107] Z. Nagy, Phys. Rev. Lett. **88** (2002) 122003.

[108] V. Del Duca, F. Maltoni, Z. Nagy and Z. Trocsanyi, JHEP **0304** (2003) 059.

[109] J. Campbell, R. K. Ellis, F. Maltoni and S. Willenbrock, Phys. Rev. D **69** (2004) 074021.

[110] J. Campbell, R. K. Ellis and F. Tramontano, Phys. Rev. D **70** (2004) 094012.

[111] S. Dittmaier, P. Uwer and S. Weinzierl, Phys. Rev. Lett. **98** (2007) 262002.

[112] T. Kinoshita, J. Math. Phys. **3** (1962) 650.

[113] T. D. Lee and M. Nauenberg, Phys. Rev. **133** (1964) B1549.

[114] R. K. Ellis, W. J. Stirling and B. R. Webber, Camb. Monogr. Part. Phys. Nucl. Phys. Cosmol. **8** (1996) 1.

[115] T. Sjöstrand, Phys. Lett. B **157** (1985) 321.

[116] M. Bengtsson, T. Sjöstrand and M. van Zijl, Z. Phys. C **32** (1986) 67.

[117] H. U. Bengtsson and T. Sjöstrand, Comput. Phys. Commun. **46** (1987) 43.

[118] G. Marchesini and B. R. Webber, Nucl. Phys. B **310** (1988) 461.

[119] B. I. Ermolaev and V. S. Fadin, JETP Lett. **33** (1981) 269 [Pisma Zh. Eksp. Teor. Fiz. **33** (1981) 285].

[120] A. H. Mueller, Phys. Lett. B **104** (1981) 161.

[121] Y. L. Dokshitzer, V. S. Fadin and V. A. Khoze, Z. Phys. C **18** (1983) 37.

[122] Y. L. Dokshitzer, V. A. Khoze, S. I. Troian and A. H. Mueller, Rev. Mod. Phys. **60** (1988) 373.

[123] H. E. Haber and G. L. Kane, Phys. Rept. **117** (1985) 75.

[124] T. Appelquist, H. C. Cheng and B. A. Dobrescu, Phys. Rev. D **64** (2001) 035002.

[125] A. Djouadi, arXiv:hep-ph/0503173.

[126] D. A. Dicus and S. Willenbrock, Phys. Rev. D **39** (1989) 751.

[127] E. Boos and T. Plehn, Phys. Rev. D **69** (2004) 094005.

[128] J. C. Collins and X. m. Zu, JHEP **0206** (2002) 018.

[129] B. P. Kersevan and I. Hinchliffe, JHEP **0609** (2006) 033.

[130] K. Hagiwara *et al.*, Phys. Rev. D **73** (2006) 055005.

[131] D. Berdine, N. Kauer and D. Rainwater, arXiv:hep-ph/0703058.

[132] R. D. Field, *Redwood City, USA: Addison-Wesley (1989) 366 p. (Frontiers in physics, 77).*

[133] G. Miu and T. Sjöstrand, Phys. Lett. B **449** (1999) 313.

[134] G. Abbiendi *et al.* [OPAL Collaboration], Eur. Phys. J. C **20** (2001) 601.

[135] P. Abreu *et al.* [DELPHI Collaboration], Z. Phys. C **59** (1993) 357.

[136] R. Akers *et al.* [OPAL Collaboration], Z. Phys. C **65** (1995) 367.

[137] R. Barate *et al.* [ALEPH Collaboration], Z. Phys. C **76** (1997) 1.

[138] A. Gehrmann-De Ridder, T. Gehrmann, E. W. N. Glover and G. Heinrich, arXiv:0707.1285 [hep-ph].

[139] A. Signer, Comput. Phys. Commun. **106** (1997) 125.

[140] Z. Nagy and Z. Trocsanyi, Phys. Rev. D **59** (1999) 014020 [Erratum-ibid. D **62** (2000) 099902].

[141] K. Hamacher and M. Weierstall, arXiv:hep-ex/9511011.

[142] A. Buckley, arXiv:0708.2655 [hep-ph].

[143] P. Abreu *et al.* [DELPHI Collaboration], Z. Phys. C **73** (1996) 11.

[144] H. Hoeth, Diploma Thesis, Fachbereich Physik, Bergishce Universität Wuppertal, 2003 [WUD 03-11] and references therein.

[145] Z. Nagy and Z. Trocsanyi, Phys. Rev. D **57** (1998) 5793.

[146] M. Bengtsson and P. M. Zerwas, Phys. Lett. B **208** (1988) 306.

[147] O. Nachtmann and A. Reiter, Z. Phys. C **16** (1982) 45.

[148] J. Pumplin, D. R. Stump, J. Huston, H. L. Lai, P. Nadolsky and W. K. Tung, JHEP **0207** (2002) 012.

[149] G. Altarelli, R. K. Ellis and G. Martinelli, Nucl. Phys. B **157** (1979) 461.

[150] J. Kubar-Andre and F. E. Paige, Phys. Rev. D **19** (1979) 221.

[151] R. Hamberg, W. L. van Neerven and T. Matsuura, Nucl. Phys. B **359** (1991) 343 [Erratum, ibid. B **644** (2002) 403].

[152] R. V. Harlander and W. B. Kilgore, Phys. Rev. Lett. **88** (2002) 201801.

[153] C. Anastasiou, L. J. Dixon, K. Melnikov and F. Petriello, Phys. Rev. D **69** (2004) 094008.

[154] R. J. Gonsalves, J. Pawlowski and C. F. Wai, Phys. Rev. D **40** (1989) 2245.

[155] R. K. Ellis and S. Veseli, Nucl. Phys. B **511** (1998) 649.

[156] C. Balazs and C. P. Yuan, Phys. Rev. D **56** (1997) 5558.

[157] A. Kulesza, G. Sterman and W. Vogelsang, Phys. Rev. D **66** (2002) 014011.

[158] R. J. Gonsalves, N. Kidonakis and A. S. Vera, Phys. Rev. Lett. **95** (2005) 222001.

[159] A. Vogt, S. Moch and J. A. M. Vermaseren, Nucl. Phys. B **691** (2004) 129.

[160] Z. Kunszt and D. E. Soper, Phys. Rev. D **46** (1992) 192.

[161] W. T. Giele, E. W. N. Glover and D. A. Kosower, Nucl. Phys. B **403** (1993) 633.

[162] W. B. Kilgore and W. T. Giele, arXiv:hep-ph/9903361.

[163] Z. Trocsanyi, Phys. Rev. Lett. **77** (1996) 2182.

[164] Z. Bern, L. J. Dixon and D. A. Kosower, JHEP **0001** (2000) 027.

[165] C. Anastasiou, E. W. N. Glover, C. Oleari and M. E. Tejeda-Yeomans, Nucl. Phys. B **601** (2001) 341.

[166] C. Anastasiou, E. W. N. Glover, C. Oleari and M. E. Tejeda-Yeomans, Nucl. Phys. B **605** (2001) 486.

[167] E. W. N. Glover, C. Oleari and M. E. Tejeda-Yeomans, Nucl. Phys. B **605** (2001) 467.

[168] Z. Bern, A. De Freitas and L. J. Dixon, JHEP **0203** (2002) 018.

[169] A. Daleo, T. Gehrmann and D. Maitre, JHEP **0704** (2007) 016.

[170] B. Abbott *et al.* [D0 Collaboration], Phys. Rev. Lett. **82** (1999) 2457.

[171] V. M. Abazov *et al.* [D0 Collaboration], Phys. Rev. Lett. **94** (2005) 221801.

[172] V. A. Khoze and W. Ochs, Int. J. Mod. Phys. A **12** (1997) 2949.

[173] F. Abe *et al.* [CDF Collaboration], Phys. Rev. D **50** (1994) 5562.

[174] M. Bengtsson and T. Sjöstrand, Nucl. Phys. B **289** (1987) 810.

[175] F. Krauss and J. Winter, in preparation.

[176] see *e.g.* : W. Hollik *et al.*, Acta Phys. Polon. B **35** (2004) 2533; A. Djouadi, arXiv:hep-ph/0503172; W. Kilian, "Electroweak symmetry breaking: The bottom-up approach", New York, USA: Springer (2003).

[177] `http://www-cdf.fnal.gov/physics/exotic/exotic.html`; `http://www-d0.fnal.gov/public/new/new_public.html`.

[178] G. Weiglein *et al.* [LHC/LC Study Group Collaboration], arXiv:hep-ph/0410364.

[179] S. Dawson, E. Eichten and C. Quigg, Phys. Rev. D **31** (1985) 1581.

[180] A. Bartl, H. Fraas and W. Majerotto, Z. Phys. C **30** (1986) 441; A. Bartl, H. Fraas and W. Majerotto, Nucl. Phys. B **278** (1986) 1.

[181] A. J. Barr, Phys. Lett. B **596** (2004) 205; J. M. Smillie and B. R. Webber, JHEP **0510** (2005) 069; A. J. Barr, JHEP **0602**, (2006) 042; A. Alves, O. Eboli and T. Plehn, Phys. Rev. D **74** (2006) 095010; C. Athanasiou, C. G. Lester, J. M. Smillie and B. R. Webber, JHEP **0608** (2006) 055.

[182] H. Bachacou, I. Hinchliffe and F. E. Paige, Phys. Rev. D **62** (2000) 015009; B. C. Allanach, C. G. Lester, M. A. Parker and B. R. Webber, JHEP **0009** (2000) 004; B. K. Gjelsten, D. J. Miller and P. Osland, JHEP **0412** (2004) 003; B. K. Gjelsten, D. J. Miller and P. Osland, JHEP **0506** (2005) 015; D. J. Miller, P. Osland and A. R. Raklev, JHEP **0603** (2006) 034.

[183] T. Plehn, D. Rainwater and P. Skands, Phys. Lett. B **645** (2007) 217.

[184] G. C. Cho, K. Hagiwara, J. Kanzaki, T. Plehn, D. Rainwater and T. Stelzer, Phys. Rev. D **73** (2006) 054002.

[185] `http://theorie.physik.uni-wuerzburg.de/~ohl/omega`; T. Ohl, arXiv:hep-ph/0011243; M. Moretti, T. Ohl and J. Reuter, LC-TOOL-2001-040 [arXiv:hep-ph/0102195]; T. Ohl, J. Reuter and C. Schwinn, *O'Mega*, in preparation.

[186] `http://www-ttp.physik.uni-karlsruhe.de/whizard`; W. Kilian, T. Ohl and J. Reuter, arXiv:0708.4233 [hep-ph].

[187] P. Skands, S. Schumann *et al.*, JHEP **0407** (2004) 036.

[188] B. C. Allanach, Comput. Phys. Commun. **143** (2002) 305.

[189] A. Djouadi, J. L. Kneur and G. Moultaka, arXiv:hep-ph/0211331; W. Porod, Comput. Phys. Commun. **153** (2003) 275.

[190] see *e.g.* : W. Hollik, E. Kraus and D. Stöckinger, Eur. Phys. J. C **23** (2002) 735; W. Hollik, E. Kraus, M. Roth, C. Rupp, K. Sibold and D. Stöckinger, Nucl. Phys. B **639** (2002) 3; D. Stöckinger, JHEP **0503** (2005) 076.

[191] B. Lee, C. Quigg and H. Thacker, Phys. Rev. Lett. 38 (1977) 883; Phys. Rev. D16 (1977) 1519.

[192] J. F. Gunion, H. E. Haber and J. Wudka, Phys. Rev. D **43** (1991) 904.

[193] M. Carena, J. R. Espinosa, M. Quiros and C. E. M. Wagner, Phys. Lett. B **355** (1995) 209; Prof. S. Heinemeyer, W. Hollik, H. Rzehak and G. Weiglein, Eur. Phys. J. C **39** (2005) 465; T. Hahn *et al*, arXiv:hep-ph/0507009.

[194] A. Denner, H. Eck, O. Hahn and J. Kublbeck, Nucl. Phys. B **387** (1992) 467; A. Denner, H. Eck, O. Hahn and J. Kublbeck, Phys. Lett. B **291** (1992) 278.

[195] E. Boos and T. Ohl, Phys. Rev. Lett. **83** (1999) 480.

[196] W. Beenakker *et al.*, Nucl. Phys. B **500** (1997) 255; E. N. Argyres *et al.*, Phys. Lett. B **358** (1995) 339; U. Baur and D. Zeppenfeld, Phys. Rev. Lett. **75** (1995) 1002; G. Passarino, Nucl. Phys. B **574** (2000) 451; A. Denner, S. Dittmaier, M. Roth and D. Wackeroth, Nucl. Phys. B **560** (1999) 33; W. Beenakker, F. A. Berends and A. P. Chapovsky, Nucl. Phys. B **573** (2000) 503; A. Denner and S. Dittmaier, Phys. Rev. D **54** (1996) 4499.

[197] A. Denner, S. Dittmaier, M. Roth and D. Wackeroth, Nucl. Phys. B **560** (1999) 33.

[198] S. Dittmaier and M. Roth, Nucl. Phys. B **642** (2002) 307.

[199] R. Kleiss and W. J. Stirling, Nucl. Phys. B **262** (1985) 235.

[200] A. Ballestrero, E. Maina and S. Moretti, Nucl. Phys. B **415** (1994) 265.

[201] T. Gleisberg, F. Krauss, K. T. Matchev, A. Schälicke, S. Schumann and G. Soff, JHEP **0309** (2003) 001.

[202] S. Schumann, Diploma thesis, Fakultät für Mathematik und Naturwissenschaften, Institut für Theoretische Physik, TU Dresden, 2002.

[203] T. Gleisberg, Diploma thesis, Fakultät für Mathematik und Naturwissenschaften, Institut für Theoretische Physik, TU Dresden, 2003.

[204] F. A. Berends, R. Pittau and R. Kleiss, Nucl. Phys. B **424** (1994) 308 [arXiv:hep-ph/9404313].

[205] R. Kleiss and R. Pittau, Comput. Phys. Commun. **83** (1994) 141 [arXiv:hep-ph/9405257].

[206] G. P. Lepage, CLNS-80/447.

[207] `http://www.fuw.edu.pl/~rosiek/physics/prd41.html`; J. Rosiek, Phys. Rev. **D41** (1990) 3464.

[208] L. J. Hall and L. Randall, Phys. Rev. Lett. **65** (1990) 2939.

[209] for a review see *e.g.* : F. Gabbiani, E. Gabrielli, A. Masiero and L. Silvestrini, Nucl. Phys. B **477** (1996) 321; G. Hiller, eConf **C030603**, MAR02 (2003) [arXiv:hep-ph/0308180].

[210] H. Murayama, I. Watanabe and K. Hagiwara, KEK-91-11; T. Stelzer, F. Long, Comput. Phys. Commun. **81** (1994) 357.

[211] W. Beenakker, R. Höpker, M. Spira and P. M. Zerwas, Nucl. Phys. B **492** (1997) 51; T. Plehn, arXiv:hep-ph/9809319; W. Beenakker, M. Krämer, T. Plehn, M. Spira and P. M. Zerwas, Nucl. Phys. B **515** (1998) 3; W. Beenakker, M. Klasen, M. Krämer, T. Plehn, M. Spira and P. M. Zerwas, Phys. Rev. Lett. **83** (1999) 3780.

[212] T. Plehn, M. Spira and P. M. Zerwas, Nucl. Phys. B **479** (1996) 46 [Erratum-ibid. B **531** (1998) 655]; A. Krause, T. Plehn, M. Spira and P. M. Zerwas, Nucl. Phys. B **519** (1998) 85.

[213] G.-C. Cho and K. Hagiwara, unpublished.

[214] E. Boos *et al.*, arXiv:hep-ph/0109068.

[215] Xavier Leroy, *The Objective Caml system, documentation and user's guide*, Technical Report, INRIA, 1997.

[216] J. Reuter, unpublished; M. Kuroda, KEK-CP-080, arXiv:hep-ph/9902340.

[217] T. Ohl, Comput. Phys. Commun. **120** (1999) 13.

[218] B. C. Allanach *et al.*, Eur. Phys. J. C **25** (2002) 113; N. Ghodbane and H. U. Martyn, arXiv:hep-ph/0201233.

[219] T. Gleisberg, F. Krauss, C. G. Papadopoulos, A. Schälicke and S. Schumann, Eur. Phys. J. C **34** (2004) 173.

[220] A. Djouadi, W. Kilian, M. Mühlleitner and P. M. Zerwas, Eur. Phys. J. C **10** (1999) 45; A. Djouadi, W. Kilian, M. Mühlleitner and P. M. Zerwas, Eur. Phys. J. C **10** (1999) 27; T. Plehn and M. Rauch, Phys. Rev. D **72** (2005) 053008.

[221] H. L. Lai *et al.* [CTEQ Collaboration], Eur. Phys. J. C **12** (2000) 375.

[222] T. Plehn, D. L. Rainwater and D. Zeppenfeld, Phys. Lett. B **454** (1999) 297; T. Plehn, D. L. Rainwater and D. Zeppenfeld, Phys. Rev. D **61** (2000) 093005; M. Schumacher, arXiv:hep-ph/0410112.

[223] O. J. P. Eboli and D. Zeppenfeld, Phys. Lett. B **495** (2000) 147; M. Dührssen, S. Heinemeyer, H. Logan, D. Rainwater, G. Weiglein and D. Zeppenfeld, Phys. Rev. D **70** (2004) 113009.

[224] `http://lepewwg.web.cern.ch/LEPEWWG`

[225] for recent updates see *e.g.*: M. Faisst, J. H. Kühn, T. Seidensticker and O. Veretin, Nucl. Phys. B **665** (2003) 649; R. Boughezal, J. B. Tausk and J. J. van der Bij, Nucl. Phys. B **713** (2005) 278; for a review including MSSM corrections, see *e.g.* S. Heinemeyer, W. Hollik and G. Weiglein, arXiv:hep-ph/0412214.

[226] G. W. Bennett *et al.* [Muon g-2 Collaboration], Phys. Rev. Lett. **92** (2004) 161802; R. R. Akhmetshin *et al.* [CMD-2 Collaboration], Phys. Lett. B **578** (2004) 285; A. Aloisio *et al.* [KLOE Collaboration], Phys. Lett. B **606** (2005) 12.

[227] see *e.g.* : M. Davier, S. Eidelman, A. Höcker and Z. Zhang, Eur. Phys. J. C **31** (2003) 503; F. Jegerlehner, Nucl. Phys. Proc. Suppl. **126** (2004) 325; K. Hagiwara, A. D. Martin, D. Nomura and T. Teubner, Phys. Rev. D **69** (2004) 093003; A. Czarnecki and W. J. Marciano, Phys. Rev. D **64** (2001) 013014; S. P. Martin and J. D. Wells, Phys. Rev. D **67** (2003) 015002; S. Heinemeyer, D. Stöckinger and G. Weiglein, Nucl. Phys. B **699** (2004) 103.

[228] K. Abe *et al.* [Belle Collaboration], Phys. Lett. B **511** (2001) 151; B. Aubert *et al.* [BaBar Collaboration], arXiv:hep-ex/0207076; S. Chen *et al.* [CLEO Collaboration], Phys. Rev. Lett. **87** (2001) 251807; R. Barate *et al.* [ALEPH Collaboration], Phys. Lett. B **429** (1998) 169; H. F. A. Group (HFAG), arXiv:hep-ex/0505100.

[229] see *e.g.*: P. L. Cho, M. Misiak and D. Wyler, Phys. Rev. D **54** (1996) 3329; J. L. Hewett and J. D. Wells, Phys. Rev. D **55** (1997) 5549; F. M. Borzumati and C. Greub, Phys. Rev. D **58** (1998) 074004 and Phys. Rev. D **59** (1999) 057501; G. Hiller and F. Krüger, Phys. Rev. D **69**, 074020 (2004).

[230] D. Acosta *et al.* [CDF Collaboration], Phys. Rev. Lett. **93** (2004) 032001; V. M. Abazov *et al.* [D0 Collaboration], Phys. Rev. Lett. **94** (2005) 071802.

[231] see *e.g.*: A. J. Buras, Phys. Lett. B **566** (2003) 115; J. L. Hewett, S. Nandi and T. G. Rizzo, Phys. Rev. D **39** (1989) 250; M. J. Savage, Phys. Lett. B **266** (1991) 135; C. Bobeth, T. Ewerth, F. Krüger and J. Urban, Phys. Rev. D **64** (2001) 074014.

[232] J. R. Ellis, J. S. Hagelin, D. V. Nanopoulos, K. A. Olive and M. Srednicki, Nucl. Phys. B **238** (1984) 453; H. Goldberg, Phys. Rev. Lett. **50** (1983) 1419; for reviews on neutralino dark matter, see G. Jungman, M. Kamionkowski and K. Griest, Phys. Rept. **267** (1996) 195; G. Bertone, D. Hooper and J. Silk, Phys. Rept. **405** (2005) 279; code used for the numerical analysis: G. Belanger, F. Boudjema, A. Pukhov and A. Semenov, Comput. Phys. Commun. **174**, 577 (2006).

[233] C. L. Bennett *et al.*, Astrophys. J. Suppl. **148** (2003) 1.

[234] B. C. Allanach, C. M. Harris, M. A. Parker, P. Richardson and B. R. Webber, JHEP **0108** (2001) 051; A. C. Kraan, Eur. Phys. J. C **37** (2004) 91; W. Kilian, T. Plehn, P. Richardson and E. Schmidt, Eur. Phys. J. C **39** (2005) 229; A. Arvanitaki, S. Dimopoulos, A. Pierce, S. Rajendran and J. Wacker, arXiv:hep-ph/0506242; A. C. Kraan, J. B. Hansen and P. Nevski, arXiv:hep-ex/0511014.

[235] J. C. Collins and W. K. Tung, Nucl. Phys. B **278** (1986) 934; F. I. Olness and W. K. Tung, Nucl. Phys. B **308** (1988) 813; M. A. G. Aivazis, J. C. Collins, F. I. Olness and W. K. Tung, Phys. Rev. D **50** (1994) 3102; J. C. Collins, Phys. Rev. D **58** (1998) 094002; M. Krämer, F. I. Olness and D. E. Soper, Phys. Rev. D **62** (2000) 096007.

[236] D. Berdine and D. Rainwater, Phys. Rev. D **72** (2005) 075003.

[237] S. Dittmaier, M. Krämer and M. Spira, Phys. Rev. D **70** (2004) 074010; S. Dawson, C. B. Jackson, L. Reina and D. Wackeroth, Phys. Rev. D **69** (2004) 074027; J. Campbell *et al.*, arXiv:hep-ph/0405302.

[238] J. Campbell, R. K. Ellis, F. Maltoni and S. Willenbrock, Phys. Rev. D **67** (2003) 095002; T. Plehn, Phys. Rev. D **67** (2003) 014018; R. V. Harlander and W. B. Kilgore, Phys. Rev. D **68** (2003) 013001; F. Maltoni, T. McElmurry and S. Willenbrock, Phys. Rev. D **72** (2005) 074024.

[239] J. Alwall and J. Rathsman, JHEP **0412** (2004) 050.

[240] E. L. Berger, T. Han, J. Jiang and T. Plehn, Phys. Rev. D **71** (2005) 115012; A. Alves and T. Plehn, Phys. Rev. D **71** (2005) 115014.

[241] P. Richardson, JHEP **0111** (2001) 029.

[242] W. Öller, H. Eberl and W. Majerotto, Phys. Lett. B **590** (2004) 273; T. Fritzsche and W. Hollik, arXiv:hep-ph/0407095; W. Kilian, J. Reuter and T. Robens, Eur. Phys. J. C **48** (2006) 389.

[243] M. Mühlleitner, A. Djouadi and Y. Mambrini, Comput. Phys. Commun. **168** (2005) 46.

[244] 3rd order LLA for ISR, as used by RacoonWW; see *e.g.*: A. Denner, S. Dittmaier, M. Roth and D. Wackeroth, Nucl. Phys. B **587** (2000) 67.

[245] T. Ohl, Comput. Phys. Commun. **101** (1997) 269.

Erklärungen

Hiermit erkläre ich, dass ich die vorliegende Arbeit ohne unzulässige Hilfe Dritter und ohne Benutzung anderer als der angegebenen Hilfmittel angefertigt habe; die aus fremden Quellen übernommenen Gedanken sind als solche kenntlich gemacht. Die Arbeit wurde bisher weder im Inland noch im Ausland in gleicher oder ähnlicher Form einer anderen Prüfungsbehörde vorgelegt.

Die vorliegende Arbeit wurde am Institut für Theretische Physik der Technischen Universtät Dresden unter wissenschaftlicher Betreuung von Herrn Prof. Dr. Gerhard Soff† und Herrn Dr. Frank Krauss angefertigt.

Es haben keine früheren erfolglosen Promotionsvorhaben stattgefunden.

Hiermit erkenne ich die Promotionsordnung der Fakultät Mathematik und Naturwissenschaften der Technischen Universität Dresden vom 20. März 2000 an.

Dresden, den 20. September 2007

Steffen Schumann